ATRM: Asteroid Thermal & Reflected light Model

Investigating the influence of reflected light at the four wavelength bands of the Wide-field Infrared Survey Explorer.

A. A. Gunessee

Master Thesis
Faculty of Aerospace Engineering
Delft University of Technology

TUDelft

ATRM: Asteroid Thermal & Reflected light Model

Investigating the influence of reflected light at the four wavelength bands of the Wide-field Infrared Survey Explorer.

by

A. A. Gunessee

to obtain the degree of Master of Science in Aerospace Engineering
at the Delft University of Technology,

Student number:	4204662	
Thesis committee:	Dr. A. Menicucci,	TU Delft, supervisor
	Dr. D. M. Stam,	TU Delft, supervisor
	Dr. A. Cervone,	TU Delft, chairman
	Dr. S. M. Cazaux,	TU Delft, examiner

An electronic version of this thesis is available at http://repository.tudelft.nl/.

Cover image is composite with satellite courtesy of JAXA, Earth courtesy of NASA, and the rest obtained from public domain or self-made.

TUDelft

Preface

I would not have been able to be where I currently am without the help and support of some people, so I would like to take this opportunity to express my sincere gratitude to them. Thank you to Dr. Cazaux and Dr. Cervone for taking the time and being part of my graduation committee. Thank you to my supervisors, Dr. Menicucci for your flexibility, and especially Dr. Stam for your understanding and support. During the literature and verification/validation phase of my master thesis, I would like to extend my thanks to Dr. Delbo, Dr. Durech, Dr. Hapke, and especially Dr. Rozitis for their invaluable inputs and clarifications. Moreover, thank you Yash, Dominique, and Abdur for your help during the coding and debugging process. Thank you to all my friends in Delft and elsewhere who made my university time an unforgettable experience. A special thank you to my Slopend friends Arthur, Yannic, Philip and Felix. Looking forward to our next 'outje'. Thank you Daniela, Alex and Jeffrey for your support. Thank you Andrei and Théo for those special evenings. And a very special thank you to Lenka and Jordi. Thank you Aurélia for your support, push, and sweetness. And finally, the two most important people without whom I perhaps would not have made in general, my dad and especially my mum. Thank you very much!

A. A. Gunessee

Abstract

Over the last five decades, thermal modelling of airless minor planetary bodies such as asteroids have experienced significant improvements. However, at lower wavelengths of the mid-infrared range, thermal models such as the widely used Near-Earth Asteroid Model (NEATM) are still considered unreliable since reflected light starts contributing significantly towards the observed flux density. Through a controversy related to the Wide-field Infrared Survey Explorer (WISE) mission, which was an infrared survey telescope with four observational bands found at 3.4, 4.6, 12, and 22 microns, Nathan Myhrvold suggested that the thermal modelling carried out did not properly account for reflected light and that the results, especially derived from the first two observation bands, were compromised since Kirchhoff's law of thermal radiation was violated. To date, the WISE mission is considered the highest yielding mission with more than 158,000 asteroids detected, however Myhrvold's findings state that the result derived for about half of those detections are compromised. This controversy motivated this master thesis project to create a numerical code, which properly combines thermal and reflected light modelling, to further investigate the influence of the latter at the four WISE observational bands. The initial aim of this master thesis was the create an advanced thermal model, but due to the time scope of this master thesis, an intermediate thermal model named the Asteroid Thermal and Reflected light Model (ATRM) was achieved. On top of being able to model simple spherical and ellipsoidal shapes, the ATRM can model irregularly-shaped asteroids with precise orbital and rotational properties taken into account as do advanced thermal models, but assumes instantaneous thermal equilibrium as do simple thermal models such as the NEATM. Furthermore, the ATRM caters to mostly convex-shaped asteroids due to the simple shadowing algorithm implemented, and not taking into account multiple scattering. However, the ATRM is able to vary the surface albedo distribution pattern of an asteroid through an octant method, which is typically not the case for simple and advanced thermal models which all assume a homogeneous surface albedo. With the aforementioned capabilities of the ATRM, the percentage of reflected light in the total flux density at the four wavelength bands of WISE were estimated for different albedo values covering the majority of asteroids falling under the three broad Bus-DeMeo taxonomic classification system (C-, S-, X-types). Furthermore, the influence of the heliocentric distance, emissivity, and shape of the asteroid on the contribution of reflected light were investigated. Ultimately, this project is another step-wise progress in the field of physical characterisation of airless planetary bodies, especially asteroids, and has far-reaching consequences in terms of planetary formation, in-situ resource utilisation (ISRU), commercial asteroid mining, and planetary defence.

Contents

List of Symbols

Roman Symbol	Unit	Definition
a	AU	Semi-major axis
a_{facet}	m^2	Facet area
A	–	Albedo
$A(\lambda)$	–	Spectral albedo
A_{bol}	–	Bolometric Bond albedo
A_{B}	–	Bond albedo
A_{IR}	–	IR-band Bond albedo
A_v	–	Visible-band Bond albedo
$A_{\text{facet}}(\lambda)$	–	Facet albedo
B_ν	$Wm^{-2}Hz^{-1}sr^{-1}$	Spectral radiance per unit frequency
B_λ	$Wm^{-3}sr^{-1}$	Spectral radiance per unit wavelength
C	$J\,kg^{-1}K^{-1}$	Heat capacity
D	m	Diameter
F	$W\,m^{-2}$	Flux
F_λ	$W\,m^{-2}m^{-1}$	Flux density
$F_\odot(\lambda)$	$W\,m^{-2}m^{-1}$	Solar spectral irradiance
G	–	Slope parameter of HG system
H	–	Absolute magnitude of HG system
i	–	Facet index
$\vec{\imath}$	m	Vector to facet
$\mathbf{I}$	–	Direction of illumination
l_s	m	Thermal skin depth
$\mathbf{n}$	m	Facet normal vector
$\hat{\mathbf{n}}$	–	Facet unit normal vector
N	–	Number of facets
$\mathbf{O}$	–	Direction of observation
p_c	m	3D coordinate of facet centroid
p	–	Geometric albedo
p_{IR}	–	IR-band geometric albedo
p_v	–	Visible-band geometric albedo
P	s	Rotation period
q	–	Phase integral
q	AU	Perihelion distance
Q	AU	Aphelion distance
r_{ao}	AU	Distance to the observer
r_{as}	AU	Distance to the Sun
r_{facet}	m	Facet radius
R_{eff}	m	Effective radius of the body
$R_i(\theta)$	–	Rotation matrix
$R_{\text{IR–Vis}}$	–	IR-Vis multiplicative factor
S	m^2	Surface area
t	s	Time
t_0	s	Initial time (Julian Epoch)
T	K	Temperature
T_{facet}	K	Facet temperature
U	J	Energy
x	m	Depth of subsoil

Greek Symbol	Unit	Definition
α	°	Phase angle
β	°	Ecliptic latitude of spin axis (J2000)
Γ	$J\,m^{-2}s^{-1/2}K^{-1}$	Thermal inertia
$\triangle$	–	Change
ε	–	Emissivity
$\varepsilon(\lambda)$	–	Spectral emissivity
ε_{bol}	–	Bolometric emissivity
$\varepsilon_{\text{facet}}$	–	Facet emissivity
η	–	Beaming parameter
θ	°	Transformation angle
θ_e	°	Angle of emission
θ_i	°	Angle of illumination
θ_o	°	Angle of observation
κ	$W\,m^{-1}K^{-1}$	Thermal conductivity
λ	°	Ecliptic longitude of spin axis (J2000)
λ	m	Wavelength
μ_0	–	Cosine of illumination angle
μ	–	Cosine of observation angle
ν	Hz	Frequency
ρ	$kg\,m^{-3}$	Material density
$\phi_\lambda(\lambda)$	–	Filter response function
φ_0	°	Initial rotation angle
$\psi(\alpha)$	–	Phase function
ω	rad/s	Rotation rate

Constant	Value	Unit	Definition
AU	$1.495978707 \times 10^{11}$ [91]	m	Astronomical Unit
c	299792458 [45]	$m\,s^{-1}$	Speed of light in vacuum
h	$6.62607015 \times 10^{-34}$ [45]	$J\,s$	Planck's constant
k_B	1.38065×10^{-23} [45]	$m^2kg\,s^{-2}K^{-1}$	Boltzmann's constant
$L_\odot$	3.828×10^{26} [49]	W	Nominal solar luminosity
R_{Sun}	6.9634×10^8 [45]	m	Nominal solar radius
$S_\odot$	1361 [49]	Wm^{-2}	Solar constant (at 1 AU)
σ	5.67051×10^{-8} [45]	$Wm^{-2}K^{-4}$	Stefan-Boltzmann's constant

List of Abbreviations

Abbreviation	Meaning
AOR	Astronomical Observation Request
ATRM	Asteroid Thermal and Reflected light Model
AU	Astronomical Unit
DAMIT	Database of Asteroid Models from Inversion technique
FIR	Far-Infrared
IAU	International Astronomical Union
IMB	Inner Main-Belt
IR	Infrared
IRS	Infrared Spectrograph
ISRU	In-Situ Resource Utilisation
JAXA	Japan Aerospace Exploration Agency
JPL	Jet Propulsion Lab
MBA	Main-Belt Asteroid
MBC	Main-Belt Comet
MIR	Mid-Infrared
MMB	Middle Main-Belt
MOID	Minimum Orbit Intersection Distance
MPC	Minor Planet Designation
NASA	National Aeronautics and Space Administration
NEA	Near-Earth Asteroid
NEC	Near-Earth Comet
NEO	Near-Earth Object
NEATM	Near-Earth Asteroid Thermal Model
NEOWISE	Near-Earth Object Wide-field Infrared Survey Explorer
NIR	Near-Infrared
OMB	Outer Main-Belt
OSIRIS-REx	Origins, Spectral Interpretation, Resource Identification, Security, Regolith Explorer
PDS	Planetary Data System
PHA	Potentially Hazardous Asteroid
PUI	Peak-Up Imaging
RP	Rotational Phase
RSMAB	Radar Shape Model of Asteroid (101955) Bennu
SBN	Small Bodies Node
SMASS	Small Main-Belt Asteroid Spectroscopic Survey
SSSB	Small Solar System Body
SST	Spitzer Space telescope
STM	Standard Thermal Model
TPM	Thermophysical Model
UT	Universal Time
WISE	Wide-field Infrared Survey Explorer
w.r.t.	With respect to
YORP	Yarkovsky–O'Keefe–Radzievskii–Paddack

1

Introduction

Asteroids can be regarded as a master key to unlocking many mysteries of our solar system, where unravelling the nature of asteroids can have multifaceted implications, be it scientific, financial, and societal. Asteroids are considered remnants of a cataclysmic past and can give crucial answers to basic principles of planetary formation, but also potentially reveal the origin of life on Earth [51]. Currently, asteroids are also being investigated as intermediate orbital milestones for extending humanity's exploration of space, both manned and un-manned, through in-situ resource utilisation (ISRU) [1]. This also opens the door to new business opportunities, which would undoubtedly lead to commercial asteroid mining, heralding a new gold rush! Lastly, but most importantly, an asteroid can be regarded as a double-edged sword, where instead of giving answers to the origin of life, it might end our own. Earth is long due for the next major asteroid impact. Furthering the understanding of the physical and orbital properties of asteroids might give us vital solutions to early detection and deflection/destruction possibilities of potentially hazardous asteroids (PHAs) [29].

Infrared (IR) observations of asteroid are used to obtain estimates of asteroidal sizes and its surface properties such as albedo, thermal inertia, and surface roughness [20]. Those estimates are usually derived through the use of thermal models. Modelling, in general, can be understood as the bridging process between observations and theory, where measurements can give rather precise clues to other unknown properties. However, modelling has its own major caveat - it is only an idealisation of reality and assumptions are made to simplify real-world problems. The thermal modelling of an asteroid predicts its surface temperature, where besides the incident solar radiation, the surface (and immediate sub-surface) temperature depends on the following properties of an asteroid [14]:

- Orbital geometry: radius, inclination, and eccentricity

- Rotational characteristics: spin axis and spin period

- Shape

- Albedo

- Emissivity

- Thermal inertia: thermal conductivity, heat capacity, and density

- Surface roughness

- Internal heat sources: radiogenic decay and tidal heating

Simple thermal models simplify the problem by assuming a non-rotating spherical body and instantaneous thermal equilibrium. Whereas advanced thermal models take into account as much as possible all the aforementioned properties, but to the very least include the orbital geometry and rotational characteristics of the asteroid, its most probable shape, and its thermal inertia through heat conduction modelling.

1

In the past decades, with major improvements in sensitivity and spatial resolution of detector arrays, there has been a significant rise in the number of objects observed at mid-infrared (MIR) range, which corresponds to a wavelength region of roughly 4-20μm [14] [45]. Space missions such as the Spitzer Space Telescope (SST) in 2003, Akari in 2006, Herschel in 2009, and the Wide-field Infrared Survey Explorer (WISE) also launched in 2009, have significantly increased the amount of known asteroids and other minor planets. The WISE telescope has four observational filter bands, namely W1, W2, W3, and W4 corresponding to 3.4 μm, 4.6 μm, 12 μm, and 22 μm respectively. The Near-Earth Object Wide-field Infrared Survey Explorer (NEOWISE) mission was a post-hibernation mission of WISE started in 2013 that only used its lower two wavelength bands to discover and characterise the NEO population. To date, the WISE/NEOWISE survey mission is considered the most successful and highest yielding mission with more than 158,000 asteroids detected, where roughly 34,000 of them are new discoveries [47]. Within those 158,000 asteroid, more than 130,000 are main-belt asteroids (MBAs), about 500 are Near-Earth asteroids (NEAs), and around 2000 are Jupiter Trojans. As Delbo and Harris (2002) [12] puts it, with this unprecedented amount of new thermal data, the rate of discovery of asteroids, especially NEAs, is said to outstrip the rate of their physical characterisation.

In 2016, Nathan Myhrvold stated that the size and albedo estimates derived from the thermal modelling performed by the WISE/NEOWISE team were wrong, especially the ones which used the lower two WISE bandpasses (W1 and W2), since the team did not properly account for the reflected light, and Kirchhoff's law of thermal radiation was violated [54]. The problem is that the shorter wavelength bands of W1 and W2 collect not only thermal IR but significant reflected sunlight too! Given that the W1 and W2 bands were used for roughly half of the total observations made, the size and albedo estimates of nearly 80,000 asteroids might be compromised. Depending on the combination of variables used, Myhrvold stated that the diameter and albedo estimates derived from the two bands were off by 5% up to 45%. A rebuttal was quickly made by NASA scientists [60], stating that Myhrvold's paper was posted before undergoing the necessary scientific peer-review process. This created significant controversy and lead to some media attention where a piece was published in the New York Times [86].

However, two years later, Myhrvold published a peer-reviewed paper to Icarus making the same original claims of mistreatment of reflected light [56]. This rekindled a media controversy (see [85], [57]). A rebuttal was made by Wright et al. (2018) (scientist working on WISE/NEOWISE) [93], where they accepted some minor mistakes were made in the coding process which could account for some systematic errors. However, they did not accept nor deny the mistreatment of Kirchhoff's law, but only said that the modified NEATM framework they used accounted for it. A counter-rebuttal was then made by Myhrvold [58] which re-emphasised his previous claims with more scientific and statistical analysis. This is still an on-going issue, but in the mean time Myhrvold started working on a new simple thermal model which would properly account for reflected light.

This controversy triggered the idea for this master thesis, where the main goal established is to understand, under different parameters, the influence and contribution of reflected light to the observable flux density of the four WISE bands. Since Myhrvold is already working on a simple thermal model, an opportunity to create an advanced thermal model combining reflected light was also identified as a scientific research gap. However, since advanced thermal models are quite complex, and this thesis is limited by time, the following research goal was proposed:

"What is the contribution of reflected light to the observable flux density of the four WISE bands, using an intermediate asteroid thermal model, that properly combines thermal and reflected light modelling?"

The intermediate asteroid thermal model would take into account the precise shape of an asteroid, its orbital and spin properties but would assume instantaneous thermal equilibrium. Thus, the exact modelling of thermal inertia is not taken into account. Moreover, if the precise shape of the asteroid is not known, the versatile ATRM created can also fall back onto a spherical model, or even a tri-axial ellipsoidal model. Furthermore, since only a simple shadowing algorithm is implemented, complex asteroid shapes with substantial concavities cannot be accurately modelled. Only convex-shaped or near convex-shaped asteroids with few and shallow protrusion/concavities can be modelled. Moreover, the following sub-research questions were identified to help answer the main research question:

1. What parameters affect the amount of reflected light in the observable flux density?

2. To which extent does reflected light contribute towards the observable flux density when looking at the four wavelength regions of the WISE mission?

3. How do different surface albedo distribution affect the observable flux density at the four WISE wavelength regions?

The first sub-question would help answer the second one, where the identified parameters would be used to understand the influence of each to the amount of reflected light. The second sub-question would also help confirm the fact that traditionally thermal models use observation data at longer wavelengths, usually $\geq 8\mu m$, where they do not account for reflected light. Since W3 and W4 fall above that limit, it would be interesting to see the actual contribution of reflected light there, and see if the common practise of ignoring reflected light at longer wavelengths is justified. Furthermore, the third sub-question originates from the fact that through the literature review, it was identified that most, if not all, simple and advanced thermal models all assume a homogeneous surface albedo. Hence, the opportunity to create a thermal and reflected light model that takes into account a heterogeneous surface albedo was identified, and to see its effect on the amount of reflected light.

To tackle the subject at hand, the outline of this master thesis is as follows. In Chapter 2, an explanation of what asteroids are and the motivations for thermal modelling will be given. Furthermore, the underlying physics of simple thermal models and advanced thermal models will be explored, before moving on to reflected light modelling and how it should be properly taken into account. Subsequently, in Chapter 3, the description of the created numerical tool named Asteroid Thermal and Reflected light Model (ATRM), will be done and its limitations will also be explained. To ensure that the ATRM is mathematically and numerically sound, a verification and validation are pursued and summarised in Chapter 4. Then, the results of the thermal and reflected flux density modelling of various asteroids under different conditions are presented and discussed in Chapter 5. Finally, the conclusion of this master thesis project with recommendations for future works are given in Chapter 6 and Chapter 7, respectively.

2

Background

Since the goal of this master thesis concerns the thermal and reflected light modelling of asteroids, this chapter is dedicated to giving an overview of the topics at hand. In Section 2.1, asteroids are described in detail. The motivations for better understanding asteroids are elaborated upon in Section 2.2. Simple and advanced thermal modelling are explained in Section 2.3 and Section 2.4, respectively, and reflected light modelling is finally presented in Section 2.5.

2.1. Asteroids

Asteroids are minor planetary bodies of the solar system, and usually have inactive rocky bodies with no atmospheres. Asteroids can vary in size from over one meter to over thousands kilometres in diameter, where they are mostly irregularly-shaped but a small number of them are nearly spherical as is the case of 4 Vesta, seen in Figure 2.1.1. Usually, asteroidal bodies with a mean radii larger than ~ 200 km are nearly spherical [45]. Asteroids often rotate and some of them tumble (rotate around a non-principal axis). About 150 asteroids are known to have a small companion moon.
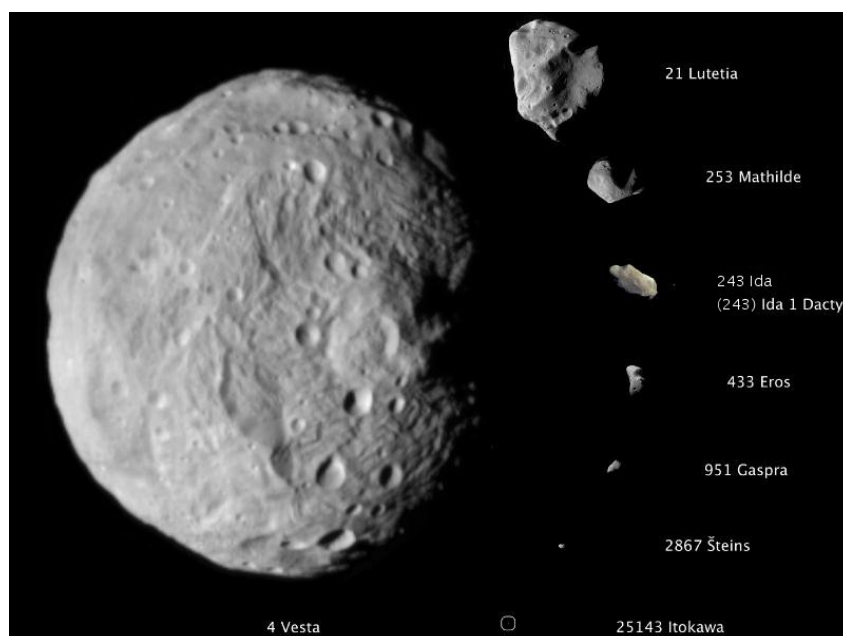
Figure 2.1.1: Composite image illustrating relative sizes of eight asteroids, where 4 Vesta has a radius of about 263 km, 21 Lutetia of 50 km, and 25143 Itokawa of about 157 m. [63] [66]

In 1801, Ceres was the first asteroid to be discovered, by Giuseppe Piazzi, but was originally thought to be

4

a new planet. It was only reclassified as an asteroid a couple of decades after its discovery when many other similar bodies were discovered. Due to being the first asteroid discovery, it was later retroactively granted the designation of 1 Ceres by the International Astronomical Union's (IAU) Minor Planet Center (MPC), which was founded in 1947. It should be noted that 1 Ceres is the largest main-belt asteroid at about 940 km in diameter [45], but is also designated as a dwarf planet. The second asteroid was shortly discovered in 1802, by Heinrich Wilhelm Olbers, and given the MPC name of 2 Pallas. The discoveries of those bodies in the early 1800 then motivated astronomer Frederick William Herschel to propose the term "asteroid", from the Greek word "aster-oeides"[1], meaning 'star-shape' or 'star-like' . A century after the first discovery of the asteroid, approximately a hundred more have been found, and nowadays there are nearly a million known according to the MPC [31].

Asteroids are considered as remnants of the formation of the solar system, and can give crucial clues to the solar system's past, planetary formation mechanisms, and perhaps even the origin of life [52]. Depending on where they are found in the solar system, asteroids can be classified as near-Earth asteroids (NEAs), main-belt asteroids (MBAs), and Trojan asteroids. NEA is a subgroup of near-Earth object (NEO), where the other subgroup is near-Earth comet (NEC). However, most NEOs are NEAs, and are classified as having a perihelion distance q, of less than 1.3 astronomical units (AU) [65]. If their aphelion distance Q and semi-major axis a are also considered, NEAs can be further sub-divided into four groups, namely Amor, Apollo, Aten, and Atira. Further details of this sub-classification are illustrated in Figure 2.1.2. Potentially Hazardous Asteroids (PHAs) are NEAs whose Minimum Orbit Intersection Distance (MOID) with respect to Earth is ≤ 0.05 AU, and whose absolute magnitude (H)[2] is ≥ 22.0. The first NEA to be discovered was 433 Eros by Carl Gustav Witt in 1898, and happens to be the second largest NEA, to date, at 18.7 km [45]. The largest NEA at about 35 km is 1036 Ganymed [51].
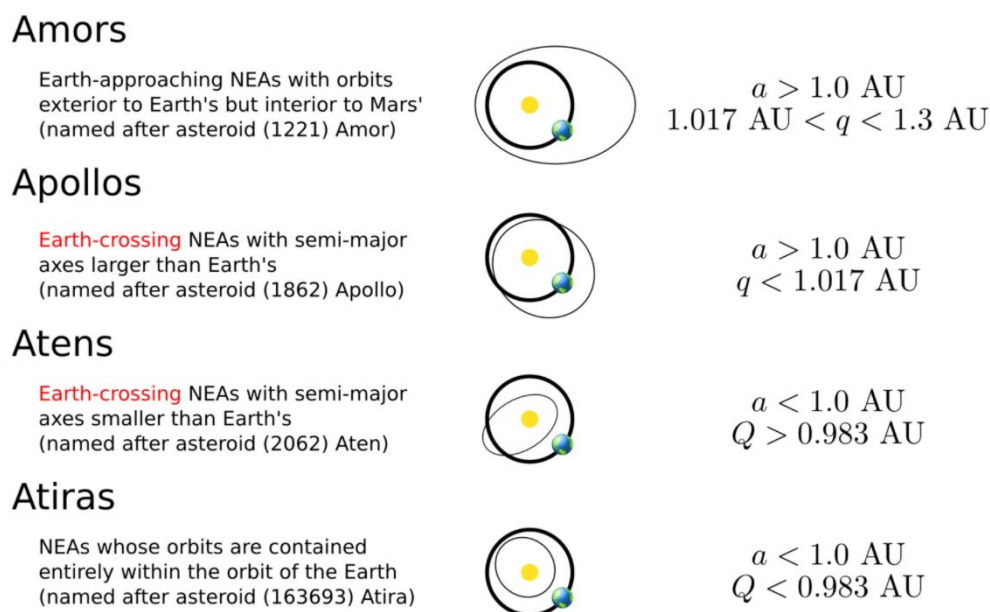
Figure 2.1.2: Near-Earth asteroid sub-classification according to perihelion distance q, aphelion distance Q, and semi-major axis a. [65]

MBAs constitute the majority of the general asteroid population. MBAs can be found in the asteroid belt, which is itself found between the orbits of Mars and Jupiter, where an estimated 1.1 to 1.9 million asteroids bigger than 1 km in diameter and millions of smaller ones are estimated to exist [61]. It is thought that during the solar system's planetary formation stage, the gravity of newly formed Jupiter stopped the formation of planetary bodies in this region, and instead caused small primordial bodies to collide and fragment [61]. The four largest MBAs are Ceres, Vesta, Pallas, and Hygiea, where their collective masses represent roughly half of the total mass of the main-belt. Compared to MBAs, NEAs are relatively smaller in size and are expected to have less "dusty" surfaces with higher thermal inertias [28]. Furthermore, NEAs tend to be more irregularly-

---

[1]"aster" meaning star, and -"eidos" meaning shape or form
[2]Visual magnitude an asteroid found at both 1 AU from the Sun and an observer, and with a phase angle (explained later) of zero.

shaped, and due to their orbits are often observed at larger solar phase angles, when compared to MBAs [26]. The solar phase angle, or simply phase angle, is the angle an asteroid makes between the Sun and an observer. Thus, it is the Sun-asteroid-observer angle, and ranges from 0° to 180° where a phase angle of 0° corresponds to the Sun and observer being collinear and found on the same side of the asteroid.

Trojan asteroids are found at the two regions of stable equilibrium, the L4 and L5 Sun-planets Lagrangian points. The most well-known Trojans are the ones of Jupiter. Mars and Neptune are known to have Trojans, and back in 2011, NASA announced the discovery of an Earth Trojan [61]. The locations of those aforementioned two types of asteroids are illustrated in Figure 2.1.3. Moreover, the first Jupiter Trojan asteroid was discovered by August Kopff in 1907, and is designated as 624 Hektor. It is the largest of the Trojan asteroids at about 200 km in diameter [45]. It is interesting to note of potential interest are three other groups of asteroids: Hungarias, Cybeles, and Hildas. They are all three a dynamical group of asteroids, where Hungarias are considered the first densely concentrated asteroid distribution (NEAs are sparsely distributed) with respect to the Sun. Cybeles and Hildas are found at the outermost edge or just beyond the main asteroid belt. Where the MBAs are in 1:1 orbital resonance with Jupiter, Hungarias are in 9:2, Cybeles are in 7:4, and Hildas are in 3:2 orbital resonance with Jupiter [45]. All three dynamical groups are named after their largest member, that is, 434 Hungaria, 65 Cybele, and 153 Hilda. Furthermore, some asteroids are found beyond the inner solar system, that is much further away than the orbit of Jupiter, but are not discussed further here since their populations are relatively small and their comet/asteroid classification is still being debated (for instance, centaurs and Kuiper-belt objects).
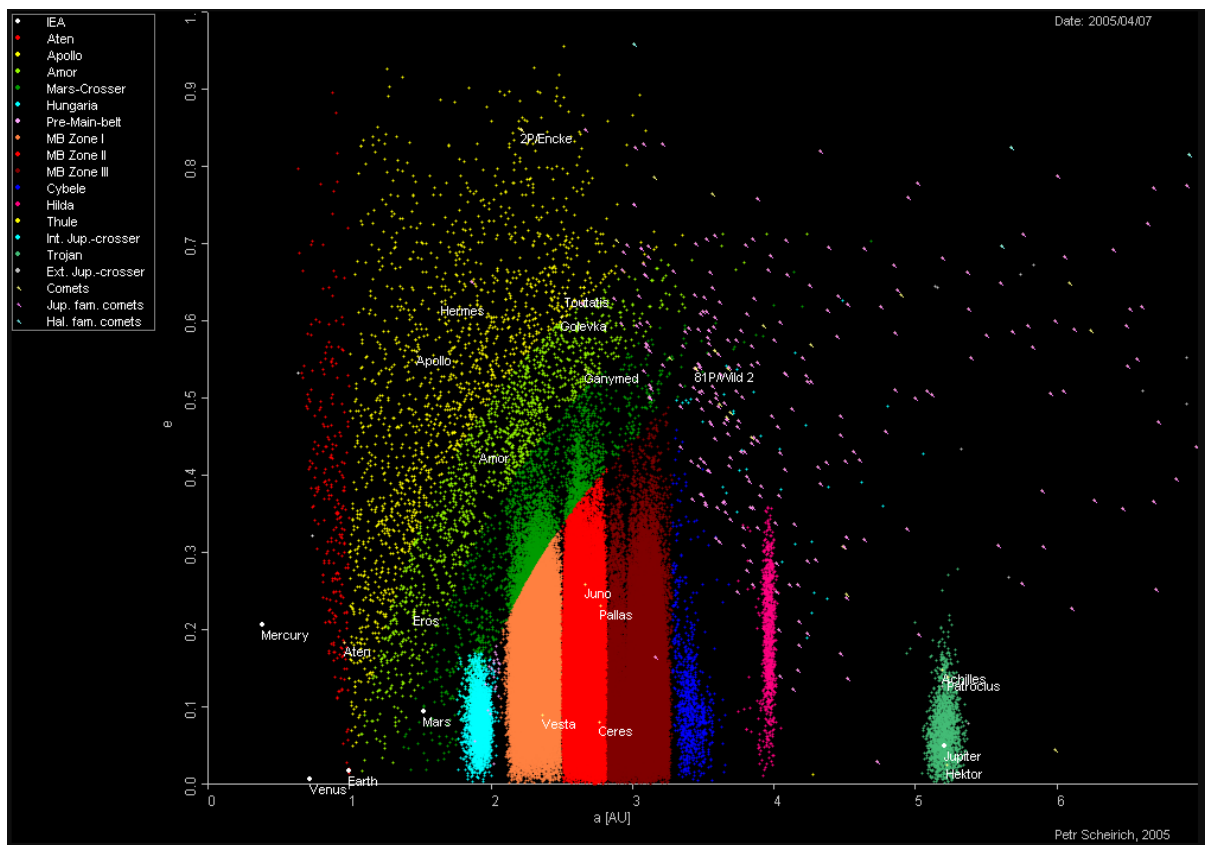
Figure 2.1.3: Asteroid distribution in solar system, where y-axis is the eccentricity of the orbit, and x-axis the semi-major axis. [69]

Since asteroids vary greatly in size, orbital characteristics, and composition, classifying asteroids is a complex issue. With the current knowledge, asteroids are also usually categorised through a taxonomic system based on their colour, albedo, and emission spectrum, where all three properties are associated to the composition of an asteroid. Albedo will be explained into more detail in Section 2.3, but simply it is the ratio of the reflected to total incident solar radiation. Taxonomic classification was pioneered by Clark R. Chapman, Ben Zellner, and David Morrison in 1975. Currently, the Tholen, Small Main-Belt Asteroid Spectroscopic Survey II (SMASS II, at times referred to as the Bus taxonomy), and Bus-DeMeo classifications are the three most widely

used ones. The Tholen classification was first proposed in 1984 by David Tholen, by using spectral features obtained from a broad band spectra of $0.31\mu m$ to $1.06\mu m$. The SMASS II system is an expansion to the Tholen one, carried out by Schelte Bus and Richard Binzel in 2002, where the taxonomic categories were increased from 14 to 26. Even though more asteroids were used in the SMASS II classification (1447 asteroids against Tholen's 978), a smaller wavelength range was used at $0.44\mu m$ to $0.92\mu m$. The most recent asteroid taxonomic system is that of Bus-DeMeo made in 2009 by Francesca DeMeo, Schelte Bus and Stephen Slivan which extends into the near-IR, and defines 25 classes. It is based on 371 asteroids and carried out over a wavelength range of $0.45\mu m$ to $2.45\mu m$. The evolution of the taxonomic classification is illustrated in Figure 2.1.4, and the relative reflectances of the 25 different Bus-DeMeo types are given in Figure 2.1.5.
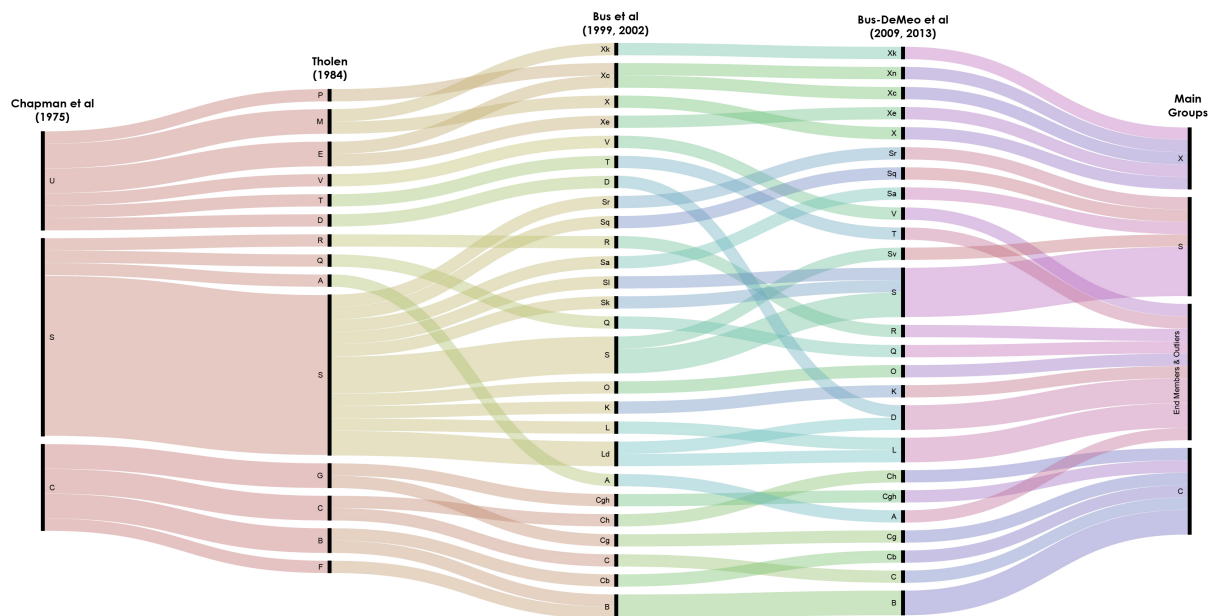
Figure 2.1.4: Evolution of asteroid taxonomic classification systems. U classification from Chapman et al. denotes unclassified since it did not fit the C- or S-types [46].

All three systems have three broad categories: C-, S-, and X-types [59]. C-type asteroids are carbonaceous in composition and make up about 75% of known asteroids. Given their large carbon composition, they are very dark with an albedo of about 0.03 to 0.09, and are found to dominate the outer edge population of the main-belt [OMB region: outer main-belt]. S-types are siliceous (stony) in composition and are the second most occurring asteroids making up around 17% of known asteroids. Given that they have a mixed composition of magnesium-silicates and metallic iron, they are moderately bright with an albedo ranging from 0.1 to 0.22. They are mostly found in the inner region of the asteroid main-belt [IMB region: inner main-belt]. Finally, most of the rest of known asteroids are X-types which are mainly metallic (nickel-iron) in composition, and are also moderately bright with an albedo range of 0.1 to 0.18. They are mostly found in the central region of the main-belt [MMB region: middle main-belt]. There also exists other spectral types of asteroids, but they are either considered sub-types of the other three main types or end members/outliers of other main three types, as can be seen in [15], which concerns the Bus-DeMeo taxonomy. The aforementioned albedos refer to the visible band geometric albedo and will be explained in Section 2.3.
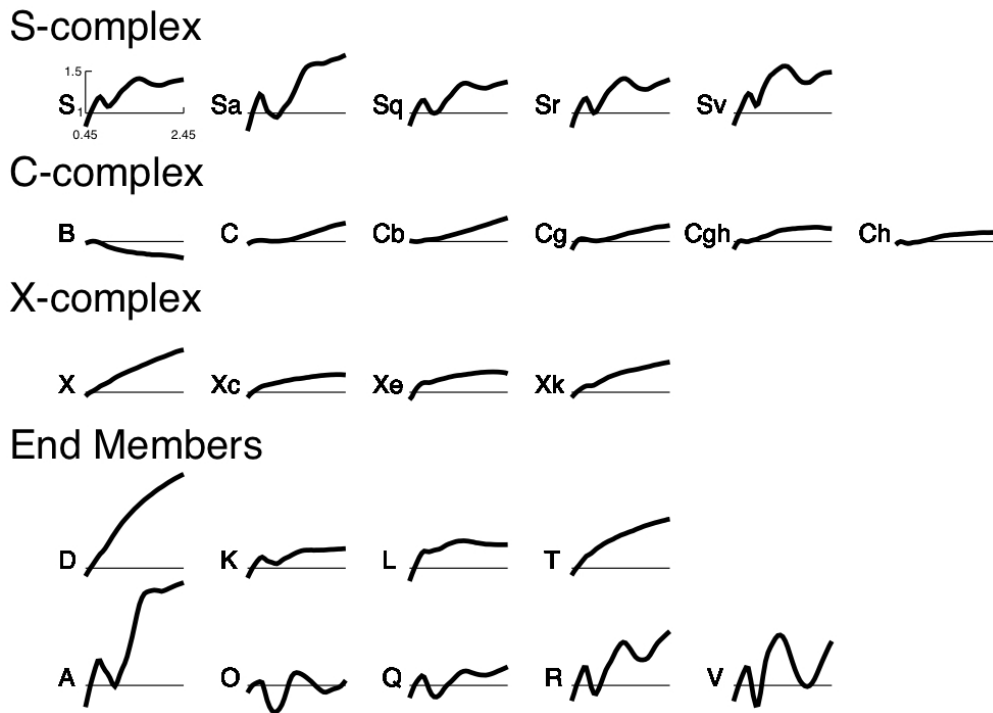
Figure 2.1.5: Bus-DeMeo taxonomy key. The scaling of all graphs follow the same as the one shown in the S-type (top-left), that is the x-axis is within $0.45\mu m$ to $2.45\mu m$. The reflectance curves are normalised such that the visible geometric albedo, centered at 0.55 microns, has a reflectance of unity [15].

2.2. Motivations for thermal modelling

Thermal modelling is the bridging gap between observation and theory to obtain estimates of an asteroid physical properties such as size, albedo, and thermal inertia which are crucial for determining their mineralogy, taxonomy, and origin. Obtaining such information can also help towards better constraining the size-frequency distribution of asteroid families and their populations. Size-frequency distributions can reveal the collisional evolution of these bodies and give clues to mechanism of planetary formation [5]. Depending on the complexity of thermal models, they can be used to obtain estimates of an asteroid's thermal inertia, surface roughness, bulk density, and bulk porosity [14]. Furthermore, modelling accurate surface temperatures can be useful for the design of the instruments of orbiters, landers, and sample return missions. For future manned missions to asteroids, knowledge of surface temperatures will be essential for planning human interaction with asteroids.

Modelling an asteroid's thermal radiation can be invaluable in understanding its effect on its orbital and spin state evolution. The Yarkovsky effect is concerned with the orbital motion, whereas the YORP (named after its four main contributors: Yarkovsky–O'Keefe–Radzievskii–Paddack) is concerned with the spin state evolution. When an anisotropic thermal emission occurs on a small solar system body (SSSB), a net recoil force and/or a net torque occurs on such a body [6] [90] where the smaller the object, the more noticeable the effect. Bottke et al. (2006) [6] shows that thermal inertia strongly influences the strength of the Yarkovsky effect. It is believed that the Yarkovsky effect is responsible for dictating the orbital dispersion of asteroidal families, and particularly responsible for the orbital evolution of MBAs of less than 40 km to enter dynamical resonance which would transform their orbits into potential Earth-crossing ones, and effectively making them PHAs [90]. The YORP and Yarkovsky effects are illustrated in Figure 2.2.1.

8
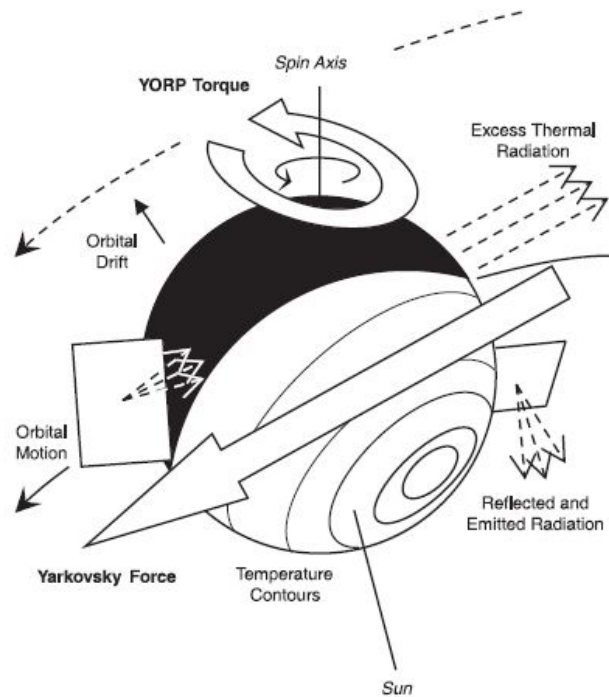
Figure 2.2.1: Yarkovsky and YORP effects on the respective orbit and spin properties of a small asteroid. [78]

If the gas diffusion formula is coupled with the heat conduction equation, advanced thermal models can be used to study the sublimation of water ice from asteroidal or cometary subsurface [10] [72] [81]. The evidence for the presence of ice on asteroidal surfaces first came from the discovery of main-belt comets (MBCs) [24], then from the localised release of water vapour from the surface of 1 Ceres [36], and more recently from the detection of water ice frost spectroscopic signatures on the surface of 24 Themis [9] [73], and of 65 Cybele [43]. The sublimation of ice is modelled by taking into account the transport of water molecules through the fine-grained regolith. Such a model can also help towards discriminating between asteroids and comets when studying SSSBs. Naturally, modelling the subsurface ice sublimation has implications for understanding the origin of life, but can also be used for ISRU applications.

Materials obtained from ISRU could potentially be used for making propellants, life support, and construction materials for colonisation purposes especially against harmful cosmic radiation, and a possible form of energy to supply the spacecraft and/or crew. Another key advantage of ISRU is its potential for reducing launch mass on Earth and thus launch costs. Currently, the idea of using asteroids as potential intermediate orbital milestones for extending humanity's exploration of space, both manned and un-manned, through ISRU is being investigated [4]. Resources extracted from NEAs would make the Moon, Mars, and beyond more accessible. However, all these concepts imply the adequate knowledge of the composition of SSSBs which is currently lacking. This leads to the next point, where ISRU would open the door to new business opportunities in the form of commercial asteroid mining. As can be seen in Table 2.2.1, the estimated profits are in the order of billions US dollars [92], which would be great motivators for the private companies to develop mineral extraction technology for space applications and make space more accessible in general.

Table 2.2.1: Potentially most cost-effective asteroid targets for mining, ranked by least amount of $\triangle V$ required, where 162173 Ryugu would demand a $\triangle V$ of 4.66 km/s to reach, whereas 2001 SG10 would need 5.88 km/s. [92]

Asteroid	Estimated Value [US$ billion]	Estimated Profit [US$ billion]	Approximate Diameter [km]	Composition
162173 Ryugu	83	30	0.85	Nickel, iron, cobalt, water, nitrogen, hydrogen, ammonia
1989 ML	14	4	0.60	Nickel, iron, cobalt
4660 Nereus	5	1	0.33	Nickel, iron, cobalt
101955 Bennu	0.7	0.2	0.49	Iron, hydrogen, ammonia, nitrogen
65803 Didymos	62	16	0.78	Nickel, iron, cobalt
2011 UW158	7	2	0.30	Platinum, nickel, iron, cobalt
1943 Anteros	5570	1250	2.30	Magnesium silicate, aluminium, iron silicate
2001 CC21	147	30	unknown	Magnesium silicate, aluminium, iron silicate
1992 TC	84	17	0.67-1.50	Nickel, iron, cobalt
2001 SG10	3	0.5	0.29	Nickel, iron, cobalt

From Table 2.2.1, asteroids composed of water, hydrogen, and ammonia can be extracted for rocket fuel. For instance, if water and carbon dioxide are readily available, methane-based propellant can be manufactured through the Sabatier process, whereas water can be used to produce the mono-propellant hydrogen peroxide [95]. In addition, water can also be used for essential life support purposes such as producing oxygen, drinking, and growing food. Moreover, there also exists the possibility of creating solar cells if elements such as aluminium, silicon, and glass are available [40].

More than half of the asteroids listed in Table 2.2.1 are also PHAs. Earth is long due for the next major asteroid impact, where in the worst of cases, a sufficiently big PHA would lead to the end of present civilisation if no appropriate measures are taken. The Torino scale, which categorises impact hazards of NEOs, sets a lower threshold of concern in diameter of 20 m [51]. Just for context, the Chelyabinsk meteoroid had a diameter of roughly 20m. Current studies recognise that impact frequencies of NEAs with smaller diameters are much higher, where their impact intervals are estimated to be around every 5-1000 years for objects less than 50m in size, which could be explained by their much larger population in the order of millions to hundreds of millions [29]. Physical properties such as thermal inertia and mineralogy derived from thermal models could indicate the presence of metal on the surfaces of asteroids [27]. It is thought that PHAs containing substantial amounts of metal would be relatively more massive and robust, two factors that would heavily influence necessary deflection or destruction techniques [29].

Unusual methods of asteroid deflection such laser ablation or even 'painting' the asteroid's surface could be employed if proper knowledge of the surface composition and its reaction to solar absorption are properly modelled by use of thermal models. For instance, effective laser ablation requires accurate knowledge of the surface composition, since different materials ablate at different temperatures. This would influence the design of the laser strength and its required power source. Then, the ablated solid material would sublimate (or vaporise if liquids are present) and produce a small but sufficient thrust, over a certain period of time, to nudge the asteroid out of a collision course [35]. Initial laboratory trials of laser ablation has demonstrated that dense metallic asteroids would respond more effectively than rockier surface, due to the shape of the ejected material [22]. Moreover, the 'painting' deflection technique would implement the theory of the YORP and Yarkovsky effect, where the paint would effectively change the albedo of the asteroid which would in turn affect its orbit evolution through the Yarkovsky effect. If done correctly, this could be used to deflect a PHA sufficiently to avoid Earth.

2.3. Simple thermal modelling

There exists two main types of simple thermal models, they are namely the Standard Thermal Model (STM) [41], and the Near-Earth Asteroid Thermal Model (NEATM) [26]. The NEATM was proposed by Alan W. Harris in 1998 to tackle the main issue experienced by the STM, that is the latter does not provide accurate fits to the observed spectral energy distributions of NEAs, where the derived albedos of NEAs would be overestimated

and the derived diameters underestimated [26]. They both have following general assumptions:

- Idealised spherical shape

- Lambertian surface

- Non-rotating body

- Instantaneous thermal equilibrium between incident solar radiation and thermal emission at each point on the surface

- No thermal emission on the night-side of the body

The NEATM can be viewed as a modified STM but correctly adjustable to not only NEAs but any asteroid. The STM, or more accurately the "refined" STM by Lebofsky et al. (1986) [41], used a fixed infrared beaming parameter η value of 0.756 empirically concluded through photometric measurements of just 1 Ceres and 2 Pallas (both MBAs) at 10 μm [41]. It was introduced since asteroidal diameters were being overestimated unless a correction was applied, namely through the beaming parameter, which allows changing the modelled surface temperature distribution of the asteroid to account for an enhancement in thermal emission at small solar phase angles [28]. However, the NEATM's does not use a fixed beaming parameter. Its modelled surface temperature distribution is adjusted by changing η to provide consistency with the observed apparent temperature of the asteroid, where now the infrared beaming parameter accounts for different physical properties being assumed such as rotation, thermal inertia, beaming effects and surface roughness [12]. Hence, η in the NEATM can be viewed as a calibration parameter allowing first-order corrections for the previously mentioned physical properties.

The basis of any thermal model is the determination of the surface temperature of the body. An asteroid's surface temperature, assuming a Lambertian element of surface area dS, depends on its distance from the Sun, its reflectance, its emissivity, and its angle with respect to the solar incident ray. A Lambertian surface reflects/emits light in a diffuse manner which approximates the rough surface behaviour of asteroid surfaces. Specular surfaces are more applicable to smooth and glossy surfaces. Reflectance and emissivity are the effectiveness of a surface's ability at reflecting and emitting radiant energy, respectively. At a given instant, the total incoming radiant energy incident dU_i on that surface element is given by the following equation [12]:

$$dU_i = \frac{S_\odot}{r_{as}^2} \mu_0 dS \tag{2.3.1}$$

Where $S_\odot$ is the solar constant given to be 1361 W/m^2 [49], and r_{as} is the heliocentric distance in AU, and $\mu_0 = \cos\theta_i$ which is the direction cosine of the angle between solar incident ray and the surface normal. Following the conservation of energy, the difference between the total incident solar energy and the total reflected energy should produce the total absorbed energy dU_a by that asteroid's surface [12], as can be seen in Equation (2.3.2). Noteworthy, transmission through the surface is not taken into account since asteroidal surfaces are opaque.

$$dU_a = dU_i(1 - A) \tag{2.3.2}$$

Where the albedo A in this case is the bolometric Bond albedo A_{bol} [12] [28]. In the field of astronomy, bolometric refers to a value being averaged across all wavelengths at the relevant constant temperature. In some circumstances, the average can be taken as a weighted average. The Bond albedo A_B is the fraction of the total incident radiation scattered by a surface, into all directions integrated over all wavelengths (or all frequencies). By definition the Bond albedo is between 0 and 1. Thus, the bolometric Bond albedo is the average Bond albedo over wavelength (i.e. spectral Bond albedo $A_B(\lambda)$), weighted by the solar spectral irradiance $F_\odot(\lambda)$ [25] [42] as shown here:

$$A_{\text{bol}} = \frac{\int_0^\infty A_B(\lambda) F_\odot(\lambda) d\lambda}{\int_0^\infty F_\odot(\lambda) d\lambda} \tag{2.3.3}$$

The term $F_\odot(\lambda)$ can be approximated by applying the Planck function of a blackbody at an effective solar temperature of 5778K. Since the spectrum of the Sun peaks at about 0.5μm, where about half of its total flux is found in the visible region, the visible-band Bond albedo A_v is usually taken as a good approximation of the bolometric Bond albedo [42]:

$$A_{\text{bol}} \approx A_v = p_v q \tag{2.3.4}$$

A_v itself can be obtained by the product of the geometric albedo in the visible band p_v and the phase integral q. The geometric albedo is the ratio of the total reflected flux of a body at a phase angle of 0° to that of a perfect Lambertian disk of the same size and at the same distance [25]. In Equation (2.3.4), q is the phase integral empirically-derived through the HG magnitude system created by Bowell et al. (1989) [7]. The phase integral can be obtained by using Equation (2.3.5), where G is the slope parameter of the phase function. If the slope parameter is unknown for a particular asteroid (which is mostlyl the case, since not many have been studied into detail), Bowell et al. (1989) advise using a standard value of 0.15 [7]. Thus, given the previous approximations, some thermal models simply refer to the albedo in Equation (2.3.2) mistakenly as the Bond albedo, where it should at least be referred to as bolometric Bond albedo or visible-band Bond albedo.

$$q = 0.29 + 0.684G \tag{2.3.5}$$

Getting back to the determination of surface temperature, the energy absorbed dU_a is balanced by the thermal emission, where the emitted energy dU_e is given by the Stefan-Boltzmann law but modified through the introduction of the emissivity ε parameter since asteroids are not perfect blackbodies, that is, they are grey bodies with $\varepsilon < 1$ [12]:

$$dU_e = \sigma \varepsilon T^4 dS \tag{2.3.6}$$

Where σ represents the Stefan-Boltzmann's constant. Most thermal models/studies refer to ε in Equation (2.3.6) as the bolometric emissivity ε_{bol} [55]. As is the case for the bolometric Bond albedo, the bolometric emissivity is the average of spectral emissivity ($\varepsilon(\lambda)$) but here weighted by the thermal spectrum [14]. The wavelength range which contributes the most to that average lies around 8 to 40 microns where the derived spectral emissivities generally lie between 0.8 and 1.0 [11] [79] [80]. However, most thermal models customarily assume ε_{bol} = 0.9, since it is the typical value for powdered silicate rock at that wavelength range [56].

When conservation of energy is applied, assuming instantaneous thermal equilibrium, it allows Equation (2.3.2) to equate to Equation (2.3.6). Hence, for a surface element found at the subsolar point, that is $\mu_0 = \cos 0 = 1$, would give Equation (2.3.7):

$$\frac{S_\odot (1 - A)}{r_{as}^2} dS = \sigma \varepsilon T^4 dS \tag{2.3.7}$$

If T from Equation (2.3.7) is made the subject of formula, the maximum surface temperature of the asteroid T_{max}, found at the sub-solar point, can be obtained by this equation:

$$T = \left[\frac{(1 - A)S_\odot}{r_{as}^2 \eta \varepsilon \sigma} \right]^{1/4} \tag{2.3.8}$$

Note the addition of the beaming parameter η in the denominator of Equation (2.3.8), related to the aforementioned NEATM corrective factor. When η is less than one, the observed surface temperature is higher than it would be have been assuming instantaneous thermal equilibrium, where more energy seems to be emitted than absorbed. This can happen due to surface roughness effects which usually tend to enhance thermal radiation back to an observer at low phase angles [47]. And the contrary applies when η is greater than one, that is, more energy is being absorbed than emitted. This can happen especially due to thermal inertia and thermal conduction which transfer thermal energy to other parts of the asteroids.

It should be noted that even despite its name, the NEATM is also useful when modelling non-NEAs [53]. A major shortcoming of the NEATM is that fitting its thermal model to the observed thermal continua of asteroids requires high-quality spectrophotometric data. If only two filter measurements with closely spaced wavelength regions are available, it is impossible to derive η via spectral fitting. Delbo et al. (2003) suggested a phase angle dependency of the beaming parameter, where $\eta = 1$ for $\alpha < 45°$ and $\eta = 1.5$ for $\alpha > 45°$ [13], that is larger phase angles would result in a bigger beaming parameter, as can be seen in Figure 2.3.1. However, Delbo et al. (2003) mentioned that those relationships are based on a limited sample of asteroids, and more research should be given to it.
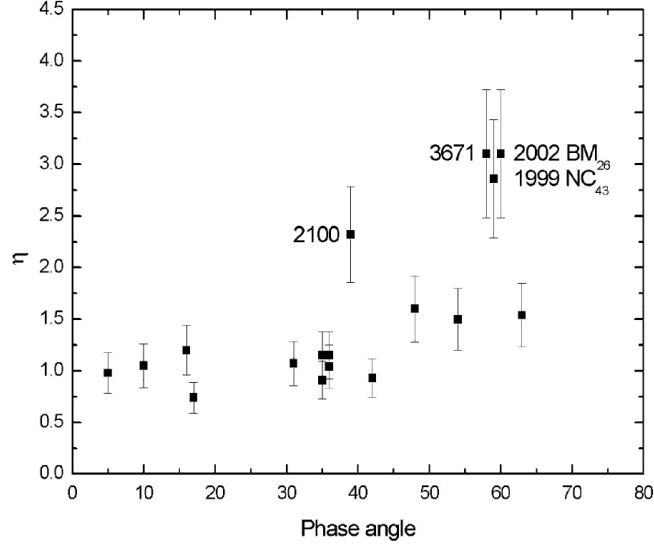
Figure 2.3.1: Beaming parameter η from NEATM fits plotted against solar phase angle α, where error bars represent a 20% uncertainty. [13]

After the introduction of the NEATM, it became the de facto simple thermal model, and is especially used over thermophysical models when there is a lack of available data about the asteroid's spin and shape. This is because in those situations, an idealised non-rotating spherical body has to be assumed, which the NEATM does. The NEATM typically allows a robust estimation of an asteroid's diameter with an uncertainty in the order of 15%, and albedo with an uncertainty of 30% [26]. However, the NEATM does not give any direct information on its thermal inertia or surface roughness, and advanced models are required for that.

The thermal flux density $F_{\lambda,\,\text{therm}}(\lambda)$ at a specified wavelength λ is computed by using this equation [26]:

$$F_{\lambda,\,\text{therm}}(\lambda) = \frac{R_{\text{eff}}^2}{r_{ao}^2}\varepsilon \int\int B_\lambda(\lambda, T)\cos\theta_e \sin\theta_e d\theta_e\, \mathrm{d}\phi \tag{2.3.9}$$

Where R_{eff} is the effective spherical radius of the asteroid, r_{ao} is the distance between the asteroid and the observer, ε is emissivity since its a grey body, $B_\lambda(\lambda, T)$ is the Planck function depending on the wavelength λ and the surface temperature T of the asteroid, θ_e is the emission angle with respect to the observer, and ϕ is the azimuthal angle, where the reference axis is taken as pointing towards the observer. The square of the asteroid radius divided by the asteroid-observer distance comes from the inverse square law. The SI unit of thermal flux density is $W/m^2/m$, thus technically, it should be referred to as the thermal spectral flux density but a lot of thermal modelling papers simply refer to it as thermal flux density or thermal flux. It should be noted that in this equation the emissivity is constant, since it assumes a spherical body with uniform emissivity. The Planck function in the wavelength form is as follows:

$$B_\lambda(\lambda, T) = \frac{2hc^2}{\lambda^5} \cdot \frac{1}{e^{\frac{hc}{\lambda k_B T}} - 1} \tag{2.3.10}$$

Where h is the Planck's constant, k_B is the Boltzmann's constant, and c the speed of light. The unit of the Planck function here is $Wm^{-3}sr^{-1}$.

Even though it is not in scope of this thesis, the radiometric method of determining asteroid diameters and albedos using simple thermal models is briefly explained here. It is an iterative method where firstly, the thermal IR flux density F_λ, at a specific wavelength is measured, and the H value is derived from optical measurements in the visible band. An initial value for p_v is 'guessed', and by applying Equation (2.3.9), an initial estimate for diameter D is produced. The latter is then inserted in Equation (2.3.11) to then obtain a better estimate of p_v. This iterative method is stopped once a sufficiently stable value of D and p_v is obtained.

$$p_v = \left(\frac{1329[km]}{D}\right)^2 10^{-0.4H} \tag{2.3.11}$$

2.4. Advanced thermal modelling

Advanced thermal models, also known as thermophysical models (TPMs), are the next natural step in improving the thermal modelling of airless bodies. When high-quality observational data[3] on shape and spin of an asteroid is available, TPMs are usually favoured over simple thermal models since the non-rotating spherical body assumption is no longer needed. Furthermore, another essential difference between simple thermal models and general TPMs, is the proper modelling of thermal inertia of the body. In TPMs, thermal inertia is not treated as a correction parameter, instead it is properly taken into account by modelling heat conduction into the surface and immediate subsurface. Hence, instantaneous thermal equilibrium is not assumed, and thermal inertia introduces a lag time between the absorption of solar radiation and its re-radiation. Increasing thermal inertia increases the lag time, but also lowers the temperature contrast across the asteroid's longitude, which results in a flatter thermal light curve [28].

Most TPMs define the global shape of an asteroid through the use of a triangular mesh, where the body rotates with a period P around a known/given spin vector. If no shape models are available, a spherical or ellipsoidal shape is assumed [53]. Similar to simple thermal models, the goal of TPMs is to calculate the surface temperature, and subsequently the thermal emission, of each facet at a given illumination and observation geometry, as can be seen Figure 2.4.1. Where simple thermal models only consider the insolation F_{SUN}, and radiation lost to space $\varepsilon\sigma T^4$, TPMs introduce complexity but also accuracy by considering the multiple scattered sunlight F_{SCAT}, reabsorbed thermal radiation F_{RAD}, and conducted heat $k(dT/dx)$ [38].
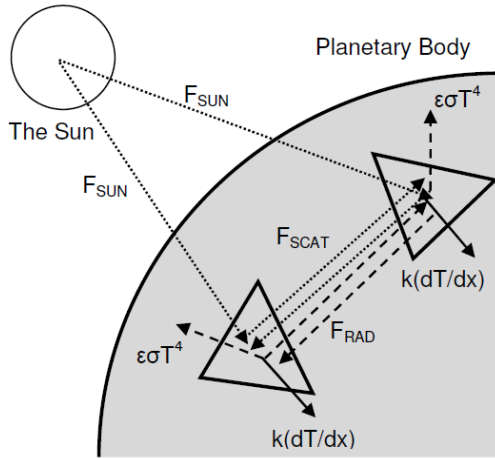
Figure 2.4.1: Energy balance and radiation between facets. F_{SUN} is the incident sunlight, F_{SCAT} is the multiple scattered sunlight, F_{RAD} is the reabsorbed thermal radiation, $\kappa(dT/dx)$ is the heat conducted, and $\varepsilon\sigma T^4$ is the emitted thermal radiation [77].
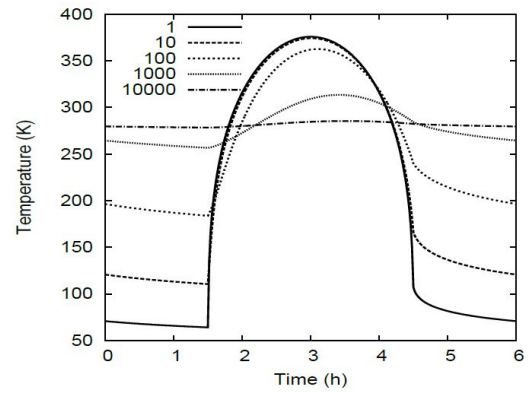
Figure 2.4.2: Diurnal equatorial temperature curves of an asteroid for varying values of thermal inertia, where spin axis is perpendicular to the orbital plane. Modelled asteroid has a heliocentric distance of 1.1 AU, a spin period of 6 h, and a Bond albedo of 0.1. [14]

The main governing equation of TPMs for finding the surface temperature of a local facet at vector $\vec{\iota}$ with respect to the origin of asteroid (center of mass), and at vector $\vec{r}_{as}$ with respect to the Sun and with surface normal $\hat{n}$, is given as follows [14]:

$$\varepsilon\sigma T^4(\vec{\iota}, t) - \left(\frac{\partial T(\vec{\iota}, t)}{\partial x}\right)_{x=0} = \frac{(1-A)S_\odot}{\vec{r}_{as}^3}(\vec{r}_{as} \cdot \hat{n})(1 - \mathscr{S}(\vec{r}_{as}, \vec{\iota})) \tag{2.4.1}$$

---

[3]Usually obtained from either optical lightcurve inversion, radar observations, stellar occultations, or in-situ imaging.

Where ε is the emissivity taken as the bolometric emissivity with usually the default value of 0.9 as mentioned previously, t is the time, x is the depth in the subsoil, A is facet albedo taken as the bolometric Bond albedo as previously explained [76], and $\mathscr{S}(\vec{r}_{as}, \vec{\imath})$ is the shadowing function of a facet where $\mathscr{S}(\vec{r}_{as}, \vec{\imath}) = 1$ indicates it being shadowed, and $\mathscr{S}(\vec{r}_{as}, \vec{\imath}) = 0$ indicates it being illuminated. Numerically, simple shadows are computed by local horizon mapping [14], but are only suitable for convex-shaped asteroids since projected shadows made by protruding shapes are not taken into account. In globally non-convex shaped asteroids, projected shadows are computed by the ray-triangle intersection of the solar illumination ray. This method is also useful since it can also be applied to account for self-heating from interfacing facets, which will tend to reduce the temperature contrast between fully illuminated facets and the ones found inside concavities. However, this is a computationally intensive method where for every orientation/rotation step, a new ray-triangle intersection test has to be performed on the remaining illuminated facets obtained after the local horizon mapping. Furthermore, the main issue of modelling complex non-convex shaped asteroids is finding out which facets 'see' other facets, and then calculating the radiation exchanged between them. This is normally tackled by applying view factors.

Looking at Equation (2.4.1), the first term in the left-hand side represents the thermal energy radiated to space given by the Stefan-Boltzmann law. The second term in the left-hand side, is the heat conducted into the sub-surface. On the right-hand side, it is the solar radiation absorbed. It should be noted that some TPMs dealing with complex shapes which have a non-negligible number of facets in view of each other also include the self-illumination and self-irradiation on the right-hand side of the equations, and are jointly also known as mutual heating. However, most TPMs do not take into account self-heating and projected shadowing effects for simplicity [14]. Furthermore, when modelling heat conduction, TPMs usually neglect the lateral heat conduction since the modelled facets are much larger than the penetration depth of the diurnal heat wave (that is, the thermal skin depth). Hence, only one dimensional heat conduction perpendicular to and into the surface is considered [14], as can be seen in the following equation:

$$\frac{\partial T}{\partial t} = \frac{\kappa}{\rho c_p} \left(\frac{\partial^2 T}{\partial x^2} \right) \tag{2.4.2}$$

Where x is the depth and $x = 0$ is found at the surface, κ is the thermal conductivity, ρ is the surface density, and c_p is the specific heat capacity. It should be noted that Equation (2.4.2) assumes the heat flow in a homogeneous and isotropic material. The thermal inertia Γ and the thermal skin depth l_s are defined by Equation (2.4.3) and Equation (2.4.4), respectively:

$$\Gamma = \sqrt{\kappa \rho c_p} \qquad (2.4.3) \qquad\qquad l_s = \sqrt{\frac{\kappa P}{2\pi \rho c_p}} \qquad (2.4.4)$$

A numerical finite-difference method (FDM) is needed to solve the 1D heat conduction equation of each facet, where an initial condition, and two boundary conditions are required. The initial condition is setting an arbitrary starting temperature to the FDM, but it is usually taken to be equal to the equilibrium temperature since it reduces the computation time of the FDM. In terms of a faceted shape model, the equilibrium temperature can be determined by averaging the facet surface temperatures over one rotational period [71] [77]. Concerning the boundary conditions, the first one is found at the surface of the asteroid, and the other at a certain depth $x = L$. At the surface, for a facet at point $\vec{\imath}$, a Dirichlet boundary condition is used in the form of the energy balance equation which neglects self-heating effects. The second boundary condition is a Neumann condition, where at a sufficient depth in the asteroid, due to the decrease in the diurnal heat wave, a temperature gradient is assumed to no longer exist [14].

Once the surface temperature of each facet is computed, the next step is to calculate the thermal emission of each facet at a given illumination and observation geometry. The emission spectrum of the asteroid is then the summation of all the facets visible to the observer, at a specific wavelength or over a certain wavelength range. The thermal (spectral) flux density of a facet seen by an observer is calculated using Equation (2.4.5) [14] [32] [77] which assumes Lambertian emission.

$$F_{\lambda,\,\text{therm}}(\lambda) = \varepsilon B_\lambda(\lambda, T) \frac{a}{r_{ao}^2} \cos\theta_e \tag{2.4.5}$$

Where ε is the emissivity, $B_\lambda(\lambda, T)$ is the Planck function in the wavelength domain, a is the facet area, r_{ao} is the distance between the asteroid and the observer, and θ_e is the emission angle.

Moreover, throughout the literature review of thermal and thermophysical models, it was mostly observed that no distinction was made between the emissivity found in Equation (2.4.1) and that of Equation (2.4.5), which are assumed to be the same. However, technically, the emissivity in Equation (2.4.1) is the bolometric hemispherical emissivity, whereas the one in Equation (2.4.5) is the spectral directional emissivity [25]. The thermal models justify their equivalency using two assumptions. Firstly, the surface/facets are assumed to be Lambertian emitters, thus have equal brightness when viewed from any direction. Hence, the distinction between hemispherical and directional no longer applies [76]. Secondly, most thermal models assume the emissivity to be constant with wavelength, or more precisely constant within the wavelength of observation/-modelling. Hence, the distinction between bolometric and spectral emissivity also no longer applies [76]. The same reasoning applies to the emissivities found in Equation (2.3.8) and Equation (2.3.9) of Section 2.3.

Some more advanced TPMs also model surface roughness, which is a measure of surface's irregularity at scales smaller than the global shape model but larger than the thermal skin depth. Those TPMs model surface roughness by either placing a hemispherical crater at the center of each facet, or by assuming a Gaussian or fractal surface [77]. Introducing surface roughness to the TPM will actually alter the effective bolometric Bond albedo of the facet, and its thermal inertia. Furthermore, it will move the mean thermal emission away from the facet's normal making it behave less like a Lambertian emitter [77]. However, there is not consensus on this issue, since Davidsson and Rickman (2014) show that surface roughness at sub-thermal-skin depth scales is quasi-isothermal and is therefore not likely to deviate from Lambertian emission overall. Nonetheless, modelling surface roughness through hemispherical craters is the preferred method since it is simpler to parameterise, and was shown to accurately reproduce the directionality of thermal emission from the Moon (an airless body) [77].

2.5. Taking into account reflected light

The transition from reflected light to thermal emission is not discrete, but continuous. This is because the solar irradiance being reflected has a spectrum covering the ultraviolet, visible, and infrared regions as can be seen in Figure 2.5.1 where Figure 2.5.2 can be used for reference of the electromagnetic spectrum. Pioneering studies of asteroid thermal modelling did not have to account for reflected sunlight, since it was not considered relevant at the time. This was because the observational bands for those studies, and that of early space mission such as IRAS, Akari, and Herschel were at longer wavelengths of the MIR range where reflected sunlight was considered negligible [56]. As was seen previously, the simple thermal model of the NEATM and TPMs by themselves have no provision to take into account reflected light. However, it was already known that estimates derived by the use of simple thermal models such as the 'refined' STM at wavelengths shorter than $8\mu m$ were considered questionable [41].
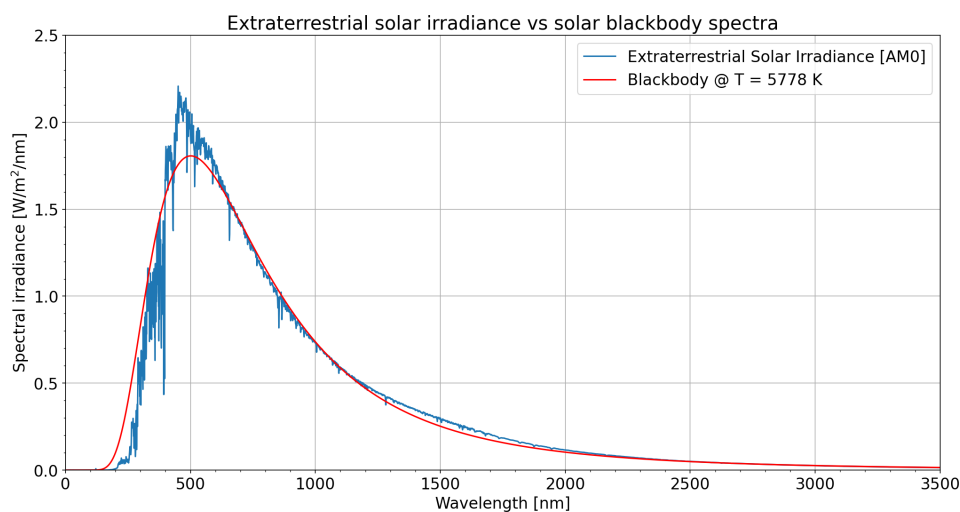
Figure 2.5.1: Extraterrestrial solar spectrum [air mass zero] versus blackbody curve of the Sun at an effective temperature of 5778 K. Solar spectral data obtained from Gueymard (2004) [23]. Distance scaling was done using a solid angle of 68.5 micro-steradians.
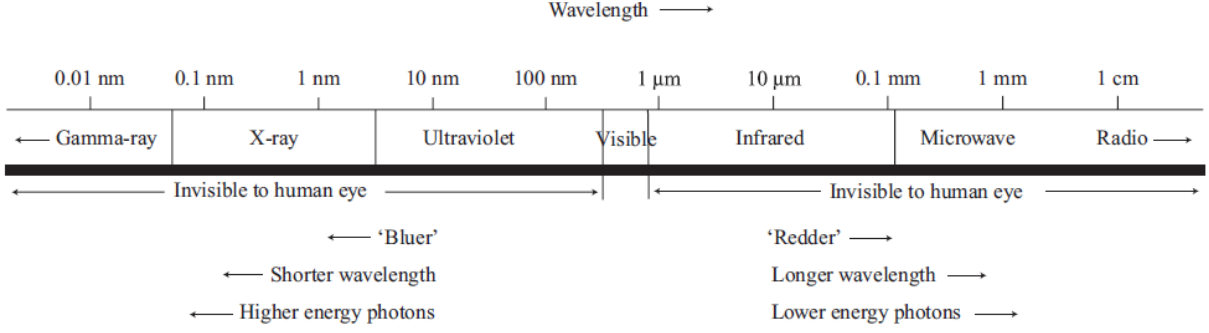
Figure 2.5.2: Electromagnetic spectrum [45].

There exists several different scattering laws to model reflected light from atmosphereless bodies, each with their advantages and disadvantages. Advanced scattering models are complex and use the volume single-scattering albedo of the regolith covering the asteroids surface, and model complex rough surfaces which do not follow Lambertian scattering anymore such as Hapke's scattering model. However, as was seen in Section 2.3 and Section 2.4, the derivation of the surface temperature, and the calculation of the thermal emission both assume a Lambertian surface. Hence, for simplicity and self-consistency between the thermal and reflected flux density modelling, the Lambertian scattering law is also used here. Even though in the field of photometry, Lambertian scattering is considered to be mostly representative of airless bodies with relatively brighter surfaces [42], for the purposes of this thesis it is deemed acceptable.

The reflected flux of an asteroid depends on the property of the star it is reflecting from, that is its temperature. In addition, following from the inverse square law and solid angle computation, it also depends on the size of the asteroid and the size of the star, the orbital distances from the asteroid to that star, and to the observer. The reflected (spectral) flux density of a spherical asteroid can be represented by the following equation, which assumes Lambertian reflection and the Sun behaving as a blackbody [83]:

$$F_{\lambda,\text{ refl}} = p(\lambda)\,\psi(\lambda)\,\pi\,B(\lambda, T_{\text{Sun}})\,\frac{R_{\text{eff}}^2 R_{\text{Sun}}^2}{r_{ao}^2 r_{as}^2} \tag{2.5.1}$$

Where p is the geometric albedo of the asteroid, ψ is the phase function of the asteroid, T_{Sun} is the solar temperature, R_{Sun} is the solar radius of the star, R_{eff} is the effective radius of the asteroid, r_{as} is the orbital heliocentric radius of the asteroid, r_{ao} is the distance to the observer, and λ is the wavelength of concern. The solar temperature is taken to be 5778K, since it is the effective temperature of the Sun [56]. That is, it is the temperature of a blackbody, having the same size and producing the same total emissive power. Looking at Figure 2.5.1, it can be seen that indeed the blackbody Planck curve [red] is a good approximation of the solar spectral irradiance.

Comparing Equation (2.5.1) to the calculation of thermal emission from a spherical body as in Equation (2.3.9), it can be observed that apart from the common parameters of asteroid size and distance to the observer, the reflected flux depends on the distance to the Sun and the asteroid's albedo. However, the heliocentric distance and surface albedo terms are implicitly found in the calculation of the asteroid's surface temperature which dictates the thermal emission. Hence, the amount of reflected light in the total observable flux density of an asteroid, where the latter itself is made up of reflected light and thermal emission, depends on asteroid's albedo, heliocentric distance, and also the thermal properties of the asteroid. The thermal properties of the asteroid are its emissivity, albedo, and thermal inertia. The last one is directly taken into account in TPMs, and idealised in simple thermal models through the beaming parameter, as explained previously.

To better understand the contribution of reflected light to the observed flux density (thermal + reflected at same wavelength regions), first, consider a circular flat plate, with radius R, where it can both reflect and emit light in space, as illustrated in Figure 2.5.3, and the plate is perpendicular to both the viewing direction and incident solar light. The term r_{ao} is the distance from the plate to the observer, and r_{as} is the distance from the plate to the Sun, and finally r_{os} is the distance from the observer to the Sun, all in SI units.

17
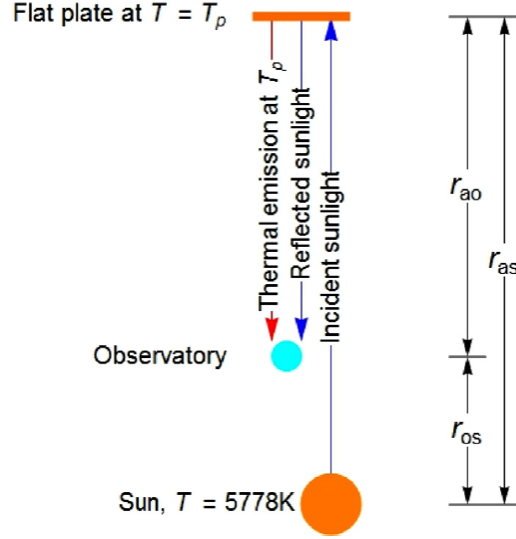
Figure 2.5.3: Flat-plate asteroidal model, taking into account both reflection and thermal emission [56].

It is assumed that the plate is in thermal equilibrium, with a constant plate temperature T_p. The plate's material is assumed to have a spectral reflectivity $\rho(\lambda)$ and spectral emissivity $\varepsilon(\lambda)$. According to Kirchhoff's law of thermal radiation, for any body in thermodynamic equilibrium, its wavelength-specific emissivity $\varepsilon(\lambda)$ and absorptivity $\alpha(\lambda)$ are equal [25]. It should be noted that absorptivity $\alpha(\lambda)$ is one minus the reflectivity $\rho(\lambda)$. Hence, this law thus establishes a complementary relationship between emissivity and reflectivity by coupling them together as follows:

$$\varepsilon(\lambda) = \alpha(\lambda) = 1 - \rho(\lambda) \tag{2.5.2}$$

This law hold true when diffuse surfaces or diffuse irradiation are being assumed [25], which is the case for Lambertian surfaces where both the Lambert cosine incidence law and Lambert cosine emission laws are being used throughout the thermal and reflected light modelling. Hence, if the reflected and thermal flux density are being modelled and/or observed at the same wavelength bands, that is spectrally, Kirchhoff's law does apply [56].

Moreover, this brings up the question of why does the bolometric Bond albedo in the surface temperature equation found in eq. (2.3.8) not get cancelled out by the bolometric emissivity if Kirchhoff's law is applied? To answer this question, first consider the weighted average over a spectral distribution $F(T, \lambda)$ of an arbitrary function $g(\lambda)$ to be given by:

$$g(\lambda) \mid F(T, \lambda) = \frac{\int_0^\infty g(\lambda) F(T, \lambda) d\lambda}{\int_0^\infty F(T, \lambda) d\lambda} \tag{2.5.3}$$

Thus, the surface temperature equation becomes:

$$T_{\text{surface}} = \left[\frac{S_\odot (1 - A_{\text{surface}}(\lambda) \mid B_\lambda(5778K, \lambda))}{\sigma(\varepsilon_{\text{surface}}(\lambda) \mid B_\lambda(T_{\text{surface}}, \lambda))} \right]^{1/4} \tag{2.5.4}$$

The term $(\varepsilon_{\text{surface}}(\lambda) \mid B_\lambda(T_{\text{surface}}, \lambda))$ can be replaced to $(1 - A_{\text{surface}}(\lambda) \mid B_\lambda(T_{\text{surface}}, \lambda))$ by applying Kirchhoff's law. However, $(1 - A_{\text{surface}}(\lambda) \mid B_\lambda(T_{\text{surface}}, \lambda))$ can not cancel out $(1 - A_{\text{surface}}(\lambda) \mid B_\lambda(5778K, \lambda))$ since they are concerned with different spectral distributions, given that the Sun peaks at a temperature of 5778K and asteroids usually have surface temperature peaking at around 150-540K [56]. Thus, they represent different region's of an asteroid's surface reflectivity spectrum $A_{\text{surface}}(\lambda)$ [56].

Getting back to the flat plate model, the total observed flux density of that flat circular plate which combines thermal and reflected flux density is given by:

$$F_{\text{obs}}(T_{\text{p}}, \lambda) = \pi \frac{R^2}{r_{\text{ao}}^2} \left[\left(1 - \rho(\lambda) \right) B_\lambda(T_{\text{p}}, \lambda) + \frac{\rho(\lambda)}{r_{\text{as}}^2} R_{\text{Sun}}^2 B_\lambda(T_{\text{Sun}}, \lambda) \right] \qquad (2.5.5)$$

For wavelengths in the visible spectrum, $\rho(\lambda)$ is equivalent to the visible Bond albedo as previously discussed, and for wavelengths in the IR spectrum, $\rho(\lambda)$ is actually not well studied/known, and is actually assumed to portray the same wavelength dependence as the geometric albedo does [89]. Thermal studies try to approximate/estimate the geometric albedo in the IR spectrum p_{IR} by looking at the reflectance curves used in the taxonomic classification of asteroids, and extrapolate its measured reflectance from the visible and/or near-IR spectrum to the mid-IR spectrum with flat reflectance (that is, no absorption/emission in the spectral lines). The Bus-DeMeo taxonomy is the one most used since it is the most recent, and covers the largest wavelength band of 0.45-2.45 microns, where the upper bound is the closest to the MIR spectrum compared to the other taxonomic system such as Tholen and SMASS II as was seen in Section 2.1.

It should be noted that this method is usually used for calculating the geometric albedo in the near-IR or lower mid-IR. At longer IR wavelengths, such as the last two WISE bands found around 12 and 22 microns, thermal studies directly assume the reflected flux density is zero, or that the $p_{IR}(\lambda)$ itself is zero, which makes the reflected flux density zero. However, since the goal of this master thesis is to also quantify the amount of reflected light in all four WISE bands, and see if the assumption of negligible reflected light at W3 and W4 holds, $p_{IR}(\lambda)$ will not be assumed to be directly zero, but is going to be estimated using the aforementioned method.

Myhrvold states that the mistake done by the WISE/NEOWISE study, is that they model the total observed flux density by assuming $\varepsilon(\lambda) = 0.9$ across W1-W4, and compute the reflected flux density using a form of Equation (2.5.1) where the IR geometric albedo is a fitting parameter in W1 and W2, and considered zero in W3 and W4. Thus, Kirchhoff's law is violated since the spectral emissivity is kept fixed, and the albedo can vary independently. Given that they are being observed/modelled within the same wavelength bands, they have to be related, especially since thermodynamic equilibrium is assumed inherent to thermal models.

3

ATRM implementation

Following from Chapter 2, it can be seen that a scientific gap is present, where thermal and reflected light modelling of asteroids are usually not carried out together. Thus, the Asteroid Thermal and Reflected light Model (ATRM) was created through this master thesis to address this scientific gap. The ATRM tool is able to model both the thermal and reflected flux densities, both monochromatically or in-band fluxes, of airless bodies which can be spherical, ellipsoidal, and fairly irregularly-shaped. The ATRM assumes an asteroid shape as a polyhedron made of a mesh of triangular Lambertian surfaces in point-wise radiative equilibrium. Assuming instantaneous thermal equilibrium, the ATRM can calculate the incident solar irradiance, surface temperature, thermal flux density, reflected flux density, and total flux density of each triangular facet at each observation epoch.

The sphere-, ellipsoid-, or the database- (listed in Section 3.1) derived shape files are the first input to the ATRM. Those shape files could be in .shp or .obj format. The asteroid's physical parameters include the spin axis orientation given in ecliptic coordinate system with the longitude being λ and latitude being β, and the sidereal spin period P, and were all obtained from the relevant shape file databases. Furthermore, the visible-band geometric albedo p_v, and the magnitude of the slope parameter G are taken from the JPL Small-Body Database Browser [63]. In addition, when relevant, the input parameters with regards to the reflected flux density validation data, that is the Julian date epoch, the brightness in intensity units, the asteroid-centric ecliptic Cartesian coordinates x, y, z of the Sun and of the observer given both in astronomical units, are taken from the DAMIT database [19].

When performing either sphere or ellipsoid modelling, their sizes and number of facets can also be user-defined. Nonetheless, the user-input data can also be used to overrule any inputs in the asteroid's physical parameters and validation parameters when required. Moreover, the output produced by the ATRM is a data frame of basic facet-related parameters as seen in Section 3.4, illumination and visibility status, facet albedo value, and computed facet insolations, surface temperatures, thermal, reflected, and total flux densities. Those outputs can be represented as light curves and 3D models. A summary of the ATRM workflow is given by a flow diagram illustrated in Figure 3.10.1. The majority of the model was created with Python 3 [75], where the python package Pandas [50] was extensively used for manipulating large data frames, and the python package Matplotlib [30] was used for 2D and 3D visualisations.

3.1. Shape file databases

Most asteroid shape models are represented as polyhedrons made up of a mesh of N triangular surface facets, as can be seen in Figure 3.1.1. The more facets, the more detailed and representative of the actual asteroid the shape file becomes. However, as the number of facets increase, so does the computing time and/or power needed to process them. Furthermore, the vertices of the facets are usually expressed in Cartesian coordinates but some databases have them in spherical coordinates. The ATRM is working in the Cartesian system but when required, spherical coordinates can be easily converted to Cartesian coordinates.
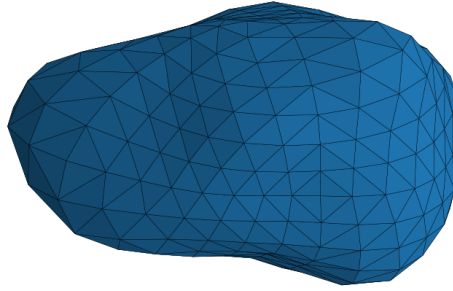
Figure 3.1.1: Example of a 3D asteroid polyhedron model, in this case 21 Lutetia, taken from the Database of Asteroid Models from Inversion techniques (DAMIT). This shape model is made up of 2040 facets and 1022 vertices.

The shape files, consisting of the 3D coordinates of the facet vertices, are obtained from the following main two databases:

- Database of Asteroid Models from Inversion techniques (DAMIT) - [19]
- Radar Shape Model of Asteroid (101955) Bennu (RSMAB) - [67]

The second aforementioned database can be obtained from the Small Bodies Node (SBN) of NASA's Planetary Data System (PDS). In most cases, these databases also include the facet order list and spin properties. The facet order list gives the combination of three vertices which make up a facet, where the order is listed as anti-clockwise seen from outside the asteroid shape model. In the case where some shape file databases do not provide a facet order list or are found to be missing, an ad-hoc Delaunay triangulation can be used to create the facet order list.

3.2. Frames of reference

The ATRM mainly deals with three frames of reference, namely the asteroid shape body reference frame, the asteroid co-rotating coordinate frame, and the asteroid-centric ecliptic coordinate frame. The frames of reference, and the relevant transformation angles are illustrated in Figure 3.2.1.

Asteroid shape body reference frame
It follows directly from the shape model databases, where the positive z-axis is aligned with the positive axis of rotation, following the right-hand rule.

Asteroid co-rotating coordinate frame
It defines the spin axis orientation with respect to the asteroid-centric ecliptic coordinate frame. They are related by the ecliptic longitude λ, and ecliptic latitude β, where the asteroid rotates with an angular frequency of $\omega = 2\pi/P$, where P is the sidereal rotational period of the asteroid. The spin modelling is further elaborated upon in Section 3.3.

Asteroid-centric ecliptic coordinate frame
It is similar to the heliocentric ecliptic coordinate frame, but the origin has been translated to the centre of mass (C.O.M.) of the asteroid. This coordinate frame was made to facilitate the validation process, since the coordinates of the Sun and observer were listed as such.
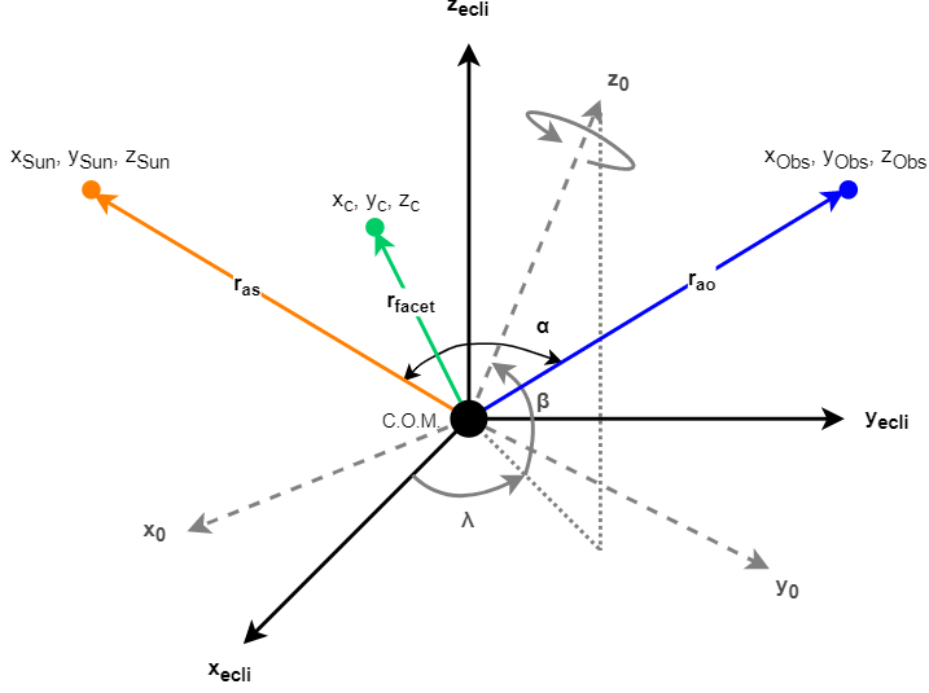
Figure 3.2.1: Illustration of the ATRM's frames of reference, where $(x_{Sun}, y_{Sun}, z_{Sun})$ is the position of the Sun, $(x_{Obs}, y_{Obs}, z_{Obs})$ is the position of the observer, both also defined by the phase angle α between them. The ecliptic longitude and ecliptic latitude are given by λ and β, respectively. r_{as} is the distance between the Sun and the asteroid, r_{ao} is the distance between the observer and the asteroid, (x_c, y_c, z_c) is the location of a facet centroid, and r_{facet} is the facet radius. C.O.M. is the centre of mass of the asteroid. [Not to scale]

3.3. Spin modelling

The ATRM's spin modelling, that is the orientation of the asteroid model at an epoch t, is given by a vector transformation between the coordinates of the triangular vertices $\mathbf{r_{ecl}}$ in the asteroid-centric ecliptic coordinate frame, and $\mathbf{r_{ast}}$ in the asteroid co-rotating coordinate frame. This transformation operation can be seen in Equation (3.3.1), and illustrated in Figure 3.3.1.

$$\mathbf{r}_{ecl} = R_{\mathbf{z}}(\lambda)\, R_{\mathbf{y}}\left(90^\circ - \beta\right)\, R_{\mathbf{z}}\left(\varphi_0 + \frac{2\pi}{P}\left(t - t_0\right)\right)\mathbf{r}_{ast} \tag{3.3.1}$$

Where it can be seen that the spin modelling only uses three Euler angles in a ZYZ transformation sequence. Only the transformations around the z-axis and y-axis are required, and given by Equation (3.3.2) and Equation (3.3.3), respectively.

$$R_{\mathbf{z}}(\theta) = \begin{pmatrix} \cos\theta & -\sin\theta & 0 \\ \sin\theta & \cos\theta & 0 \\ 0 & 0 & 1 \end{pmatrix} \tag{3.3.2}$$

$$R_{\mathbf{y}}(\theta) = \begin{pmatrix} \cos\theta & 0 & \sin\theta \\ 0 & 1 & 0 \\ -\sin\theta & 0 & \cos\theta \end{pmatrix} \tag{3.3.3}$$

In Equation (3.3.1), $R_i(\theta)$ represents a generic rotation matrix corresponding to the rotation of a vector through an angle θ along the i-axis in the anti-clockwise direction. The ecliptic longitude and ecliptic latitude of the spin axis (J2000) are given by λ and β, respectively. Then, P is the sidereal rotational period of the asteroid, t_0 is the initial time in Julian date epoch, and its initial rotation angle is given by φ_0 (degrees) [19]. If any of the mentioned parameters are not listed in their respective shape databases, then they were obtained from the JPL Small-Body Database Browser [63].
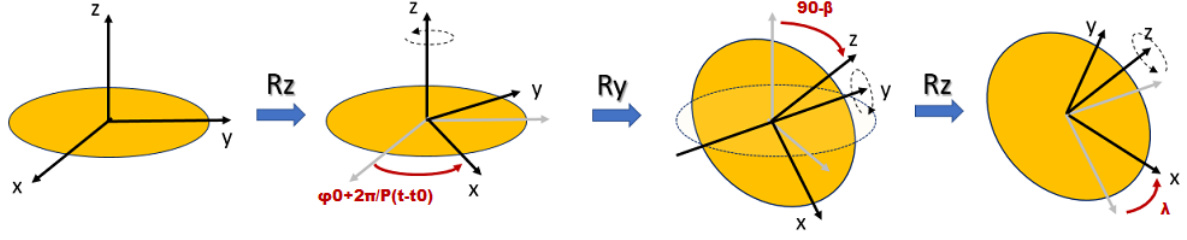
Figure 3.3.1: Illustration of order of elementary rotations to obtain accurate spin modelling. Modified from [70]

From Figure 3.3.1, it can be seen that the $R_z(\lambda)$ and $R_y(90° - \beta)$ terms rotate the coordinate vectors so that spin axis is correctly aligned in the asteroid-centric ecliptic coordinate frame. Subsequently, it is only the $R_z(\varphi_0 + \frac{2\pi}{P}(t - t_0))$ term that then dictates the amount of spin the asteroid has at a specific time.

3.4. Facet-related calculations

Before the actual insolation, temperature, thermal or reflected light calculations can be carried out, the defining parameters of a facet need to be obtained first. They include the facet normal, facet centroid, facet area, and facet radius, plus the angles of illumination and observation, which are illustrated Figure 3.4.1.
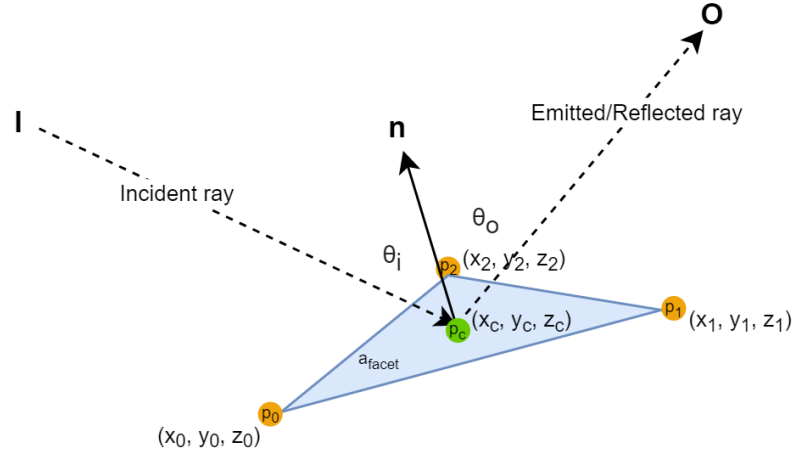
Figure 3.4.1: Illustration of facet geometry, where **I** and **O** are the vectors of the incident and emitted/reflected rays respectively, (x_c, y_c, z_c) are the coordinates of the facet centroid, θ_i and θ_o are the angles of illumination and observation, respectively, and finally **n** is the facet normal. [Not to scale]

The facet normal **n**, is computed using the cross-product of its demarcating coordinate points (vertices) as seen in Equation (3.4.1), where the unit facet normal $\hat{\mathbf{n}}$ is also shown. It should be noted that p_0 is the 3D point made at coordinates (x_0, y_0, z_0), and that the same logic applies for points p_1 and p_2.

$$\mathbf{n} = (p_1 - p_0) \times (p_2 - p_0) \quad \text{where} \quad \hat{\mathbf{n}} = \frac{\mathbf{n}}{|\mathbf{n}|} \tag{3.4.1}$$

Note that the order of the cross-product is essential to obtain the outward-facing normal. The right-hand rule is applied to determine the correct order.

Furthermore, the facet centroid p_c given by the coordinates (x_c, y_c, z_c), is computed using Equation (3.4.2) which uses the properties of triangles.

$$p_c = \frac{1}{3}(p_0 + p_1 + p_2) \tag{3.4.2}$$

The facet area a_{facet}, is computed using Equation (3.4.3) which uses the properties of vectors and the cross-product.

$$a_{\text{facet}} = \frac{1}{2} |(p_1 - p_0) \times (p_2 - p_0)| \quad = \quad \frac{1}{2} |\mathbf{n}| \tag{3.4.3}$$

The facet radius r_{facet}, which is distance between the C.O.M. of the asteroid and the facet centroid, is calculated using Equation (3.4.4). Since the C.O.M. of the asteroid is usually found at the origin of the frame of reference, the facet radius is simply the modulus of the facet centroid.

$$r_{\text{facet}} = |\text{origin}_{\text{asteroid}} - p_c| \quad = \quad |p_c| \tag{3.4.4}$$

Furthermore, the cosines of the angles of illumination and observation were computed using the properties of dot products and are given in Equation (3.4.5) and Equation (3.4.6), respectively. $\mathbf{I}$ denotes the direction of illumination and $\mathbf{O}$ the direction of observation, both with respect to the asteroid origin.

$$\mu_0 = \cos\theta_i = \frac{\mathbf{I} \cdot \mathbf{n}}{|\mathbf{I}|\,|\mathbf{n}|} \tag{3.4.5}$$

$$\mu = \cos\theta_o = \frac{\mathbf{O} \cdot \mathbf{n}}{|\mathbf{O}|\,|\mathbf{n}|} \tag{3.4.6}$$

It is important to note that all facet angle calculations, which uniquely uses each facet's normal, are made with respect to the r_{as} and r_{ao} vectors which are taken from the asteroid's centre of mass and not the facet centroid. This is a fair assumption given the significantly large distances involved. Since the distance of the facet radius is significantly smaller than the distance of the Sun's or observer's position, the small-angle approximation is valid. Moreover, every calculation with respect to a facet was then carried out with respect to the facet's centroid. This has implications in the shadowing of the facet, which will be discussed upon in the following Section 3.5.

3.5. Facet shadowing and visibility

Since the ATRM tool is mostly dealing with asteroids with sparse and shallow protrusions and intrusions, a simple shadowing algorithm was implemented through local horizon mapping. The algorithm detects at each local facet if the angle of illumination, measured from the facet normal, is greater than 90°, then the facet is considered not be illuminated, that is, shadowed. The same logic was applied when determining if a facet was in view of an observer.

$$\text{if } \cos\theta_i < 0, \ F_{\text{facet, insolation}} = 0 \text{ and } T_{\text{facet}} = 0 \tag{3.5.1}$$

$$\text{if } \cos\theta_o < 0, \ F_{\text{facet, thermal}} = 0 \tag{3.5.2}$$

$$\text{if } \cos\theta_i < 0 \text{ and } \cos\theta_o < 0, \ F_{\text{facet, reflected}} = 0 \tag{3.5.3}$$

It is important to note that the local horizon mapping algorithm was applied at the location of the facet's centroid. This is not an ideal condition since depending on the size and shape of the facet, part of the facet can be illuminated/visible whereas the other can be shadowed. This can be exacerbated with highly skewed facets, where one vertex lies much further away than the other two from the facet's centroid. Nonetheless, for convex-shaped and approximately symmetrical asteroids, the local horizon mapping rejection criteria effectively removes about half the total number of facets, where the remaining ones are either illuminated or visible at a specific orientation, depending on the orbital geometry.

A ray tracing algorithm was initially explored to deal with more complex and concave-shaped asteroids. However, it was ultimately abandoned since it would increase the computing time by a factor proportional to the square of the number of facets left after the local horizon mapping was carried out [82]. Thus, since no ray-tracing is used in the ATRM, it can only handle fairly simple asteroid shapes, which are mostly convex-shaped.

3.6. Sphere Modelling

There are two main methods of creating a polyhedron sphere, namely, a UV sphere, and an Icosphere. These two methods have their accompanying advantages and disadvantages, which will be further discussed here. A UV sphere follows from the concept of UV mapping, where a 3D model is created from the projection of a 2D image on its resulting 3D shape. In the case of a sphere, a quadrilateral mesh (where 1 quadrilateral mesh cell can be further sub-divided into 2 triangular cells) is wrapped around to produce a sphere, and the vertices at the top and bottom of the global mesh converge to form the poles, as seen in Figure 3.6.1. This UV sphere is especially useful when latitude and longitude positions are required, for instance Earth Observation applications, and permits easy terrain/texture projections, and easily moving between 2D and 3D projections.
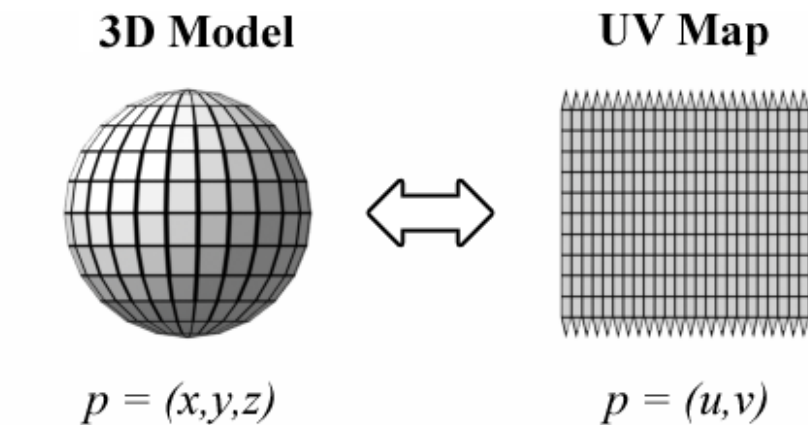
Figure 3.6.1: UV mapping to produce UV sphere [87].
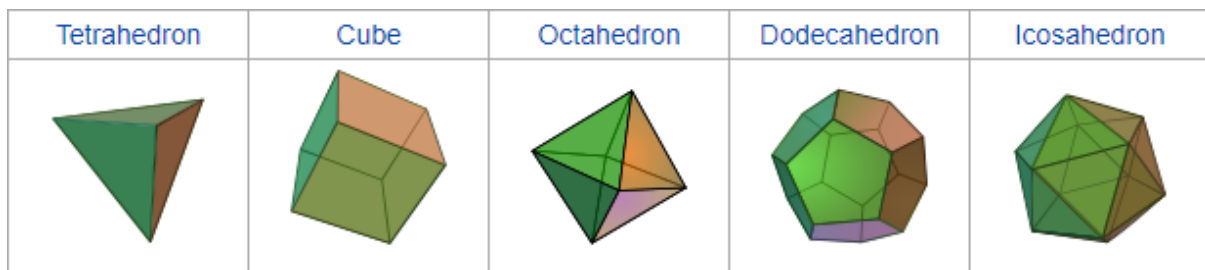
Figure 3.6.2: Illustration of the five platonic solids [16].

An Icosphere is a modelled sphere created from a base platonic solid. The latter is a convex-shaped polyhedron made up of congruent polygonal facets, where the same amount of facets meet at each vertex. There are only five platonic solids, namely, the tetrahedron, cube, octahedron, dodecahedron, and icosahedron, all illustrated in Figure 3.6.2. Their respective affixes indicate the number of identical facets they have, that is, four, six, eight, ten, and twenty. However, the higher the number of facets from the base platonic solid, the more idealised the final 3D model of the Icosphere will be. Hence, this sets the icosahedron as the best primitive shape to make the Icosphere. An example of the both the UV sphere and Icosphere, produced by the ATRM, are illustrated in Figure 3.6.3 and Figure 3.6.4, respectively. They were created with the help of a modified Python subpackage, namely meshzoo [68].
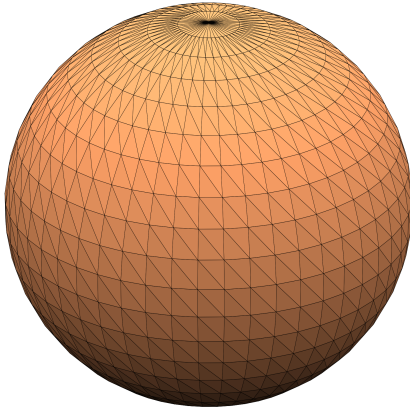
Figure 3.6.3: Example of a unit radius UV sphere, made up of 2000 facets.
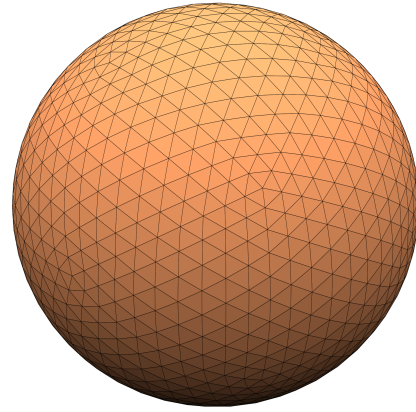
Figure 3.6.4: Example of a unit radius Icosphere, made up of 2000 facets.

From Figure 3.6.3 and Figure 3.6.4, some advantages and disadvantages can already be observed. For instance, the Icosphere mesh pattern seems to be most consistent across any orientation, whereas at the poles of the UV sphere, the facet distribution is highly packed with thin and elongated facets. Thus, regardless of orientation, an Icosphere will display less variations in flux density than a UV sphere given by its nature. Moreover, since the facet shapes of Icospheres tend to be more equilateral triangles, they are more effective when considering shadowing. On the other hand, the elongated facet triangles of UV spheres become an issue with shadowing since at some orientations, part of the elongated facets could be potentially illuminated and the other shadowed. The poles of a UV sphere can be especially affected by this as can be seen in Figure 3.6.3, where the facets are most elongated.

Furthermore, for comparison purposes assuming a sphere of radius 1 km, looking at both a UV sphere and an Icosphere of 2000 facets (2000 since this is the average number found in most databases of asteroid shape models), the UV sphere produces a relative standard deviation in facet radius of 0.06% whereas the Icosphere produces a difference of 0.03%. The UV sphere has a smaller deviation, but they are both significantly small, and indicate that a facet number of 2000 produces nearly spherical bodies. On the other hand, the UV sphere produces a relative standard deviation in facet area of 42.4% whereas the Icosphere produces a difference of 13.1%. This shows that the Icosphere would be better for shadowing and visibility purposes, and making different surface albedo distributions, given that its facet area varies less. Thus, for the aforementioned reasons, an Icosphere will be used in all instances of sphere modelling (and as base to ellipsoid modelling) in the ATRM.

3.7. Ellipsoid Modelling

An ellipsoid is basically a sphere but with at least one of its principle axes having a different length compared to the other two. If all three principle axes are unique, that is all have different lengths, then the ellipsoid is said to be tri-axial (also known as a scalene). The Cartesian equation defining a tri-axial is given by Equation (3.7.1), where a, b, and c are positive real numbers. If only one axis has a different length and the other two are of the same length, then it is known as a spheroid. The difference between a sphere and ellipsoid can be seen in Figure 3.7.1.

$$\frac{x^2}{a^2} + \frac{y^2}{b^2} + \frac{z^2}{c^2} = 1 \tag{3.7.1}$$

From Equation (3.7.1), it is clear that if $a = b = c = $ const. k, it would result in the Cartesian equation defining a perfect sphere centered at (0, 0, 0), and with radius $\sqrt{\text{const. k}}$.
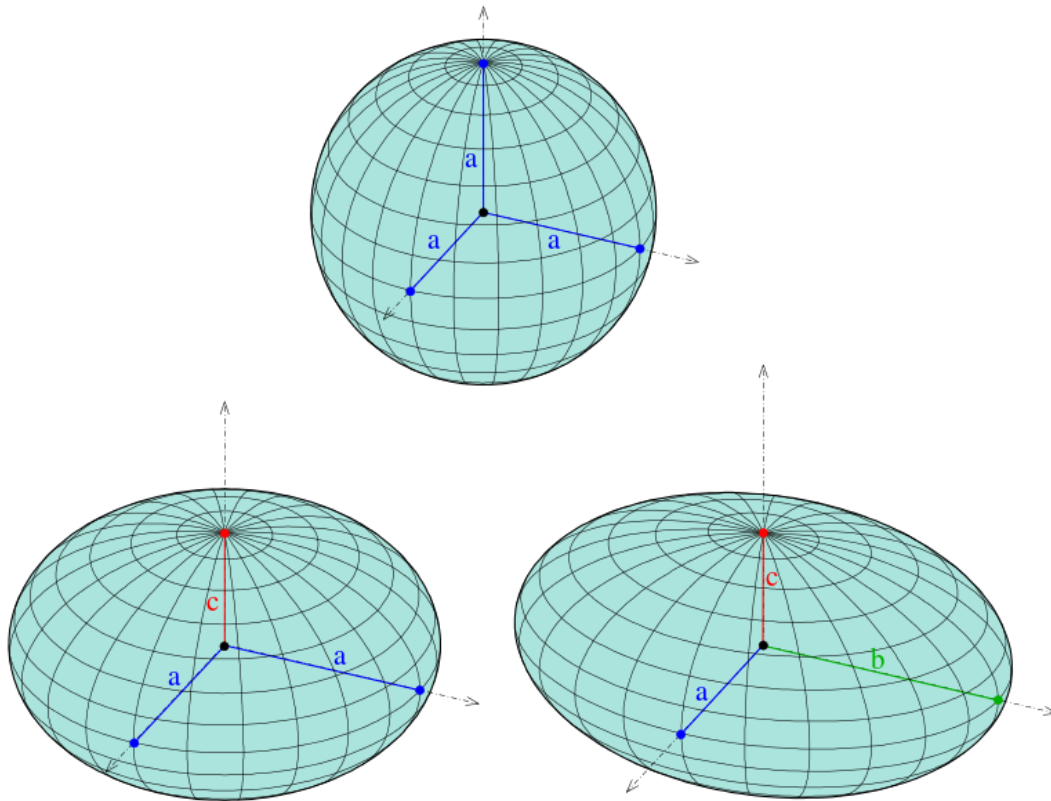
Figure 3.7.1: Examples of different ellipsoids. Top is a perfect sphere, bottom left is a spheroid, and bottom right is a tri-axial [2].

A spheroid is invariant under the rotation around the third unique axis. A spheroid can be oblate or prolate. Oblate in the case where the unique third axis is shorter than the other two ($a = b > c$), and prolate when the unique third axis is longer than the other two ($a = b < c$). Thus, a custom sized tri-axial, oblate or prolate spheroid can be obtained by scaling a perfect sphere by a factor of a, b, and c for their corresponding x, y, and z coordinates to obtain the desired ellipsoidal shape representative of an elongated asteroid [8].

3.8. Heterogeneous albedo modelling

The ATRM is able to vary the surface albedo distribution of any asteroid shape through an octant allocation system. It is relatively straightforward and follows from the Cartesian coordinate system, where an asteroid found in its shape body reference frame has the centroids of its facets within one of the eight regions forming an octant as can be seen in Figure 3.8.1. Thus, using the boundaries of the x, y, and z axes, a particular albedo value can be assigned to facets whose centroids lie within that certain octant. It should be noted that in the cases when the facet centroids lie exactly on a boundary line, the ATRM randomly assigns it to one of the two adjacent regions of concern. Furthermore, since the positive z-axis of the asteroid body reference frame is aligned with the positive spin axis of the asteroid, the resulting octant albedo distribution will also be with respect to the spin axis of the asteroid.
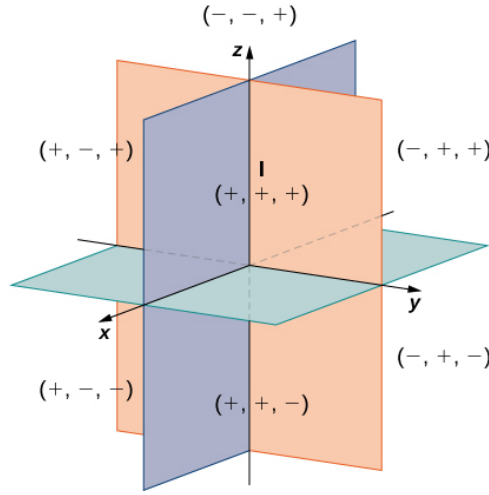
Figure 3.8.1: Octant allocation system of assigning surface albedos to obtain heterogeneous distribution [44].

3.9. Flux modelling

The modelling of the different fluxes (flux densities) will be explored into more details per the following sub-subsections.

3.9.1. Facet insolation

Facet insolation (also referred to as solar irradiance), is obtained by applying Equation (3.9.1) [45], where r_{as} is in astronomical units. The $\cos\theta_i$ term follows from Lambert's cosine incidence law. The resulting unit of facet insolation is in W/m^2.

$$F_{\text{facet, insolation}} = \frac{S_\odot \cdot \cos\theta_i}{r_{as}^2} \tag{3.9.1}$$

Of relevance to the verification afterwards, is the incident solar power on a facet which is just the addition of the facet area term. The unit is W.

$$P_{\text{facet, incident}} = \frac{S_\odot \cdot a_{\text{facet}} \cdot \cos\theta_i}{r_{as}^2} \tag{3.9.2}$$

The shadowing condition follows from Section 3.5. The total insolation at a specific orbital geometry is obtained by summing all the contributing illuminated facets:

$$F_{\text{tot. insol.}} = \sum_i^N F_{\text{facet i, insol.}} \tag{3.9.3}$$

Where i is the facet number, and N the total number of facets.

3.9.2. Thermal flux density

Before computing the facet thermal flux density, the facet temperature has to be calculated first. This is done by applying Equation (3.9.4) [12] [14] [28], where r_{as} is again in astronomical units since it scales the solar constant. The resulting unit of facet temperature is obtained in K.

$$T_{\text{facet}} = \left[\frac{(1 - A_{\text{facet}}) \cdot S_\odot \cdot \cos\theta_i}{\eta \cdot r_{as}^2 \cdot \varepsilon_{\text{facet}} \cdot \sigma} \right]^{1/4} \tag{3.9.4}$$

Where A_{facet} and $\varepsilon_{\text{facet}}$ are the surface albedo and surface emissivity of that specific facet, respectively. If not explicitly mentioned otherwise, then $\varepsilon_{\text{facet}} = 0.9$ which follows from the standard bolometric emissivity of asteroids [14], and $A_{\text{facet}} = A_\nu$ which is visible Bond albedo as explained in Section 2.3. A_{facet} is adjusted when heterogeneous surface albedos are being modelled. Stefan-Boltzmann constant is represented by σ. It should be noted that the beaming parameter η was kept as $\eta = 1$, unless stated otherwise such as in the case of the

thermal flux density validation.

Subsequently, for a given wavelength λ, the facet thermal flux density is obtained by applying Equation (3.9.5) [12] [14] [28] [39] [77], where r_{ao} is now in SI units, that is, meters. The resulting unit of facet thermal flux density is obtained in $W/m^2/m$. The $\cos\theta_o$ term follows from Lambert's cosine emission law.

$$F_{\text{facet, therm.}}(\lambda,\ T_{\text{facet}}) = B_\lambda(\lambda,\ T_{\text{facet}}) \cdot \frac{a_{\text{facet}} \cdot \cos\theta_o \cdot \varepsilon_{\text{facet}}(\lambda)}{r_{ao}^2} \tag{3.9.5}$$

If not explicitly mentioned otherwise, then $\varepsilon_{\text{facet}} = 0.9$ as is the case in the thermal flux density validation. However, it should be noted that if Kirchhoff's law is respected when computing thermal and reflected light in the same bands/wavelength regions, then in Equation (3.9.5), $\varepsilon_{\text{facet}}(\lambda) = 1 - A_{\text{facet}}(\lambda)$ which is applied in Chapter 5. The facet thermal intensity per unit wavelength $B_\lambda(\lambda,\ T_{\text{facet}})$ is obtained by applying the Planck function as previously seen in Equation (2.3.10), but using the temperature of the facet. Since instantaneous thermal equilibrium is assumed, the shadowing condition follows from Section 3.5. The total thermal flux density at a specific orbital geometry is obtained by summing all the contributing illuminated and visible facets:

$$F_{\text{tot. therm.}} = \sum_i^N F_{\text{facet i, therm.}}(\lambda,\ T_{\text{facet}}) \tag{3.9.6}$$

3.9.3. Reflected flux density

For a given wavelength λ, the facet Lambertian reflected flux density is obtained by applying Equation (3.9.7) [25] [39] [56], where r_{ao} is also in SI units, that is, meters. The resulting unit of facet reflected flux density is obtained in $W/m^2/m$.

$$F_{\text{facet, refl.}}(\lambda) = B_\lambda(\lambda,\ T_{\text{Sun}}) \cdot \frac{R_{\text{Sun}}^2}{r_{as}^2 \cdot r_{ao}^2} \cdot A_{\text{facet}}(\lambda) \cdot a_{\text{facet}} \cdot \cos\theta_i \cdot \cos\theta_o \tag{3.9.7}$$

Where R_{Sun} is the solar radius, and the reflected intensity per unit wavelength $B_\lambda(\lambda,\ T_{\text{Sun}})$ is obtained by applying the Planck function as previously seen in Equation (2.3.10), but now T_{Sun} is the effective blackbody solar temperature at 5778 K [45]. The shadowing condition follows from Section 3.5. The total reflected flux density at a specific orbital geometry is obtained by summing all the contributing illuminated and visible facets:

$$F_{\text{tot. refl.}} = \sum_i^N F_{\text{facet i, refl.}}(\lambda) \tag{3.9.8}$$

3.9.4. Total flux density

The total flux density is simply the summation of the thermal and reflected flux densities at a specific orientation and observation wavelength or bandpass, under the same shadowing conditions, as seen in Equation (3.9.9) and is obtained in $W/m^2/m$.

$$F_{\text{tot.}} = F_{\text{tot. therm.}} + F_{\text{tot. refl.}} \tag{3.9.9}$$

3.10. ATRM flow diagram
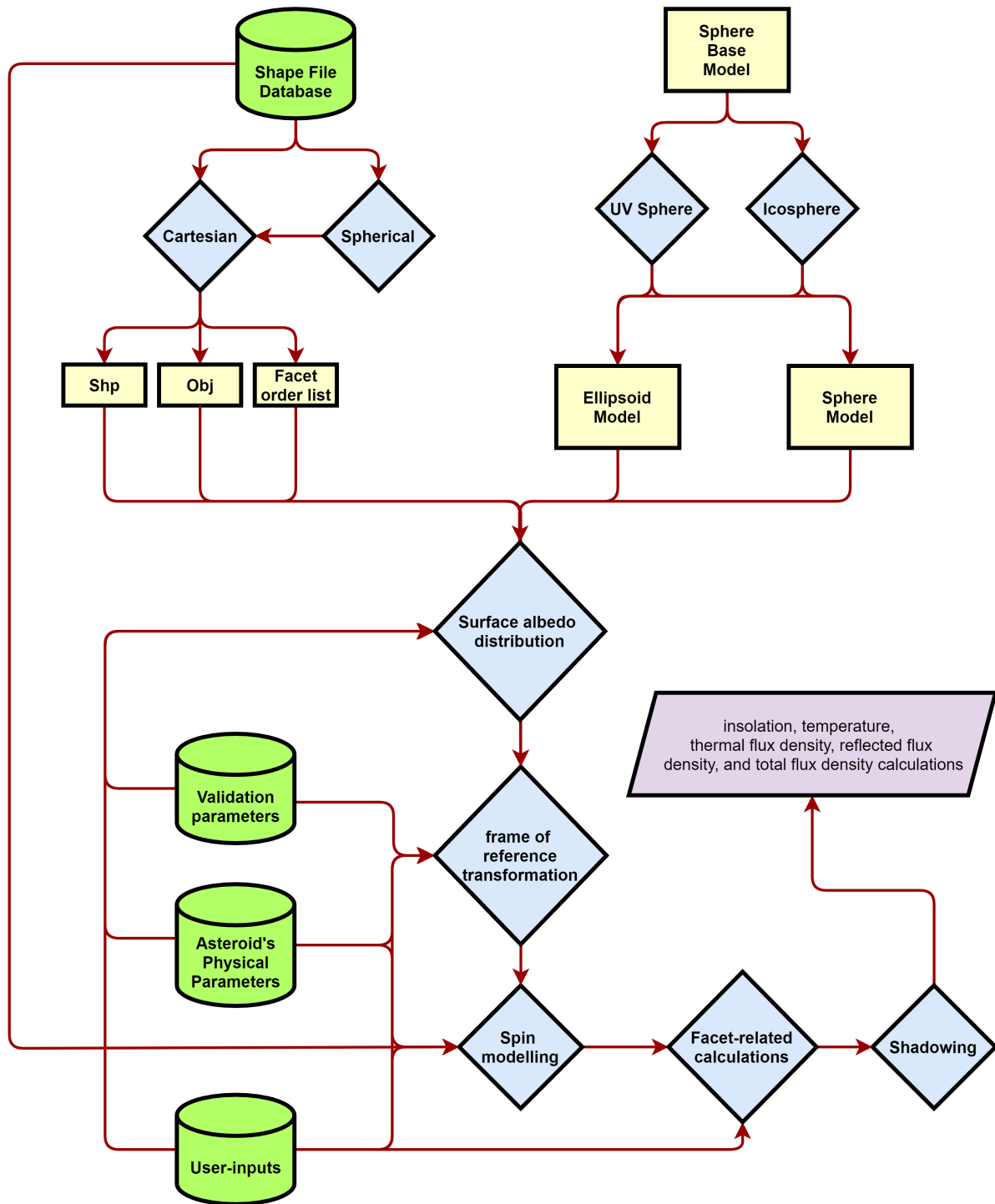
Figure 3.10.1: Flow diagram of ATRM. Note the UV sphere modelling is included in the sphere modelling give that it forms part of the ATRM, and was used for making a choice between UV- and Ico- spheres.

<div style="text-align: right; font-size: 3em; font-weight: bold;">4</div>

ATRM Verification & Validation

This chapter explores the verification and validation carried out to make sure the ATRM is correct. In Section 4.1, the uniformity of the various fluxes across the shape of a sphere are investigated. In Section 4.2, the facet temperature variation with respect to the heliocentric distance and incidence angle is verified. In Section 4.3, the relationship between phase angle and reflected flux density is used to verify the latter. Finally, some general verifications are summarised in Section 4.4.

This chapter also explores the validation carried out to make sure the ATRM is correct against actual external data. The two main aspects of the ATRM, that is, its thermal flux density modelling and its reflected flux density modelling are validated in Section 4.5 and Section 4.6, respectively. Furthermore, for transparency, the necessary unit conversation of fluxes are elaborated upon in Appendix A.

4.1. Sphere uniformity verification

Since the ATRM is able to model a sphere amongst others, the uniformity of the sphere's surface can be verified by looking at its flux density, over its rotational phase. A perfect sphere, at a given orbital distance and viewing angle, irrespective of its orientation should have a constant total incident solar power, total thermal flux density, and reflected flux density, ceteris paribus. An Icosphere consisting of 2000 facets, with (vertex) radius of 1000 m was modelled. Note that the number of facets selected is representative of what most DAMIT shape models are made of. The Sun-asteroid and observer-asteroid distances were set to 1 AU, and a thermal and reflected wavelengths of 12 microns and 0.551 microns were used respectively. A sidereal period of 6 hours was used. A facet albedo of 0.1, and an emissivity of 0.9 was used. Firstly, the uniformity of the total insolation was investigated, where the results are illustrated in Figure 4.1.1.

Table 4.1.1: Results of maximum, minimum, average, standard deviation, and relative standard deviation of total incident solar power of modelled Icosphere experienced across its rotation. The icosphere made of 2000 facets and a vertex radius of 1000 m. [Rel. std. dev. = Relative standard deviation]

	Total incident solar power [W]
Maximum	4263603574.6343
Minimum	4262018592.0682
Average	4262828465.5133
Standard deviation	497162.5767
Rel. std. dev. [%]	0.0117
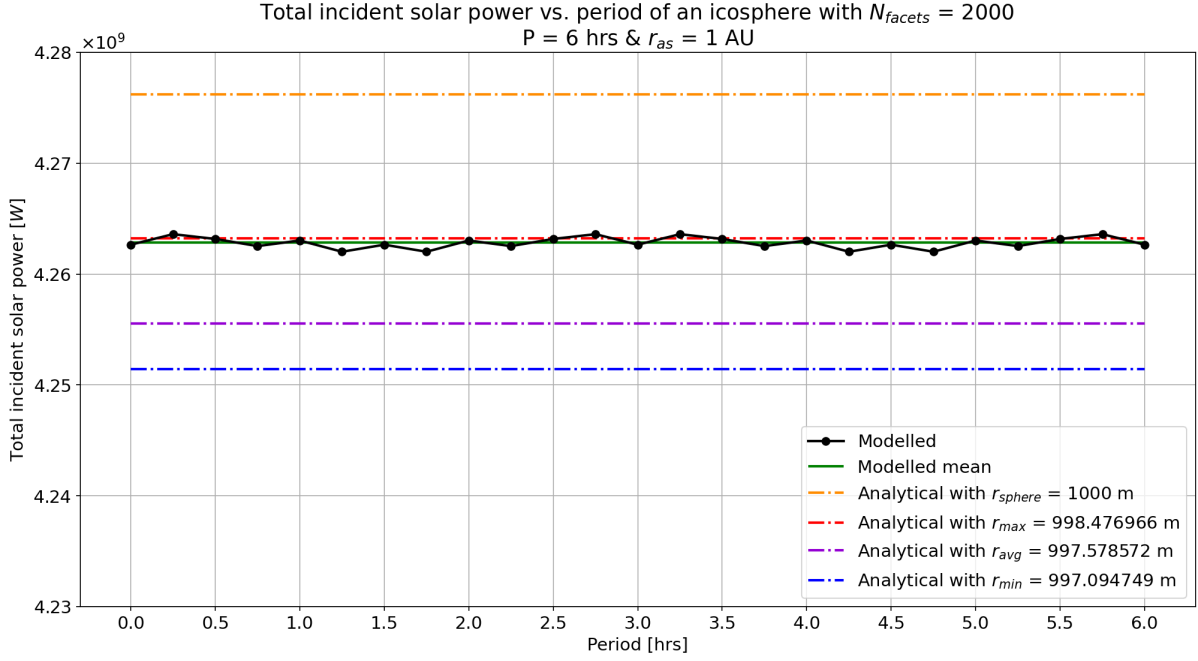
Figure 4.1.1: Modelled total incident solar power versus rotational period of modelled Icosphere compared to expected analytical results. Given that the modelled Icosphere is not a perfect sphere, r_{max}, r_{min}, and r_{avg} correspond to its maximum, minimum and average radii, respectively.

From Figure 4.1.1, it can be seen that for this modelled sphere, a variation [solid black] in total incident solar power per orientation is present. This is expected since an Icosphere is an idealised sphere made from the expansion of an icosahedron. The maximum, minimum, and mean total incident solar power obtained are summarised in Table 4.1.1. It can be observed that the variation is relatively small, where the standard deviation is 497162.5767 W, which is equivalent to a relative standard deviation of 0.0117%. This low percentage indicates that the Icosphere modelled has a very low deviation in total incident solar power across its shape, and is thus acceptable for the purposes of this master thesis.

Moreover, it can also be noticed that the mean of the modelled total incident solar power [solid green] is lower than that of a perfect sphere of the same size and sharing the same heliocentric distance [dashdot dark-orange]. This lower value is expected since the facet-related calculations of the Icosphere are made at the respective facet centroids. Since a facet is a 2D plane connecting its demarcating vertices, the facet centroid will naturally be found slightly away from the curve of the sphere, and thus would have a facet centroid radius smaller than the distance of the vertices from the sphere's origin (vertices radii). The analytical formula used to calculate the total incident solar power on a sphere is given by the following equation:

$$P_{\text{tot. insol.}} = \frac{L}{4 \cdot \pi \cdot r_{as}^2} \cdot \pi \cdot r_{\text{sphere}}^2 \tag{4.1.1}$$

Where L is the solar luminosity which is constant, r_{as} is the heliocentric distance which is kept fixed at 1 AU, and r_{sphere} is the radius of a perfect sphere. r_{sphere} was taken as the 1000 m [dashdot dark-orange], and r_{max} [dashdot red], r_{min} [dashdot blue], and r_{avg} [dashdot violet], are the maximum, minimum, and average facet radius of the modelled 2000 faceted Icosphere. It can be seen that the mean modelled total incident solar power [solid green] is closer to the analytical formula using r_{max} as r_{sphere}. However, since the mean of the modelled total incident solar power falls between the r_{max} and r_{min} lines, the modelled mean value seems reasonable.

Table 4.1.2: Results of average, standard deviation, and relative standard deviation of total thermal and reflected flux densities of modelled Icosphere experienced across its rotation, at phase angles of 0, 45, 90, and 135 degrees. Icosphere is made of 2000 facets and a vertex radius of 1000 m. [Tot. = Total, Std. dev. = Standard deviation, Rel. std. dev. = Relative standard deviation]

Phase angle [°]		Tot. thermal flux density $[W/m^2/m]$	Tot. reflected flux density $[W/m^2/m]$
0	Average	2.1017e-09	4.5779e-16
	Std. dev.	2.2290e-14	8.3671e-32
	Rel. std. dev. [%]	0.0011	0.1828e-13
45	Average	1.5889e-09	3.4579e-16
	Std. dev.	2.5545e-13	5.7577e-20
	Rel. std. dev. [%]	0.0161	0.0167
90	Average	6.7849e-10	1.4569e-16
	Std. dev.	2.1087e-13	1.8440e-20
	Rel. std. dev. [%]	0.0311	0.0127
135	Average	1.0271e-10	2.2086e-17
	Std. dev.	2.8537e-13	5.7577e-20
	Rel. std. dev. [%]	0.2778	0.2607

It can be seen from Table 4.1.2 that the relative standard deviations for the total thermal and reflected flux densities are less than 0.3% (as is the case for total insolation too) for all phase angles. However, it can be seen that the larger the phase angle, the greater the relative standard deviations. This can be explained by the fact that both flux density calculations use the cosine of the observation angle, and since the Sun-asteroid direction is kept fixed, when the phase angle is increased by moving the observer, that cosine plays a larger role. In doing so, it is more representative of the uniformity of the sphere since that cosine depends on facet normal. It should be noted that, even though not tabulated, the thermal and reflected flux densities and their corresponding relative standard deviations at a phase angle of 180 degrees are both zero. Ultimately, the relative standard deviations in thermal and reflected flux densities are low enough for the purposes of this master thesis.

4.2. Facet temperature verification

In Section 2.3, it was shown through Equation (2.3.8) how the facet temperature of a modelled asteroid will depend on the heliocentric distance of the asteroid r_{as}, the cosine of incidence angle θ_i, and its facet albedo A_{facet}, given that the Solar constant $S_\odot$, Stefan-Boltzmann constant σ, and emissivity ε remain unchanged in this case. Those dependencies are verified here, where it is expected that facet temperature increases with decreasing heliocentric distance, with decreasing angle of incidence, and with decreasing facet albedo. In Figure 4.2.1, it can be seen that the model facet temperature does indeed decrease with increasing heliocentric distance. Furthermore, at a given heliocentric distance, the model facet temperature does also indeed decrease with increasing angle of incidence.
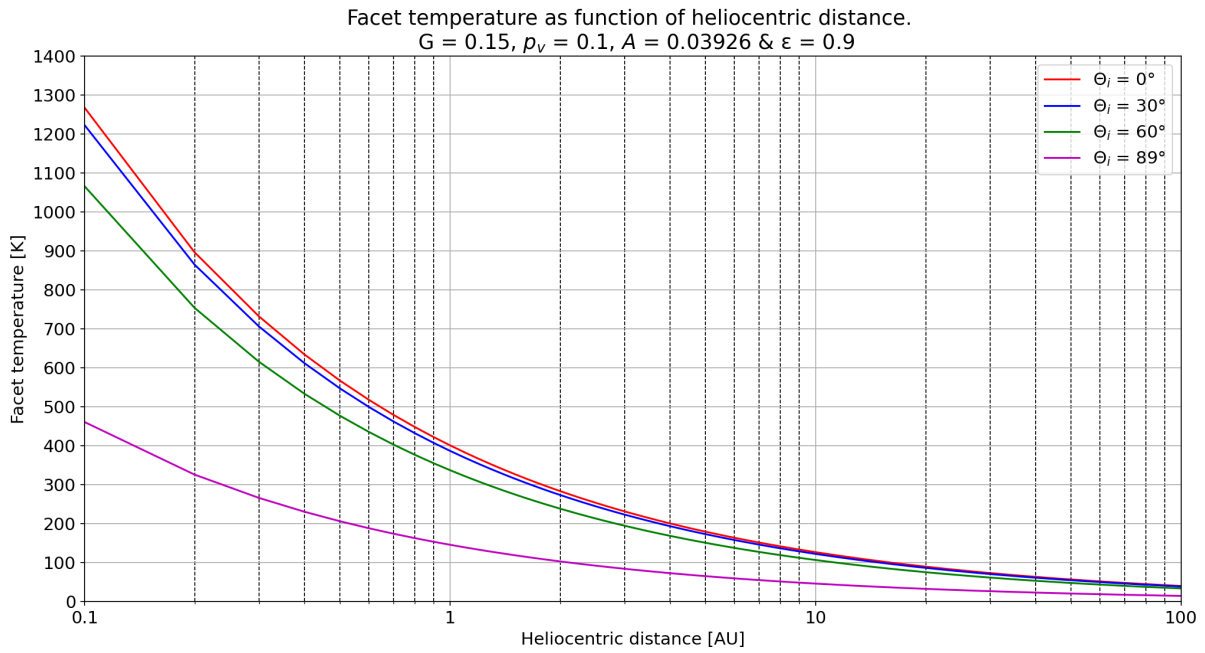
Figure 4.2.1: Facet temperature as function of heliocentric distance with varying angles of incidence, where G = 0.15, p_v = 0.1, A = 0.03926, & ε = 0.9.

In Figure 4.2.2, it can be seen that the modelled facet temperature does again indeed decrease with increasing angle of incidence. Furthermore, it can also be observed that the facet temperature also decreases with increasing albedo. This is expected, since albedo is the ratio of reflected energy to total incident energy. Thus, a higher albedo means more energy being reflected, and less being absorbed which leads to a lower facet temperature. An albedo of zero [solid black] would provide the maximum facet temperature, conversely an albedo of one would actually give a zero facet temperature. It is interesting to note in Figure 4.2.2 the rapid decrease in facet temperature at high incidence angles, that is when the incident ray is getting more parallel to the facet plane.
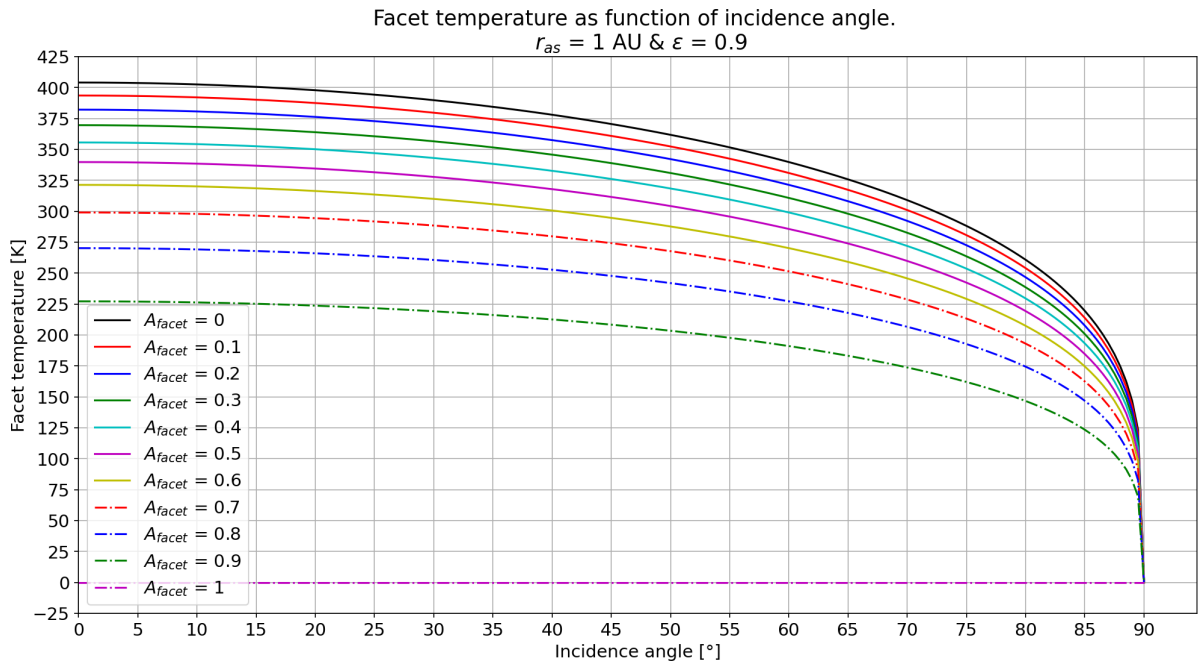
Figure 4.2.2: Facet temperature as function of incidence angle. r_{as} = 1 AU, ε = 0.9.

This implicitly verifies the temperature portion of the thermal flux density calculations.

4.3. Reflected flux density verification across phase angle

In this section, it will be explored if the total reflected flux density varies with phase angle and sphere size. From Figure 4.3.1, it can be observed that the normalised total reflected flux density curves of the modelled Icospheres of different radii all observe the same trend, that is, the total reflected flux density decreases with increasing phase angle. This is expected since less of the sphere is being visible to the observer.

The disk-integrated reflected light of the ATRM can be verified by using its normalised modelled total reflected flux density and comparing it against the analytical form for the phase function of a Lambertian reflecting sphere. The latter formula is given in Equation (4.3.1) [88], where A_{facet} is the (surface) facet albedo, and α the phase angle. The normalisation of the modelled total reflected flux density was carried out where the Planck function of the Sun, its solar radius, and the orbital radii to the Sun and Observer were removed. Then, the normalised reflected flux was computed, where the result was again normalised by the effective average facet radius of the sphere in view which would take into account the a_{facet} term. This normalisation is necessary to be able to compare the phase dependent parameters of the ATRM's Equation (3.9.7) to Equation (4.3.1). It can be seen that the terms of special interest for this dependency are $\cos\theta_i$ and $\cos\theta_o$.

$$\psi(\alpha) = \frac{2}{3\pi} A_{\text{facet}}(\sin(\alpha) + \pi\cos(\alpha) - \alpha\cos(\alpha)) \tag{4.3.1}$$
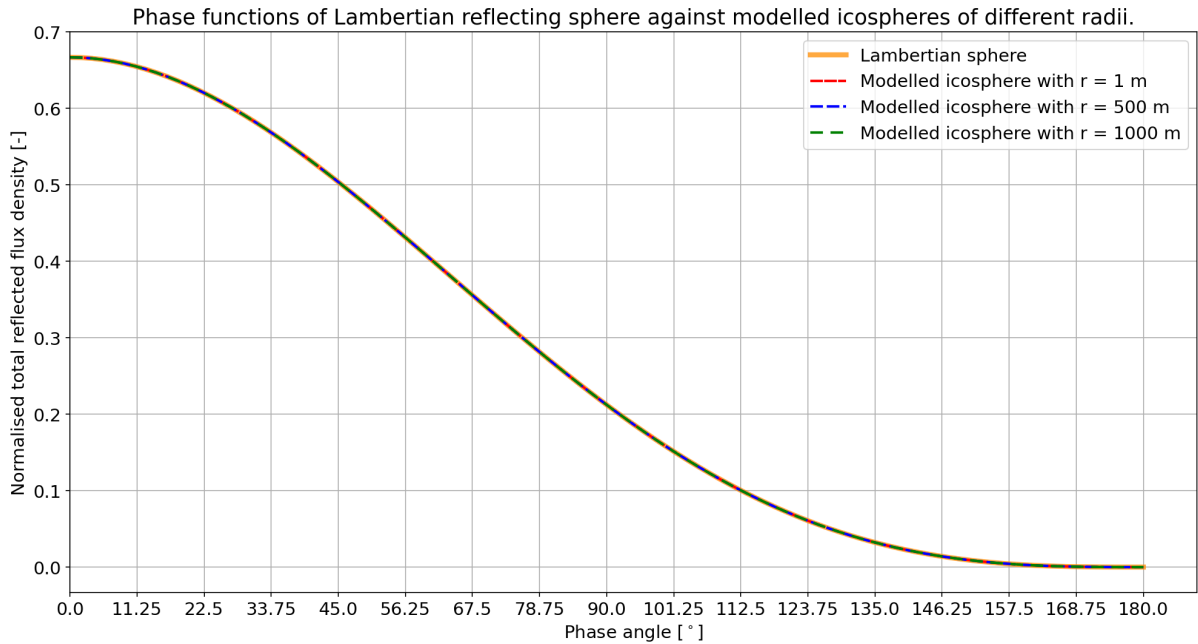
Figure 4.3.1: Phase function of normalised reflected flux densities of Lambertian sphere versus modelled Icospheres of different radii.

From Figure 4.3.1, it can be observed that the curves for the Lambertian sphere and the modelled Icospheres of different radii are virtually indistinguishable. Hence, since the curves of the analytical and modelled normalised total reflected flux densities are practically similar, this verifies the ATRM's treatment of phase angle contribution towards the reflected light. It should be noted that an analytical formula of the phase dependence of the thermal flux density does not exist, so such a verification could not be carried out.

4.4. General verifications

In this section, general but non-trivial verifications will be listed but not elaborated too much upon since they are rather straightforward.

- SI units were used throughout all calculations, and conversion to other units and order of magnitudes was tested on a sand-boxed calculation.

- Visual inspection of asteroidal shape models derived from different shape databases were carried out against the actual supposed shape.

- Depending on the situation, either visual or numerical verification that the facet normal is pointed outwards and not inwards was implemented.

- Verified that individual rotation matrices correspond to actual transformation about axis of interest.

- All the defining parameters of a facet, that is, its area, vector normal, centroid, and cosines of both its angle of illumination and observation, were all computed separately using Microsoft Excel for both a sphere model and actual asteroid shape model. No discrepancy was found.

- Furthermore, all facet temperature, insolations, and thermal, reflected, and total flux densities were also all computed separately using Microsoft Excel for both a sphere model and actual asteroid shape model. No discrepancy was found.

- Checked that the total insolation, and total thermal and reflected flux densities corresponded to the sum of all contributing facets. That is, the ones being both illuminated by the Sun, and visible to the observer. No discrepancy was found.

- Per asteroid use-case, since the extraction of the shapes files, the physical parameters of the asteroids, and the validation parameters (vector positions of the Sun and observer at specific time frames) were all automated in the numerical tool, a check was made that the actual relevant data and folder locations were being used by varying individually each input variable and seeing an expected associated change.

- Verified that all data frames, 2D, and 3D plots produced by the ATRM all corresponded to the actual asteroid under investigation with the proper physical, user-defined, and validation parameters when applicable.

The above listed verifications were all carried out successfully.

4.5. Thermal flux density validation

Since the ATRM is only an intermediate modelling tool which assumes no thermal emission on the night-side due to instantaneous thermal equilibrium, it would be difficult to completely validate it against advanced thermal models which do not assume it. However, such a validation is still carried out since valuable understanding in the lack of direct thermal inertia/heat conduction modelling will be gained. The validation of the thermal flux density produced by the ATRM was carried out against the thermal emission modelled by Emery et al. (2014) [henceforth referred to as Emery et al. for convenience], found in the paper titled "Thermal infrared observations and thermophysical characterization of OSIRIS-REx target asteroid 101955 Bennu" [21]. Bennu is a Apollo NEA and a PHA. It is a carbonaceous asteroid with a SMASS II B-type classification, with a diameter of 492km [63]. The data used by Emery et al.'s model used observation data of Bennu from the Spitzer Space Telescope (SST) which took eleven observations referred to as Astronomical Observation Requests (AORs) during the night of the 8th of May 2007. During that observation period, the average heliocentric distance r_{as} of Bennu was around 1.142825 AU, the average SST's distance r_{ao} was 0.53268 AU, and the phase angle α was about 61.76°.

The exact 3D positions of Bennu with respect to the Sun and the SST are essential for facet shadowing and facet visibility purposes. However, they were not listed in Emery et al.'s paper. Thus, the ecliptic Cartesian positions of Bennu at the respective 11 AORs w.r.t. the Sun and w.r.t. the SST were obtained from the JPL Horizon's Ephemeris tool [62]. A straightforward transformation was applied to those coordinates to be applicable in the ATRM's frame of references. Bennu's 3D shape file was taken from the same source as Emery et al., that

is, the radar-derived shape model [67]. The same longitude rotation shift of 74° in the radar shape model done by Emery et al. was also applied to the ATRM, and the initial time of this orientation was taken to be the Julian epoch corresponding to the first AOR. Bennu's sidereal rotational period and orientation of the spin axis were taken from the radar shape model also. They are 4.29746 hours for the sidereal rotation, and 45.4° and -88.4° for the ecliptic longitude and ecliptic latitude, respectively. For their investigation, Emery et al. used the wavelength region corresponding to the SST IRS PUI's (Infrared Spectrograph Peak-Up Imaging) red channel with an effective wavelength $\lambda_{\text{eff}} = 22.25\mu m$ and bandwidth $\triangle\lambda = 7.50\mu m$ [3]. Moreover, they fixed the emissivity at $\varepsilon = 0.9$ for both the temperature and thermal flux density calculations, and the facet albedo was taken from the product of the geometric albedo and the phase integral, where $p_\nu = 0.046$ and $q = 0.367$ [21]. It should be noted that Emery et al. used a value of $S_\odot = 1366 W m^{-2}$ instead of the more commonly used $S_\odot = 1361 W m^{-2}$ (also used by the ATRM). However, for this validation the ATRM's $S_\odot$ was adjusted to Emery et al.'s case.

It is important to note that during the initial validation of the ATRM against the results of Emery et al., the ATRM produced some major differences compared to those of Emery et al.'s. Several possible options were explored to try to justify the differences but none were found. After a subsequent e-mail exchange with Dr. Emery, he clarified that the illustrations of the distribution of facet temperatures and resulting facet thermal flux densities, as seen in Figure 4.5.1 and Figure 4.5.3 actually correspond to AOR #6, since it is found at about halfway across the eleven AORs, but the longitude rotation shift of 74° in the radar shape model was actually not applied in this case. [Initially, with the longitude rotation shift, it was thought that this orientation corresponded to AOR #3.] Furthermore, he also mentioned that for those shape visualisations, neither the filter+instrument functions nor the bandwidth were taken into account, where only the effective wavelength of $\lambda_{\text{eff}} = 22.25\mu m$ was directly used. He noted that the filter+instrument functions, bandwidth, and longitude shift were only applied to produce the thermal light curve, which will be explored in Section 4.5.1. Moreover, he also shared the exact ecliptic Cartesian coordinates they used, which were found to be in good agreement with what was initially retrieved from the JPL horizons tool.

Following all those clarifications, the same was applied to the ATRM. A side by side comparison is made where Emery et al.'s modelled facet temperature and facet thermal flux density distributions are illustrated in Figure 4.5.1 and Figure 4.5.3, respectively. That of the ATRM are illustrated in Figure 4.5.2 and Figure 4.5.4, respectively. It should be noted that the exact colour coding of the colour bar produced by the ATRM to represent the range of facet thermal flux density does not completely match that of Emery et al. given that their modelling tool was not made in Python. Different scaling methods were explored to correct for this difference, but this was the best result obtained by the ATRM where the labelled colour bar values are slightly higher relative to the same colours obtained by Emery et al.
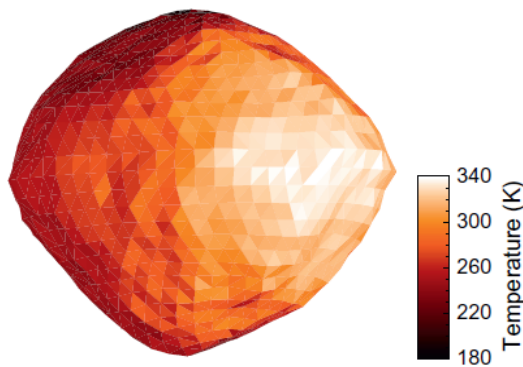
Figure 4.5.1: Emery et al. (2014)'s surface temperature distribution of Bennu, where $\Gamma = 250$ Jm^{-2}s$^{-1/2}$K^{-1} [21].
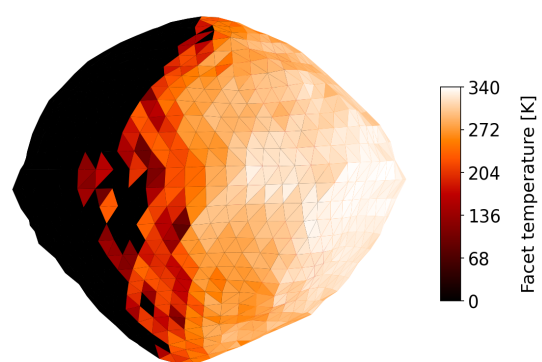
Figure 4.5.2: ATRM's surface temperature distribution of Bennu, using $\eta = 1.5$.
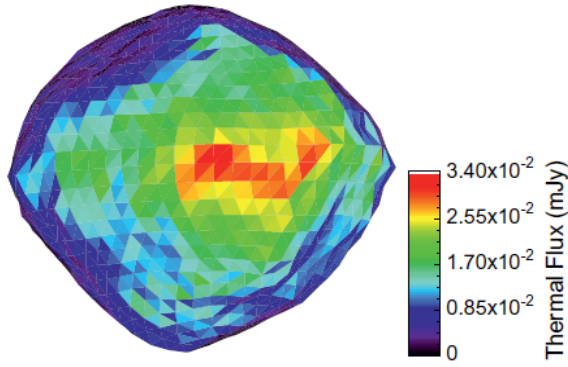
Figure 4.5.3: Emery et al. (2014)'s corresponding thermal flux density of Bennu using $\lambda_{\text{eff}} = 22.25 \mu m$ [21].
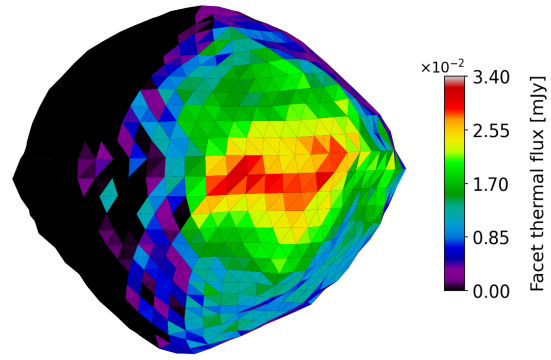
Figure 4.5.4: ATRM's thermal flux density distribution of Bennu at $\lambda_{\text{eff}} = 22.25 \mu m$.

In Emery et al.'s paper, NEATM-derived beaming parameters for each of the eleven AORs were given, which would be representative of the thermal inertia effects in this case. However, given that the visualised data does not correspond to any practical AOR (since no longitude shift was applied), as an alternative it was assumed that $\eta = 1.5$ given that the phase angle is more than $45°$, which follows from the findings of Delbo et al. (2003) [13], as already presented in Section 2.3. It can be seen in Figure 4.5.2, that the same maximum facet temperature of 340 K is obtained by the ATRM when compared to that of Emery et al.'s, suggesting that for this case, the beaming parameter of 1.5 is appropriate for scaling the temperature distribution. The location of the warmest facet temperatures is similar to the ones obtained by Emery et al. (right side of the asteroid), re-enforcing the fact that the 3D coordinates taken from JPL was correctly carried out, where the Sun is found more to the right of the asteroid when looking into the paper at the figures.

Furthermore, as seen in Figure 4.5.2, the ATRM produced black coloured facets on the left side of Bennu, indicating surface temperatures of 0 K. This is expected since the facets not in view of the Sun have zero temperature by definition. This illustrates a limitation of the ATRM where at non-zero phase angles, the ATRM will obtain zero surface temperatures for facets not in view of the Sun, which would effectively lower the thermal flux density seen by an observer. However, this limitation is mitigated at small to zero phase angles. The minimum facet temperature obtained by Emery et al. is 180 K which corresponds to temperatures on the night-side of Bennu, and are a result of the thermal inertia taken into account. Concerning the ATRM results, the minimum non-zero temperature is 47 K, the overall average facet temperature is 137 K, whereas the overall average of illuminated facet temperature is 262 K.

Looking at the thermal flux density produced by the ATRM, as seen in Figure 4.5.4, versus those of Emery et al. seen in Figure 4.5.3, it can be observed that the left side has no thermal emission as expected since the facet temperatures are zero in that region. However, the location and pattern of intermediate to maximum thermal flux densities found on the right side of Bennu match significantly with Emery et al's. This is expected since the maximum thermal emission is directly related to the regions of highest surface temperature which themselves are related to where maximum solar insolation occurs. However, the ATRM's maximum thermal flux density of 3.10×10^{-2} mJy versus Emery et al.'s 3.35×10^{-2} mJy gives a difference of 7.5%. This difference could be due to several factors. For instance, perhaps the constants of Planck, Boltzmann, and speed of light or even the value for 1 AU, are slightly different from the ones used in the ATRM [1]. The difference can not come from the observer's location and/or distance given that these parameters were provided/confirmed from the scientific author. The difference also can not come from the emissivity or facet area since the same ε value and shape file were used. Nonetheless, the percentage difference is rather small, and considered acceptable for the purposes of this validation of the ATRM's. Note that the necessary flux density conversion from the ATRM's $W/m^2/m$ to Emery et al.'s mJy are given in Appendix A.

---

[1] Further clarification from the scientific author was pursued on this issue, but no response was received at the time of the conclusion of this thesis project.

4.5.1. Attempting to correct for the assumption of no night-side thermal emission

Further investigation was carried out to try to match the surface temperature and thermal flux density distributions of the ATRM's result to that of Emery et al.'s, especially with regards to the ones with 0 K. To do so, the following method was explored. Firstly, the mean temperature of each facet was determined by computing the equilibrium temperature of each facet over one rotational period, and taking their respective average resulting in a mean equilibrium temperature $\bar{T}_{eq}$ for every facet. This corresponds to what is done in advanced thermophysical models, where this value is used as an initial facet temperature for the FDM calculation of heat conduction, as was explained in Section 2.4. Looking at Figure 4.5.5, the ATRM was ran for different sampling intervals over a rotation period, where it can be seen that as from 50 sampling intervals, the facet equilibrium temperatures stabilise. This means that for this given orbital geometry, the facet equilibrium temperatures are calculated every 5.2 minutes till one full rotation is completed. Subsequently, the maximum mean equilibrium facet temperature obtained is 163 K, the minimum mean facet equilibrium temperature is 88 K, the overall average of the mean equilibrium facet temperature is 150 K.
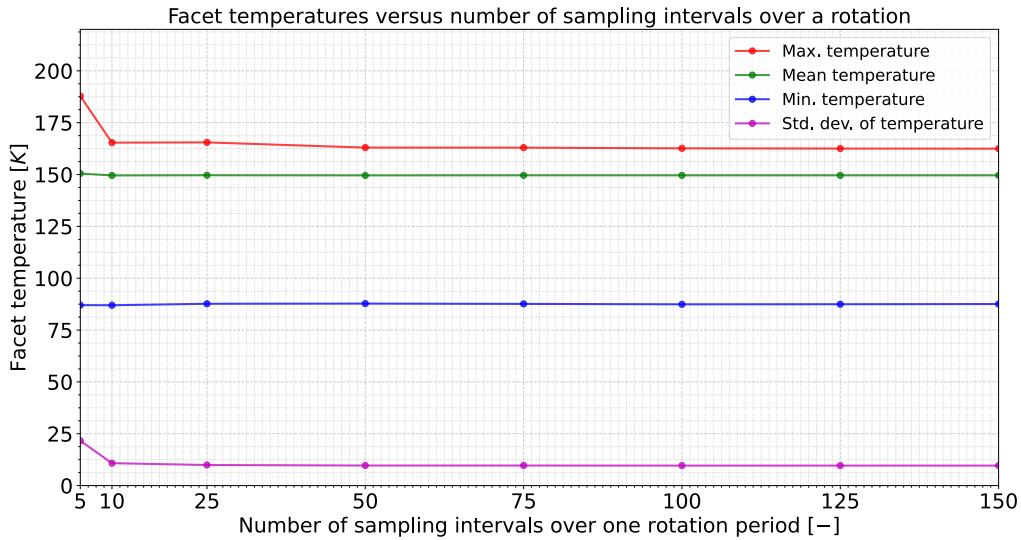
Figure 4.5.5: Facet equilibrium temperatures versus sampling interval over one sidereal rotation period of 101955 Bennu, where P = 4.29746 hours. A sampling interval of 5 corresponds to an equilibrium facet temperature calculated every 51.6 minutes over one rotation period. A sampling interval 150 corresponds to an equilibrium facet temperature calculated every 1.7 minutes over one rotation period but increases the computation time by a factor of about 33 compared to that of a sampling interval of 5.

Afterwards, the following condition was applied to all the facets: if the old facet temperature value is lower than their facet equilibrium temperature, it is replaced by the latter. The condition is summarised in Equation (4.5.1). This will lead to all facets having non-zero temperatures.

$$\text{if} \quad T_{\text{old facet i}} < \bar{T}_{\text{eq facet i}} \quad \text{then} \quad T_{\text{new facet i}} = \bar{T}_{\text{eq facet i}} \tag{4.5.1}$$

The new ATRM modelled facet temperatures and their resulting facet thermal flux densities are illustrated in Figure 4.5.6 and Figure 4.5.7. The new ATRM results obtained with the adjusted mean equilibrium temperature thus give a minimum facet temperature of 88 K as was previously derived, and an overall average facet temperature of 210 K. As expected, they are higher than for the initial case assuming no night-side thermal emission seen in Figure 4.5.2. The maximum facet temperature remains the same since it is not affected by the applied condition of Equation (4.5.1). Note that Figure 4.5.8 and Figure 4.5.9 are already given under Figure 4.5.6 and Figure 4.5.7, respectively for ease of comparison later on. The derived 1.975 factor listed in captions of the last two figures will be explained in the following paragraphs concerning the thermal light curves.
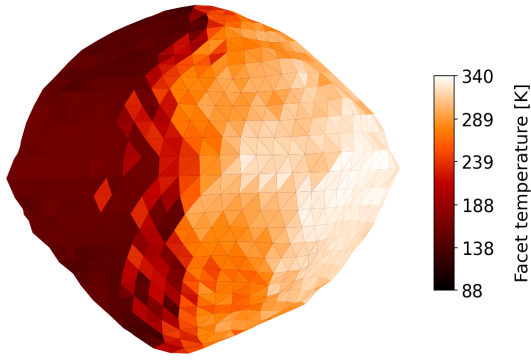
Figure 4.5.6: ATRM's modelled surface temperature distribution of Bennu using adjusted mean equilibrium facet temperature $\bar{T}_{eq}$.
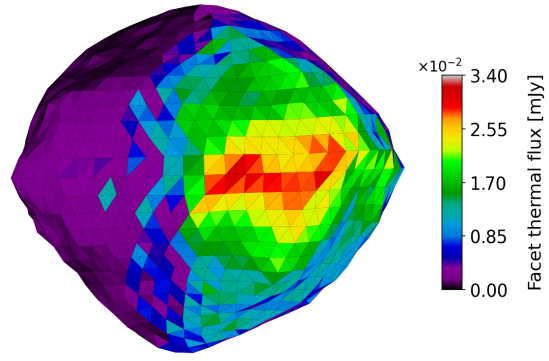
Figure 4.5.7: ATRM's modelled thermal flux density distribution of Bennu using adjusted mean equilibrium facet temperature $\bar{T}_{eq}$, at $\lambda_{eff} = 22.25\mu m$.
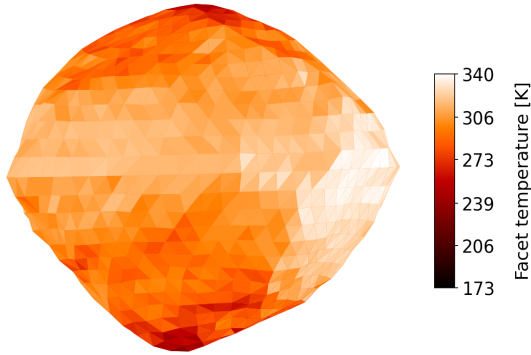
Figure 4.5.8: Idem as Figure 4.5.6 but adjusted using $1.975 \times \bar{T}_{eq}$
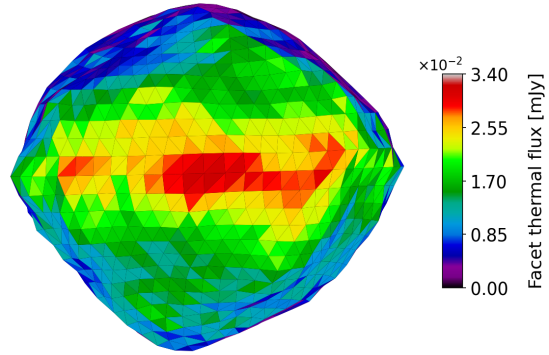
Figure 4.5.9: Idem as Figure 4.5.7 but adjusted using $1.975 \times \bar{T}_{eq}$

From Figure 4.5.6, it can now be seen that the left side of Bennu is not longer shaded black. However, the facet temperatures are still lower than the minimum facet temperature of 180 K obtained by Emery et al. as seen in Figure 4.5.1, as expected. Looking at the effect of those new non-zero facet temperatures at the thermal flux density, as seen Figure 4.5.7, the left side is now producing thermal emission but lower than that of Emery et al.'s since the facet temperatures themselves are too low to match the same thermal emission found in Figure 4.5.3. Nevertheless, it can be seen that even with adjusted non-zero facet temperatures, the ATRM modelled results do not match those of Emery et al.'s. Higher values of facet temperatures are needed to better match them. This will be addressed by looking at the thermal light curves of Emery et al.'s.

Since it was found that a beaming parameter of 1.5 appropriately scaled the temperatures of the illuminated facets in Figure 4.5.2, to calculate the surface temperature and resulting thermal emissions at the respective eleven AORs, it is assumed that the corresponding eleven NEATM-derived beaming parameters by Emery et al.'s should be accurate given that they are close to 1.5. They are listed as follows: [1.53, 1.55, 1.53, 1.54, 1.55, 1.57, 1.59, 1.56, 1.49, 1.57, 1.53]. Furthermore, Emery et al. weighted their modelled thermal flux density calculations with the corresponding filter function of the SST's IRS instrument. To match them as accurately as possible in this case, the ATRM also took into account the instrument + filter responses, where the IRS PUI red channel filter response curve can be found in Appendix B. The mathematical approach of having the modelled flux densities weighted by the filter response is given in the following equation [38]:

$$B_\lambda(T, \lambda) = \frac{\int B_\lambda(T, \lambda)\, \phi_\lambda(\lambda)\, d\lambda}{\int \phi_\lambda(\lambda)\, d\lambda} \tag{4.5.2}$$

Where $B_\lambda(T, \lambda)$ is the Planck function and $\phi_\lambda(\lambda)$ is the filter+instrument response. The denominator in Equation (4.5.2) represents a normalisation of the filter function over the bandwidth. It should be noted that since the emissivity is assumed fixed and not to vary across wavelengths, as Emery et al. do, it was not represented

in this equation. The filter response has to be taken into account since when comparing theoretical to observation data, observation instruments use specific filters to collect light within certain wavelength regions. However, those filters have a certain transmission of light at different wavelengths. Thus, this spectral transmission has to be accounted for, which usually decreases the overall measured flux of an object.

Numerically, the filter response was taken into account by integrating the Planck function over the bandwidth limits of the filter. The Planck function was first integrated using a custom made mid-point Riemann sum function, which would compute the thermal flux density of each facet at specific wavelength intervals over the filter bandwidth. It was found that 1000 intervals was sufficient to achieve convergence of the values. Furthermore, at each specific wavelength intervals, the facet thermal flux densities were already converted to the final unit of concern, that is mJy in this case, for accuracy purposes. Moreover, the filter spectral response values were normalised as to produce an area under the curve of one, and thus produce a relative spectral response. Then, at each wavelength interval of the previously calculated Planck function, the corresponding relative filter response was multiplied to it. It should be noted that, since the thermal flux densities have been modelled at different wavelength intervals as the ones available from the filter response, a linear 1D interpolation was applied to 'fill-in' the gaps. Finally, the resulting 'filtered Planck function' was divided by the bandwidth of the filter. The thermal lightcurves of Emery et al.'s are given in Figure 4.5.10, and that of the ATRM's are given side-by-side in Figure 4.5.11.
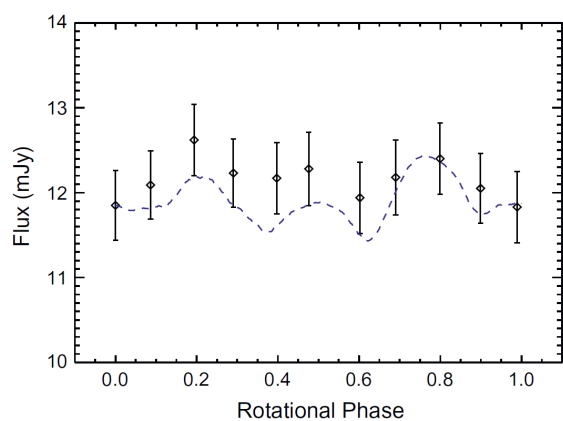
Figure 4.5.10: Emery et al.'s modelled thermal light curve [dotted] of Bennu with IRS PUI red filter superimposed over SST observations [diamonds] [21].
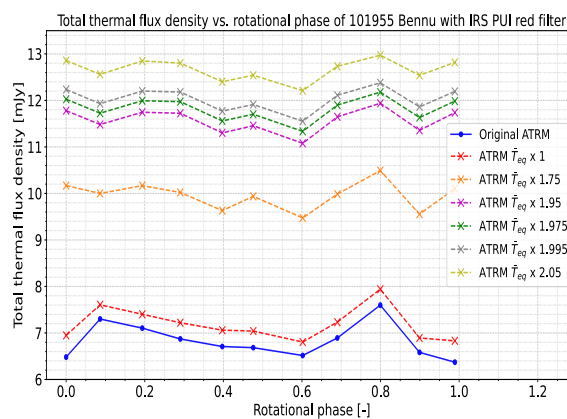
Figure 4.5.11: ATRM's thermal light curves of Bennu modelled with IRS PUI red filter wavelength band. Dotted curves represent thermal flux density calculated using mean equilibrium facet temperatures multiplied by a specified factor.

Comparing both graphs, it can be seen that the ATRM's modelled thermal light curve obtained by assuming no thermal emission on the night-side as seen in Figure 4.5.11 [blue curve], is substantially lower than the one obtained by Emery et al.'s model. When the ATRM's thermal flux density is computed using the condition explained in Equation (4.5.1), there is a small increase in thermal emission when non-zero facet temperature are obtained [red curve] but still not enough to match the result of Emery et al.'s. Interestingly, the peak found in the ATRM's blue and red curves at a rotational phase (henceforth referred to as RP) of 0.1 does not have a corresponding peak in that of Emery et al's at the same RP. Only the peak found at RP 0.8 match in both cases. To try to better match the thermal light curves, different factors were multiplied to the mean equilibrium facet temperature found initially, which would effectively raise the threshold of replacing the older facet temperatures and make the new facet temperatures higher and thus the thermal flux densities also higher.

Now looking back at Figure 4.5.11, it can be seen that using an arbitrary factor of $1.75 \times \bar{T}_{eq}$ causes the thermal light curve [orange] to shift upwards where the mean thermal flux density is now around 10 mJy. Furthermore, at RPs 0-0.4 and 1.0, it is interesting to note that there is also a slight upward shift in the thermal light curve itself when compared to the red and blue curves. This is potentially because at those orientations the facet temperature replacement condition is being applied to more facets, perhaps due to the inclinations of the facets, and thus raising its overall thermal flux density more. Subsequently, by trial and error, the following multiplicative factors of 1.95 [magenta], 1.975 [green], 1.995 [grey], and 2.05 [olive] were used to aim for

a better match against Emery et al.'s. It can be seen that now with the aforementioned four factors, it seems that the peaks found in Emery et al.'s at RPs 0.2, 0.5, and 0.8 have roughly corresponding peaks in the ATRM's modelled thermal light curves. This suggests that the new factors produces a surface temperature distribution representative enough to produce the same thermal flux density distribution as the ones modelled by Emery et al.'s using heat conduction. However, it is not perfect since as can be seen at RP 0.0 and 1.0, there is peak in the higher thermal light curves of the ATRM's whereas for Emery et al.'s it is flat.

Furthermore in Figure 4.5.11, with increasing multiplicative factor, there seems to be a flattening of the curves. This can be explained since the higher the multiplicative factor, the less extreme the variation in facet temperatures since the range between the minimum and maximum facet temperatures decreases, and thus the more flat the overall thermal flux density will be. When comparing Figure 4.5.11 to Figure 4.5.10, a factor of 1.975 [green curve] seems to produce the most similar results to Emery et al.'s modelled thermal light curve. If a slightly higher factor of 1.995 or lower factor of 1.95 were used, the match would not have been as ideal. However, even with those corresponding multiplicative factors, the pattern in thermal light curves between Emery et al.'s and those of the ATRM are not perfectly the same since the method used here is only a simple correction and does not account for thermal conduction. This is why a perfect match would be impossible.

Even though a direct comparison between the information obtained from the thermal light curves to the ones of the visualised radar shape is not possible given that the latter does not take into account the filter+instrument functions and the longitude shift in the radar shape, the derived factor of $1.975 \times \bar{T}_{eq}$ is selected to see its influence on the radar shape models since it produces the best match in thermal light curves. The new distribution of facet temperatures and thermal flux densities using that factor are illustrated in Figure 4.5.8 and Figure 4.5.9. For the thermal flux density, it can be seen that the left side now contributes more towards the thermal emission, even though it does not quite have the same distribution pattern as the one of Emery et al. seen in Figure 4.5.3. This is because at the equatorial region, given that the facet temperatures are warmer there (less facet inclination) and no lag in thermal inertia is being modelled, the thermal flux densities are expected to be higher.

Looking at the facet temperatures in Figure 4.5.8, the new adjusted minimum facet temperature is 173 K, and the overall average facet temperature is 298 K. It can be observed that indeed the new minimum facet temperature is a factor of 1.975 higher than the previous one at 88 K. Furthermore, this new facet minimum temperature is not far from the one obtained by Emery et al. at 180 K, as can be seen in Figure 4.5.1. A multiplicative factor of 2.05 would be required to match the minimum facet temperature of 180 K, but as can be seen in Figure 4.5.11, the thermal light curve with that factor [olive curve] is higher than the one modelled by Emery et al. [ignoring the differences due to filter functions and longitude shift]. Nonetheless, if a multiplicative factor of 2.05 was applied, the resulting thermal flux densities would have been even higher and the left side distribution of Bennu would no longer start to resemble its previous temperature and thermal density distributions found using a factor of 1.975. Hence, for the purposes of this attempted correction of the assumption of no thermal emission on the night-side of the ATRM, a factor of 1.975 seems to be the most ideal.

The method explored here to try to compensate for the lack of thermal conduction modelling, that is the assumption of no thermal emission in the night-side, will not be replicated further into the ATRM's results since the factor of correction found is only applicable to the parameters of this validation. Since this factor depends on the orbital properties, wavelength region, shape properties, and much more, they cannot be generally applied elsewhere. Hence, the assumption of instantaneous thermal equilibrium is maintained, but the limitation of assuming no thermal emission on the night-side can be mitigated by modelling fluxes at small to zero phase angles. Ultimately, given that the difference in the maximum facet thermal flux density between that of ATRM's and that of Emery et al.'s is less than 8%, the ATRM is considered validated for its calculation of thermal flux density.

4.6. Reflected flux density validation

The reflected flux density was validated against the light curves available in DAMIT [19]. It is important to note that most, if not all, of the available DAMIT light curves are relative (that is, not calibrated), meaning that the magnitude zero point is unknown [17]. DAMIT scales its light curves such that the mean brightness of an

object across a specific observation period equals to one. Hence, since the light curves are normalised on a per observation dataset, the amplitudes from different observation campaigns are not expected to match. The same normalisation procedure was applied to the ATRM's total reflected flux densities, where the necessary conversions for the reflected density flux are given in Appendix A. An initial attempt was made to compare the ATRM's reflected flux density in magnitude units to the observed data where an attempt to retrace the original measurements was carried out. However, given that most of the observation data collected was relatively old and not properly documented or archived, the magnitude zero point could not be found. Hence, that is why a normalised light curve was also preferred to remove this unknown dependency. Finally, no uncertainties in normalised reflected flux densities were provided in DAMIT.

However, it should be noted that this form of validation actually only validates the scattering law under use. The asteroid shape models derived through the light curve inversion technique, and catalogued in DAMIT used Equation (4.6.1) [19] [34] to obtain the brightness contribution dL of a surface patch dS. It can be seen that when a normalisation to mean is carried out, since the optical inversion technique assumes a single homogeneous surface albedo, the choice of that parameter does not matter given that it is constant. Only the geometrical dependent terms of μ, μ_0 and dS will contribute towards the normalised light curve. For the sake of simplicity, Equation (4.6.1) actually omits the contribution of the scaling factors of the square of orbital distances, that is r_{as} and r_{ao}, in that equation but does take it into account in its inversion since they do scale the brightness as the asteroid moves, albeit by a relatively small amount during its rotation period. The exact Cartesian ecliptic positions of the Sun and the observer with respect to the asteroid were given in DAMIT's light curve parameter files. Hence, no fetching of orbital positions in the JPL horizons database and necessary transformation of reference frames were needed.

$$dL = S\left(\mu, \mu_0\right) \bar{\omega} dS \tag{4.6.1}$$

In Equation (4.6.1), $S\left(\mu, \mu_0\right)$ is the surface reflectance of the patch under a specific scattering law, and $\bar{\omega}$ is the patch albedo. The resulting 3D shapes of the asteroids in DAMIT were obtained using a combination of a weighted Lambertian (L) scattering law and a Lommel-Seeliger (LS) scattering law. The surface reflectance of two laws are given in Equation (4.6.2) and Equation (4.6.3) respectively, where $\mu_0 = \cos\theta_i$ and $\mu = \cos\theta_o$. The combined Lommel-Seeliger-Lambertian (LSL) scattering law is given in Equation (4.6.4), where c is the weight factor assigned to the Lambertian part, where DAMIT derived a value of 0.1 to be suitable in most cases.

$$S_L\left(\mu, \mu_0\right) = \mu\mu_0 \tag{4.6.2} \qquad\qquad S_{LS}\left(\mu, \mu_0\right) = \frac{\mu\mu_0}{\mu + \mu_0} \tag{4.6.3}$$

$$S_{LSL}\left(\mu, \mu_0\right) = \left[S_{LS}\left(\mu, \mu_0\right) + cS_L\left(\mu, \mu_0\right)\right] \tag{4.6.4}$$

As explained earlier, even though the choice of the facet albedo will not have any effect on the relative light curves given the normalisation, the visual Bond albedo was still selected given that those light curves were produced with observations carried out in the visible spectrum using a Johnson V-filter ($\lambda_{\text{eff}} = 0.551\mu m$) [33] [37]. Thus, also given that this will not have any effect on the relative light curve, the Planck function found in the reflected flux density equation was still weighted by the corresponding filter function. The Johnson V-filter function can be found in Appendix B, where basically the same methodology described in Section 4.5 was used. However, it is interesting to note that the weighted Planck functions were numerically faster to compute since now the temperature component of the Planck function is the effective blackbody solar temperature.

The choice of asteroid from DAMIT was initially motivated by looking for convex-shaped asteroids with resulting light curves covering full rotations, and with the minimum amount of noise. However, it was found that there were very few purely convex-shaped asteroids which met those criteria. Especially in the case of near-spherical asteroids, too much noise was present in the light curves, coupled with the low amplitudes of such shaped asteroids, no substantial validation could be carried out with them. Finally, two asteroids were selected from DAMIT, namely 15 Eunomia and 216 Kleopatra. 15 Eunomia is a near-convex MBA, and has a diameter of 232 km [63]. It has an S-type classification in both the Tholen and SMASS II, and a K-type (end-member) classification in the Bus-DeMeo system. Its DAMIT 3D shape is composed of 402 vertices and 800 facets. From Figure 4.6.1, it can be seen that it has an oblong like shape. 216 Kleopatra is an MBA, with an approximate diameter of 122 km, and thought to be a rubble pile mostly metallic in composition. It is an M-type in the Tholen system, and an Xe-type in both the SMASS II and Bus-DeMeo classification, which

are both subgroups of X-type group [63]. Its DAMIT 3D shape is composed of 578 vertices and 1152 facets. From Figure 4.6.2, it can be seen that it has a ham-bone shape and has quite a few protrusions. However, in a study that actually used this modelled DAMIT shape using a ray-tracing algorithm to account for projected shadows, it found that only about 0-5% of remaining facets after the local horizon mapping would be affected by the ray-tracing algorithm depending on the orientation of the asteroid [82]. Given those findings, the use of 216 Kleopatra is justified in this case, even with a simple local horizon mapping being used to account for shadowing.

15Eunomia - front

216Kleopatra - front

15Eunomia - side1

216Kleopatra - side1
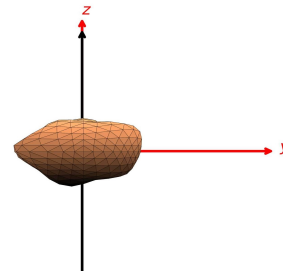
15Eunomia - top

216Kleopatra - top
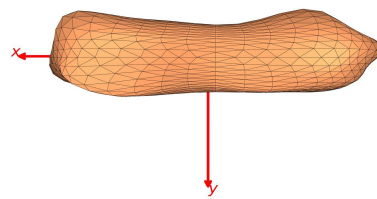
Figure 4.6.1: DAMIT shape model of 15 Eunomia 3D plotted in asteroid shape body reference frame. Spin axis aligned with the z-axis. Shadowing in the colour map is included to help orient between the three figures.

Figure 4.6.2: DAMIT shape model of 216 Kleopatra 3D plotted in asteroid shape body reference frame. Shading and spin axis orientation same as described in Figure 4.6.1. Not to scale with each other.

4.6.1. Reflected flux validation w.r.t. 15 Eunomia

The validation of the reflected flux density of 15 Eunomia was done against data gathered by Groeneveld & Kuiper (1954), Chang et al. (1959), Lagerkvist & Williams (1997), and Melillo (1986), but all reproduced in DAMIT [19]. The four light curves are illustrated in Figure 4.6.3 to Figure 4.6.6. The purely Lambertian reflected flux density, which is the default reflected flux density computation of the ATRM carried out using Equation (3.9.7), is illustrated as a green curve in all the graphs. The purely Lommel-Seeliger is represented

by the blue curve and is computed using Equation (4.6.3), and the combined Lommel-Seeliger-Lambertian is computed using Equation (4.6.4) and represented as a red curve. The weight factor listed in DAMIT for this asteroid is 0.1. All four figures cover, or nearly cover, the full sidereal rotational period of 15 Eunomia (6.083 hrs). Given the shape of 15 Eunomia, a complex sinusoidal behaviour is expected in its light curve. If the asteroid was a perfect sphere of homogeneous surface albedo, the light curve would have been flat. If the asteroid was a perfect ellipsoid with a homogeneous surface albedo, it would have matching sets of maximas and minimas.
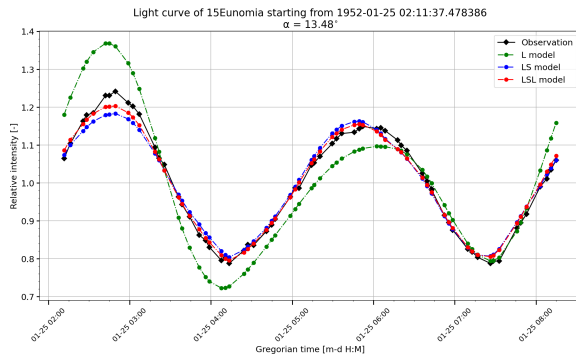
Figure 4.6.3: ATRM's light curves of 15 Eunomia against observation taken from Groeneveld & Kuiper (1954) - DAMIT light curve ID #3.
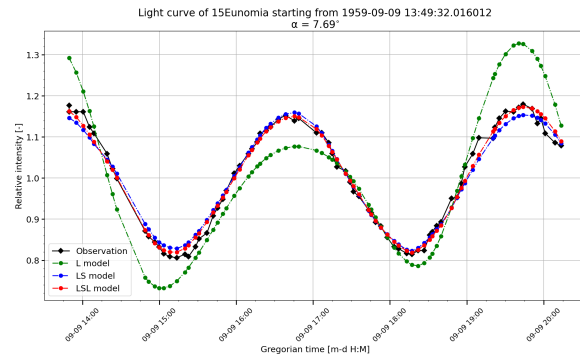
Figure 4.6.4: ATRM's light curves of 15 Eunomia against observation taken from Chang et al. (1959) - DAMIT light curve ID #8.
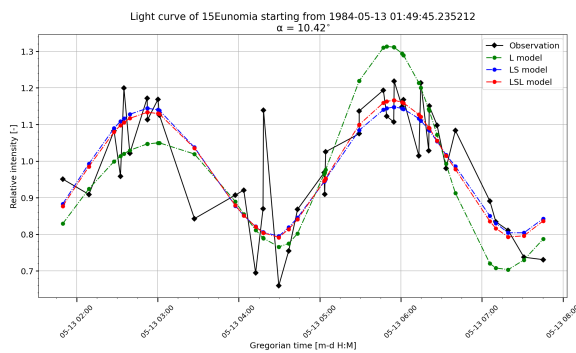
Figure 4.6.5: ATRM's light curves of 15 Eunomia against observation taken from Lagerkvist & Williams (1997) - DAMIT light curve ID #39.
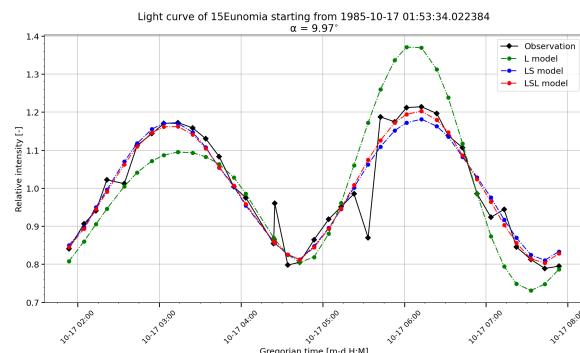
Figure 4.6.6: ATRM's light curves of 15 Eunomia against observation taken from Melillo (1986) - DAMIT light curve ID #43.

As can be seen in the above four graphed light curves, 15 Eunomia is displaying a near-bimodal characteristic in its observed data [black diamond curve] given its shape property. That is, it has two maximas and two minimas of slightly different amplitude. This is most apparent in Figure 4.6.3, albeit that the minimas are relatively in the same amplitude range, and the slight variation could also be attributed to potential noise/uncertainty in the data. However, this bimodal behaviour depends also on the illumination and viewing geometry with respect to the spin axis of the asteroid. For instance, in Figure 4.6.4, the maximas appear to be of the same amplitude.

Since a homogeneous surface albedo is being assumed, the light curve's behaviour is solely being influenced by the shape of the asteroid. The maximas represent the orientation where the maximum illuminated and visible area of the asteroid is being observed, and the contrary applies to the minima. Looking at the LSL [red] curves in all four graphs with respect to the observation, they appear to have a near-perfect match, when ignoring variations due to potential noise/uncertainty. In Figure 4.6.5 and Figure 4.6.6, the observed dataset seems to be subject to noise, especially in the former. For instance, in Figure 4.6.5, it is impossible for two consecutive observed data points to vary from a relative intensity of 0.7 and jump to 1.15 to then drop back down to about 0.65. However, even within the noise of that dataset, the LSL curve follows the overall pattern of the observed dataset.

Looking at the ATRM's Lambertian light curve [green] in all four graphs, the same apparent pattern is present. There is a consistent over-estimation in one of the maximas, and in one of the minimas, when compared to the LS, LSL curves and observed data. There is a slight over-estimation in the other minima, and an under-estimation in the other maxima. The Lambertian curve is implicitly validated since it can be observed that the LSL curves lie in between the L and LS curves at all times. Given that the L part of the LSL curves is only weighted by a factor of 0.1, it is naturally expected to be closer to the LS curve than the L curve. Furthermore, every time the L curve crosses the LS curve, the LSL curve also crosses the LS curve, showing that the L curve has been properly plotted.

4.6.2. Reflected flux validation w.r.t. 216 Kleopatra

The validation of the reflected flux density of 216 Kleopatra was done against data gathered by Scaltriti & Zappala (1978), Kennedy & Tholen (1982), and Weidenschilling et al. (1987), but all reproduced in DAMIT [19]. The four light curves are illustrated in Figure 4.6.7 to Figure 4.6.10. It should be noted that the sidereal rotation period of 216 Kleopatra is 5.385 hrs. Hence, apart for Figure 4.6.9, which covers about half a rotation period of 216 Kleopatra, the other three figures cover at least a full rotational period. Figure 4.6.7 actually covers a rotation of about one and a half of 216 Kleopatra. The colour coding of the curves follows the same logic as the graphs from previous Section 4.6.1. As specified in DAMIT for this asteroid, the LSL curves were plotted with a weight factor of 0.1. Moreover, it can be seen that the three modelled L, LS, and LSL light curves match rather well the observed data in the overall temporal pattern, as was also the case in Section 4.6.1, strongly suggesting that the shape plotting done by the ATRM is accurate, and the frame of reference were correctly taken into account. Furthermore, having a matching temporal pattern suggests that the spin axis orientation and the sidereal period used are also valid.
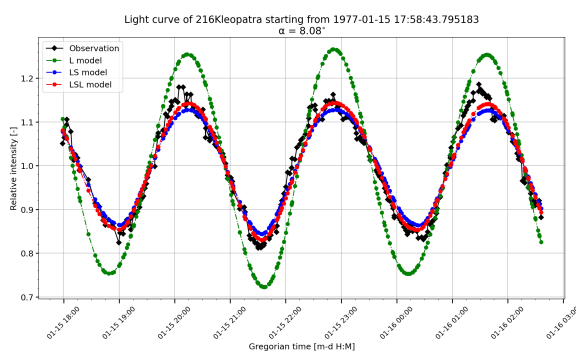
Figure 4.6.7: ATRM's light curves of 216 Kleopatra against observation taken from Scaltriti & Zappala (1978) - DAMIT light curve ID #1.
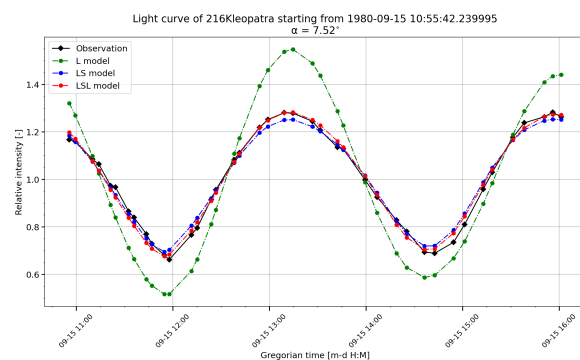
Figure 4.6.8: ATRM's light curves of 216 Kleopatra against observation taken from Kennedy & Tholen (1982) - DAMIT light curve ID #8.
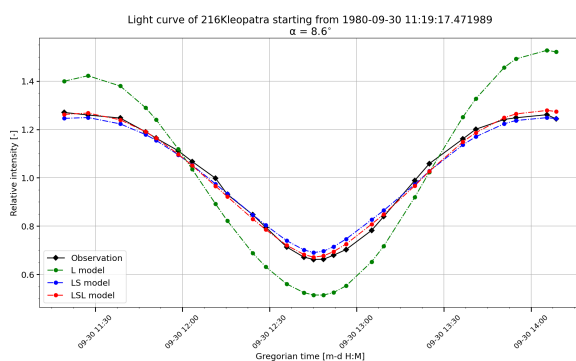
Figure 4.6.9: ATRM's light curves of 216 Kleopatra against observation taken from Kennedy & Tholen (1982) - DAMIT light curve ID #15.
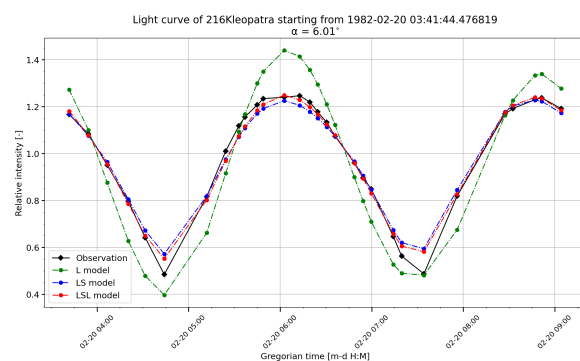
Figure 4.6.10: ATRM's light curves of 216 Kleopatra against observation taken from Weidenschilling et al. (1987) - DAMIT light curve ID #29.

Looking at all four graphs, even though 216 Kleopatra has an elongated non-symmetrical ham-bone shape, a bimodal light curve is not as apparent in the observed data, also when looking at the LS and LSL curves. This leads to suggest that the complex shape of 216 Kleopatra under those illumination and viewing parameters portrays a unimodal behaviour, given that the minimas and maximas have about the same amplitude. This shows that it is some times difficult to differentiate between a unimodal behaviour or bimodal behaviour (where it can happen for an ellipsoid with a homogeneous surface albedo, or a sphere with a surface patch of dissimilar albedo along its longitude). Looking at the consecutive observed data points present in Figure 4.6.7, the noise does not make it clear if the maximas and minimas are of different amplitude. If the exact shape file was not available in this case, an extremely oblate spheroid could have been used as an approximation of this asteroid. A bimodal behaviour is best seen in the Lambertian light curve, as was the case of 15 Eunomia too. Perhaps for a given asteroid shape, this suggests that a Lambertian scattering law is more appropriate over the Lommel-Seeliger law to recognise the actual rotation period of an asteroid? From this small sample size, it seems so.

Nonetheless, in most cases, the LSL curve [red] is the closest matching to the observed data, as expected. However, when looking at the minimas of Figure 4.6.10, and one of the maximas of Figure 4.6.7, it can be seen that the LSL curve and the observed data do not match as well. In Figure 4.6.10, the L curve is even closer to the observed data than the LSL curve. However, when looking at the other graphs, the LSL curve is actually matching well across both minimas and maximas. Hence, the deviations in those two figures is most probably due to noise or uncertainty in the data. Furthermore, the L curve is again seen over-estimating the maximas and minimas when compared the LS and LSL curves, as expected. Since the LSL curves lie between the LS and L curves, this again implicitly validates the reflected flux density plotted using the Lambertian scattering law.

Ultimately, given that the LSL curves match the observed data rather well in most cases, this confirms that under those conditions the LSL scattering law, assuming a homogeneous surface albedo, was appropriate to derive the shapes of those asteroids. Furthermore, both those asteroid shape models actually have a quality flag of 4 (range 0-5) [18], meaning that they have been derived from a wide photometric dataset and/or stellar occultations, and no ambiguity is present in the axis of the rotation. Hence, those shape models are considered representative of the real asteroid shape. This thus suggests that indeed under the LSL law, those asteroids have a homogeneous surface albedo. On the other hand, this creates the opportunity of seeing if the same asteroid shape models are used and their reflected light are calculated using the Lambertian scattering law but with varying surface albedo distributions, can a match be obtained with the observed dataset? This will be further explored in Section 5.3, where the influence of a heterogeneous surface albedo will be explored and how it affects the amount of reflected light in the total observable flux density.

Results & Discussion

In this chapter, all the results of interest produced by the ATRM will be shown and discussed. Firstly, in Section 5.1, the modelling of the flux densities at the four different WISE bands is explained, where a simpler method of taking into account the filter+instrument response functions is given. Then, in Section 5.2, following from the parameters affecting the reflected light identified in Section 2.5, a high-level investigation of the effect of different homogeneous surface albedos across different heliocentric distances on the fraction of reflected light in the total flux density is explored. The effect of different emissivity values is also investigated. Furthermore, as initially presented in Section 4.6, potential heterogeneous albedo distribution maps of 15 Eunomia and 216 Kleopatra, under Lambertian scattering law, are investigated by first going through a homogeneous albedo refinement then a distributed one, which is explained in Section 5.3. Then, in Section 5.4, the resulting albedo maps of interest is investigated across the four different WISE bands to see the effect of heterogeneous surface albedos on the fraction of the reflected light in the total flux density. Finally, in Section 5.5, the effect of different ellipsoidal shapes on the amount of reflected light is also investigated.

5.1. Flux density corrections for WISE bandpass filters

The earlier method used for taking into account the filter+instrument response functions in the calculation of the integrated flux densities, as was initially seen in Section 4.5 and Section 4.6, is simplified in the case of the WISE bandpasses by a set of quadrature formulas derived by Wright (2013) [94]. The quadrature formulas estimate the effect of the filter+instrument functions by attributing a best fit weight factor at a given wavelength within the filter bandpass. The four quadrature equations corresponding to their respective four WISE filter bandpasses are as follows:

$$
\begin{aligned}
F_{\lambda,\,W1} &= 0.5117 \times F_\lambda(3.0974\mu\text{m}) + 0.4795 \times F_\lambda(3.6298\mu\text{m}) \\
F_{\lambda,\,W2} &= 0.5811 \times F_\lambda(4.3371\mu\text{m}) + 0.4104 \times F_\lambda(4.9871\mu\text{m}) \\
F_{\lambda,\,W3} &= 0.1785 \times F_\lambda(8.0145\mu\text{m}) + 0.4920 \times F_\lambda(11.495\mu\text{m}) \\
&\quad + 0.2455 \times F_\lambda(15.256\mu\text{m}) \\
F_{\lambda,\,W4} &= 0.7156 \times F_\lambda(21.15\mu\text{m}) + 0.2753 \times F_\lambda(24.69\mu\text{m})
\end{aligned}
\tag{5.1.1}
$$

Where F_λ is the spectral flux density function in the wavelength domain. The location of the weight factors across the four spectral response filters are illustrated in Figure 5.1.1.
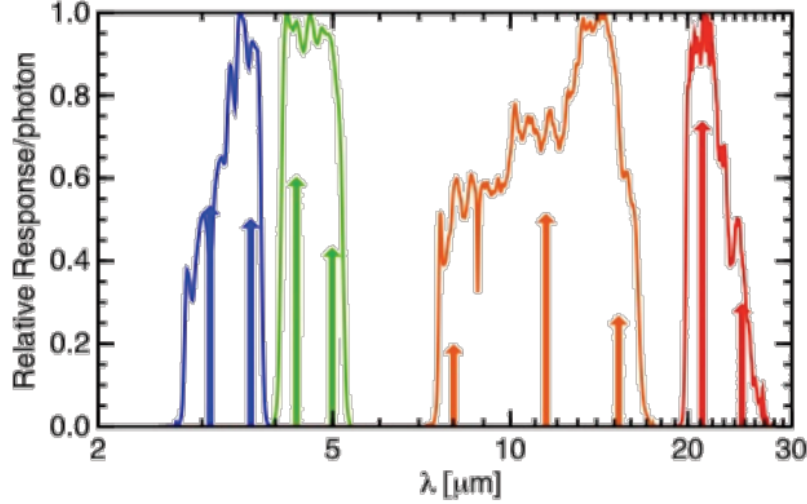
Figure 5.1.1: WISE filter spectral response functions with best-fit weights shown at corresponding wavelengths by vertical arrows. Blue: W1, Green: W2, Orange: W3, and Red: W4 [94].

It can be observed that for bandpasses W1, W2, and W4, only two best fit weight factors at two wavelengths are needed, whereas W3 has three. This is because to achieve a percentage deviation of less than 0.5% between the method of derived quadrature formulas against the conventional method, three best fit weights were required for bandpass W3 [94], since it covers a relatively broader wavelength region as can be seen in Figure 5.1.1. Only two weight factors were necessary for the other three filter bands to achieve the same accuracy. Through the literature review, even though the conventional approach of taking the filter+instrument response function is also possible, it was found that most studies, including the one of Myhrvold, use the simpler quadrature method to model fluxes in the different WISE bands. Hence, this method is also preferred here.

5.2. Influence of homogeneous surface albedo, heliocentric distance, and emissivity on percentage of reflected light in total observable flux density.

As was previously seen in Section 2.5, the amount of reflected light will depend on the surface albedo, the heliocentric distance, and the thermal properties of the asteroid. Thus, in this section, a high-level investigation of those different parameters will be explored with respect to the four different WISE bands. Given the complexity of many different shapes of asteroids, a sphere is used for convenience. The total reflected flux density of the sphere is computed using Equation (3.9.8), and that of the thermal flux density is computed using Equation (3.9.6), where the facet temperatures are calculated using Equation (3.9.4). Since the size of the asteroid is taken into account in both the reflected and thermal flux density calculations, the choice of asteroid's size actually does not matter when estimating the fraction of reflected in the total flux density.

The distance to the observer also does not matter since those terms are both present in the thermal and reflected flux density calculations. However, for transparency, the asteroidal radius is taken as 1km, and $r_{ao} = 1$ AU. Unless stated otherwise, the bolometric emissivity was set to the default 0.9 value for the surface temperature calculations. The conversion from visible geometric to bolometric Bond albedo was done using the conventional value $G = 0.15$. No beaming parameter was taken into account in the surface temperature computations, that is η was set to one, which is justified since the phase angle is set to zero to minimise the effect of the assumption of no thermal emission on the night-side of the asteroid. Kirchhoff's law of thermal radiation was respected by relating the albedo from the reflected flux density to the emissivity in the thermal flux density as $\varepsilon(\lambda) = (1 - \rho(\lambda))$ as was explained in Section 2.5.

Three taxonomic types were selected for further investigation, namely the three broad and most commonly

49

occurring ones, that is the C-, S-, and X-types, where more than 95% of asteroids fall within those three taxonomic categories or their sub-categories as was presented in Section 2.1. An estimation of their IR geometric albedo $p_{IR}(\lambda)$ by the conventional application of a linear extrapolation of their relative reflectance curves in the VNIR has to be carried out to obtain the IR to visible ratio R_{IR-Vis}. This process is illustrated in Figure 5.2.1 to Figure 5.2.3, where the extrapolated values were taken at the effective wavelengths of each WISE bands, namely being 3.368, 4.618, 12.082, and 22.194 microns. Those values are then multiplied to the p_v values of each taxonomic types to obtain their corresponding $p_{IR}(\lambda)$ at the four different WISE bands. This can be done as such since p_v in those relative reflectance graphs have been normalised to one.
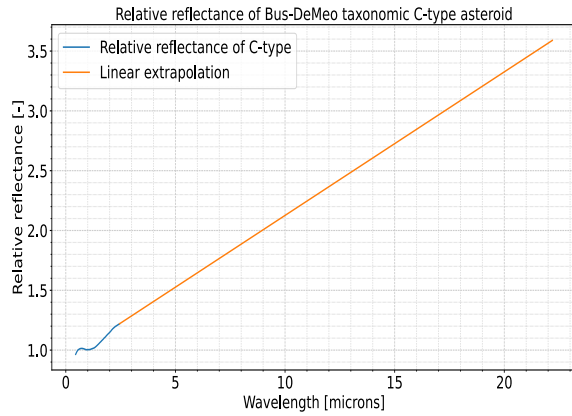
Figure 5.2.1: Extrapolation into the WISE wavelengths of the relative reflectance of Bus-DeMeo taxonomic C-type.
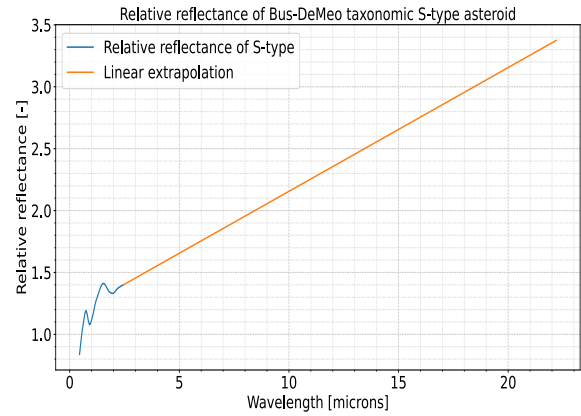
Figure 5.2.2: Extrapolation into the WISE wavelengths of the relative reflectance of Bus-DeMeo taxonomic S-type.
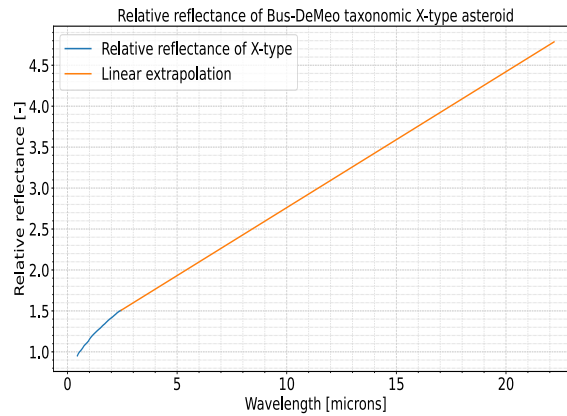
Figure 5.2.3: Extrapolation into the WISE wavelengths of the relative reflectance of Bus-DeMeo taxonomic X-type.

The IR-Vis ratio R_{IR-Vis} extrapolated from the relative reflectance graphs at the corresponding four WISE bands are summarised as follows, in order from W1 to W4:

- R_{IR-Vis} of C-types: 1.33, 1.48, 2.38, 3.59

- R_{IR-Vis} of S-types: 1.49, 1.62, 2.36, 3.37

- R_{IR-Vis} of X-types: 1.66, 1.86, 3.11, 4.79

With the previous definition of parameters, the results for the percentage of reflected light in the total flux density in W1 to W4 are illustrated in Figure 5.2.5 to Figure 5.2.8. Furthermore, the contribution of reflected light to the observable flux density at the four WISE bands classified by asteroid type, heliocentric distance, and Bus-DeMeo taxonomic type is summarised in Table 5.2.1. To better understand the locations and distributions of various asteroids with respect to heliocentric distance, Figure 5.2.4 was included. The heliocentric distances

50

have been associated to where some asteroids are usually found, that is with increasing heliocentric distance: NEAs, MBAs, and Trojans. Some smaller asteroid families such as Hungarias, Cybeles, and Hildas have also been considered. In addition, to investigate the influence of assuming a constant R_{IR-Vis} across all four bands, C-type being the most commonly occurring asteroid type, its geometric albedo range was selected. A constant value of $R_{IR-Vis} = 1.22$ was applied to its lower and upper range of geometric albedos (0.03-0.09) across the four WISE bands. $R_{IR-Vis} = 1.22$ was selected since it corresponds to the known relative reflectance of C-types at the NIR wavelength of 2.45 microns [15], as can be seen in Figure 5.2.1.
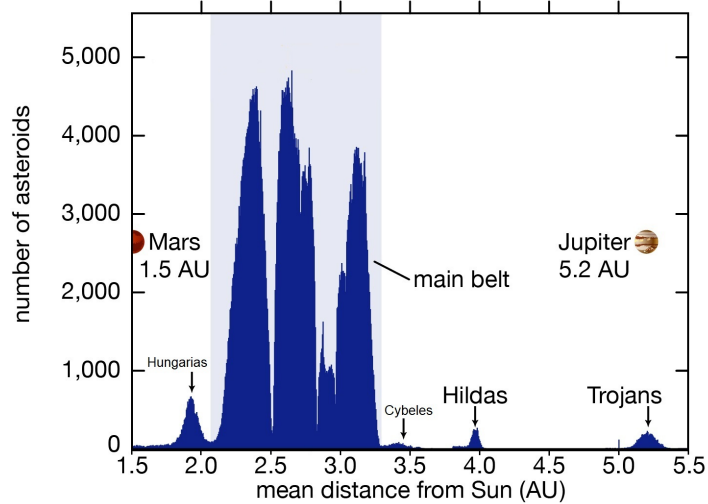
Figure 5.2.4: Distribution of asteroids according to their numbers across mean heliocentric distance, between the orbits of Mars and Jupiter. [84].
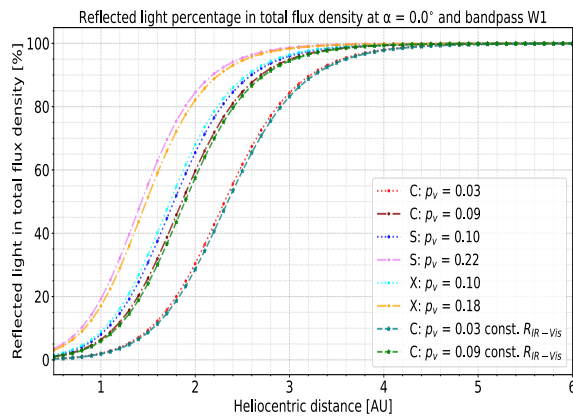
Figure 5.2.5: Percentage of reflected light in total flux density for various ranges of albedos per taxonomic type, across heliocentric distance, at bandpass W1. Note: $\alpha = 0°$, $\varepsilon = 0.9$, and $G = 0.15$.
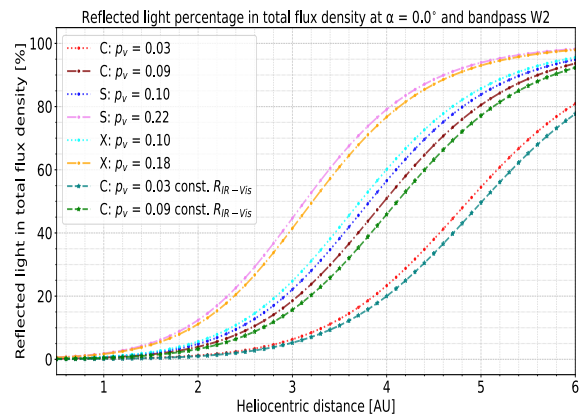
Figure 5.2.6: Idem as Figure 5.2.5 but at W2.
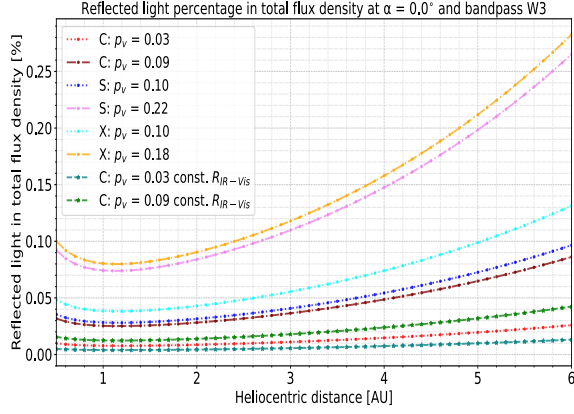
Figure 5.2.7: Idem as Figure 5.2.5 but at W3.
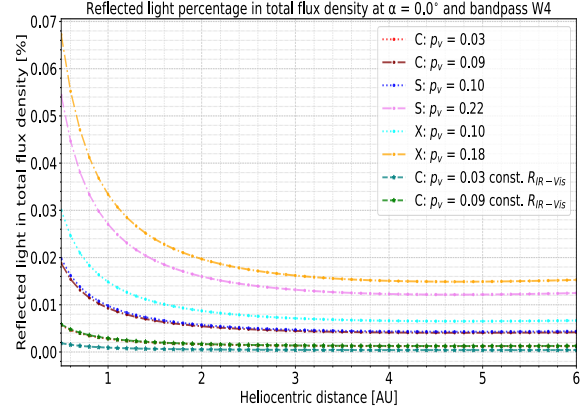
Figure 5.2.8: Idem as Figure 5.2.5 but at W4.

Table 5.2.1: Summary of minimum and maximum percentages of reflected light in total flux density of various asteroids across heliocentric distance and Bus-DeMeo taxonomic type. NEAs: near-Earth asteroids, IMB-i: inner heliocentric distance of inner main-belt asteroids, MMB-i/MMB-o: inner and outer heliocentric distance of middle main-belt asteroid, OMB-o: outer heliocentric distance of outer main-belt asteroids. Note that MMB-i intersects with IMB-o, and MMB-o intersects with OMB-i, and hence have not been reproduced in the table. Note for legibility, only the maximum reflected light percentages are given for bandpasses W3 and W4. The complete reflected percentages including the lower bound at W3 and W4 can be found in Table C.0.1.

Asteroid type	r_{as} [AU]	Minimum and maximum percentages of reflected light in total flux density [%]											
		W1			W2			W3			W4		
		C	S	X	C	S	X	C	S	X	C	S	X
NEAs	~1	2.0-6.4	8.0-19.2	8.9-17.0	0.2-0.6	0.7-1.9	0.8-1.7	0.025	0.074	0.080	0.009	0.027	0.033
Hungarias	2	30.4-59.7	65.5-84.5	68.0-82.1	1.2-4.0	4.9-12.4	5.6-11.1	0.028	0.084	0.090	0.005	0.016	0.020
IMB-i	2.2	42.8-71.8	76.5-90.4	78.5-88.8	1.7-5.6	6.8-17.0	7.9-15.3	0.030	0.088	0.095	0.005	0.016	0.019
MMB-i	2.5	61.8-84.7	87.6-95.4	88.8-94.6	2.9-9.0	11.0-25.8	12.6-23.5	0.032	0.095	0.103	0.005	0.014	0.017
MMB-o	2.8	77.1-92.1	93.7-97.8	94.4-97.4	4.7-14.1	17.0-36.7	19.2-33.8	0.035	0.104	0.111	0.005	0.014	0.017
OMB-o	3.3	91.5-97.4	98.0-99.3	98.2-99.2	9.7-26.7	31.3-56.7	34.6-53.4	0.040	0.120	0.129	0.004	0.013	0.016
Cybeles	~3.5	94.4-98.3	98.7-99.6	98.8-99.5	12.7-33.2	38.3-64.1	41.8-60.9	0.042	0.127	0.136	0.004	0.013	0.015
Hildas	4	98.0-99.4	99.5-99.9	99.6-99.8	23.3-51.0	56.5-79.1	60.1-76.7	0.049	0.147	0.158	0.004	0.012	0.015
Trojans	5.2	99.8-99.9	100	100	60.9-84.3	87.1-95.3	88.6-94.6	0.069	0.210	0.225	0.004	0.012	0.015

Figure 5.2.5 corresponds to reflected light at bandpass W1 which is centered around 3.4 microns, where it can be observed that there are significant amounts of reflected light in the observable total flux density. Naturally, having a higher albedo will result in having more reflected light present, since the latter scales proportionally with it as was seen in Equation (3.9.7). Thermal flux density scales twice decreasingly with increasing albedo, once in the temperature calculation as $(1 - A)$ as seen in Equation (3.9.4), and the other in the thermal emission calculation itself when taking into account Kirchhoff's law of radiation as seen in Equation (3.9.5). As can be seen in Figure 5.2.5, from around 5 AUs, the observable flux density can be considered to be purely reflected light for S- and X-types, and nearly purely reflected light for C-types. Hence, the modelling of Trojan asteroids usually found around 5.2 AUs do not have to account for thermal flux density. Hildas found at 4 AUs, have nearly purely reflected light where it can dip to 98% if the asteroid's surface is relatively dark with a visible geometric albedo of 0.03, that is, belonging to C-types.

Still in the W1 band, but now looking at MBAs which span from 2.2 to 3.3 AUs, they can be further divided into three zones. The IMB is found at $r_{as} < 2.5$ AUs, the MMB is between 2.5 AUs $< r_{as} < 2.8$ AUs, and the OMB is at $r_{as} > 2.8$ AUs [45]. To obtain the precise percentage contribution of reflected light per region of the main-belt, the reader is referred to the table, but at MBAs in general, C-type asteroids can have 43-97% of reflected light in their observable flux density, S-types can have 77-99%, and X-types can have 79-99%. However, it should be noted that since S- and X-types asteroids are more likely to be dominating the IMB and MMB regions respectively, IMB asteroids would be more likely to have a slightly lower range of 77-95%, and MMB asteroids would more realistically have a reflected percentage around 89-97%. On the other hand, C-type asteroids actually dominate more the OMB region, so their reflected percentage is more likely to be around 77-97%. Finally, NEAs have heliocentric distances close to 1 AU, so NEAs can have around 2-17% reflected light in their observ-

able flux density, depending on their reflectances/taxonomies. Hence, even the darkest NEAs have a non-zero contribution of reflected light at W1.

In Figure 5.2.6, that is concerning bandpass W2 which is centered around 4.6 microns, it can be seen that the curves have shifted towards increasing heliocentric distance. Thus, depending on the albedo properties of Hildas and Trojans, they can no longer be considered to have purely reflected light in their observable flux density. Hildas can have around 23-79% of reflected light, whereas Trojans have around 61-95% reflected light. MBAs have less reflected light now. Looking at the dominant taxonomies at the relevant main-belt regions, IMB asteroids have from 7-26% for S-types, and 13-34% reflected light from X-types in MMB, and OMB asteroids can have from 5-27%. Finally, NEAs can have around 0.2-2%. Hence, depending on the application and specific albedo, it can be said that the thermal modelling of NEAs can already ignore reflected light at this wavelength region.

Now looking at Figure 5.2.7, that is at bandpass W3, it can be observed the percentage of reflected light has considerably decreased, in the order of less than 0.25% from NEAs to MBAs to Trojans, as can be seen in Table 5.2.1. It is interesting to note that bandpass W3, which is centered at about 12 microns, is a wavelength region which is typically used in thermal modelling of asteroids, and reflected light is usually not taken into account at this wavelength region. The substantially low percentage of reflected light results obtained for this bandpass does support this assumption of not it into account.

Finally, looking at Figure 5.2.8, that is bandpass W4 which is centered around 22 microns, the reflected light percentage decrease is again significant where in general it is mostly below 0.04% for the C-, S-, and X-types. Furthermore, a bandpass of about 22 microns is also another IR spectrum where thermal modelling is commonly carried out, and not taking into account reflected light is again supported by the results obtained here. Moreover, as can be seen in Figure 5.2.8, the relationship of increasing reflected light contribution with increasing heliocentric distance is inverted now, where at shorter heliocentric distances, there is a increase in reflected light. This suggests that at this higher wavelength, heliocentric distance does not play as much of a role in determining the reflected light given that it plateaus. However, at heliocentric distances lower than 2 AU, there is a substantial increase in reflected light of about a factor of 2 compared to the longer distances. This suggests that even though the reflected percentage is very small, the contribution of reflected light is relatively higher at shorter distances to the Sun.

It can be observed in Table 5.2.1 that the percentage of reflected light of S- and X-type asteroids are mostly around the same range across distances and bandpasses. This is because they share about the same range of visible geometric albedo, where S-types have a range of 0.1-0.22, and X-types have a range of 0.1-0.18 as was previously presented in Section 2.1. Furthermore, they also have about the same R_{IR-Vis} at W1 and W2 bands. At W3 and W4, X-types have slightly higher reflected light contributions compared to S-types given that its R_{IR-Vis} are higher than those of S-types at the corresponding WISE bands.

Furthermore, as can be seen from Figure 5.2.5 to Figure 5.2.8, the relationship between the amount of reflected light in the total flux densities across various heliocentric distances and wavelength bands is not as straightforward, and affects various types of asteroids differently. It is indeed confirmed that W1 and W2 bands contain the most amount of reflected light, where in W1, it can even be considered purely reflected light for asteroids beyond 5 AUs, even for relatively dark surfaces with geometric albedo of 0.03 such as those of C-type asteroids. Furthermore, negligible amounts of reflected light, in the order of less than 0.25% and 0.04% are present in W3 and W4, respectively. This was expected, since W3 and W4 are found at the longer wavelength regions of MIR which are typically used by thermal models and do not account for reflected light. Hence, it can be said that in general, not taking into account the contribution of reflected light at W3 and W4 is acceptable.

What if a constant R_{IR-Vis} factor was applied independent of the WISE bands? Well this can be seen in Figure 5.2.5 to Figure 5.2.8, where the C-type albedo boundary values (0.03, 0.09) were plotted with constant $R_{IR-Vis} = 1.22$ in all four bandpasses. Across all bands, the curves corresponding to constant R_{IR-Vis} both follow the same pattern of increasing reflected percentage with increasing heliocentric distance, which is expected since R_{IR-Vis} is just a scaling factor. It can be observed that at W1, the difference with its other C-type counterpart having an $R_{IR-Vis} = 1.33$ is small at about 0-3%. At W2, the difference increases to about 0-5%. The increase in percentage difference is again correlated to the fact that now the other C-type counterpart has a

higher R_{IR-Vis} factor of 1.48. At W1, the highest percentage difference is achieved around the MBA region, and at W2, between the outer limits of the MBA region to the Trojans given that the curves shift rightwards. At W3 and W4, given that the reflected light contribution is already very small, even though the pairs have a bigger difference between their R_{IR-Vis} factors of 0.51 and 0.34 respectively, the difference in reflected percentage is negligible between the pairs.

In the calculation of those percentages of reflected light, the default or conventional values of some variables were used, such as $\varepsilon = 0.9$, and $G = 0.15$. What would be effect if those variables were different? In the calculation of the thermal flux density of asteroids by the ATRM, the thermal properties of the asteroid's surface are influenced by two parameters from Equation (3.9.4) and Equation (3.9.5). The two parameters are namely the facet albedo A_{facet} and the facet emissivity ε_{facet}. It was already seen that with increasing albedo, the surface temperature decreases since it is taken into account as $(1 - A)$, and thus the fraction of reflected light increases. Concerning the facet emissivity, looking at Equation (3.9.4), since the emissivity ε_{facet} is in the denominator and by definition varies between 0 and 1 (but has a range of 0.8-1.0), the higher the emissivity, the lower the facet temperature, and thus the lower the thermal flux density, and the higher the fraction of reflected light. This behaviour is confirmed by looking at Figure 5.2.9 to Figure 5.2.12, where the reflected light percentages across the four WISE bands were re-plotted for the three most common Bus-DeMeo taxonomic types but this time for the boundary emissivities values of 0.8 and 1.0 as was already presented in Section 2.3.
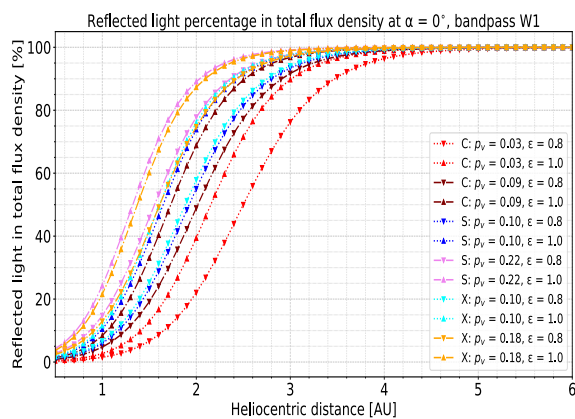
Figure 5.2.9: Percentage of reflected light in total flux density across heliocentric distance for various albedos within bandpass W1. Downward pointing markers used for $\varepsilon = 0.8$, and upward pointing markers for $\varepsilon = 1.0$. $\alpha = 0°$ and $G = 0.15$.
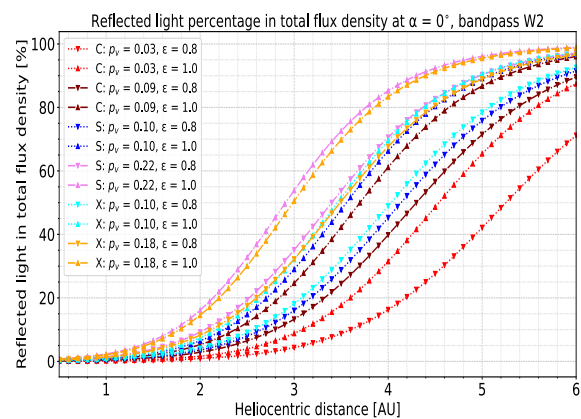
Figure 5.2.10: Idem as Figure 5.2.9 but at W2.
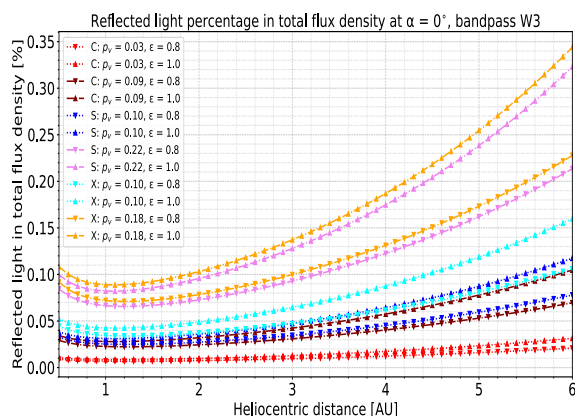
Figure 5.2.11: Idem as Figure 5.2.9 but at W3.
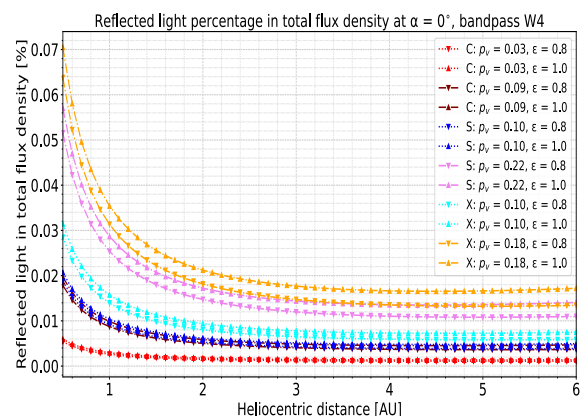
Figure 5.2.12: Idem as Figure 5.2.9 but at W4.

From Figure 5.2.9 to Figure 5.2.12, it can be observed that the reflected percentage curves for the different taxonomies behave in the same way as in Figure 5.2.5 to Figure 5.2.8, that is there is an increase in the amount

of reflected light with increasing heliocentric distance for bandpasses W1 to W3, and a plateau occurring with increasing heliocentric distance at bandpass W4. Furthermore, the curves with an emissivity of 0.8 have a lower reflected percentage than those with a emissivity of 1.0, and confirms what was explained previously. Again, the same regions of heliocentric distance seem to be most affected by the change in emissivity values, that is around the 1-3.5 AUs region for bandpass W1, 2-6 AUs for bandpass W2, 3-6 AUs for bandpass W3, and 0.5-2 AUs for bandpass W4. To better understand the increase and decrease in reflected light due to an emissivity of 0.8 or 1.0, Figure 5.2.9 to Figure 5.2.12 were re-plotted with respect to a reflected light percentage computed with the conventional emissivity of 0.9, for the three different taxonomic types, and various asteroids categorised by their heliocentric distances. The results are illustrated in Figure 5.2.13 to Figure 5.2.16 for bandpasses W1 to W4 respectively. It can already be observed that at W3 and W4, even with a higher emissivity of 1.0, the amount of reflected light in the observable flux density is still negligible where it is below 0.3% at W3, and below 0.04% at W4.
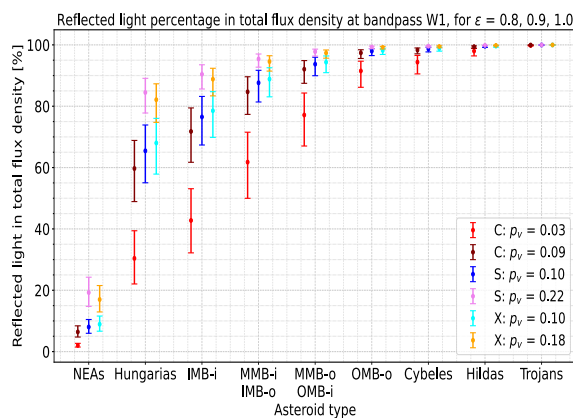
Figure 5.2.13: Effect of emissivity on percentage of reflected light in total flux density for different asteroid types with various albedos within bandpass W1. Lower bar is due $\varepsilon = 0.8$, upper bar is due to $\varepsilon = 1.0$, and middle point is due $\varepsilon = 0.9$. Same parameters as in Figure 5.2.9.
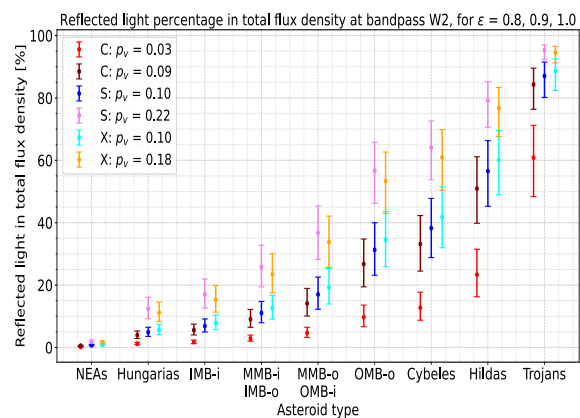
Figure 5.2.14: Idem as Figure 5.2.13 but at W2.
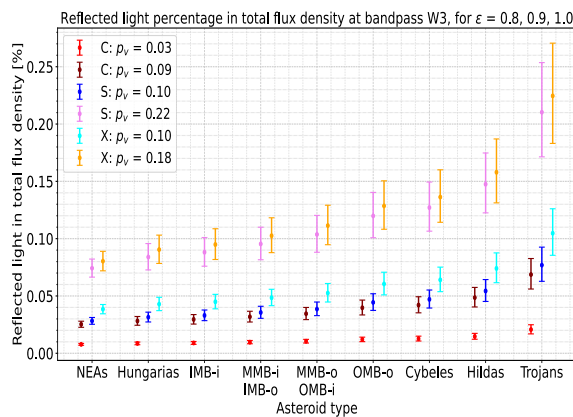
Figure 5.2.15: Idem as Figure 5.2.13 but at W3.
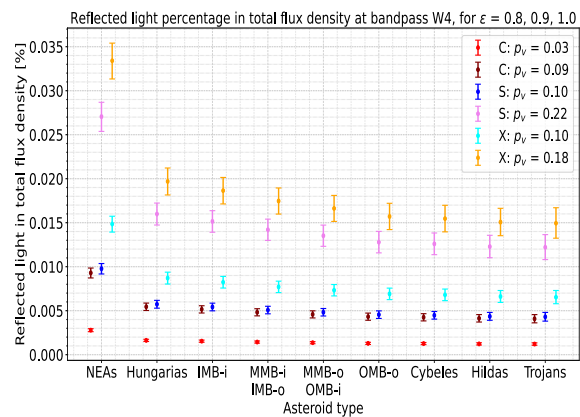
Figure 5.2.16: Idem as Figure 5.2.13 but at W4.

Looking at bandpass W1 from Figure 5.2.13, in general it can be observed that as from the Hungarias (r_{as} = 2 AUs) the lower albedo values from the range of the three taxonomic types show the most variation in reflected light compared to their counterparts with the higher albedo value. However, for the NEAs, the contrary applies. This can be seen by the length of the bars. This suggests that as from r_{as} = 2 AUs, the emissivity has a greater effect on the amount of reflected light for asteroids with lower surface albedos. Moving on to bandpass W2 from Figure 5.2.14, there seems to have an opposite relationship. That is, the most variation in reflected light is achieved by the higher albedo of the respective taxonomies. However, with increasing heliocentric dis-

tance as from around the Hildas, the previous relationship occurs again where the lower albedos show more variation. This illustrates how it is not as straightforward to decouple the effect of emissivity on the amount of reflected light since the latter also depends on the heliocentric distance and surface albedo. At bandpass W3 and W4, seen in Figure 5.2.15 and Figure 5.2.15 respectively, since there are significantly smaller amounts of reflected light, the relationship seems more straightforward. At W3, the most variation in reflected light due to a change in emissivity is seen with increasing heliocentric distance, and with the higher albedos of the three taxonomies. At W4, the highest variation is found around the 1 AU region, where the higher albedos show again the most variation. However, even though the variation is not as much as at 1 AU, there seems to be an increase in variation around the Trojans asteroids compared to the asteroids from 2-4 AUs.

Since the maximum increase and decrease in the amount of reflected light in the total flux density due to a change of the thermal property of an asteroid, that is its emissivity in this case, is more interesting in the scope of this master thesis, the focus will be given to that, and to which asteroid type it occurs per bandpass. From Figure 5.2.13, at W1, for C-types with a visible geometric albedo of 0.03 [red bar], the largest increase and decrease in reflected light percentages due to using an emissivity of 1.0 and 0.8 respectively, is +10.3% and −11.8%. The maximum increase occurs at the inner IMB region, and the maximum decrease at the outer IMB (or inner MMB) region. For C-types with a visible geometric albedo of 0.09 [maroon bar], it is +9.2% and −10.8%, and occur at Hungarias for both the increase and decrease. For S-types with $p_v = 0.10$ [blue bar], it is +8.4% and −10.4%, and occurs at Hungarias for both the increase and decrease. For S-types with $p_v = 0.22$ [violet bar], it is +5.0% and −6.7%, and occurs at NEAs for the increase, and at Hungarias for the decrease. Finally, for X-types with $p_v = 0.10$ [cyan bar], it is +8.0% and −10.1%, and both occur at the Hungarias for the increase and decrease. For X-types with $p_v = 0.18$ [yellow bar], it is +5.2% and −7.4%, and occur again at Hungarias. Overall for bandpass W1, the maximum increase and decrease occur for C-type asteroids with $p_v = 0.03$ in the inner IMB region with a change of about less than ±12%.

At bandpass W2, as shown in Figure 5.2.14, for C-types with $p_v = 0.03$, the largest increase and decrease in reflected light percentages is +10.4% and −12.5%. Both the maximum increase and decrease occur with the Trojan asteroids. For C-types with $p_v = 0.09$, it is +10.2% and −11.1%, and occur at Hildas for both the increase and decrease. For S-types with $p_v = 0.10$, it is +9.8% and −11.3%, and occur again at the Hildas for both. For S-types with $p_v = 0.22$, it is +9.1% and −10.4%, and occur both at the outer OMB region for the increase and decrease. Finally, for X-types with $p_v = 0.10$, it is +9.7% and −11.2%, and occurs at Cybeles for the increase, and at Hildas for the decrease. For X-types with $p_v = 0.18$, it is +9.3% and −10.5%, and occurs at the outer OMB region for the increase, and at the Cybeles for the decrease. In general for bandpass W2, the maximum increase and especially decrease occur again for C-type asteroids with $p_v = 0.03$ but for Trojan asteroids with a change of no more than ±12.5%. It should be noted that C-types with $p_v = 0.09$ have about the same percentage increase as C-types with $p_v = 0.03$ at +10.2%, however for the former it occurs at Hildas.

From Figure 5.2.15, that is at bandpass W3, the maximum percentage increase and decrease occur with the longest heliocentric distance, hence for the Trojan asteroids for all three taxonomic types. This is confirmed by also looking at the diverging curves occurring with increasing heliocentric distance as seen in Figure 5.2.11. For C-types with $p_v = 0.03$, the largest increase and decrease in reflected light percentages is around ±0.004%. For C-types with $p_v = 0.09$, it is +0.014% and −0.013%. For S-types with $p_v = 0.10$, it is 0.016% and −0.014%. For S-types with $p_v = 0.22$, it is +0.043% and −0.039%. Finally, for X-types with $p_v = 0.10$, it is +0.021% and −0.019%. For X-types with $p_v = 0.18$, it is +0.046% and −0.041%. Overall for bandpass W3, the maximum increase and decrease occur this time for X-type Trojan asteroids with $p_v = 0.18$ with a change of no more than ±0.05%. It should be noted that S-type asteroids with $p_v = 0.22$ have nearly similar percentage changes.

Now, at bandpass W4 as seen in Figure 5.2.16, the contrary holds where the maximum percentage increase and decrease occur with the shortest heliocentric distance, hence for NEAs in this case for all taxonomic types. This is not as apparent this time in Figure 5.2.12 due to the scaling of the graphs and the small reflected percentage values obtained. Nonetheless, for C-types with $p_v = 0.03$, the largest increase and decrease in reflected light percentages is around ±0.0002%. For C-types with $p_v = 0.09$, it is about ±0.0006%. For S-types with $p_v = 0.10$, it is around ±0.0006%. For S-types with $p_v = 0.22$, it is around ±0.002%. Finally, for X-types with $p_v = 0.10$, it is about ±0.0009%. For X-types with $p_v = 0.18$, it is around ±0.002%. In general for bandpass W4, the maximum increase and decrease of around ±0.002% occur again for X-type asteroids with $p_v = 0.18$ and similarly for S-type asteroids with $p_v = 0.22$, but at this bandpass it happens to NEAs.

Interestingly, it can be seen that even though the 0.9 emissivity value is the average of the range from 0.8-1.0, the percentage increase and decrease due to using the two boundary values is not equal. This is because the emissivity is scaled by $1/\varepsilon^{0.25}$ in the surface temperature calculation seen in Equation (3.9.4). Furthermore, it can be seen that across all bandpasses and taxonomic types, a lower emissivity of 0.8 produces a slightly higher change in the reflected light percentage than a change due to an emissivity of 1.0. Moreover, most thermal models assume $\varepsilon = 0.9$, where this assumption could have significant consequences when performing thermal modelling in the lower two WISE bands, given that it can maximally shift the reflected percentage positively by around 10% in bandpasses W1 and W2, and maximally reduce it by around 12% at the same two bandpasses. Moreover, even though the beaming parameter was assumed to be 1, if it was not the case, it is expected to have the same effect as the emissivity given that it is also found in the denominator of the facet temperature calculation. This is confirmed by a high-level analysis carried out in Appendix D.1, where $\eta = 0.8$ and $\eta = 1.2$ were computed w.r.t. to $\eta = 1.0$. Furthermore, what if a value of G greater than 0.15 were used? Well since those values are directly multiplied to the geometric albedo, the higher they are the higher the reflected light percentage would be, and the contrary holds if they were lower. This is confirmed with a high-level analysis carried out for a general $p_v = 0.1$ and different G values as summarised in Appendix D.2.

In the investigation carried out in this section, the reflected fraction was computed at a phase angle of zero degree, due to the limitation of the instantaneous thermal equilibrium and no emission on the night side assumed by the ATRM. However, from Section 4.3, it was seen that the reflected flux density of a Lambertian scattering surface follows a 'reverse S-curve' pattern, where with increasing phase angle, the reflected flux density deceases. Around 70°, about half of the normalised reflected flux density is reached relative to a fully illuminated disc. Hence, depending on the thermal inertia and rotation speed of the asteroid, it can be predicted that with increasing phase angle, the fraction of reflected light in the observable flux density will also decrease. This is because more of the night-side of the asteroid will be in view, and assuming non-zero surface temperatures, this prediction should hold.

Nevertheless, it can be said that the higher the thermal inertia, the more time it will take for the asteroid to lose heat on the night side, and given a certain rotation speed, the lower the fraction of reflected light will be with increasing phase angle. On the other hand, the lower the thermal inertia and the slower the asteroid rotates, the faster the asteroid will lose heat on the night-side, and the decrease of reflected with increasing phase angle is more difficult to predict. It should be noted that this thought exercise assumes the spin axis of the asteroid to be perpendicular to the orbital plane. If the spin axis was parallel, only one hemisphere of the asteroid would constantly be receiving sunlight and the other side would be constantly in the dark. Hence, in this situation, with increasing phase angle, the thermal flux density would potentially follow the same pattern as the reflected light. To exactly answer those questions, the thermal inertia has to be properly modelled which is beyond the scope of this project. Ultimately, with Table 5.2.1, thermal modellers or any other users can have a quick reference as to how much reflected light is present in any of the four WISE bands, at a certain heliocentric distance for a given asteroid surface reflectivity, and then decide whether there is a need to account for it.

5.3. Optimising surface albedo distributions under Lambertian scattering of irregularly-shaped asteroids

In Section 5.2, the effect of different albedo values with homogeneous surface distribution on the percentage of reflected light was investigated. Hence, it would now be interesting to investigate the effect of a heterogeneous surface albedo distribution on the percentage of reflected light. Instead of just randomly varying different surface albedo distributions, in this section, a more focused approached will be carried out. As was seen in Section 4.6, the light curves of the two investigated asteroids modelled using the Lambertian scattering law did not completely match the observed data. As previously discussed, the main reason is that the asteroid shape models of DAMIT were derived using a weighted Lommel-Seeliger-Lambertian (LSL) scattering law and a homogeneous surface albedo, and this reason is supported by the fact that the LSL light curves match well with the observation. However, this gives the opportunity to use the Lambertian model but vary its surface albedo distribution to try to obtain a better matching light curve to the observed data. Thus, in this section, such a method will be explored, before moving onto investigating its effect on the percentage of reflected light. Moreover, the following three criteria are used to select one of the four light curves for further investigation:

- Light curve covers a full rotation of the asteroid.

- Light curve corresponds to an orbital geometry with smallest phase angle.

- Light curve with dataset least subject to noise.

The first criteria is straightforward since a full rotation is needed to be able to see the whole asteroid, and facilitate the optimisation of the albedo distribution method. For the purposes of this investigation, a near-full rotation is also acceptable given that is covers both sets of minimas and maximas appropriately. The second criteria comes from the fact that the derived surface albedo distribution of the asteroids using the Lambertian scattering law will be plotted in the four WISE bands to investigate the effect of distributed albedo on the reflected and thermal flux densities. Thus, this criteria stems from the limitation of ATRM in its thermal flux density modelling at non-zero phase angles, given its assumption of no thermal emission on the night-side, which was discussed in Section 4.5, where minimising the phase angle as much as possible is necessary. The last criteria is introduced to also facilitate the method explored. A light curve with the least amount of noise would make matching the maximas and minimas easier, and less guessing would be involved in trying to find the actual maxima or minima through the noise.

The method explored is as follows: Firstly, only homogeneous surface albedos are considered. The visible Bond albedo A_v of the respective asteroids is assumed to be the facet albedo, and given that the observed data is in relative intensity, the normalisation to the mean of the ATRM Lambertian modelled light curves will be done with respect to A_v. This is a fair assumption given that those light curves were obtained in the visible bandwidth. Besides the visible Bond albedo, a set of four different homogeneous surface albedo values are used in the ATRM to try to match the maximas and the minimas as much as possible. A set of four is used, since as was seen previously, the asteroids have irregular shapes and produce two different ranges of minimas and maximas, especially using the Lambertian scattering law. By trial and error, those four surface albedos were refined so that their resulting light curves would match the two crests and two troughs in the light curves.

Once the most optimal set of four homogeneous surface albedos were found, only two are selected. Depending on the circumstance, either the surface albedo matching the most amount of minimas and/or maximas is selected, or the average of two surface albedos is taken when there is none matching at least two minimas/maximas. From the selected two albedos, an octant distribution of the facet albedo is carried out. That is, the asteroid is divided into eight different sections with respect to the spin axis as explained in Section 3.8, and the two selected albedos are applied in different combinations to see which one produces the best matching light curves. This resulted in twelve unique octant distributions. If all four albedos were selected, this would have resulted in seventy two unique octant distributions which is considered too extensive and out of the time scope of this master thesis. The optimisation of albedo distribution of 15 Eunomia and 216 Kleopatra are found in Section 5.3.1, and Section 5.3.2, respectively.

5.3.1. Optimising facet albedo distribution of 15 Eunomia

From Section 4.6, the observation data plotted in Figure 4.6.4 is selected to further explore the effect of heterogeneous surface albedos. This is because out of the four light curves, this observation period is the only one that meets the aforementioned three criteria. Observation data from Figure 4.6.3 failed criterion 2 when compared to Figure 4.6.4, and both Figure 4.6.5 and Figure 4.6.6 failed criterion 3. After trial and error, the best matching set of four homogeneous albedos are 0.1219 [brown] and 0.1149 [red] for the first and second minimas respectively, and 0.0987 [blue] and 0.1189 [purple] for the first and second maximas respectively. The light curves are shown in Figure 5.3.1.
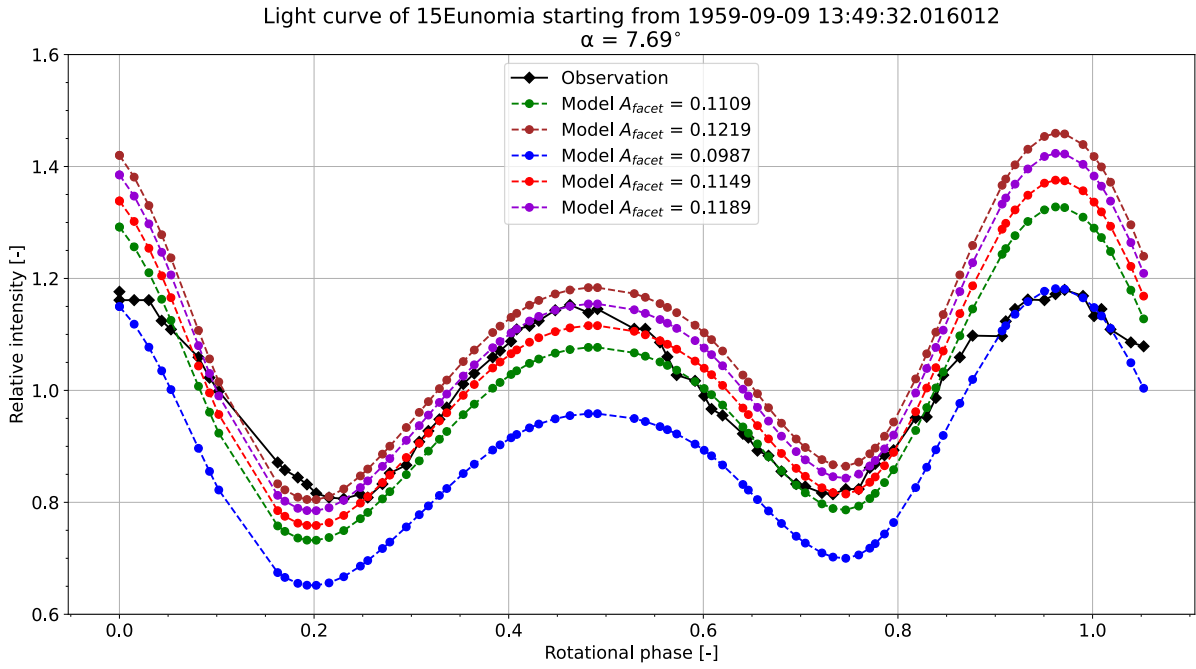
Figure 5.3.1: ATRM's Lambertian light curves of 15 Eunomia against observation taken from Chang et al. (1959) - DAMIT ID #8, plotted with 4 different homogeneous surface albedos, and the visible Bond albedo A_v. The observation light curve is always plotted in solid black with a diamond marker, and the A_v light curve is plotted in solid green with a circular marker. The set of best matching four surface albedos are in dashed lines.

As can be observed in Figure 5.3.1, light curves brown, purple, and red are found rather close to each other, and their corresponding albedo values differ from around 9.9%, 7.2%, and 3.6% respectively from the visual Bond albedo value of 0.1109, where the albedo value of 0.1189 seems to be matching rather well with not only the middle crest, but also quite close to the two troughs as well. Under the assumption of a Lambertian surface, this could suggest that for about three-quarters of its surface, this asteroid has around the same surface albedo distribution. Then, only a lower albedo value of 0.0987 [blue] is able to match the other maxima, where this albedo value is 11.0% lower with respect to the visual Bond albedo value. Thus, the derived maximum and minimum homogeneous surface albedo differ by about the same percentage to match the highest and lowest value of the observation.

From Figure 5.3.1, given that a facet albedo of 0.1189 [purple] matches well with one of the maximas, and is close to the other two minimas it is selected for further investigation in the octant albedo distribution method. The other selected albedo value is naturally 0.0987 [blue], since it is the only one matching with the second maxima. The twelve resulting asteroid albedo mosaic maps are illustrated in Figure 5.3.3 and Figure 5.3.4. The yellow facets have an albedo of 0.1189, and the orange facets have an albedo of 0.0987. The illustrated four asteroids views under their respective octant albedo maps (referred to as mosaic), represent from left to right the data points 13, 36, 56, and 72 corresponding to the first minima, first maxima, second minima, and second maxima of the light curve under investigation. That is the orientations found at rotational phases of 0.2, 0.5, 0.75, and 0.95. The spin vector is illustrated by the black arrow and follows the right-hand rule. It can be observed that the twelve mosaics work in pairs, where the albedos values are flipped from one octant/quadrant region to the next when comparing pairs 1 and 2, 3 and 4, and so on.

Given the phase angle is small at around 7.7°, the Sun and observer are from around the same direction, and the figures are orientated so that the reader looking at the paper is representative of the observer and Sun position. Figure 5.3.2 shows the reflected flux density under the mosaic 1 distribution. This is given so that readers understand better how the incoming flux is being reflected back to the observer, and which regions are being shadowed. The bright-yellowish regions correspond to facets having maximum reflected flux density, and the dark regions to minimum or zero reflected flux density. From the twelve unique albedo mosaics, the corresponding light curves are plotted in sets of four, that is, the light curves of mosaics 1 to 4 are found in

Figure 5.3.5, of mosaics 5 to 8 are found in Figure 5.3.6, and mosaics 9 to 12 are found in Figure 5.3.7.
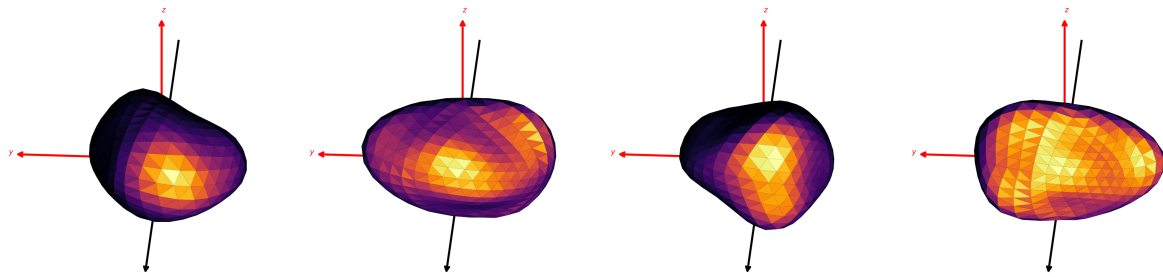
Figure 5.3.2: Reflected flux density of 15 Eunomia with mosaic 1 as surface albedo distribution. The four asteroids, from left to right, represent the orientations found at rotational phases 0.2, 0.5, 0.75, and 0.95 corresponding to the same minimas and maximas as in the facet albedo maps. Given the small phase angle, the Sun and observer are found in the direction, that is from the reader looking at the paper. The bright-yellowish regions correspond to facets having maximum reflected flux density, and the dark regions to minimum or zero reflected flux density. The spin vector is illustrated by the black arrow and follows the right-hand rule.
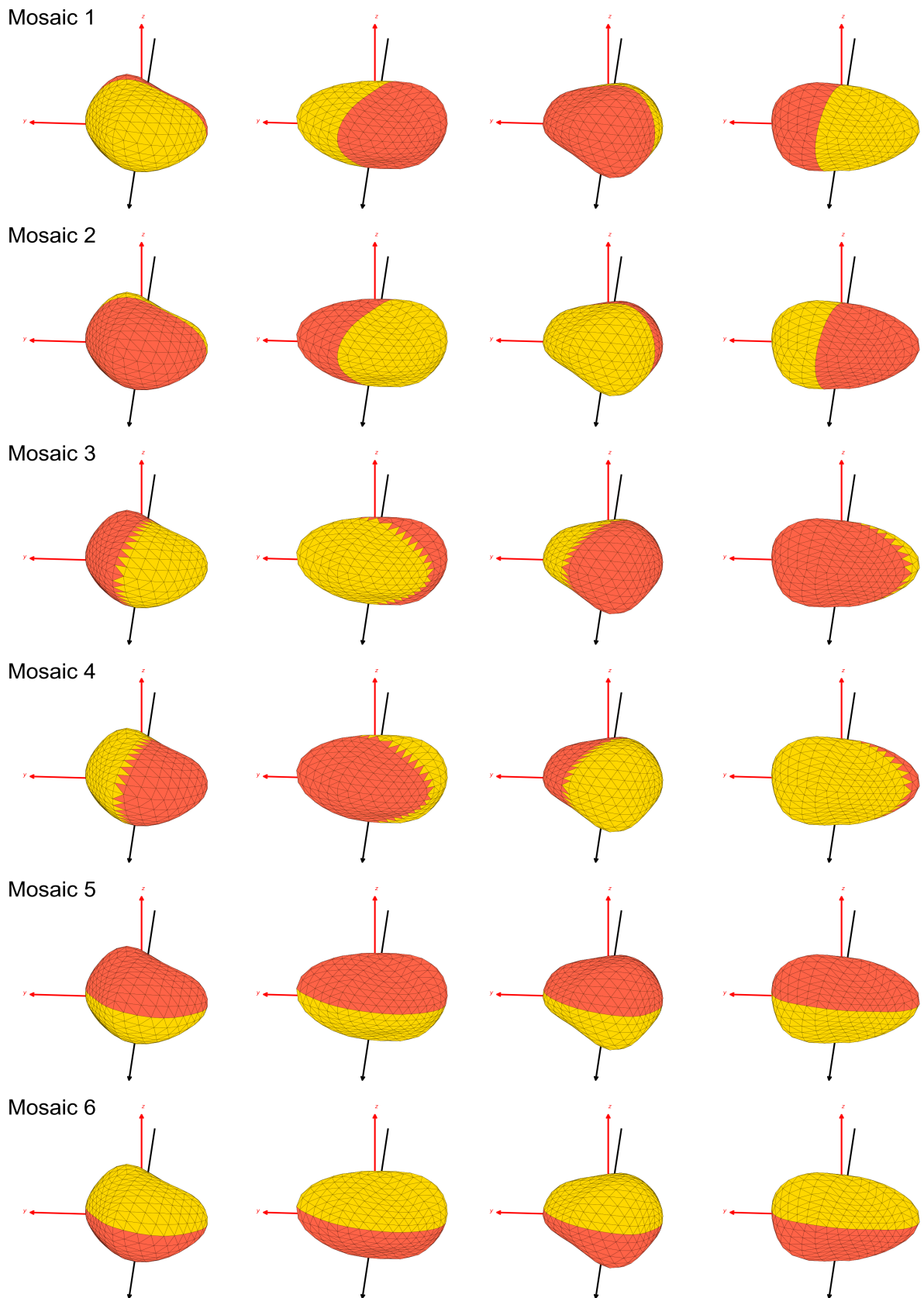
Figure 5.3.3: Octant facet albedo distribution maps of 15 Eunomia for mosaics 1 to 6, where the yellow facets have an albedo of 0.1189, and the orange facets have an albedo of 0.0987. The four asteroids, from left to right, represent the orientations found at rotational phases 0.2, 0.5, 0.75, and 0.95 corresponding to the first minima, first maxima, second minima, and second maxima of the light curve under investigation, respectively. Other parameters follow from Figure 5.3.2.

Mosaic 7

Mosaic 8

Mosaic 9

Mosaic 10
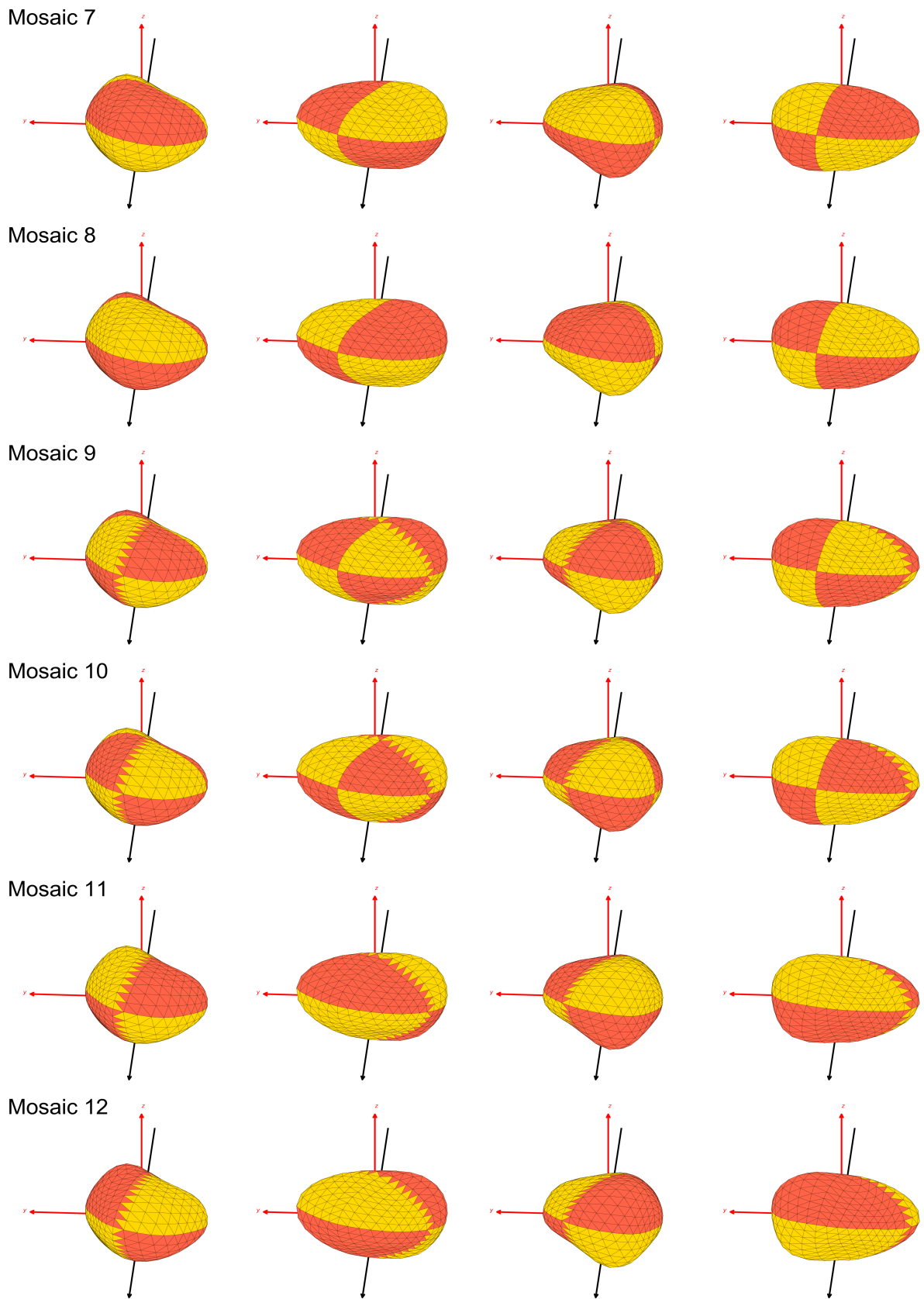
Mosaic 11

Mosaic 12

Figure 5.3.4: Octant facet albedo distribution maps of 15 Eunomia for mosaics 7 to 12. The same parameters from Figure 5.3.3 also apply here.
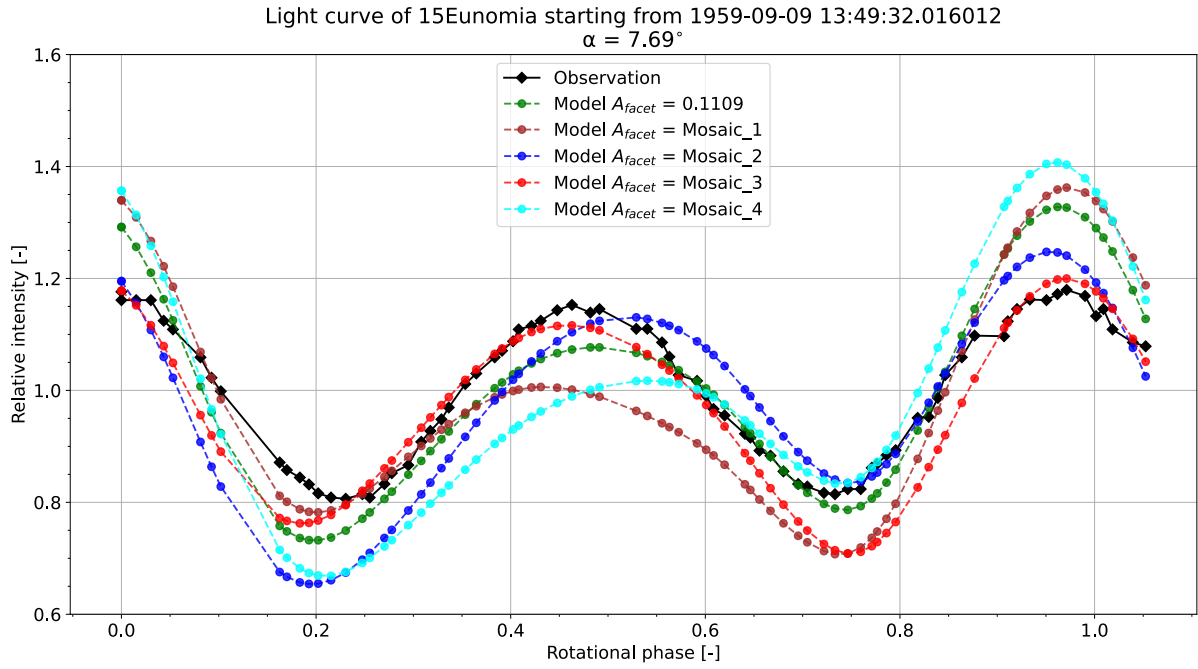
Figure 5.3.5: ATRM's light curve of 15 Eunomia against observation taken from Chang et al. (1959) - DAMIT ID #8. ATRM light curves correspond to mosaics 1, 2, 3, & 4. ATRM light curve produced by a homogeneous facet albedo of A_v plotted in solid green for reference.

From Figure 5.3.5, it can be seen that mosaics 1-4 are producing large variations in light curves compared to the original one with a homogeneous surface albedo [green], as expected. Looking at their respective facet albedo maps in Figure 5.3.3, it can be seen that the mosaics are varied in a two segment manner around the spin axis, where their values are either flipped or moved 90° around the spin axis. Focus will only be emphasised to regions where the light curves made from heterogeneous albedos are matching closely with the observed data, since this is the goal of this section. Mosaic 1 [brown] only matches relatively well at the first minima, and this is confirmed since the albedo value in view at that rotational phase corresponds to 0.1189. This is also confirmed by looking at the effective facet area in view[1] at the first minima in Figure E.1.1, where it can be indeed seen that the albedo region of 0.1189 is mostly in view, and the other albedo region has a near-zero contribution. Mosaic 2 [blue] is close to matching at the first and second maxima. However, given how the albedo has been distributed in this mosaic, it seems to shift the light curve rightwards between the mid-crest to the second minima, given that between those regions the higher albedo is more dominant as can be seen Figure E.1.2.

Mosaic 3 [red] in Figure 5.3.5 matches relatively well at the mid-crest and second maxima, and is not too far off at the first minima. This mosaic together with mosaic 2 seem to match well with the last maxima given that the lower albedo value is in view. Perhaps a better albedo distribution for this albedo region would have been the left most side of the fourth image of mosaic 2 to be covered with more values 0.0987, as is the case of mosaic 3. Mosaic 4 [cyan] is only matching relatively well at the second minima. Compared to mosaic 2, this is expected, since in both cases at that rotational phase the facet albedo with value 0.1189 [orange] is most in view of the observer, as seen in in Figure 5.3.3, and confirmed by looking at Figure E.1.2 and Figure E.1.4. However, mosaic 2 provides a better match between the second minima to the last maxima. Ultimately, from those four mosaics, it seems the most optimal albedo map would be a combination of mosaics 3 for the first minima and maxima, and mosaics 2 for the second minima and maxima.

---

[1]The effective facet area in view is the product of the facet area and the cosines of its illumination and observation angles.
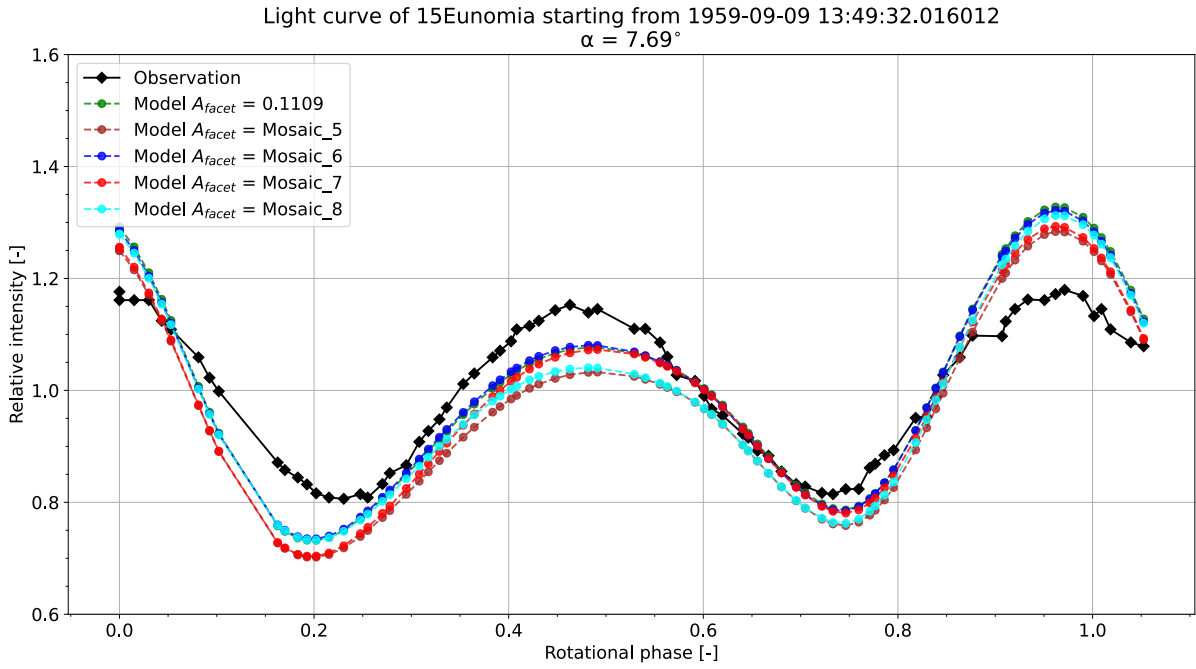
Figure 5.3.6: Idem as Figure 5.3.5 but now ATRM light curves correspond to mosaics 5, 6, 7, & 8. ATRM light curve produced by a homogeneous facet albedo of A_v plotted in solid green for reference.

From Figure 5.3.6, it can be seen that there is not much variation not only between the light curves produced by mosaics 5 to 8, but also when compared to the light curve with homogeneous albedo of 0.1109. This goes to show how, for a given orbital and rotational geometry, certain types of heterogeneous surface albedo distributions can be mistaken for either a homogeneous albedo or other distributed albedo maps. This can be observed between the beginning of the light curve till the first minima, where mosaics 6 [blue] and 8 [cyan] are superimposed on the homogeneous albedo curve [green]. Mosaic 6 actually continues to closely follow the homogeneous albedo curve throughout the whole period, and is joined back by mosaic 8 around the last maxima. Mosaic 7 [red] follows the homogeneous albedo curve from the mid-crest until around the second minima. This is interesting since it points out that those albedo maps, at those specific orientation and observation, seem indistinguishable from one another, at this scale.

Looking at mosaic 6 in Figure 5.3.3, perhaps the similarity in mosaic 6's light curve pattern to that of the homogeneous albedo can be attributed to how the different albedo values from the top [0.1189] and bottom [0.0987] 'hemispheres' average out to an asteroid seeming to have a single surface albedo of 0.1109. Mosaics 5 and 7 look identical between the beginning of the observation period until the first minima. Looking at their illuminated region in view at the first minima, that is, the second albedo map of mosaics 5 and 7 from Figure 5.3.3 and Figure 5.3.4, respectively, it is only their left sides that are matching in values, and their right sides are flipped. The same logic applies to mosaics 6 and 8 at the first minima, however, their left sides are matching but their right sides are flipped. That is why mosaics 6 and 8 match at the first minima. This is confirmed by looking at their effective facet area in view again as seen in Figure E.1.5 to Figure E.1.8. Moreover, at the mid-crest and the second minima, mosaics 6 and 7 are not only closely matching with each other but also with the global albedo. This is expected since at that orientation, the albedo maps are nearly similar apart from the top right part of mosaic 7 [third albedo map]. The same logic applies for mosaics 5 and 8 at the second minima.

Looking at their respective facet albedo maps in Figure 5.3.3 and Figure 5.3.4, it can be seen that the albedo distributions of mosaics 5 and 6 are symmetrical along their axis of rotation. However, mosaic 5 [brown] produces a relatively lower light curve compared to its flipped counterpart of mosaic 6 [blue]. This can be explained by looking at Figure 5.3.2, where it can be seen that the upper 'hemisphere' w.r.t. the spin axis contributes more towards the flux than the lower one, and this is confirmed looking at Figure E.1.5 and Figure E.1.6. Hence, the albedo in the upper region will influence the total reflected flux density more. Furthermore, overall,

mosaic 6 seems to be producing the closest matching light curve to the observed data, especially looking at the first minimas and maximas, and the second minima. Mosaic 7 is also close to matching at the first maxima and second minima, and together with mosaic 5, are the closest to the second maxima.
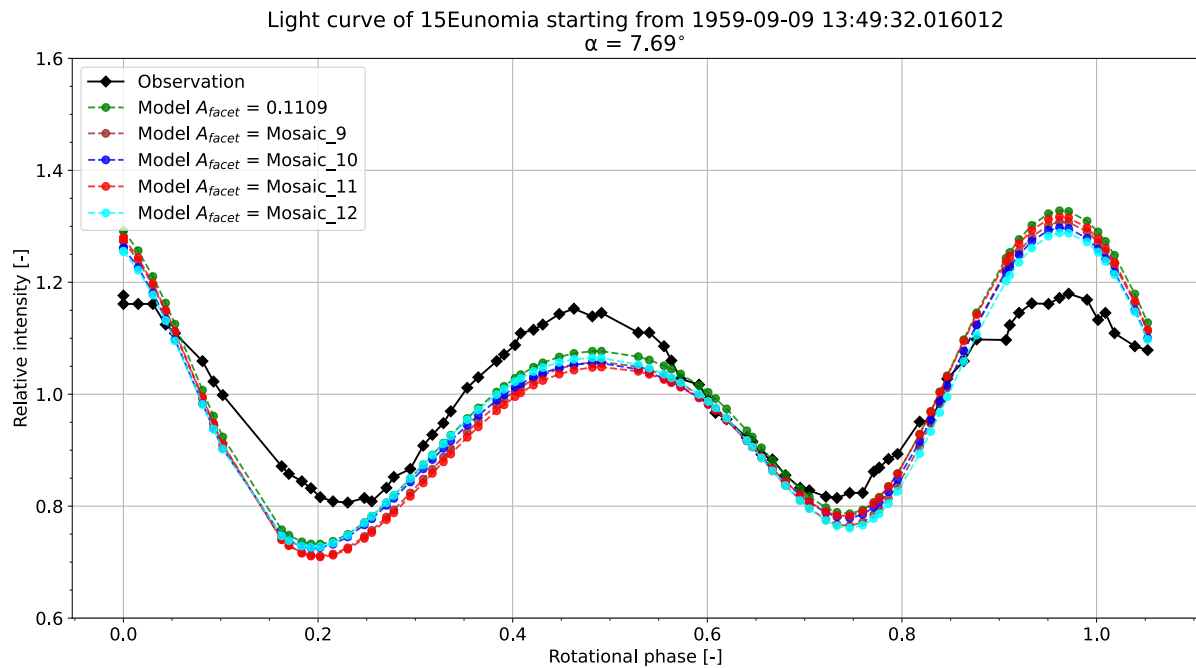
Figure 5.3.7: Idem as Figure 5.3.5 but now ATRM light curves correspond to mosaics 9, 10, 11, & 12. ATRM light curve produced by a homogeneous facet albedo of A_v plotted in solid green for reference.

From Figure 5.3.7, it can be seen that again there is not much variation between not only the light curves produced by mosaics 9 to 12, but also when compared to the one with a homogeneous facet albedo. Hence, this strengthens the same points made from the mosaic 5-8 seen in Figure 5.3.6, where, for a given orbital and rotational geometry, certain types of surface albedo distributions can be mistaken for either a homogeneous albedo distribution or other distributed albedo maps. The light curves of mosaics 10 [blue] and 12 [cyan] are mostly similar. However, when looking at their respective albedo maps in Figure 5.3.4, they only appear similar at the first minima. At the other minima and maxima locations, their light curves do not differ by much even though albedo maps do not match. Looking at Figure E.1.10 and Figure E.1.12, this could perhaps be explained by the fact that the effective facet area in view of each corresponding albedo region scales suitably to portray a similar relative intensity. In other words, the lower albedo region is having an effective facet area in view larger than the higher albedo region, thus compensating for its lower albedo and producing about the same relative intensity. Since the higher albedo is about 7% higher than the reference A_v and the lower albedo is about 11% lower, some albedo surface distributions can indeed produce mosaics which would have matching relative intensities. Even if they were scaled higher and proportional to each other, the same logic would apply. To obtain the most contrast, only one albedo would have to be scaled. The same can be said for light curves of mosaics 9 [brown] and 11 [red].

Nonetheless, the potential facet distribution of 15 Eunomia, for those observation and parameter circumstances, is an amalgamation of mosaic 1 for the first minima, mosaics 2 and 3 for the first and second maximas, and mosaics 2 and 4 for the second minima. However, for further investigation in the effect of distributed albedos on the amount of reflected light in the total flux density of the four WISE bands, only four will be selected for simplicity. Given that mosaics 2 and 3 match in several places, they are selected. Moreover, apart from mosaics 1 and 4, mosaics 2 and 3 are the ones most different from the homogeneous case, so it would be interesting to see how their corresponding reflected percentages will also differ. Mosaic 6 is selected since it matches most of the homogeneous albedo's light curve, and it would be interesting to see if this behaviour

carries out across different wavelength bands of WISE. Finally, mosaic 8 is also selected for the same reason even though it does not match as well as mosaic 6 does.

5.3.2. Optimising facet albedo distribution of 216 Kleopatra

From Section 4.6, Figure 4.6.8 is selected to further explore the effect of distributed surface albedos since it best respects the three selection criteria. Figure 4.6.7 fails criterion 3 due to the noise present. Figure 4.6.9 does not cover a full rotation, hence fails criterion 1. Finally, even though the orbital parameters concerning Figure 4.6.10 has the smallest phase angle, it fails criterion 3 given the potential noise, but also is not taken since the number of data points in this observation campaign is considered too low for a suitable matching of light curves, especially concerning the minimas. After trial and error, the best matching set of four homogeneous surface albedos are 0.0724 [red] and 0.0668 [brown] for the first and second minimas respectively, and 0.0468 [blue] and 0.0508 [purple] for the first (mid-crest) and second maximas respectively. The light curves are shown in Figure 5.3.8.
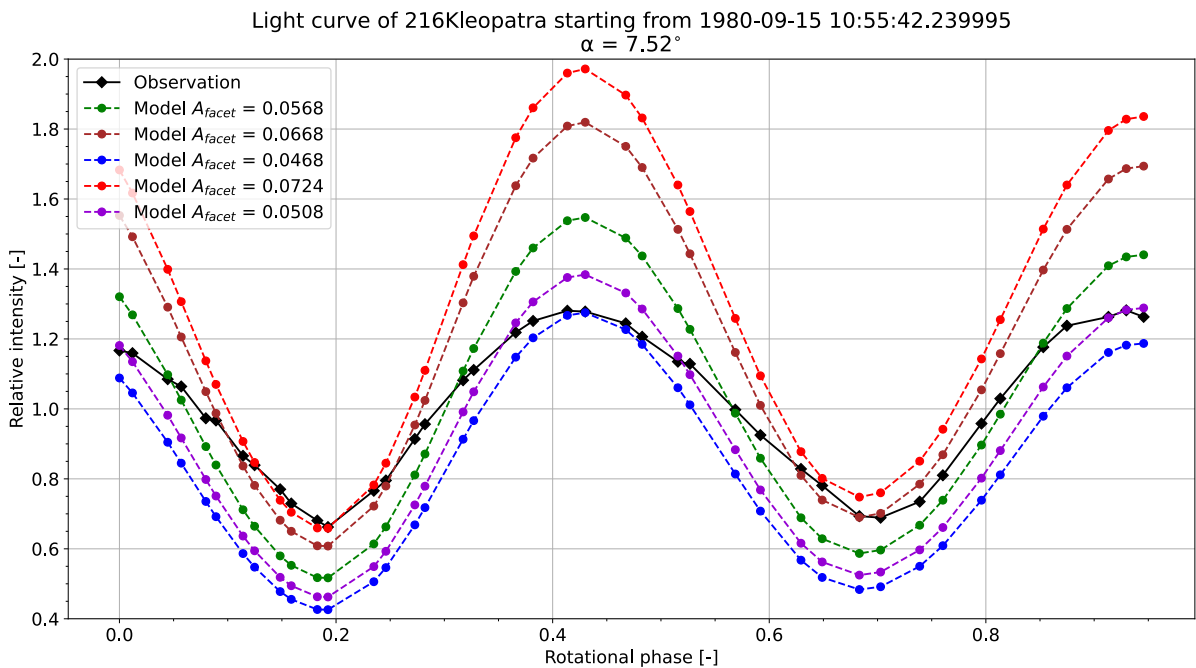
Figure 5.3.8: ATRM's Lambertian light curves of 216 Kleopatra against observation taken from Kennedy & Tholen (1982) - DAMIT ID #8, plotted with 4 different homogeneous surface albedos, and the visible Bond albedo A_v. The same labelling system follows from Figure 5.3.1.

From Figure 5.3.8, it can be observed that each albedo value matches best at a specific location of the observed light curve, but given that only two albedos will be selected to further investigate the effect of a distributed surface albedo, the average of the albedo values matching the pair of maxima and minima values will be used. That is, 0.0696 for the relatively higher albedo and 0.0488 for the relative lower albedo. This results in two albedo values 22.5% higher, and 14.1% lower than the visual Bond albedo of 0.0568. The twelve resulting asteroid albedo mosaic maps are illustrated in Figure 5.3.10 and Figure 5.3.11. The mosaic maps follow the same distribution carried out in 15 Eunomia's mosaics from 1 to 12. Now, the yellow facets have an albedo of 0.0696, and the orange facets have an albedo of 0.0488.

The illustrated four asteroid views under their respective mosaics, represent from left to right the data points 12, 22, 32, and 41, corresponding to the first minima, first maxima, second minima, and second maxima of the light curve under investigation. That is for orientations found at rotational phases of 0.2, 0.45, 0.7, and 0.95. The same logic follows from the albedo maps of 15 Eunomia concerning the spin vector, and the pairing of mosaics where the albedo values are flipped in between pairs. Given a small phase angle again, the

Sun and observer are from around the same direction, and the figures are orientated so that the reader looking at the paper is representative of the observer and Sun position. Figure 5.3.9 shows the reflected flux density under the mosaic 1 distribution. The corresponding light curves from those twelve unique distributed surface albedo mosaics are illustrated in Figure 5.3.12 for mosaics 1 to 4, in Figure 5.3.13 for mosaics 5 to 8, and in Figure 5.3.14 for mosaics 8 to 12.
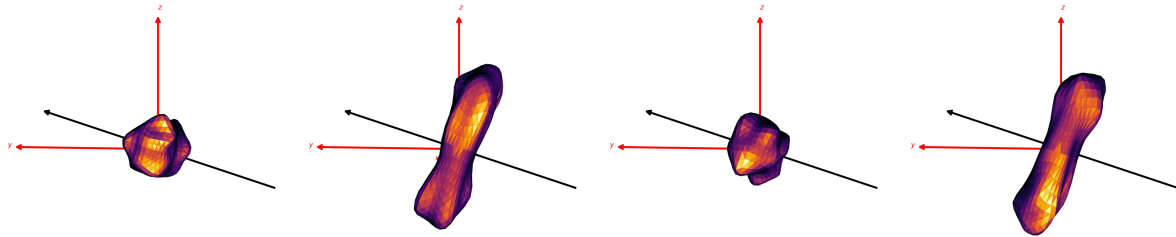
Figure 5.3.9: Reflected flux density of 216 Kleopatra with mosaic 1 as surface albedo distribution. The four asteroids, from left to right, represent the orientations found at rotational phases of 0.2, 0.45, 0.7, and 0.95 corresponding to the same minimas and maximas as in the facet albedo maps. Given the small phase angle, the Sun and observer are found in the direction of the reader looking at the paper. The spin vector is illustrated by the black arrow and follows the right-hand rule. The colouring of the facets follows the same logic as explained in Figure 5.3.2.
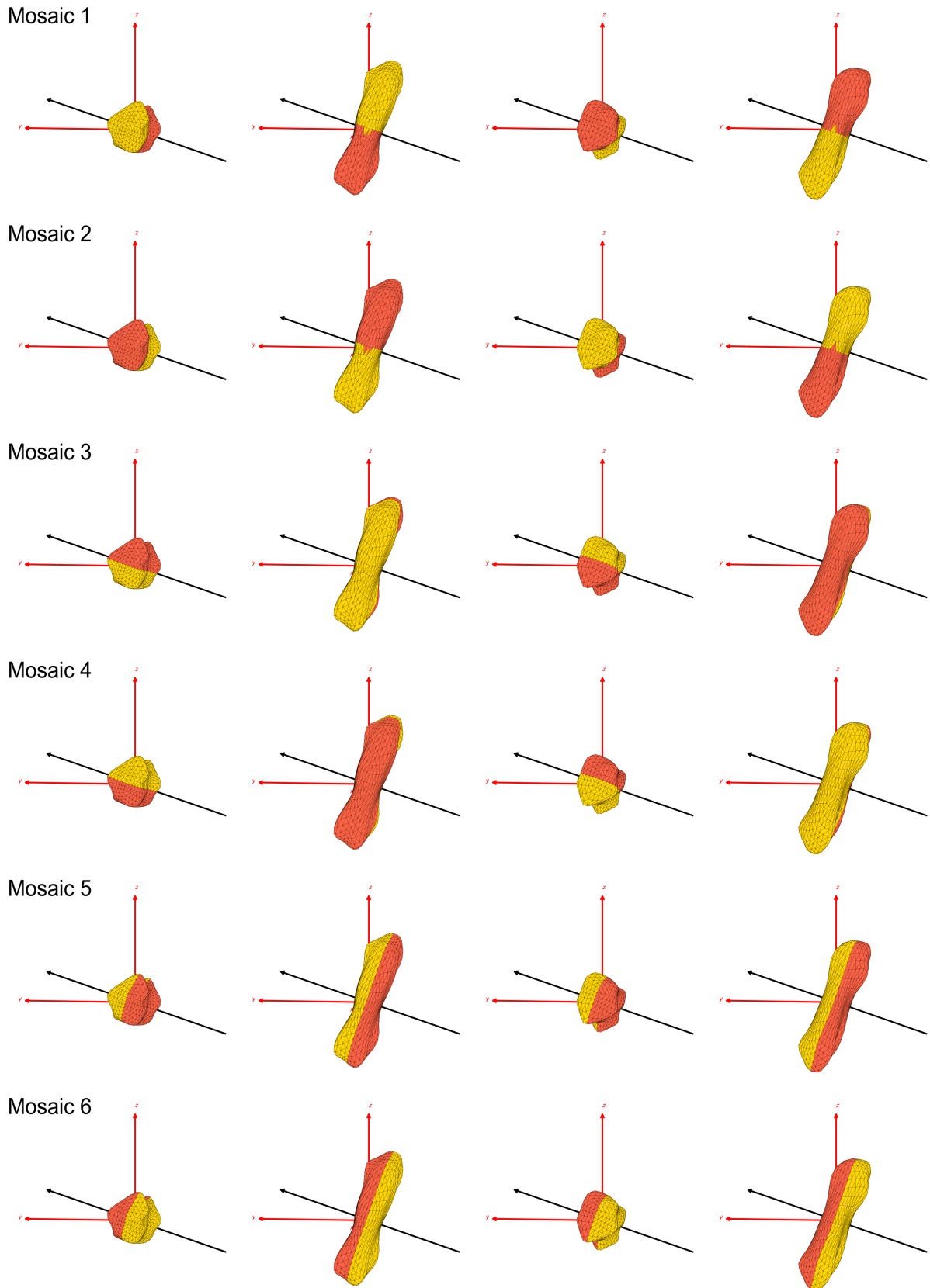
Figure 5.3.10: Octant facet albedo distribution maps of 216 Kleopatra for mosaics 1 to 6, where the yellow facets have an albedo of 0.0696, and the orange facets have an albedo of 0.0488. The four asteroids, from left to right, represent the orientations found at rotational phases of 0.2, 0.45, 0.7, and 0.95 corresponding to the first minima, first maxima, second minima, and second maxima of the light curve under investigation, respectively. The other parameters follow from Figure 5.3.9.

Mosaic 7

Mosaic 8

Mosaic 9

Mosaic 10
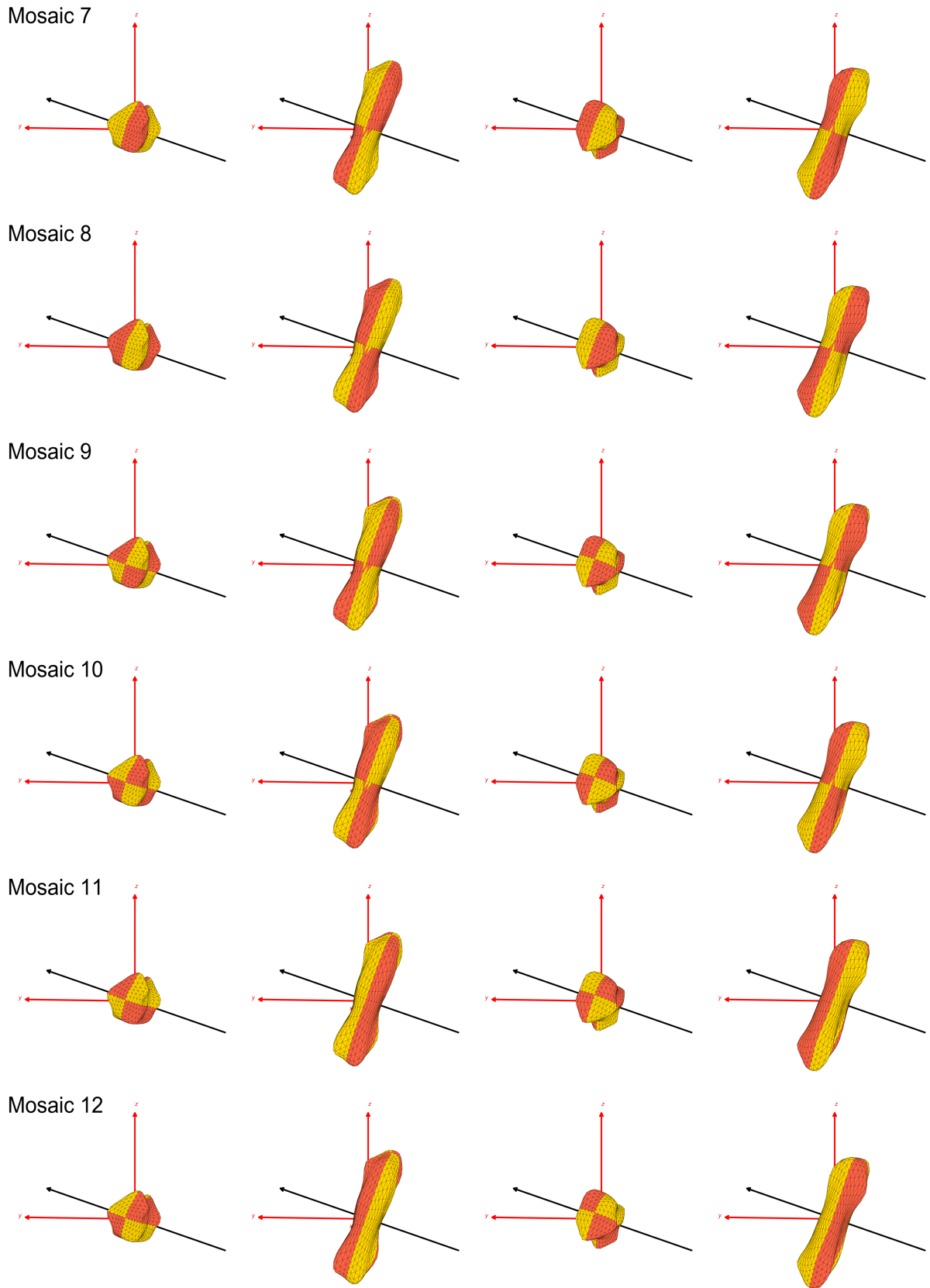
Mosaic 11

Mosaic 12

Figure 5.3.11: Octant facet albedo distribution maps of 216 Kleopatra for mosaics 7 to 12. The same parameters from Figure 5.3.10 also apply here.
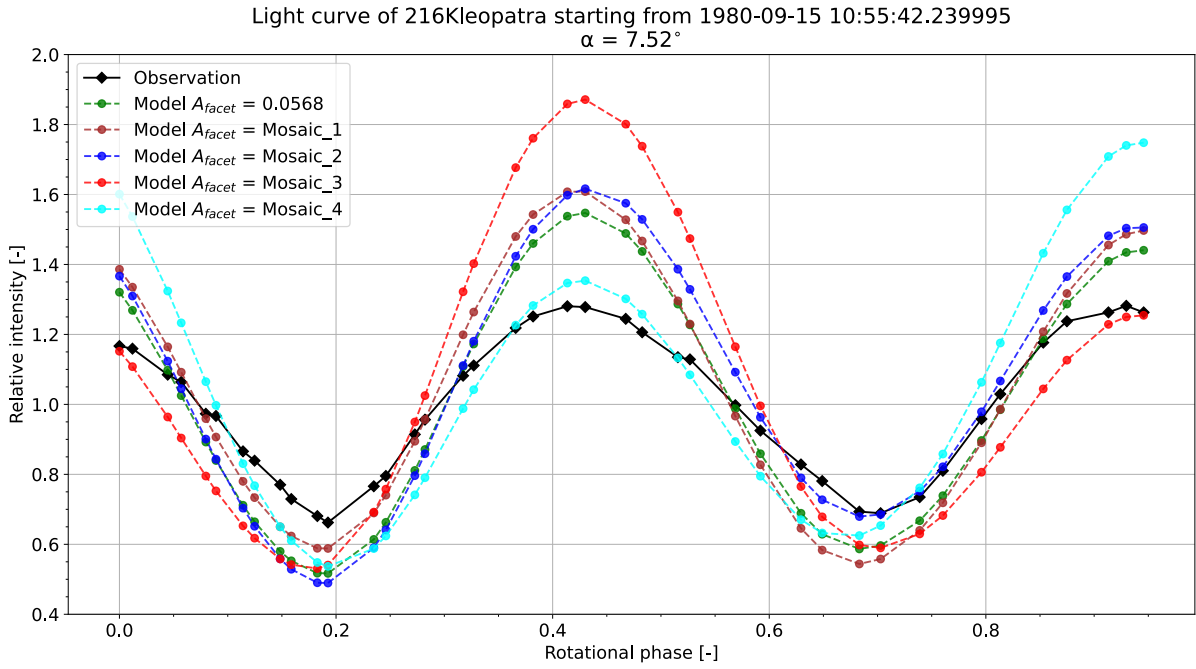
Figure 5.3.12: ATRM's light curve of 216 Kleopatra against observation taken from Kennedy & Tholen (1982) - DAMIT ID #8. ATRM light curves correspond to mosaics 1, 2, 3, & 4. ATRM light curve produced by a homogeneous facet albedo of A_v plotted in solid green for reference.

From Figure 5.3.12, mosaics 1 to 4 are producing different light curves compared to each other and to the homogeneous albedo light curve [green]. This is again because the albedo variations of those mosaics are around the spin vector. Mosaic 1 [brown] does not match at any minima and maxima of the observed light curve, but out of this set of four mosaics, it is the closest to the first minima. Mosaic 2 [blue] is the best match at the second minima, and actually the best match out of the twelve mosaics. Looking at the third image of mosaic's 2 albedo map in Figure 5.3.10, it suggests that this side of 216 Kleopatra must have an albedo of 0.0696, under those viewing conditions. However, given that at this orientation, the background side is also being illuminated and visible to the observer, it would be difficult to say that it is only because of the yellow albedo region of 0.0696 that the light curve is closest to the observed data. However, looking at the effective facet area in view in Figure E.2.2, it can be seen that the lower albedo region of 0.0488 does have a slight contribution.

Looking at mosaics 1 and 2 at the mid-crest, it is interesting to note that mosaic 1 slightly shifts the light curve leftwards, and mosaic 2 shifts it slightly rightwards. Looking at their respective albedo mosaics maps in Figure 5.3.10, that is their second image, it suggests that the higher albedo region will determine a shift in the light curve. As in the case of mosaic 2, if the higher albedo region is coming more into view as the asteroid rotates, it will shift the light curve rightwards. On the other hand, as in the case of mosaic 1, as the asteroid rotates, the higher albedo region becomes less in view, and it shifts the light curve leftwards. This is confirmed by looking at their respective effective facet area in view in Figure E.2.1 and Figure E.2.2, where the higher albedo region is found leftwards and rightwards respectively for mosaics 1 and 2.

Mosaic 3 [red] only matches well at the second maxima, and is actually the only one mosaic of that set of twelve that matches best there. As can be seen in the fourth image of the albedo maps of mosaic 3 in Figure 5.3.10, it suggests that this side of Kleopatra is nearly completely covered in an albedo of 0.0488. However, its only the peak of the maxima itself that is matching. The regions before and after the second maxima of mosaic 3 do not match as well with the observation. Mosaic 4 [cyan] matches best at the mid-crest but is off at the second maxima and the first minima. However, after mosaic 2, it is the second closest to the second minima within that set of four mosaics. Looking at the second image of the albedo maps of mosaic 4 in Figure 5.3.10, it suggests that this side of the asteroid is covered in a single albedo of 0.0488. However, since the mosaic 4 still has a higher relative intensity compared to the observed light curve at the mid-crest, the value of 0.0488 seems too high if the same facet area are considered. Looking back at Figure 5.3.8, a lower facet albedo value of 0.0468 would be more appropriate to lower the light curve for a better match. However, looking at Figure E.2.4,

it can be observed that the higher albedo value 0.0696 has a non-zero contribution to the observable flux at that orientation. Perhaps, if those facets with 0.0696 as facet albedo contributing to the flux at that particular orientation were replaced by the other value of 0.0488, there would be a better match with the observed data.
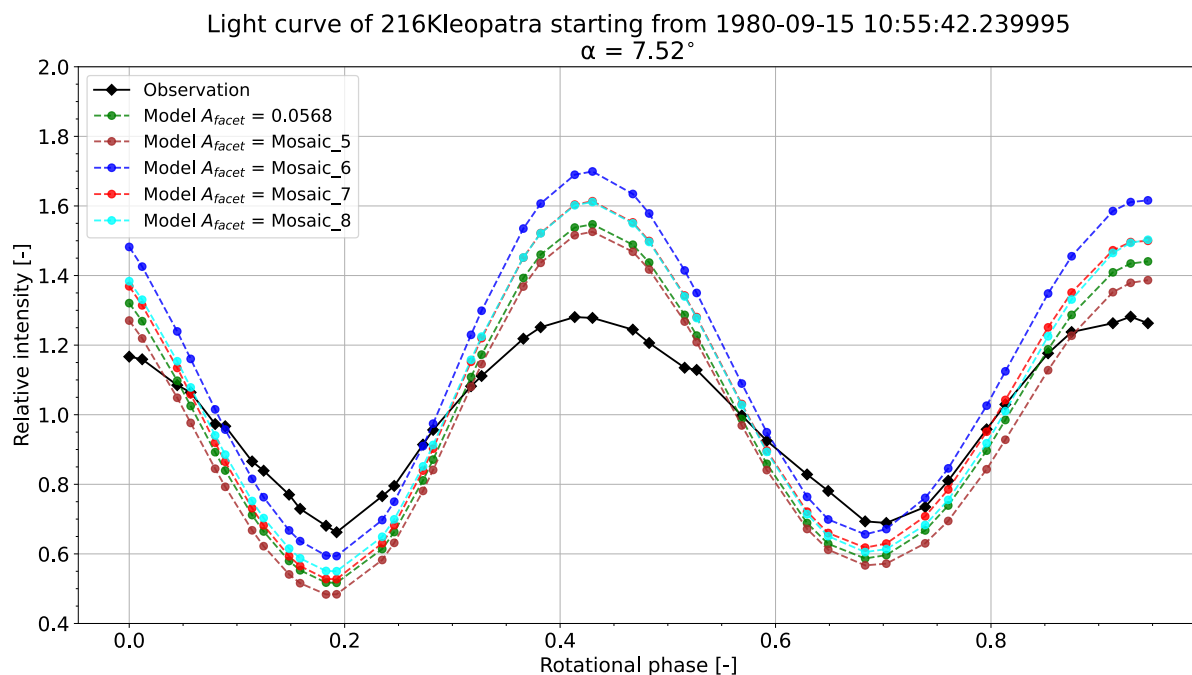
Figure 5.3.13: Idem as Figure 5.3.12 but now ATRM light curves correspond to mosaics 5, 6, 7, & 8. ATRM light curve produced by a homogeneous facet albedo of A_v plotted in solid green for reference.

Mosaics 5 and 6 are symmetrical along the spin axis of 216 Kleopatra. Hence, most of the resulting pattern in light curve produced will be relatively governed more by the shape of the asteroid and less by the albedo itself. The surface albedo will be there to scale the light curve of asteroid. Looking at Figure 5.3.13, it can be seen that mosaics 5 and 6 are nearly consistently shifted downwards and upwards, respective to the solid green light curve. This is confirmed by looking at their effective facet areas in Figure E.2.5 and Figure E.2.6, where there is a general scale shift between the two albedo regions. Moreover, looking back at Figure 5.3.13, between the first minima to the mid-crest, and the mid-crest to the second minima, it can be seen that mosaic 5 actually closely follows the homogeneous facet albedo's light curve. This suggests that a combination of those two albedos at the specific orientation can be mistaken for an asteroid having single albedo value.

From Figure 5.3.13, it can be seen that mosaic 6 is the closest to the first trough, and matches even better with the second trough, suggesting that the facet albedo distribution of that mosaic matches well when the ends (minor aspect) of the asteroid is in view. Comparing the albedo pattern of mosaic 2 and 6 at the second minima, it can be observed that for two different albedo patterns, around the same relative intensity can be reached. This is confirmed by looking at their effective facet area again, as seen in Figure E.2.2 and Figure E.2.6, where they have about the same pattern at the second minima. It shows that even given a specific asteroid shape, different distributed surface albedos can give about the same relative intensity at specific orientations.

Mosaics 7 and 8 do not particularly match well in any region of the light curve, apart from the region between the second minima to the last maxima. It is interesting to note that at both maximas and the region between the mid-crest to the second maxima, the two mosaics are indistinguishable in their light curves. Looking at the albedo maps at those two regions in Figure 5.3.10, that is the second and fourth image, it can be seen that even though the shapes are not symmetrical and the albedo values are flipped, the same relative intensity is reached by both mosaics. This is possible given that this particular albedo distribution, match in their overall effective facet area in view at the mid-crest as can be seen in Figure E.2.7 and Figure E.2.8.
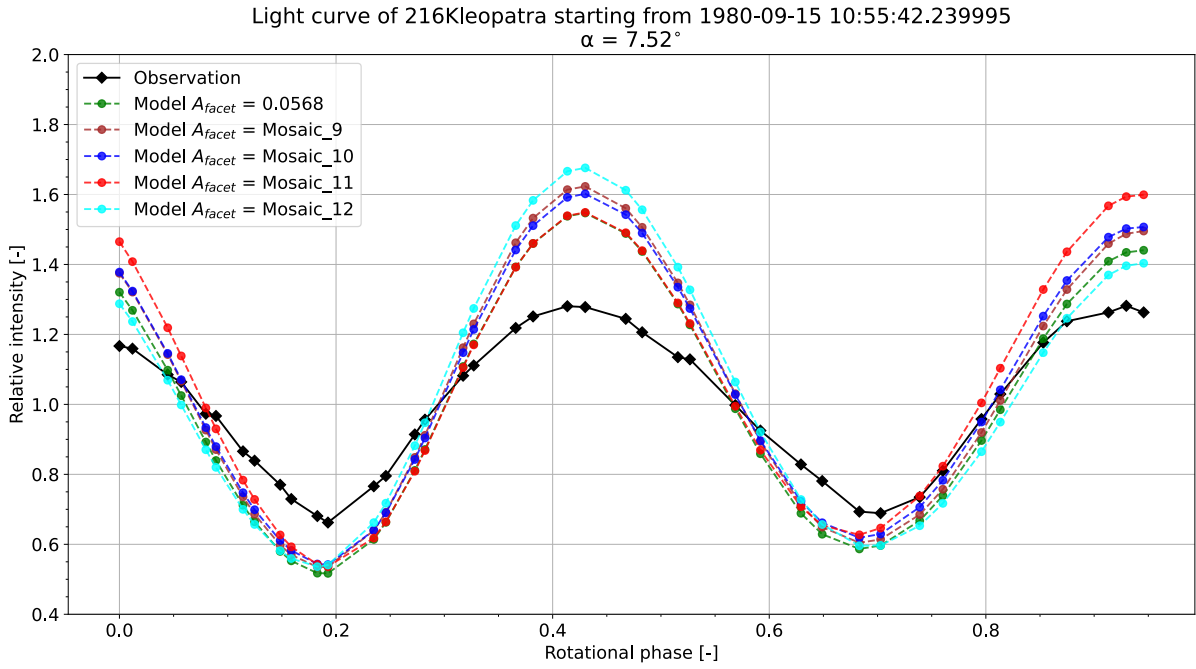
Figure 5.3.14: Idem as Figure 5.3.12 but now ATRM light curves correspond to mosaics 9, 10, 11, & 12. ATRM light curve produced by a homogeneous facet albedo of A_v plotted in solid green for reference.

From Figure 5.3.14, it can be seen that none of the mosaics match well in any region of the observed light curve, except partially at the region between the second minima to the last maxima, where mosaics 9 and 10 follow about the same upward pattern. However, only mosaic 12 is the closest to the observed last maxima. It appears to have the same relative intensity as mosaic 5. This is confirmed since looking at both their albedo maps at that particular data point, they have identical albedo patterns, and this is further reinforced by looking at their effective facet area curves at the last maxima in Figure E.2.5 and Figure E.2.12, where they share nearly the same pattern. At that same location of the second maxima, the same thing can be said for mosaics 6 and 11. That is, they share the same amplitude, given that they have the same albedo distribution at those viewing angles. This is again confirmed by looking at Figure E.2.6 and Figure E.2.11

Mosaics 9 and 10 are nearly identical between the beginning of the light curve till mid-way between the first minima and the mid-crest, and again between the mid-crest till the second minima. Looking at their respective albedo maps in Figure 5.3.11, this behaviour is expected since the time between those rotations, the same albedo pattern is effectively in view. This is confirmed by looking at Figure E.2.9 and Figure E.2.10. Furthermore, it is interesting to see that mosaic 11 is identical to that of a homogeneous facet albedo of 0.0568 between the first and second minimas. This is again another casing point to show how a distributed facet albedo can have the same behaviour as an asteroid with a single albedo.

Thus, the potential facet distribution of 216 Kleopatra, for those observation and parameter circumstances, is an amalgamation of mosaic 1 and 6 for the first trough, mosaic 2 and 6 for the second trough, solely mosaic 4 for the mid-crest, and lastly potentially mosaic 3 for the first and last crests. However, again only four will be selected for further investigation on the effect of heterogeneous surface albedos on the amount of reflected light in the total flux densities at the different WISE bands. Mosaic 2 is selected given it matches well the observed data at the second minima. Mosaics 3 and 4 are selected given that they closely or nearly match at the maximas. In addition, mosaics 3 and 4 actually have the same distributed segment pattern but with their corresponding albedo values flipped, so it would be interesting to see how this affects the amount of reflected light at the WISE bands. Moreover, mosaics 2, 3 and 4 are the ones most different from the homogeneous case, so it would be interesting to see how different their reflected percentages will also differ. Finally, mosaic 11 is also selected to see the effect of having a distributed surface albedo appearing like an asteroid of a single homogeneous albedo for about half its rotation.

5.4. Influence of heterogeneous surface albedo of irregularly-shaped asteroids on percentage of reflected light in total observable flux density.

In Section 5.2, a high-level analysis of the reflected light contribution was carried out for a sphere with homogeneous surface albedo. In this section, a local-level investigation will be carried out on the contribution of reflected light for differently complex-shaped asteroids with different heterogeneous albedo distributions. From the previous section, mosaics 2, 3, 6, & 8 of 15 Eunomia, and mosaics 2, 3, 4, & 11 of 216 Kleopatra were selected for further investigation in the four different WISE bands, where as can be recalled have their effective wavelengths at 3.368, 4.618, 12.082, 22.194μm, respectively. The flux densities were computed using the quadrature formulae representative of the WISE filter+instrument response functions, which were already presented in Section 5.1. As was similarly done in Section 5.2, the IR albedos in the respective four WISE bands were scaled according to their Bus-DeMeo taxonomic type, where 15 Eunomia is a K-type and 216 Kleopatra is an Xe-type. The extrapolations are shown in Figure 5.4.1 and Figure 5.4.2.
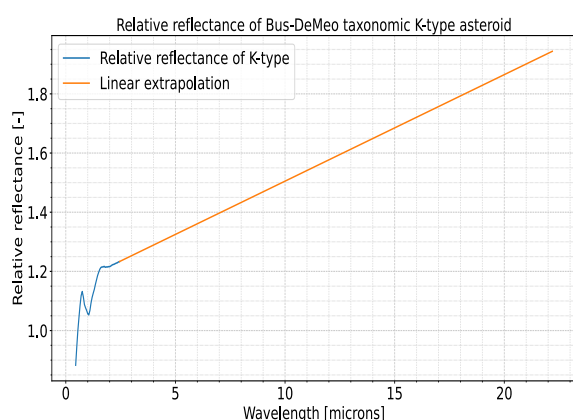
Figure 5.4.1: Extrapolation into the WISE wavelengths of the relative reflectance of Bus-DeMeo taxonomic K-type to which 15 Eunomia belongs.
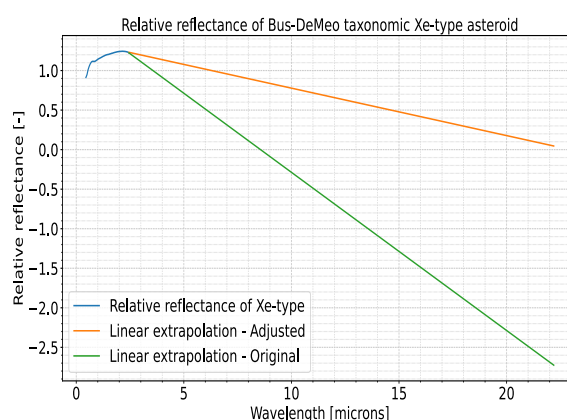
Figure 5.4.2: Extrapolation into the WISE wavelengths of the relative reflectance of Bus-DeMeo taxonomic Xe-type to which 216 Kleopatra belongs.

The IR-Vis ratio R_{IR-Vis} extrapolated from the relative reflectance graphs at the corresponding four WISE bands are summarised as follows, in order from W1 to W4:

- R_{IR-Vis} of K-types (15 Eunomia): 1.27, 1.31, 1.58, 1.94

- R_{IR-Vis} of Xe-types (216 Kleopatra): Adjusted: 1.18, 1.10, 0.65, 0.05. Original ones: 1.04, 0.79, -0.70, -2.73

It should be noted that the linear extrapolation in the case of the Xe-type had to be adjusted, where if it had been completely aligned with its downward slope in the NIR, the relative reflectances at W3 and W4 would have been negative as can been seen in Figure 5.4.2 which is not possible. Thus, it can be said that if the true extrapolation of the NIR trend in Xe-type was carried out, and the W3 and W4 were not considered or assumed to be zero, the R_{IR-Vis} factor at W1 and W2 would be lower at 1.04 and 0.79 respectively, and their reflected light percentages would hence have been lowered too. However, since the reflected light contribution at W3 and W4 wants to be quantified, and not directly assuming it to be zero, this correction is justified. Nonetheless, the results concerning 15 Eunomia will be explored first in Section 5.4.1, and then of 216 Kleopatra in Section 5.4.2.

5.4.1. Influence on 15 Eunomia

The percentage of reflected light in the case of 15 Eunomia across the respective four WISE bands are illustrated in Figure 5.4.3 to Figure 5.4.6. The reflected light percentage produced by a homogeneous surface albedo of $A_v = 0.1109$, which was also used earlier in Section 5.3.1, times its corresponding R_{IR-Vis} in the relevant WISE band is also plotted in solid green for reference. It should be noted that mosaics 6 and 8 were the closest matching to the light curve of homogeneous surface albedo from the previous section, and mosaics 2 and 3

were closest matching with parts of the observation but did not have any clear match with the homogeneous case. Hence, a match in reflected percentage between mosaics 2 and 3 to that of the homogeneous case should not be expected to occur here. The two albedo values used in the facet albedos of the four mosaics in this case are 0.0987 and 0.1189, as was determined in Section 5.3.1. The minimum, maximum, and mean percentages of reflected light in the total flux density of the various surface albedo distributions under investigation across the four WISE bands are summarised in Table 5.4.1.
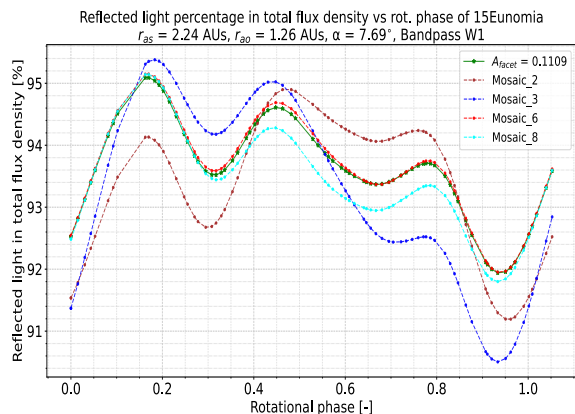
Figure 5.4.3: Percentage of reflected light in total flux density at bandpass W1 of 15 Eunomia using orbital parameters from DAMIT validation ID #8 taken from Chang et al. (1959). Percentage curves correspond to mosaics 2, 3, 6, & 8. The reflected light percentage produced by a homogeneous facet albedo of A_v plotted in solid green for reference.
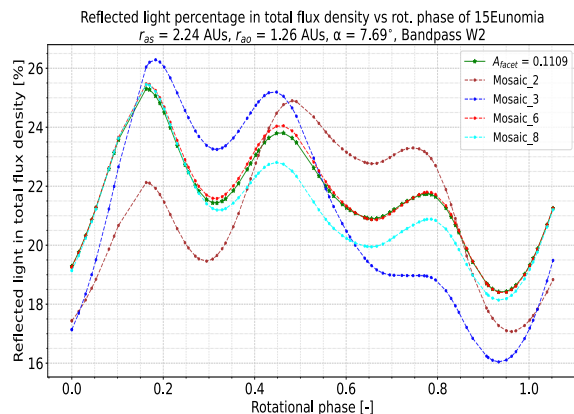
Figure 5.4.4: Idem as Figure 5.4.3 but at bandpass W2.
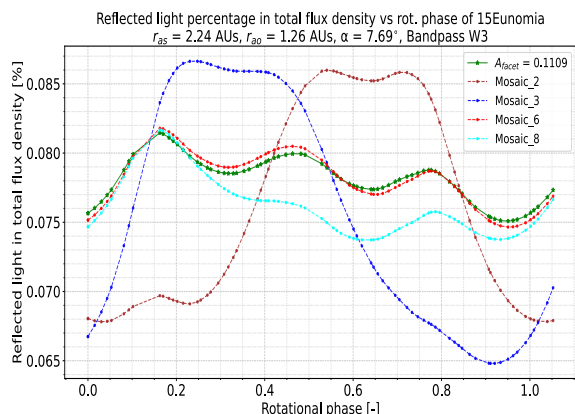
Figure 5.4.5: Idem as Figure 5.4.3 but at bandpass W3.
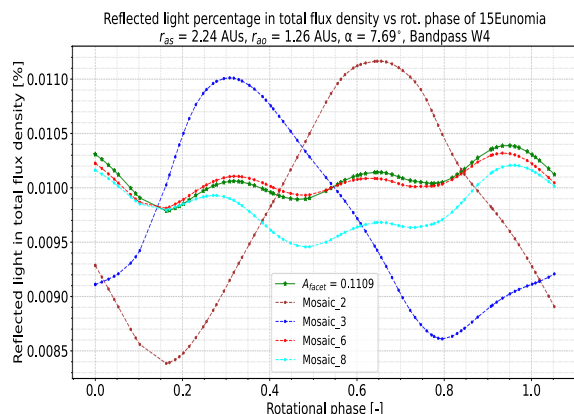
Figure 5.4.6: Idem as Figure 5.4.3 but at bandpass W4.

Table 5.4.1: Summary of minimum, maximum, and mean percentages of reflected light in total flux density percentages of 15 Eunomia for different surface albedo distributions across the four WISE bands.

Albedo distribution	Percentage of reflected light in total flux density [%]											
	W1			W2			W3			W4		
	Min	Max	Mean	Min	Max	Mean	Min	Max	Mean	Min	Max	Mean
Homogeneous	91.94	95.09	93.60	18.42	25.30	21.55	0.075	0.081	0.078	0.0098	0.0104	0.0101
Mosaic 2	91.19	94.90	93.35	17.07	24.90	21.07	0.068	0.086	0.076	0.0084	0.0112	0.0098
Mosaic 3	90.50	95.38	93.18	16.04	26.29	20.87	0.065	0.087	0.075	0.0086	0.0110	0.0097
Mosaic 6	91.95	95.15	93.63	18.40	25.47	21.63	0.075	0.082	0.078	0.0098	0.0103	0.0101
Mosaic 8	91.80	95.14	93.39	18.14	25.45	21.05	0.074	0.082	0.076	0.0095	0.0102	0.0098

Looking at the percentage of reflected light in total flux density in all four graphs or Table 5.4.1, it can be observed again that with increasing wavelengths there is a lower percentage of reflected flux density present in the total observable flux density, as expected from the previous investigation carried out in Section 5.2. Firstly, focusing on the homogeneous surface albedo case, at W1, the percentage of $F_{\text{refl.}}/F_{\text{tot.}}$ is varying between 91.9-95.1%, at W2 between 18.4-25.3%, at W3 between 0.075-0.081%, and finally at W4 between about 0.0098-0.0104%. Given that in Section 5.2, no investigation of the K-type or Xe-type were carried out, it would difficult to have a direct comparison between the obtained reflected light percentages. However, given the orbital parameters of 15 Eunomia used here has r_{as} = 2.24 AUs, the percentages obtained here are roughly in the same order of percentages than an IMB-i (found at 2.2 AUs) S-type asteroid which has an upper bound of 90.4%, 17.0%, 0.088%, and 0.016% for wavelength regions W1 to W4, respectively. The percentages here are relatively higher in the case of W1 and W2, given that the visible geometric albedo of 15 Eunomia is 0.248 [63], whereas the upper limit of S-types is at 0.22. Furthermore, they do not share the same $R_{\text{IR}-\text{Vis}}$ factors, where those of K-types are lower than S-types. But 15 Eunomia having a higher albedo, and a higher slope parameter at G = 0.23 compensates for the lower $R_{\text{IR}-\text{Vis}}$. At W3 and W4, 15 Eunomia and S-types have around the same percentages of reflected light, where the $R_{\text{IR}-\text{Vis}}$ factors of the S-types are much higher than those of K-types, which makes up for the earlier mentioned difference.

Furthermore, the range of reflected percentages across the rotation of the asteroid shows that even though the size of an asteroid does not have an effect on the fraction of reflected light as previously discussed, its shape does have an influence. Still focusing on the homogeneous case, at W1, the difference due to the shape of 15 Eunomia is around 3.15%, at W2 around 6.89%, at W3 about 6.38×10^{-3}%, and at W4 around 6.01×10^{-4}%. It can be seen that the percentage difference is highest at W2, which is about twice that of W1. At W3 and W4, even though the reflected light percentages themselves are negligible, the difference in W3 is similar to that in W4 but an order of magnitude higher. Hence, it seems in this case that the effect of the shape of the asteroid has the greatest influence on the reflected light percentage at W2.

Interestingly, in Figure 5.4.3 to Figure 5.4.6, it can be seen that there are three maximas and three minimas, even though as was seen previously in their normalised reflected light curves in Section 5.3.1, only two of each were present which was solely influenced by the shape of the asteroid since a homogeneous surface albedo was assumed. However, in the reflected percentage curves under investigation here, both the reflected light percentage curves of heterogeneous and the homogeneous surface albedos themselves are producing those three minimas and maximas. Hence, the new minimas and maximas can not be attributed to the effect of a distributed surface albedo since it is also present in the homogeneous case. It seems that the shape of the asteroid is responsible, but with another compounded effect. A potential explanation for those extra minimas and maximas in the reflected light percentages can be explained by Wien's displacement law.

To better understand the origin of the new local maximas and minimas, the thermal and reflected flux densities of 15 Eunomia versus its rotational phase, across W1 to W4, are illustrated in corresponding pairs from Figure 5.4.7 to Figure 5.4.14. It can already be observed that the reflected flux density, illustrated in Figure 5.4.8 to Figure 5.4.14, has exactly the same light curve pattern throughout W1 to W4, where only the magnitude of the reflected flux density decreases from 10^{-7} to 10^{-10} $W/m^2/m$. This is expected since the reflected flux density is governed by the reflection of the thermal emission from the blackbody temperature of the Sun found at a much higher temperature of 5778 K, which peaks at around 0.5 microns. However, in the case of the thermal flux density, the thermal light curve patterns change with different wavelength bands under investigation. This is because the different wavelength bands 'favour' different regions of the asteroid contributing towards the thermal emission, due to Wien's displacement law, where those regions themselves are influenced by their surface temperatures. This will be explained into further details in the following paragraphs. In Figure 5.4.7 to Figure 5.4.13, it can be seen that the magnitudes of the thermal flux density increase from 10^{-8} to 10^{-6} $W/m^2/m$, respectively. A side note, it can be observed that in the reflected light curves, when the mosaics with relatively higher albedos are in view, they increase the reflected flux density, whereas they decrease the thermal light curves, as expected given the $(1-A)$ relationship found in the latter. When the relatively lower albedos of the mosaics are in view, the opposite effect occurs.
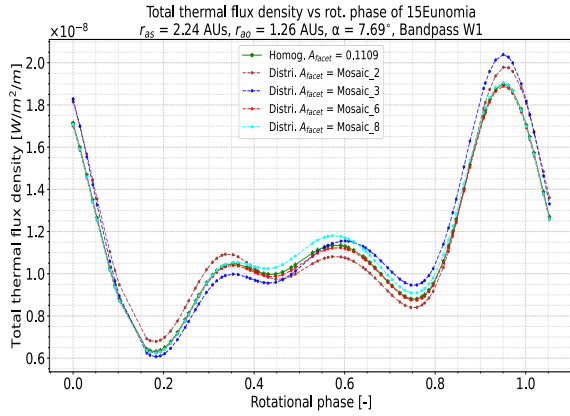
Figure 5.4.7: Thermal flux density at bandpass W1 of 15 Eunomia against same parameters as in Figure 5.4.3. Light curves correspond to mosaics 2, 3, 6, & 8. Light curve produced by a homogeneous facet albedo of A_v plotted in solid green for reference.
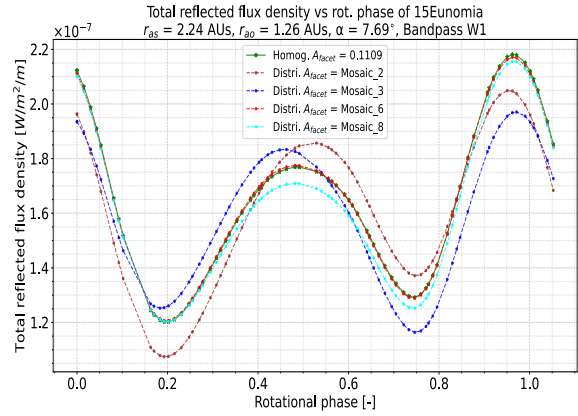
Figure 5.4.8: Reflected flux density at bandpass W1 of 15 Eunomia against same parameters as in Figure 5.4.3. Light curves correspond to mosaics 2, 3, 6, & 8. Light curve produced by a homogeneous facet albedo of A_v plotted in solid green for reference.
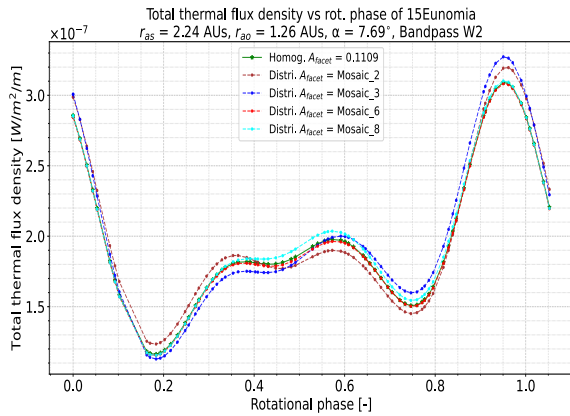
Figure 5.4.9: Idem as Figure 5.4.7 but at bandpass W2.
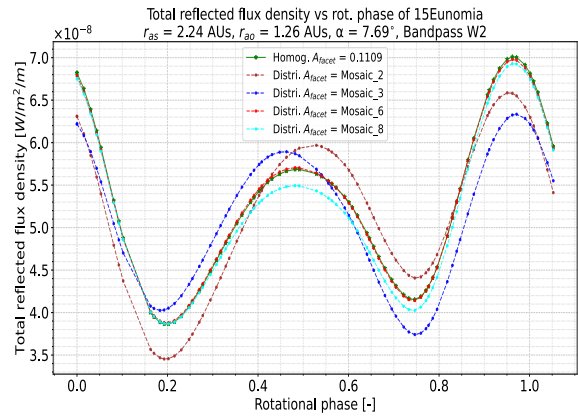
Figure 5.4.10: Idem as Figure 5.4.8 but at bandpass W2.
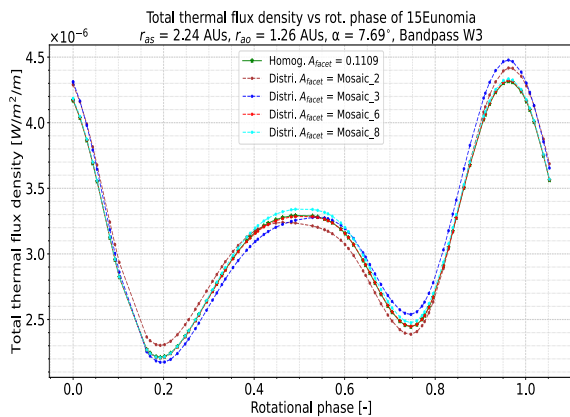
Figure 5.4.11: Idem as Figure 5.4.7 but at bandpass W3.
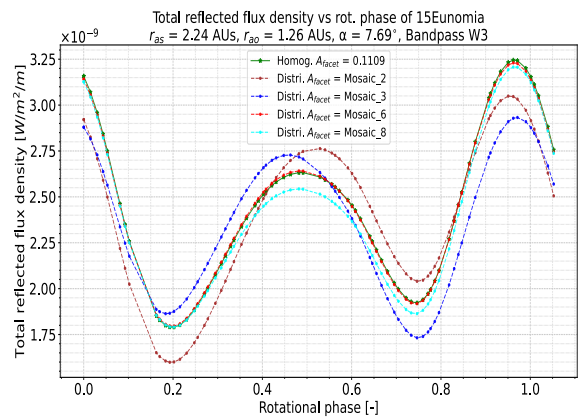
Figure 5.4.12: Idem as Figure 5.4.8 but at bandpass W3.
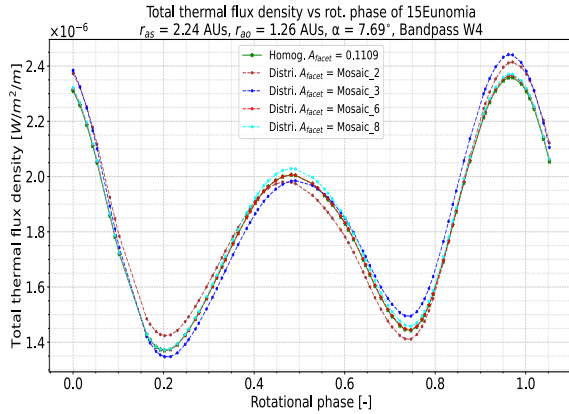
Figure 5.4.13: Idem as Figure 5.4.7 but at bandpass W4.
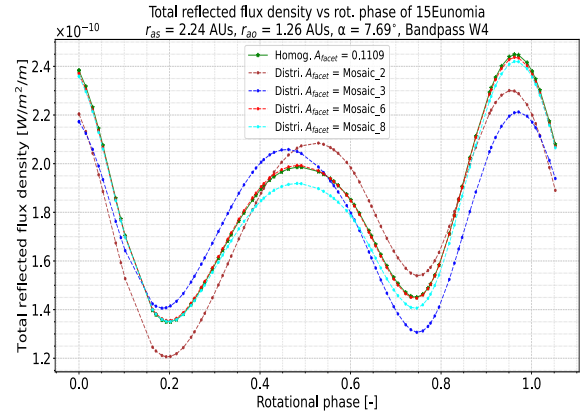
Figure 5.4.14: Idem as Figure 5.4.8 but at bandpass W4.

Looking at the homogeneous albedo curve from W1 to W3 in Figure 5.4.3 to Figure 5.4.5, it can be seen that around a rotational phase (henceforth referred to as RP) of 0.15-0.2 there is a maxima in the reflected percentage, which actually corresponds to when the smaller side of the asteroid is in view as corroborated by their thermal and/or reflected flux density light curves seen in Figure 5.4.7 to Figure 5.4.12. At around RP 0.45, there is a another maxima in the reflected percentage, where this time it matches when the larger side of the asteroid is in view. Finally, the last reflected percentage maxima at RP 0.75-0.8 is actually again when the smaller side is in view. This suggests that even when the smaller sides of the asteroids are in view, the reflected flux density is contributing relatively more towards the total flux density than the thermal flux density, even at the longer wavelength of W3 where the reflected light has a substantially small contribution of about 0.078%.

Looking at the locations of the local minimas in the reflected percentage curves also at only W1-W3, the three minimas are at RPs 0.3-0.35, 0.65-0.7, and 0.95. Looking again back at the thermal and/or reflected flux density light curves seen in Figure 5.4.7 to Figure 5.4.12, the 0.95 minima in the reflected percentages is actually matching with a maxima in the light curves. This suggests that for the other larger side, the thermal flux density has a greater contribution to the total flux density than the reflected flux density. The other two minimas occurring at RPs 0.3-0.35 and 0.65-0.7 can be explained by looking at the thermal flux density light curves from Figure 5.4.7 to Figure 5.4.13. It can be seen that the pattern in the curve changes at different different wavelength bands, where this is especially apparent in the middle section of the light curves, from RP 0.3 to 0.7. Especially at W1 and W2, there are local maximas at about RPs 0.35 and 0.6, which are close to the RP locations in the reflected percentage curves. At W3, seen in Figure 5.4.11, the middle region has become more like a single flat maxima, which could perhaps explain why the extra two minimas are still present. At W4 seen in Figure 5.4.13, the middle region has become even more of a local maxima with a central peak, but there are still 3 minimas and 3 maximas present in its corresponding reflected percentage curves as seen in Figure 5.4.6. However, interestingly, it can be seen that a flip has occurred in the local minimas and maximas of Figure 5.4.6.

At W4, there is a flip in the local minimas and maximas for both the homogeneous and heterogeneous surface albedo distributions as can be seen in Figure 5.4.6. That is the maximas have become minimas, and vice versa, when comparing them to their counterparts in W1-W3. This means that even though the percentage of reflected light in the total flux density is very small at bandpass W4, for those particular locations on 15 Eunomia, at the new minimas, the thermal flux density now has more contribution towards the total flux density than the reflected flux density, and at the new maximas the contrary applies. The minimas at around RPs 0.15-0.2 and 0.95 match with the minimas present in 15 Eunomia's light curve. However, concerning the maximas, only the maxima at RP 0.95 matches with the light curve one. The other light curve maxima at RP 0.5 actually corresponds to a minima in the reflected percentage curves. Thus, at this location, it seems that the reflected flux density has a relatively greater contribution still than the thermal flux density. The two other local maximas found at RPs of about 0.3-0.35 and 0.65-0.7 are close to that of RP 0.5.

Wien's displacement law is illustrated in Equation (5.4.1), where b is Wien's displacement constant in metre Kelvin [$m \cdot K$ not to be confused with milli Kelvin]. This law explains that a particular temperature will have its

maximum spectral irradiance, that is its peak thermal emission occur at a particular wavelength [45]. As can be seen in Equation (5.4.1), an inverse relationship is present, where with increasing temperature, the peak of the emission wavelength decreases. Hence, this means the warmest facets would contribute the most towards the thermal emission at shorter wavelengths, whereas at longer wavelengths, thermal emission is also received by the cooler facets. Typical asteroid surface temperatures ranging from 50-500 K were applied to Equation (5.4.1) to obtain the corresponding peak emission wavelengths which are summarised in Table 5.4.2. It can be seen that the relatively higher temperatures of about 500 K have peaks occurring at the lower bandpasses, close to W1 and W2. Whereas at W3 and W4, the thermal emission peaks of the relatively lower temperatures of 100-250 K occur.

$$\lambda_{peak} = \frac{b}{T} \quad \text{where } b = 2.897771955 \cdot 10^{-3}\, m \cdot K \qquad (5.4.1)$$

Table 5.4.2: Typical asteroidal surface temperatures with associated Wien's displacement peak emission wavelengths.

Asteroid surface temperature [K]	Wien's peak wavelength [microns]
50	57.96
100	28.98
150	19.32
200	14.49
250	11.59
300	9.66
350	8.28
400	7.24
450	6.44
500	5.80

Furthermore, the explanation attributed to Wien's displacement law across the W1-W4 is strengthened by looking at the temperature and thermal flux density distributions, seen respectively in Figure 5.4.16 and Figure 5.4.15, of 15 Eunomia at the respective orientations producing the local minimas and maximas, where the images given correspond to RPs 0.2, 0.5, 0.75 and 0.95. It should be noted that the temperature and flux density plots are for a homogeneous surface albedo. However, if a distributed albedo was used, the locations/orientations where there would have been a higher albedo would have resulted in lower temperatures, lower thermal flux densities, and higher reflected flux densities, thus higher reflected percentages, and vice-versa for regions with lower albedos. Nonetheless, for the homogeneous case, as can be seen in Figure 5.4.15, the temperature distribution is about 210-262 K in the central region, and about 100-210 K in the outer regions. Looking at Table 5.4.2, it can be seen that the peak thermal emission will be around 11-14.5 microns for the 210-262 K, and for 100-210 K, around 14-29 microns. Thus, as can be observed in Figure 5.4.16, with increasing wavelengths from W1 to W4, more of the non-central regions are contributing towards the observable flux density. At W3, which has a wavelength center of around 12 microns, the facets with temperatures 210-262 K will contribute most, and at W4, the lower facet temperatures around 100-210 K, which are found at the outer regions will contribute most.

Looking at W3 and W4 in Figure 5.4.16, Wien's law also explains why the highest thermal flux density in the central region of Eunomia is reached with a magnitude of $10^{-10}\ W/m^2/m$, whereas at W4, the same magnitude is also obtained but the maximum facet thermal flux densities are about half that in W3's case, given that the central regions with facet temperatures between 210-262 K peak around 12 microns which falls within bandpass W3. This reasoning also applies when comparing the total thermal flux densities found Figure 5.4.11 and Figure 5.4.13, for bandpasses W3 and W4 respectively. The reflected light percentage decrease across W1 to W4 can be confirmed by also looking at the facet reflected flux densities illustrated in Figure 5.4.3. Here it can be observed that even with increasing wavelength, the same regions of the asteroid contribute towards the reflected flux density, as was explained previously. That is, there is no increase contribution from the outer region of the asteroid as was the case in the thermal flux density. This is because the calculation of the reflected flux density uses the effective blackbody temperature of the Sun, which is 5778 K and peaks around 0.5

microns which is found much lower than bandpass W1.
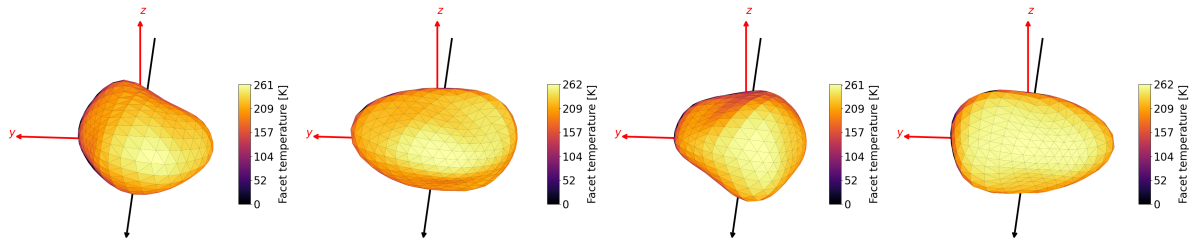
Figure 5.4.15: Facet temperature distribution of 15 Eunomia at rotational phases 0.2, 0.5, 0.75 and 0.95. These rotational phases correspond to computation intervals 13, 36, 56, and 72 across the four WISE bands.
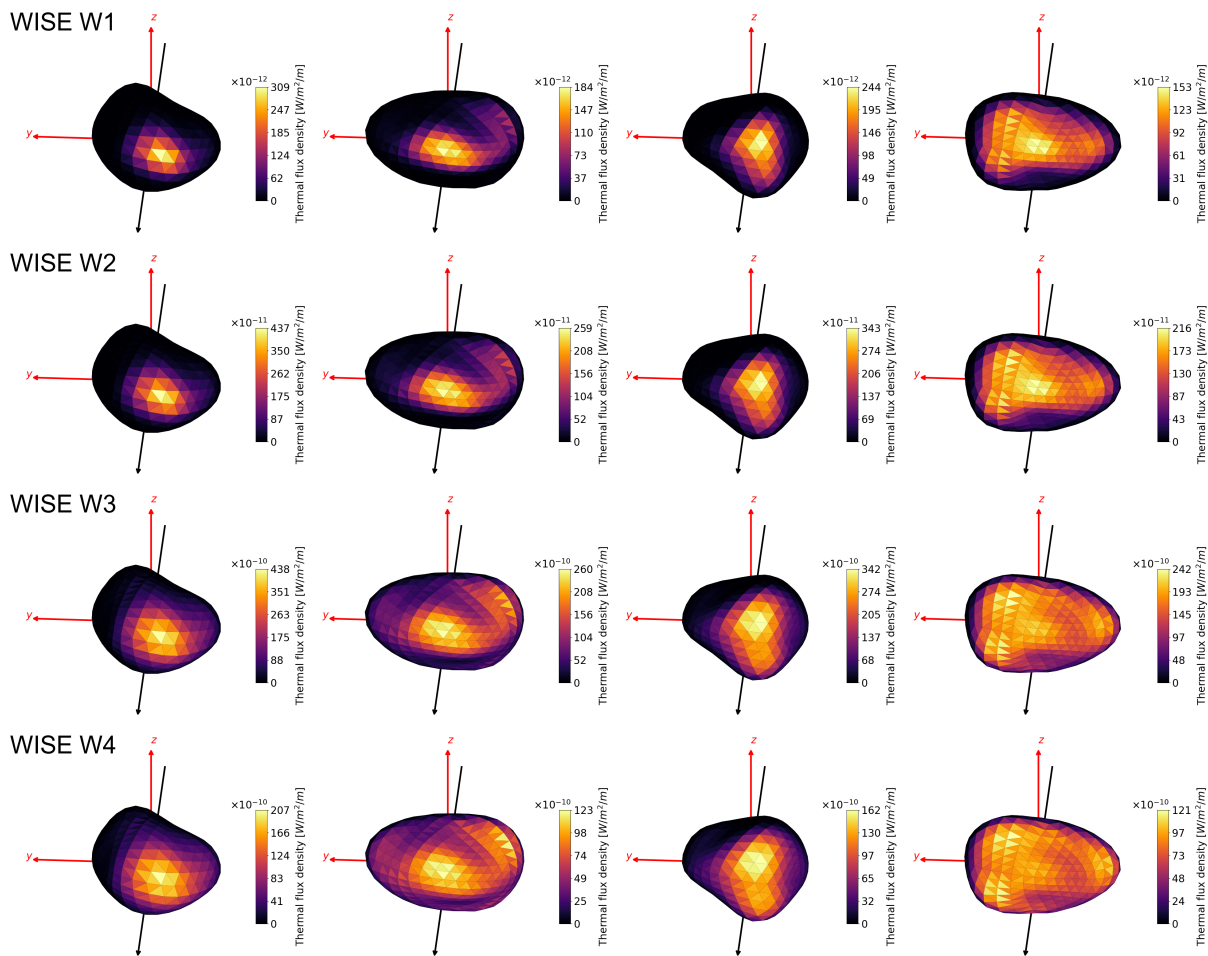
Figure 5.4.16: Thermal flux density distribution of 15 Eunomia at rotational phases 0.2, 0.5, 0.75 and 0.95 across the four WISE bands.
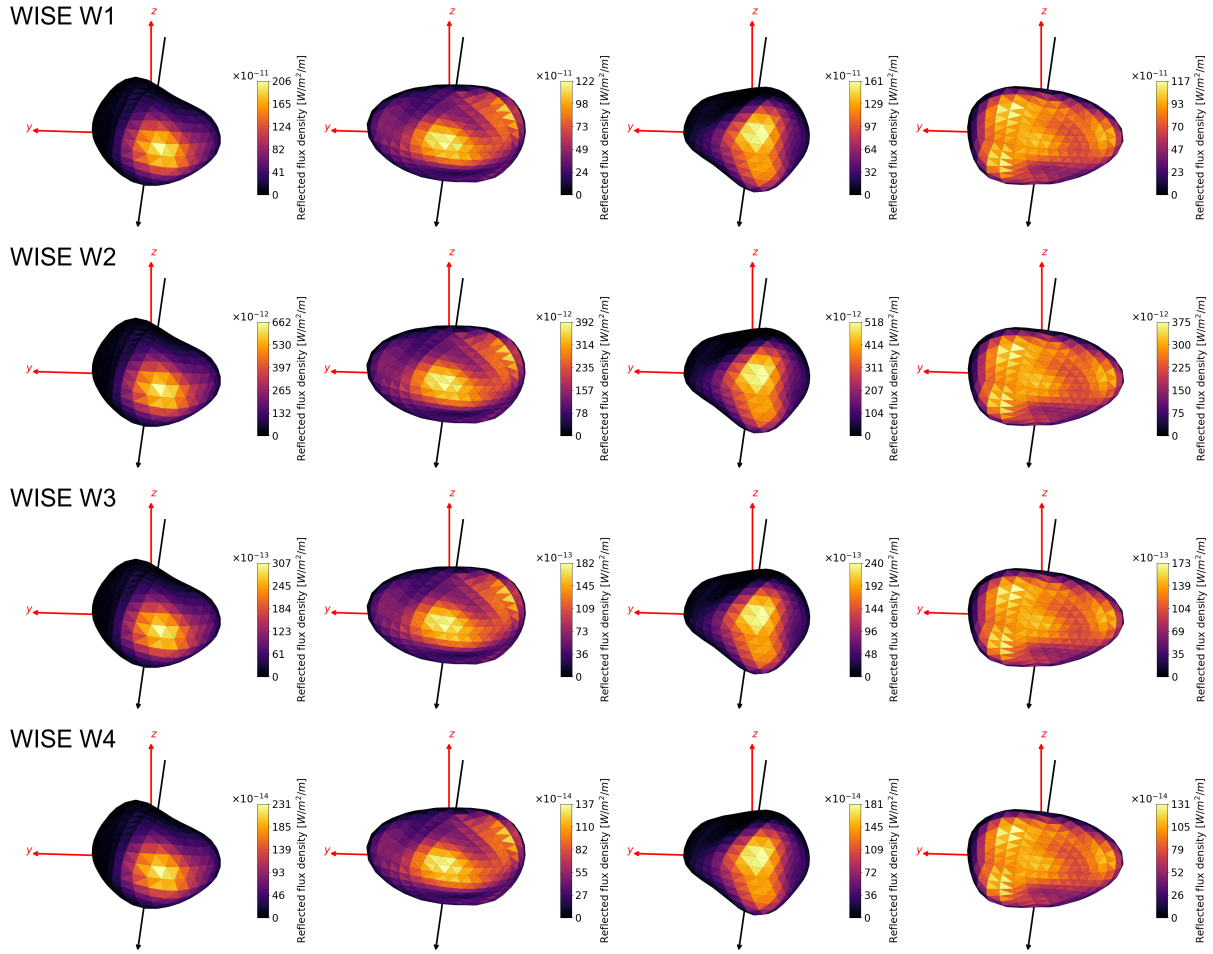
Figure 5.4.17: Reflected flux density distribution of 15 Eunomia at rotational phases 0.2, 0.5, 0.75 and 0.95 across the four WISE bands.

Now focusing on the influence of the heterogeneous albedo distributions, where the two facet albedo values used for 15 Eunomia's case are 0.1189 and 0.0987, which are respectively 7.2% and 11.0% higher and lower than its visible bond albedo at 0.1109. Naturally again when the relatively higher albedo is in view, the corresponding region in view of that albedo value shifts the reflected fraction upwards as can be seen in for instance mosaic 2's case between RPs 0.5-0.8, and the contrary applies when the relatively lower albedo at RPs 0-0.4 is in view. As mosaics 2 and 3 have their albedo distribution maps vary perpendicular to the spin axis as seen in Figure 5.3.3, they naturally will create the most variation in the reflected fraction as well, where at W1 they raise the reflected light percentage by up to 0.6% seen at RPs of roughly 0.3 and 0.65, and lower it by about 1.5% at roughly RP 0.95. At W2, the reflected percentage is increased by about 1.5% at RPs 0.3 and 0.65, and decreased by less 3.3% at RP 0.25, and at W3 and W4, the increase and decrease are negligible given the already low fraction of reflected light, however they do occur around the same RP regions in both cases. It can be observed again in this case that the biggest change occurs at W2 suggesting that a change in albedo has a greater influence at that wavelength region. Furthermore, it can be seen that the reflected light percentage increase and decrease with respect to the homogeneous albedo case across the four WISE bands are not similar given that the thermal and reflected flux density do not behave in a linear manner, and are affected by the Planck function. However, when looking at the mean of the reflected percentages, as summarised in Table 5.4.1, the difference between the homogeneous and the heterogeneous albedo distributions (and between themselves) do not vary that much. At W1, they are within less than 0.5% of each other, at bandpass W2 within about 0.75%, and very close to each other at bandpasses W3 and W4.

Furthermore, the patterns in the reflected percentage for all four mosaics are nearly identical in W1 and W2, which can be explained by the fact that those two wavelengths are quite close to each other at about 3.4 and 4.6 microns, respectively. However, looking at the longer wavelengths of W3 and W4, there is a significant

change in the reflected percentage pattern, especially in the case of mosaics 2 and 3, whereas the patterns from mosaics 6 and 8 continue to closely follow the reflected percentage of homogeneous case across all four bands. This shift in pattern for mosaics 2 and 3 seems to be caused by the surface albedos having a stronger influence on the reflected fraction than the shape at higher wavelengths. This is supported by looking at the effective facet area of each albedo value in view, and seeing if it matches at the corresponding RPs. Hence, comparing the patterns in Figure 5.4.5 and Figure 5.4.6, to the effective facet area in view found in Figure E.1.2 and Figure E.1.3 for mosaics 2 and 3 respectively, it seems that there is an agreement between when the highest albedo value in view with the highest shift in the reflected percentage, and vice versa. More specifically, in the case of mosaic 2, it can be seen that when the higher albedo of 0.1189 is in view between the RPs of about 0.4-0.9, the highest reflected percentage is also achieved. In the case of mosaic 3, it can be seen that the higher albedo of 0.1189 is in view between RPs of about 0.1-0.6, the highest albedo is dominating. The contrary holds when the lower albedo of 0.0987 is dominating the view.

Comparing the reflected percentage patterns made by mosaics 2 and 3 between bandpasses W3 and W4, it can be seen that the pattern in W4 matches most with the effective facet areas in view of the relatively higher albedo value in each case, as seen in Figure E.1.2 and Figure E.1.3. It seems that the small dips in the maximum reflected percentage of mosaics 2 and 3 present at W3 are due to the shape of 15 Eunomia, where this is confirmed by looking at the homogeneous reflected percentage curve [green] which can be used to disentangle the reflected light contribution of the shape from the contribution of the distributed surface albedos of the four mosaics. The dips match the local minimas in the homogeneous case, which is due to shape effects. Ultimately, the investigation carried out here points out that the shape of the asteroid has a considerable effect on the amount of reflected light in the observable flux density, especially at the first two WISE bandpasses, where a possible explanation is due to the varied surface temperatures in view which influences the thermal flux density differently for different wavelength regions due to Wien's displacement law. Furthermore, at the last two bandpasses, the distributed surface albedos (or the different surface albedo values themselves) seems have a greater impact on the reflected percentage. Lastly, it was seen that the greatest change in both the reflected percentage due to the different surface albedo values and the shape of 15 Eunomia itself occurred at bandpass W2. In the following section 5.4.2, it will be explored if the same findings are obtained but for a different asteroid.

5.4.2. Influence on 216 Kleopatra

The percentage of reflected light in the case of asteroid 216 Kleopatra at the respective four WISE bands are illustrated in Figure 5.4.18 to Figure 5.4.21. The reflected light percentage produced by a homogeneous surface albedo of $A_\nu = 0.0568$, which was also used earlier in Section 5.3.2, times its corresponding R_{IR-Vis} in the relevant WISE band is also plotted in solid green for reference. It should be noted that mosaics 2, 3 and 4 were the closest matching to the observation, and not the light curve with a homogeneous albedo from the previous section. Hence, a match in reflected percentage between those three mosaics to that of the homogeneous case should not be expected to occur here. Mosaic 11 only had a partial match for about half of its rotation around the mid-RP with the light curve of the homogeneous surface albedo, thus this partial match is expected to occur here too. The two albedo values used in the facet albedos of the four mosaics in this case are 0.0488 and 0.0696, as was determined in Section 5.3.2. The minimum, maximum, and mean percentages of reflected light in the total flux density of the various surface albedo distributions under investigation across the four WISE bands are summarised in Table 5.4.3.

Reflected light percentage in total flux density vs rot. phase of 216Kleopatra
r_{as} = 2.19 AUs, r_{ao} = 1.2 AUs, α = 7.52°, Bandpass W1

Reflected light percentage in total flux density vs rot. phase of 216Kleopatra
r_{as} = 2.19 AUs, r_{ao} = 1.2 AUs, α = 7.52°, Bandpass W2
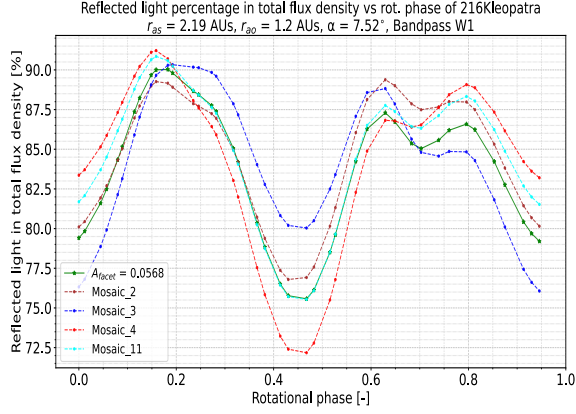
Figure 5.4.18: Percentage of reflected light in total flux density at bandpass W1 of 216 Kleopatra using orbital parameters from DAMIT #8 Kennedy & Tholen (1982). Percentage curves correspond to mosaics 2, 3, 4, & 11. The reflected light percentage produced by a homogeneous facet albedo of A_v plotted in solid green for reference.
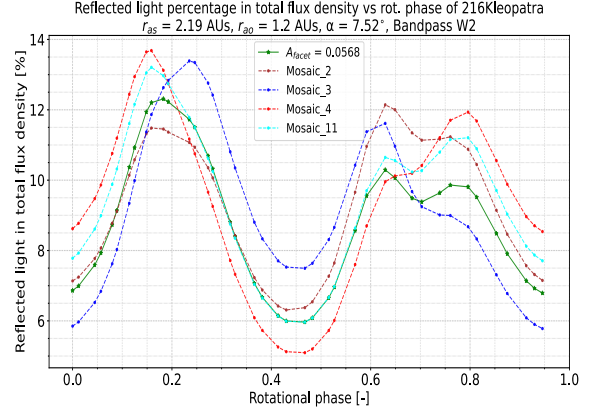
Figure 5.4.19: Idem as Figure 5.4.18 but at bandpass W2.

Reflected light percentage in total flux density vs rot. phase of 216Kleopatra
r_{as} = 2.19 AUs, r_{ao} = 1.2 AUs, α = 7.52°, Bandpass W3

Reflected light percentage in total flux density vs rot. phase of 216Kleopatra
r_{as} = 2.19 AUs, r_{ao} = 1.2 AUs, α = 7.52°, Bandpass W4
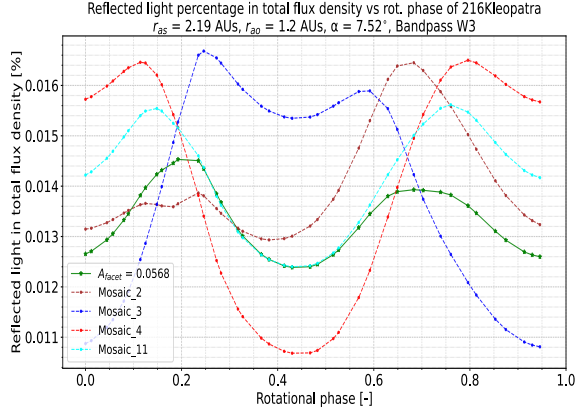
Figure 5.4.20: Idem as Figure 5.4.18 but at bandpass W3.
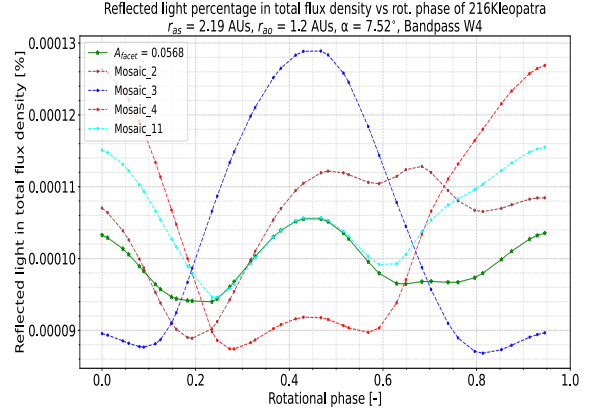
Figure 5.4.21: Idem as Figure 5.4.18 but at bandpass W4

Table 5.4.3: Summary of minimum, maximum, and mean percentages of reflected light in total flux density percentages of 216 Kleopatra for different surface albedo distributions across the four WISE bands.

Albedo distribution	Percentage of reflected light in total flux density [%]											
	W1			W2			W3			W4		
	Min	Max	Mean	Min	Max	Mean	Min	Max	Mean	Min	Max	Mean
Homogeneous	75.57	90.03	83.82	5.97	12.31	8.87	0.012	0.015	0.013	0.00009	0.00011	0.00009
Mosaic 2	76.79	89.38	84.52	6.31	12.14	9.25	0.013	0.016	0.014	0.00009	0.00011	0.00010
Mosaic 3	76.07	90.33	84.19	5.78	13.39	9.18	0.011	0.017	0.014	0.00009	0.00013	0.00010
Mosaic 4	72.18	91.22	84.34	5.10	13.68	9.45	0.011	0.017	0.014	0.00009	0.00013	0.00010
Mosaic 11	75.54	90.85	84.76	5.96	13.21	9.48	0.012	0.016	0.014	0.00009	0.00012	0.00011

As was the case in Section 5.2 and Section 5.4.1, the percentage of reflected light in total flux density decreases at longer wavelengths as can be seen in Table 5.4.3, or in Figure 5.4.18 to Figure 5.4.21. Concerning the homogeneous surface albedo case, at W1, the percentage of $F_{\text{refl.}}/F_{\text{tot.}}$ is varying between 75.6-90.0%, at W2 between about 6.0-12.3%, at W3 between 0.012-0.015%, and finally at W4 between about 0.00009-0.00011%. Given that in Section 5.2, no investigation of the Xe-type was carried out, it would difficult to have a direct comparison between the obtained reflected light percentages. It would be natural to want to compare it to its parent member, that is the X-type. However, even though the lower bound of visible geometric albedo of

X-types at 0.1 is close to the visible geometric albedo of 216 Kleopatra which is 0.1164 [63], it would make more sense to compare the case of 216 Kleopatra to the S-types given that they also share the same lower bound of albedos at 0.1, but also have closer matching R_{IR-Vis} factors, especially at the W1 and W2 bands. At the W3 and W4 bands, given that the trend of the extrapolated relative reflectances tend downwards, the R_{IR-Vis} factors get close to zero, and that is why the reflected percentages are even smaller in this case.

Given the orbital parameters of 216 Kleopatra has r_{as} = 2.19 AUs, the reflected percentages obtained here are roughly again in the same order of percentages as an IMB-i (found at 2.2 AUs) S-type asteroid at around 77-90%, 7-17%, < 0.09%, and < 0.02% for wavelengths regions W1 to W4, respectively. The reflected percentages of 216 Kleopatra are relatively quite high and close to the upper bounds produced by a visible geometric albedo of 0.22 for S-types, especially for the case of W1 and W2, which can be explained by Kleopatra's higher slope parameter at G = 0.29 [63] which is nearly twice as much as the standard one of G = 0.15 used in Section 5.2. At W3 and W4, 216 Kleopatra has a much lower R_{IR-Vis} at 0.65 and 0.05, respectively, explaining why the orders of magnitude of reflected percentages are smaller by a factor of 10 and 100 at W3 and W4.

Moreover, the range of reflected light percentages across the rotation of the asteroid shows again that even though the size of an asteroid does not have an effect on the fraction of reflected light as previously discussed, its shape does have an influence. In this case, given that 216 Kleopatra is more elongated than 15 Eunomia, more variation in the reflected percentage can be observed. Still focusing on the homogeneous case, at W1, the difference due to the shape of 216 Kleopatra is around 14.45%, at W2 around 6.34%, at W3 about 2.14×10^{-3}%, and at W4 around 1.15×10^{-5}%. In this case, it can be seen that the percentage difference is highest at W1 and not W2 as was previously the case in Section 5.4.1. The difference in W1 is more than twice that of W2. The difference can not potentially come from the heliocentric distance, since the previously investigated 15 Eunomia shares a similar heliocentric distance at r_{as} = 2.24 AUs. Perhaps the difference can come from the fact that 216 Kleopatra has a lower geometric albedo than 15 Eunomia, and/or also due to the fact that here the R_{IR-Vis} factor has a decreasing value from W1 to W4. Thus, due to the latter, the difference at W1 will be amplified by a higher corresponding R_{IR-Vis} factor. Moreover, at W3 and W4, even though the reflected light percentages themselves are negligible again, the difference in W3 is similar to that in W4 but two orders of magnitude higher. Here, the magnitude difference is by a factor of 100 whereas the difference for 15 Eunomia between W3 and W4 was by a factor of 10. This difference can be again explained by the fact that the R_{IR-Vis} factor at W4 is much smaller than in Eunomia's case.

It seems that the R_{IR-Vis} factor has an influence on where the shape of the asteroid has the greatest influence on the range of percentage reflected light. However, to ascertain whether the biggest difference in minimum and maximum reflected percentage is at bandpass W1 for 216 Kleopatra and at bandpass W2 for 15 Eunomia, in Appendix F.2, the reflected light percentage curves of 216 Kleopatra of Figure 5.4.18 to Figure 5.4.21 were re-plotted with a constant R_{IR-Vis} = 1 across all bandpasses, and the maximum difference in minimum and maximum reflected percentage was still achieved at bandpass W1. Hence, it seems that the lower albedo value of 216 Kleopatra is the one responsible for governing at which bandpass the biggest difference will occur. Te same thing was done for 15 Eunomia, where its reflected percentage curves were re-plotted with a constant R_{IR-Vis} = 1 across all bandpasses as seen in Appendix F.1, and the greatest difference in that case remained unchanged at bandpass W2. Hence, this strengthens the idea that the albedo itself has a greater influence than the R_{IR-Vis} factor in determining within which bandpass the greatest variation in minimum and maximum reflected light percentage will occur.

Interestingly again in the homogeneous surface albedo reflected curve, as can be seen in Figure 5.4.18 and Figure 5.4.21, there are three maximas and three minimas this time at only bandpasses W1 and W2 only, even though as was seen previously in their normalised reflected light curves in Section 5.3.2, only two of each were present which was influenced by the shape of the asteroid. Note at bandpass W4, there seems to be potentially a slight local maxima at RP 0.7 which would then render it having three pairs of minimas and maximas too. However, it is not as clear as in the first two bandpasses. Looking at the homogeneous albedo curve from W1 and W2, at around RP 0.15-0.2 there is a maxima in the reflected percentage curve, which corresponds to when the smaller side of the asteroid is in view. At around RP 0.45, there is now a minima in the reflected percentage curve, where this time it matches with when the larger side of the asteroid is in view. At RPs 0.6-0.65 and 0.8, there are two other maximas which do not correspond to any maximas or minimas really in the normalised reflected light curves seen in in Section 5.3.2. However, the local minima at RP 0.7 corresponds to the nor-

malised reflected light curve minima. Finally, the last reflected percentage minima at RP 0.95 is actually again when the other larger side of Kleopatra is in view. Hence, this time in the reflected percentage curves, the local minimas occur both times when the larger side of the asteroid is in view at bandpasses W1-W3.

Comparing the reflected percentage patterns in W3 and W4 again for the homogeneous surface albedo case, as seen in Figure 5.4.20 and Figure 5.4.21, it can be seen that apart from the flip in local minimas and maximas that occur again at W4, at those two wavelength regions, there are only two pairs of minimas and maximas, especially more apparent at bandpass W3 since the slight potential local maxima at RP 0.7 at W4 does not make it clear for the latter case. Nonetheless, the two pairs of minimas and maximas are found at nearly the same RPs as their corresponding counterparts at W1 and W2, that is RPs 0.2, 0.45, 0.7, and 0.95. Across bandpasses W1 to W4, since the additional minimas and maximas in the reflected light percentage curves occur for not only the heterogeneous but also the homogeneous surface albedo cases, the same phenomenon attributed to Wien's displacement law as was explored previously Section 5.4.1 seems to be happening here.

The thermal and reflected flux densities of 216 Kleopatra versus its rotational phase, across W1 to W4, are provided in corresponding pairs from Figure 5.4.22 to Figure 5.4.29 to again better understand the source of the new local maximas and minimas. As was the case in Section 5.4.1, it can be seen that the reflected flux density, illustrated in Figure 5.4.23 to Figure 5.4.29, has exactly the same light curve pattern throughout W1 to W4, where only the magnitude of the reflected flux density decreases from 10^{-8} to 10^{-12} $W/m^2/m$. In the case of the thermal flux density, the thermal light curve patterns change with the different wavelength bands under investigation, as expected and explained previously. In Figure 5.4.22 to Figure 5.4.28, it can be seen that the magnitudes of the thermal flux density increase from 10^{-8} at W1 to 10^{-7} at W4 and to 10^{-6} $W/m^2/m$ at W3. The highest total thermal flux density is actually reached at bandpass W3, which makes sense since most the temperature of 216 Kleopatra, found around 160-270 K, peak at that wavelength region. This was also seen in Eunomia's case, where even though the same magnitude of thermal flux density at 10^{-6} $W/m^2/m$ was reached for both bandpass W3 and W4, the mean of the total thermal flux density at W4 was about half that of W3.
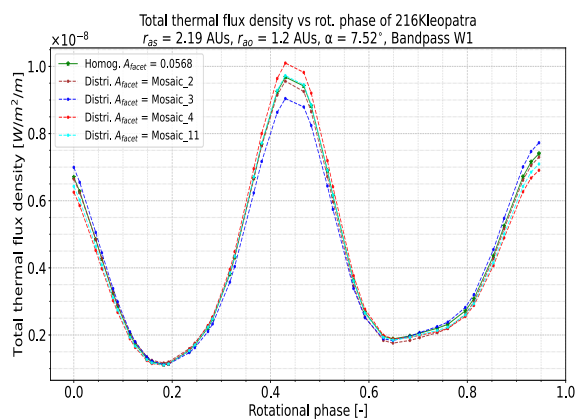
Figure 5.4.22: Thermal flux density at bandpass W1 of 216 Kleopatra against same parameters as in Figure 5.4.18. Light curves correspond to mosaics 2, 3, 4, & 11. Light curve produced by a homogeneous facet albedo of A_v plotted in solid green for reference.
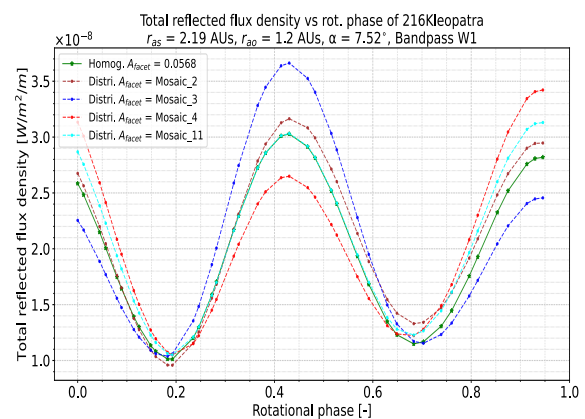
Figure 5.4.23: Reflected flux density at bandpass W1 of 216 Kleopatra against same parameters as in Figure 5.4.18. Light curves correspond to mosaics 2, 3, 4, & 11. Light curve produced by a homogeneous facet albedo of A_v plotted in solid green for reference.
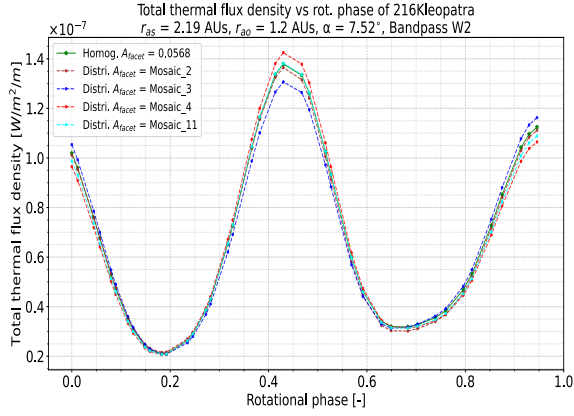
Figure 5.4.24: Idem as Figure 5.4.22 but at bandpass W2.
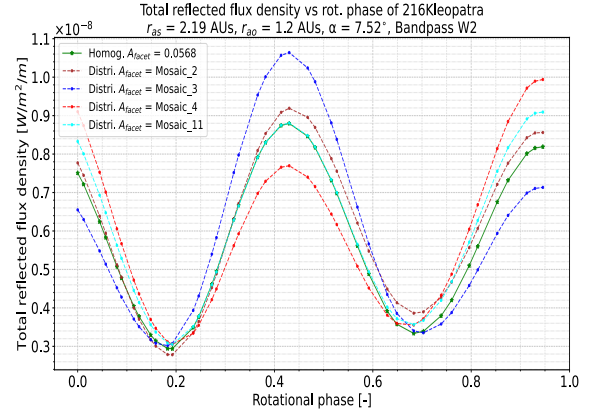
Figure 5.4.25: Idem as Figure 5.4.23 but at bandpass W2.
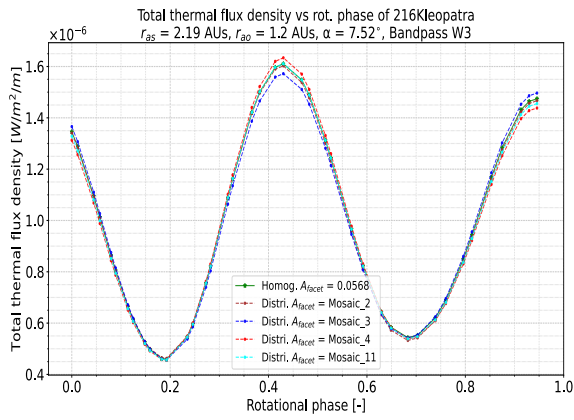
Figure 5.4.26: Idem as Figure 5.4.22 but at bandpass W3.
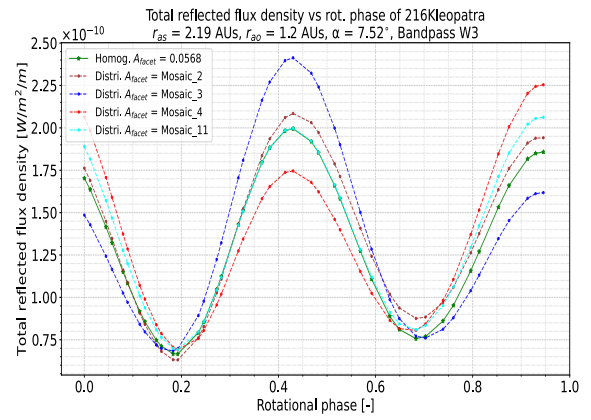
Figure 5.4.27: Idem as Figure 5.4.23 but at bandpass W3.
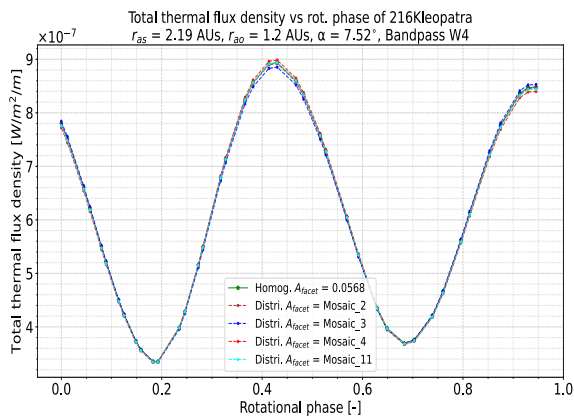
Figure 5.4.28: Idem as Figure 5.4.22 but at bandpass W4.
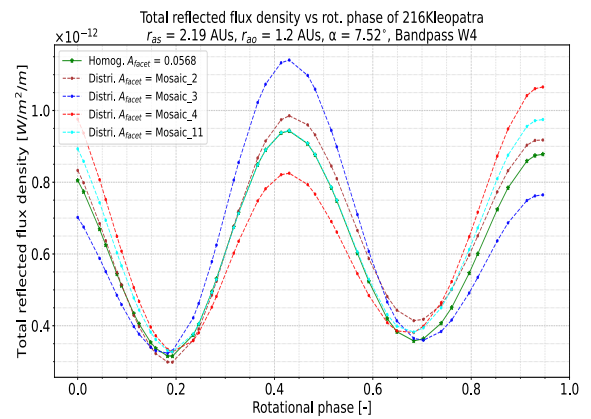
Figure 5.4.29: Idem as Figure 5.4.23 but at bandpass W4.

The two local maximas in the reflected light percentage curves between RPs 0.6 and 0.8 at bandpasses W1 and W2, as seen in Figure 5.4.18 to Figure 5.4.19, seem to be due to the fact that at the corresponding RP range in thermal flux density curves seen in Figure 5.4.22 and Figure 5.4.24 respectively, there is a wider trough compared to its reflected flux density trough, seen in Figure 5.4.23 and Figure 5.4.25, creating those local minimas and maximas. Furthermore, the same trough at bandpasses W3 and W4 seen in their corresponding thermal flux density curves, that is Figure 5.4.20 and Figure 5.4.21, become less flat and potentially explain why those local minimas and maximas seem to disappear at the longer wavelength bands.

Furthermore, to further strengthen the aforementioned points, the temperature and thermal flux density distributions, seen respectively in Figure 5.4.31 and Figure 5.4.30, of 216 Kleopatra with homogeneous surface albedo at the respective orientations producing the local minimas and maximas are given. As can be seen in Figure 5.4.30, the temperature distribution is about 230-269 K in the central region, and about 150-230 K in the outer regions since the normals of the latter facets are inclined away from the Sun direction. Looking at Table 5.4.2, it can be seen that the peak thermal emission will be around 10-12.5 microns for the 230-269 K facets, and for 150-230 K, around 13-19 microns. Thus, as can be observed in Figure 5.4.31, with increasing wavelengths from W1 to W4, more of the non-central regions are contributing towards the observable flux density. At W3, which has a wavelength center of about 12 microns, the facets with temperatures 230-269 K will contribute most, and at W4, the lower facet temperatures around 150-230 K, which are found at the outer regions will contribute most but will not peak in its emission since bandpass W4 'favours' lower temperatures of around 100-150 K.

Looking at W3 and W4 in Figure 5.4.31, Wien's law also explains why the highest thermal flux density in the central region of 216 Kleopatra is reached with a magnitude of 10^{-10} $W/m^2/m$ at RP 0.45 (second image), whereas at W4, a lower magnitude of 10^{-11} $W/m^2/m$ at the same RP is obtained, given that the central regions with facet temperatures between 230-269 K peak around 12 microns which is found in bandpass W3. The reflected light percentage decrease across W1 to W4 can be confirmed by also looking at the facet reflected flux densities illustrated in Figure 5.4.18. Here it can be observed that even with increasing wavelength, the same regions of the asteroid contribute towards the observable flux density, as was explained previously.
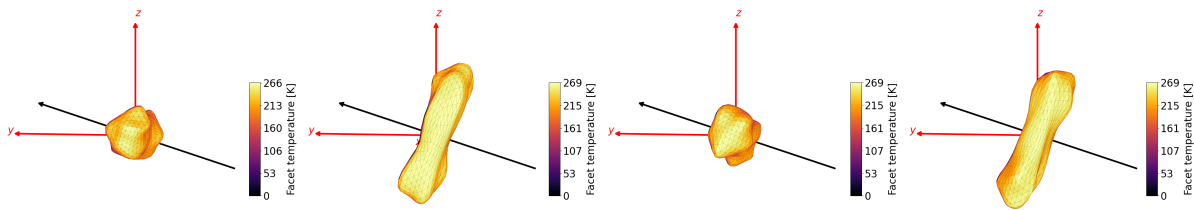
Figure 5.4.30: Facet temperature distribution of 216 Kleopatra at rotational phases 0.2, about 0.45, 0.7, and 0.95. These RPs correspond to computation intervals 12, 22, 32, and 41 across the four WISE bands.

86
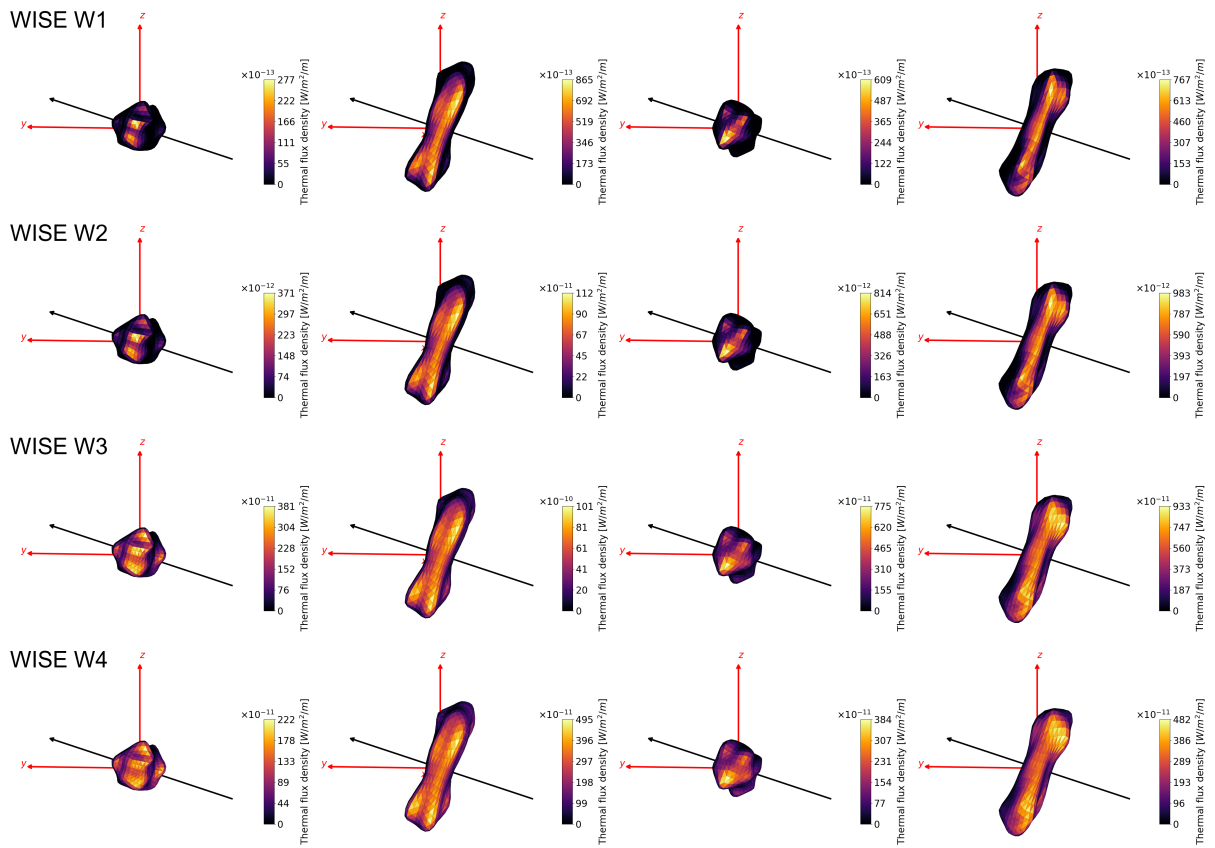
Figure 5.4.31: Thermal flux density distribution of 216 Kleopatra at RPs 0.2, about 0.45, 0.7, and 0.95 across the four WISE bands.
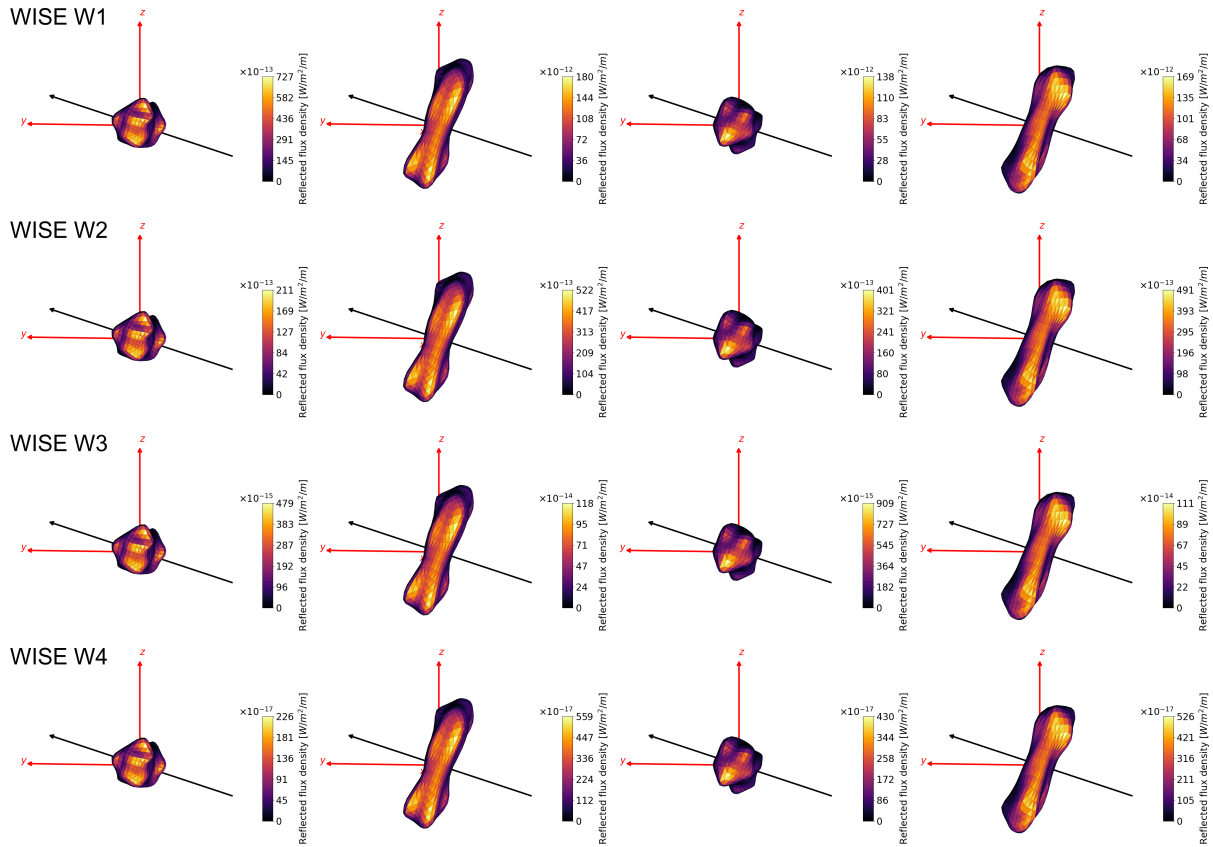
Figure 5.4.32: Reflected flux density distribution of 216 Kleopatra at RPs 0.2, about 0.45, 0.7, and 0.95 across the four WISE bands.

Focusing on the influence of the heterogeneous albedo distributions on 216 Kleopatra, where the two facet albedo values used are 0.0488 and 0.0696, which are 14.1% lower, and 22.5% higher relatively, than its visual Bond albedo of 0.0568. Again when the relatively higher albedo is in view, the corresponding region in view of that albedo value shifts the reflected fraction upwards as can be seen in mosaic 3's case between RPs 0.2 to 0.7, and the contrary applies when the relatively lower albedo is in view at the other RPs. Since all the mosaics have their albedo distribution maps vary mostly perpendicular to the spin axis as seen in Figure 5.3.10, they naturally will create the most variation in the reflected fraction as well, where at W1 they raise the reflected percentage by up to 4.5%, and lower it by about 3.5%, both at around RP 0.45. At W2, the reflected percentage is increased by about 1.75% at RP 0.25, and decreased by less than a percent at several regions, and at W3 and W4, the increase and decrease are again negligible given the already low percentage of reflected light but the maximum change are occurring around the mid RP region in both cases. Hence, it this case again, the greatest increase and decrease in reflected percentages are found at bandpass W1. This strengthens the previously mentioned point that bandpass W1 is more susceptible to percentage changes in its reflected percentage due to a change in albedo distribution. However, concerning the mean of the reflected percentages, as summarised in Table 5.4.3, the difference between the homogeneous and the heterogeneous albedo distributions (and between themselves) do not vary that much again. At W1, they are within less than half a percentage, whereas at W2 they are less than three quarters of a percentage difference between them, and since the reflected percentage is very small at W3 and W4, the difference in means are small too for the last two bandpasses.

Furthermore, the patterns in the reflected light percentage curves for all four mosaics are mostly similar between W1 and W2 again, given that those two bandpasses are rather close to each other. Looking at the longer wavelengths of W3 and W4, there is a significant change in the patterns of reflected light percentage curves, especially in the case of mosaics 2, 3 and 4, whereas the patterns from mosaic 11 continue to closely follow the reflected percentage of homogeneous case across all four bands at the middle region of its RP. As initially suggested in Section 5.4.1, this shift in pattern for mosaics 2, 3 and 4 seems to be caused by the distributed facet albedos having a stronger influence on the reflected light percentage than the shape at higher wavelengths. This is supported by looking at the effective facet area of each albedo value in view, and seeing if

it matches at the corresponding RPs. Hence, comparing the patterns in Figure 5.4.20 and Figure 5.4.21, to the effective facet area in view found in Figure E.2.2, Figure E.2.3, and Figure E.2.4 for mosaics 2, 3 and 4 respectively, it seems that there is an agreement between when the highest albedo value is in view with the highest shift in the reflected percentage, and vice versa, where it is especially most apparent at W4. More specifically, in the case of mosaic 2, it can be seen that when the higher albedo of 0.0696 is in view between the RPs of about 0.4 to 0.95, the highest reflected percentage is also achieved for those corresponding RPs. In the case of mosaic 3, it can be seen that when the higher albedo of 0.0696 is in view between the RP of about 0.2 to 0.65, the highest reflected percentage is dominating and actually closely following the same effective facet area plot seen in Figure E.2.3. The contrary holds when the lower albedo of 0.0488 is dominating the view, which can be seen with mosaic 4 which actually has its distributed surface albedo pattern flip from that of mosaic 3.

5.5. Influence of different ellipsoidal dimensions on the percentage of reflected light in the total observable flux density

In Section 5.4, it was previously observed that the combination of asteroidal shape influencing the surface temperature together with the effect of Wien's displacement law on the thermal flux density, all affect the amount of reflected light in the observable flux density. Asteroids can have very different shapes, where it would be unfeasible to investigate every shape. In general, asteroid shapes are idealised in two ways: as a sphere and as an ellipsoid. Since a sphere is invariant due to the nature of its shape, in addition to the fact that its influence on the percentage of reflected light in the total observable flux density of the four WISE bands was already carried out in Section 5.2, in this section, the influence of different ellipsoidal dimensions will be investigated. During the literature review, no concrete piece of literature was found which would indicate the general dimensions of an ellipsoidal asteroid, or the distribution of ellipsoidal shapes of asteroids. Hence, a sampling of some elongated/ellipsoidal asteroids was carried out in the JPL small-bodies database [62], where the following retrieved ellipsoidal dimensions are summarised in Table 5.5.1. They were all found to be oblate spheroids.

Table 5.5.1: Summary of various ellipsoidal dimensions sampled from JPL small-bodies database.

Asteroid	Dimensions [Km]	Normalised dimensions
216 Kleopatra	276x94x78	3.5x1.2x1.0
243 Ida	59.8x25.4x18.6	3.2x1.4x1.0
433 Eros	34.1x11.2x11.2	3.0x1.0x1.0
951 Gaspra	18.2x10.5x8.9	2.0x1.2x1.0
1620 Geographos	5.0x2.0x2.0	2.5x1.0x1.0
2063 Bacchus	1.11x0.53x0.50	2.2x1.1x1.0
4486 Mithra	2.35x1.65x1.44	1.6x1.5x1.0
25143 Itokawa	0.535x0.294x0.209	2.6x1.0x1.0

It should be noted that during the sampling process, numerous asteroids did not have an ellipsoidal dimension listed, since the differences between their three axes were too small, and an effective diameter was given instead, thus assuming a spherical body, which was the case of 15 Eunomia in the JPL database. From Table 5.5.1, it can be seen that most of the time the semi-minor axes b and c have about the same dimensions, whereas semi-major axis a is around 2-3 times bigger than the other two. Hence, besides a spherical body with dimensions 1.0x1.0x1.0, the following five general ellipsoidal dimensions were used for further investigation:

- 3.5x1.5x1.0

- 3.0x1.0x1.0

- 2.5x1.0x1.0

- 2.5x1.5x1.0

- 5.0x2.0x2.0

The last dimension of 5.0x2.0x2.0 was chosen since it is double that of 2.5x1.0x1.0. As was explained previously, the size of the asteroid itself does not matter on the reflected percentage, hence the resulting reflected

percentage curves of ellipsoids 2.5x1.0x1.0 and 5.0x2.0x2.0 should be identical, and provide supporting evidence for the aforementioned explanation. Moreover, for transparency, the asteroidal shapes are composed of 2000 facets, and the dimensions of the three axes were taken in kilometres.

For an initial high-level analysis, a choice has to be made on the heliocentric distance and albedo value, before a more detailed analysis will be carried out across different heliocentric distances and albedo values. Since the largest number of asteroids are MBAs, and the Bus-DeMeo C-type is the most abundant and usually found at a heliocentric distance of 2.8 AUs (OMB region) [59], those parameters are selected together with the upper bound of the visible geometric albedo range of C-type asteroids (i.e. 0.09). The corresponding R_{IR-vis} of C-types across W1-W4 is also applied, where they were already derived in Section 5.2. The standard value of the slope parameter $G = 0.15$, and the conventional bolometric emissivity $\varepsilon = 0.9$ were used here again. The phase angle is again kept at zero for previously mentioned reasons. Even though this will not have an effect on the results of the fraction of reflected light being investigated, for transparency, the observer distance is fixed at 1 AU. The reflected percentages of the different ellipsoids across the four WISE bands are illustrated in Figure 5.5.1 to Figure 5.5.4, where the minimum, maximum, and mean reflected percentages are summarised in Table 5.5.2. If the reader is interested in the actual thermal and reflected flux densities of the various ellipsoids under investigation, versus their rotational phase at the four WISE bands, they can refer to Appendix G.
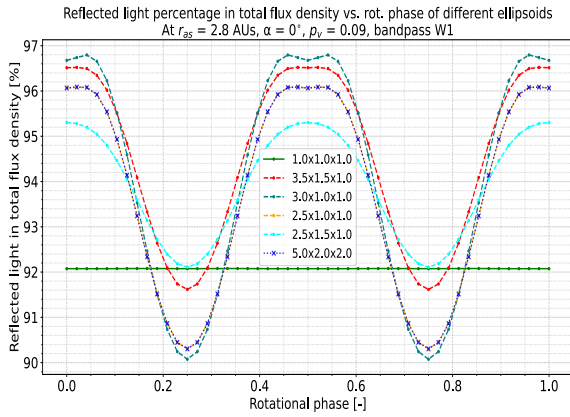
Figure 5.5.1: Percentage of reflected light in total flux density versus rotational phase of differently shaped ellipsoids, at bandpass W1. All curves have a homogeneous surface albedo of $p_v = 0.09$. Green curve corresponds to that of a sphere. Heliocentric distance $r_{as} = 2.8$ AUs. $\alpha = 0°$, $\varepsilon = 0.9$, and $G = 0.15$.
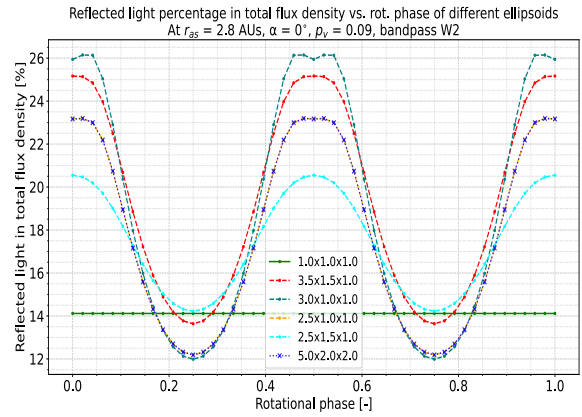
Figure 5.5.2: Idem as Figure 5.5.1 but at bandpass W2.
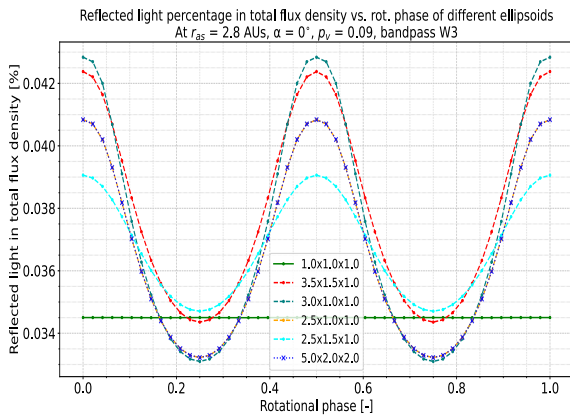
Figure 5.5.3: Idem as Figure 5.5.1 but at bandpass W3.
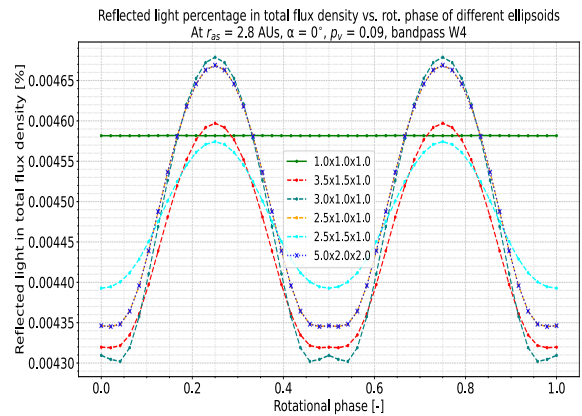
Figure 5.5.4: Idem as Figure 5.5.1 but at bandpass W4.

Table 5.5.2: Summary of minimum, maximum, and mean percentages of reflected light in total flux density of different spheroid dimensions across the four WISE bands.

Spheroidal dimensions	Percentage of reflected light in total flux density [%]											
	W1			W2			W3			W4		
	Min	Max	Mean	Min	Max	Mean	Min	Max	Mean	Min	Max	Mean
1.0x1.0x1.0	92.08	92.08	92.08	14.12	14.12	14.12	0.0345	0.0345	0.0345	0.00458	0.00458	0.00458
3.5x1.5x1.0	91.62	96.52	94.51	13.64	25.17	19.40	0.0344	0.0424	0.0379	0.00432	0.00460	0.00444
3.0x1.0x1.0	90.08	96.80	94.08	11.97	26.15	18.98	0.0331	0.0428	0.0373	0.00430	0.00468	0.00447
2.5x1.0x1.0	90.30	96.09	93.74	12.19	23.19	17.71	0.0332	0.0408	0.0366	0.00435	0.00467	0.00449
2.5x1.5x1.0	92.11	95.30	93.91	14.23	20.56	17.42	0.0347	0.0391	0.0368	0.00439	0.00457	0.00448
5.0x2.0x2.0	90.30	96.09	93.74	12.19	23.19	17.71	0.0332	0.0408	0.0366	0.00435	0.00467	0.00449

From Figure 5.5.1 to Figure 5.5.4, as was similar in Section 5.2, the percentage of reflected light significantly decreases from W1 to W4. A flip in maximas and minimas is still occurring at W4, as was seen initially in Section 5.4. This means that at bandpasses W1-W3, the smaller sides/aspects of the ellipsoid have relatively more reflected light, and at bandpass W4, the larger sides/aspects have relatively more reflected light. Furthermore, given the ellipsoids are symmetrical, it can be seen that the reflected percentage patterns are horizontally mirrored at RP 0.5. Moreover, as a sanity check, looking at just the spherical case [green curve], it can be seen in Figure 5.5.1 to Figure 5.5.4 that its reflected percentage curve is flat and confirmed by looking at Table 5.5.2 where its minimum, maximum, and mean reflected percentages are the same within each bandpass. This is expected since a sphere should have a constant flux density across its full rotation. Furthermore, comparing the reflected percentages of a sphere obtained here to the ones of MMB-o (equivalent to OMB-i since they share a heliocentric distance of 2.8 AUs) C-type asteroid with $p_v = 0.09$ in Section 5.2, it can be seen that the reflected percentages of 92.1%, 14.1%, 0.035%, and 0.005% of W1-W4 respectively are in good agreement with the ones listed in Table 5.2.1 for the aforementioned parameters. To better understand the shape of the ellipsoid and its effect on the surface temperature distribution which would have implications on the amount of reflected light in the observable flux density, two ellipsoids of dimensions 3.5x1.5x1.0 and 3.0x1.0x1.0, both with the same homogeneous surface albedo of $p_v = 0.09$ at $r_{as} = 2.8$ AUs, are given for reference in Figure 5.5.5. Their surface temperatures were computed using the same parameters found in Figure 5.5.1 to Figure 5.5.4.
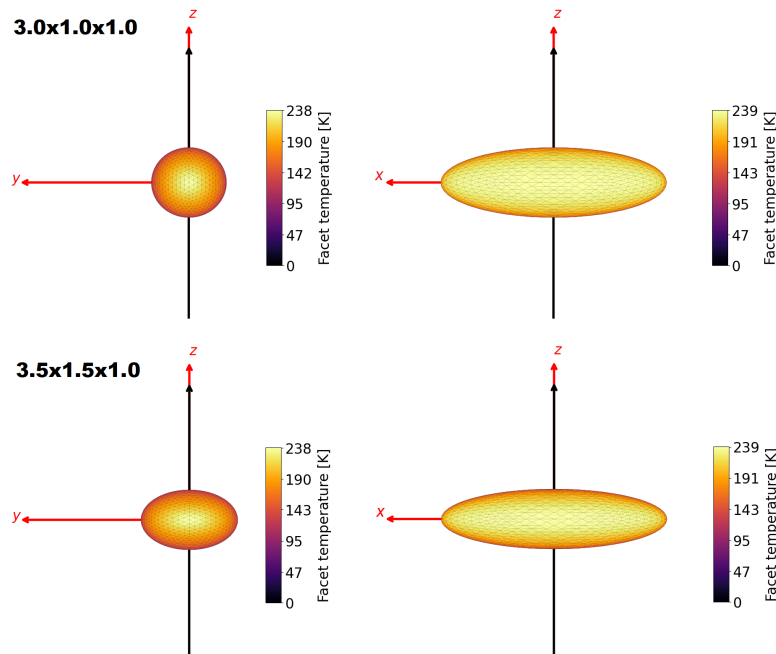
Figure 5.5.5: Left images: illustration of facet temperature distribution of smaller side/aspect (s.s.) of the ellipsoid, and right images shows corresponding facet temperature distribution on larger side/aspect (l.s.). Apart from dimensional differences, both ellipsoids have same parameters such as a homogeneous surface albedo with $p_v = 0.09$, and heliocentric distance of $r_{as} = 2.8$ AUs, the rest follows remaining parameters as used in Figure 5.5.1. Note the 3.0x1.0x1.0 and 3.5x1.5x1.0 ellipsoids are not to scale with each other, but only with themselves. Spin axis is the black arrow and follows the right-hand rule. The left images corresponds to the asteroid in view at RPs 0, 0.5, and 1.0, and the right images corresponds to the asteroid in view at RPs 0.25 and 0.75, in Figure 5.5.1 to Figure 5.5.4.

Moreover, in Figure 5.5.1 to Figure 5.5.4, it can be observed that the combined effect of a longer semi-major axis a and shorter semi-minor axis b produces the highest variation in reflected light percentage across the full rotation of an ellipsoid, as illustrated by the ellipsoid with dimensions 3.0x1.0x1.0 [teal curve]. Even though the 3.5x1.5x1.0 ellipsoid [red curve] has a relatively longer semi-major axis a than that of the 3.0x1.0x1.0 ellipsoid, the former also has a longer semi-minor axis b which causes a decrease in the percentage of reflected light achieved. This is because the longer semi-minor b axes of the 3.5x1.5x1.0 ellipsoid make the facets in that positive and negative axis direction less inclined away from the Sun and observer (that is facing them more), and thus have higher facet temperatures which lead to higher thermal flux densities and lower reflected percentages. This is confirmed when comparing the surface temperature distributions of the 3.0x1.0x1.0 and 3.5x1.5x1.0 ellipsoids found in Figure 5.5.5, where it can be seen that the 3.5x1.5x1.0 ellipsoid has a bigger region of higher surface temperatures.

Furthermore, the reflected light percentage pattern of the ellipsoid with dimensions 3.0x1.0x1.0 has small dips in its maximas at W1 and W2, and small upward kinks in its minimas at W4, and no such apparent effect at bandpass W3. They are all occurring when the smaller sides/aspects of the ellipsoid are in view. This phenomenon suggests that for those orientations, at bandpasses W1 and W2, there is relatively more thermal light, or relatively less reflected light, and the contrary applies at bandpass W4. However, it seems to be more likely due to a change in thermal emission than reflected light since the effect is not constant across all bandpasses. If the effect is due to thermal emission, it could be perhaps due again to Wien's displacement law and the effect of the facets' inclination towards the Sun and observer, where the more elongated and flat the ellipsoid is, the more thermal light would be present when the smaller sides are in view at bandpasses W1-W2. And relatively less thermal light will be present at bandpass W4, when the smaller sides are in view. In addition, the fact that this phenomenon is indeed not constant across all four bandpasses, and that according to Wien's displacement law, higher temperatures peak at lower wavelengths, seems to strengthen the possibility that this effect is due to the aforementioned explanation.

If attention is given to the apex of the maximas of ellipsoids 5.0x2.0x2.0 [crossed blue] and 2.5x1.0x1.0 [yellow curve] at bandpasses W1 and W2, it can be seen that there is also a slight dip in the maxima, and at bandpass W4, a slight upward kink. Furthermore, the fact that the ellipsoid with dimensions 3.5x1.5x1.0 has no apparent dips/kinks when the smaller sides are in view even though it has a longer semi-major a axis (which is however counter-acted by its longer semi-minor b axis making the outer facets less inclined away from the Sun and observer) supports this potential explanation due to Wien's displacement law coupled with the elongation + flatness of the ellipsoid. This possible explanation is further strengthened when looking at the thermal flux density graphs of the various ellipsoids, given in Appendix G. It can be seen from bandpass W1 to W4, that is from Figure G.0.1 to Figure G.0.7, the peaks for the most elongated ellipsoids are lowering and becoming flatter w.r.t. the other flux density curves, where it is most apparent with ellipsoid 3.0x1.0x1.0. It should be noted that to verify that the dips/kinks of the ellipsoid with dimensions 3.0x1.0x1.0 were not due to the number of facets of the base icosphere used in this case, the results were recomputed with an icosphere of 4500 and 8000 facets, and also with a UV sphere of 2000, 4500, and 8000 facets. The dips and kinks were still present at the same location and by approximately the same amount. Hence, the aforementioned explanation seems more likely.

In Figure 5.5.1 to Figure 5.5.3, it can be seen that the reflected percentage of the sphere is closer to the minimas of the ellipsoidal curves. At W4, the contrary applies, that is the green curve is closer to the maximas of the ellipsoids, due to the flip. This means that the larger sides of the ellipsoids are closer to behaving like spheres when only the reflected percentages are considered. This is perhaps due to the fact that the smaller sides of the ellipsoids have a more stretched out aspect visible to the observer as can be seen in Figure 5.5.5, where the outer non-central facets would have lower surface temperatures since their facets are inclined further away from the Sun. At the larger sides of the ellipsoids, there would be more facets less inclined away from the Sun, and thus the facets would have higher surface temperatures, and hence lower reflected light percentages. Furthermore, it is interesting to note that the ellipsoids with dimensions 2.5x1.5x1.0 [cyan curve] and 3.5x1.5x1.0 [red curve] have their minimas at W1-W3, and their maximas at W4, approach that of the spherical case [green curve]. Thus, it can be said that they behave similarly to spheres for those orientations, that is their larger sides, when only reflected light percentages are considered, and seems to be due to the fact that those two ellipsoids share the same semi-minor b value of 1.5 which effectively makes their elongation less extreme.

Interestingly, even though the reflected light patterns of the various ellipsoidal dimensions produce distinctive variations in maximas and minimas, their mean reflected percentage values of the ellipsoidal dimensions are not too far off from each other, and are within 2.4% at W1, 5.3% at W2, 3.4 $\times 10^{-3}$% at W3, and 1.4 $\times 10^{-4}$% from the mean of the sphere. The percentage difference in their mean is greatest at bandpass W2, suggesting that the shape of the ellipsoids has the greatest effect around the 4.5 microns region. This was also the case of 15 Eunomia as was seen Section 5.4.1, where due to only its shape, the homogeneous surface albedo's reflected percentage light curve had the biggest variation at W2. However, for 216 Kleopatra, the biggest variation in its reflected percentage light curve due to homogeneous surface albedo was found at W1 as was discovered Section 5.4.2. Hence, it does not look as straightforward that the greatest variation in reflected percentage due to shape effect occurs at W2. A potential explanation will be explored at the end of this section. Furthermore, as previously mentioned, the ellipsoid with dimensions 5.0x2.0x2.0 [crossed blue] is given to illustrate the point that the size of the asteroid does not matter in determining the reflected percentage. Since dimensions 5.0x2.0x2.0 is exactly twice that of 2.5x1.0x1.0 [yellow curve], the reflected percentage curves of those two dimensions match perfectly across all bandpasses, as seen Figure 5.5.1 to Figure 5.5.4, and also by looking at their minimum, maximum, and mean reflected percentages summarised in Table 5.5.2.

The ellipsoid with dimensions 3.0x1.0x1.0 raises the maximum reflected light percentage by 4.7% and lowers it by 2% at W1, raises it by 12.0% and lowers it by 2.2% at W2, raises it by 8.3$\times 10^{-3}$% and lowers it by 1.4$\times 10^{-3}$% at W3, and raises it by 1.0$\times 10^{-4}$% and lowers it by 2.8$\times 10^{-4}$% at W4. Naturally, it is more lowered than raised at W4 since the maximas and minimas have been flipped. Ultimately, for further investigation into how much the reflected light percentage would vary due to an ellipsoidal shape, at different heliocentric distances and for different taxonomic types, the ellipsoid with dimensions 3.0x1.0x1.0 is selected given that is produces the largest difference in both the minimas and maximas with respect to the spherical case. The percentage of reflected light in the total flux density across W1 to W4 for that selected ellipsoidal dimension are illustrated in Figure 5.5.6 to Figure 5.5.9. It should be noted that the summarised range of the reflected percentages were obtained from the maximum and minimum calculated reflected light percentages of the 3.0x1.0x1.0 ellipsoid at different heliocentric distances and for different surface albedos. If no dips/kinks were present, they were found to be at RPs 0, 0.25, 0.5, 0.75, and 1.0, that is when the smaller or larger sides/aspects were in view.
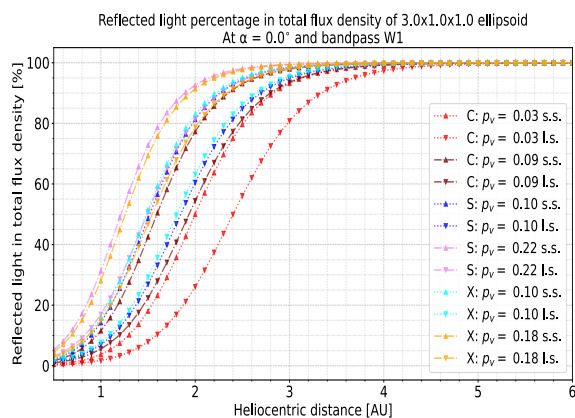
Figure 5.5.6: Percentage of reflected light in total flux density of a 3.0x1.0x1.0 ellipsoid, for various ranges of albedos per taxonomic type, across heliocentric distance, at bandpass W1. Downward pointing markers used for larger side (l.s.), and upward pointing markers for smaller side (s.s.). Note: $\alpha = 0°$, $\varepsilon = 0.9$, and $G = 0.15$.
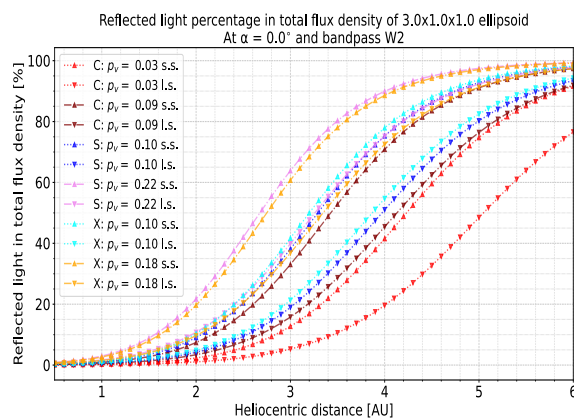
Figure 5.5.7: Idem as Figure 5.5.6 but at W2.
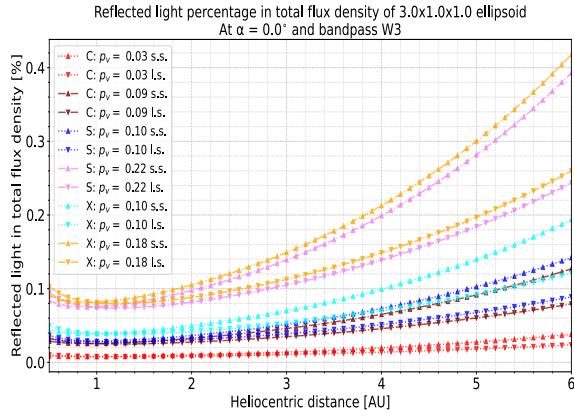
Figure 5.5.8: Idem as Figure 5.5.6 but at W3.
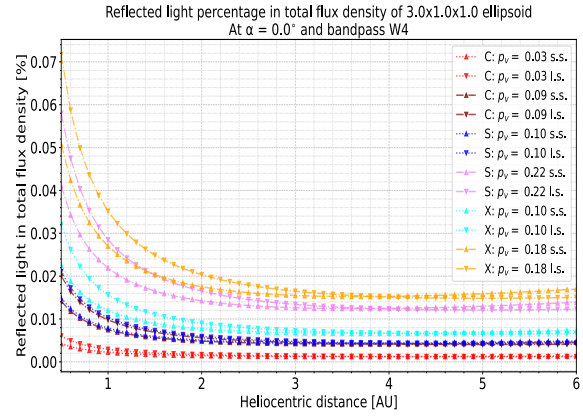
Figure 5.5.9: Idem as Figure 5.5.6 but at W4.

From Figure 5.5.6 to Figure 5.5.9, it can be seen that the reflected percentage curves for the different taxonomies behave mostly in the same way as in Figure 5.2.5 to Figure 5.2.8 for the spherical case seen in Section 5.2, that is there is an increase in reflected light with increasing heliocentric distance for bandpasses W1 to W3, and mostly a plateau with increasing heliocentric distance at W4. As a verification, at 2.8 AUs in Figure 5.5.6 to Figure 5.5.9, the reflected light percentage for a C-type with visible geometric albedo of 0.09 [brown curve] has a value for its respective larger and smaller sides of 90.1% and 96.8% at W1, 12.0% and 26.2% at W2, 0.033% and 0.043% for W3, and 0.004% and 0.005% at W4, which are all in good agreement with the values for the same parameters found in Table 5.5.2. Note, at W3 and W4, due to the scaling in the corresponding figures, this verification is not as apparent, but has been successfully verified numerically in all cases.

Naturally, as was seen in Figure 5.5.1 to Figure 5.5.3, the smaller sides/aspects will produce the most amount of reflected light in the total flux density, which is the case at W1 and W2, but partially the case at W3 and W4. At the longer two bandpasses, as seen in Figure 5.5.8 and Figure 5.5.9, it can be observed that there is a switch in the side/aspect producing the most reflected light at a certain heliocentric distance. At W3, below 1 AU, the larger side for every taxonomic type is producing a higher reflected light percentage. The same thing occurs at W4, but for heliocentric distances below 4 AUs. This also explains why there is a flip in maximas and minimas occurring for the previous investigation at bandpass W4 seen in Figure 5.5.4, since it is found below 4 AUs, and also in section 5.4, where the investigated 15 Eunomia and 216 Kleopatra were found at around 2.2 AUs. This suggests that at longer wavelengths, and for shorter heliocentric distances, since there are negligible amounts of reflected light at those wavelength regions and the thermal flux density itself is more dominant, the flip is potentially due to the latter. As was previously seen in Section 5.4, the outer non-central facets in view have lower surface temperatures (due to being inclined further away from the Sun), and start contributing more towards the observable flux density at W3 and W4, due to Wien's displacement law. Since the smaller sides of the ellipsoids have more non-central facets in view than the larger sides due to being more stretched as confirmed by looking at Figure 5.5.5, at longer wavelengths, the smaller sides will contribute more towards the thermal flux density relative to the larger sides. This is why the larger sides would have relatively more reflected light, where it is most apparent at shorter heliocentric distances as seen in Figure 5.5.8 and Figure 5.5.9.

Interestingly, it can be observed that in some cases, the smaller sides of the ellipsoid with a relatively lower albedo nearly matches the reflected light percentage of the larger sides of the same ellipsoid but with a relatively higher albedo value. This is most apparent at bandpasses W1 and W2 as seen in Figure 5.5.6 to Figure 5.5.7, where the smaller sides of X-type with $p_v = 0.10$ [cyan curve] and the smaller sides of S-type with $p_v = 0.10$ [blue curve] are around the same reflected percentages as that of the larger sides of their same taxonomic groups but for their relatively higher albedo values of X-type with $p_v = 0.18$ [yellow curve], and S-type with $p_v = 0.22$ [violet curve], respectively. Moreover, to better understand the increase and decrease in reflected light percentages due to the smaller and larger sides of a 3.0x1.0x1.0 ellipsoid, Figure 5.5.6 to Figure 5.5.9 were re-plotted with respect to the reflected light percentage computed for a sphere, for the three different taxonomic types, and various asteroids categorised by their heliocentric distances. The results are illustrated in

94

Figure 5.5.10 to Figure 5.5.13 for bandpasses W1 to W4, respectively. It can already be observed that at W3 and W4, even with an ellipsoid, the amount of reflected light in the observable flux density is still negligible where it is below 0.35% at W3, and below 0.04% at W4.
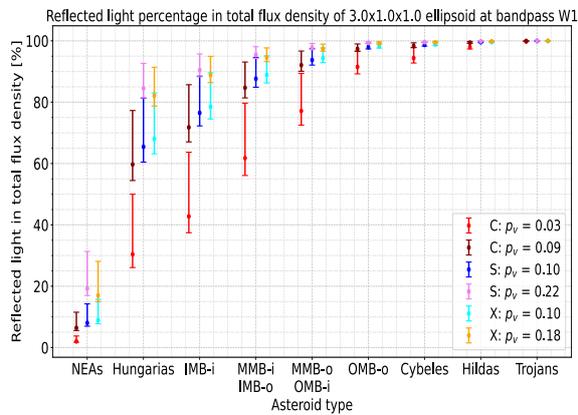
Figure 5.5.10: Effect of 3.0x1.0x1.0 ellipsoid on percentage of reflected light in total flux density for different asteroid types with various albedos within bandpass W1. Lower bar and upper bar are due to the larger side (l.s.), and smaller side (s.s.) of the ellipsoid, respectively. Middle point is obtained from a sphere of dimensions 1.0x1.0x1.0 for reference. Same parameters as in Figure 5.5.6.
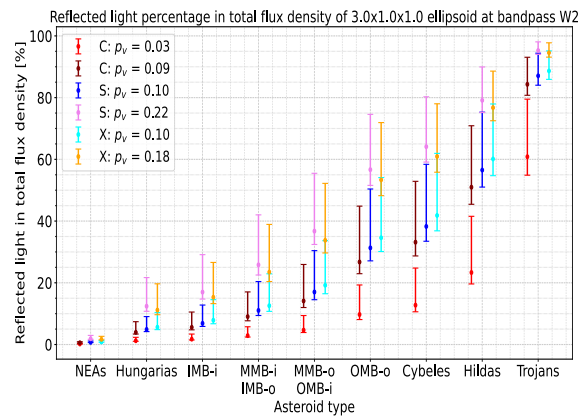
Figure 5.5.11: Idem as Figure 5.5.10 but at W2.
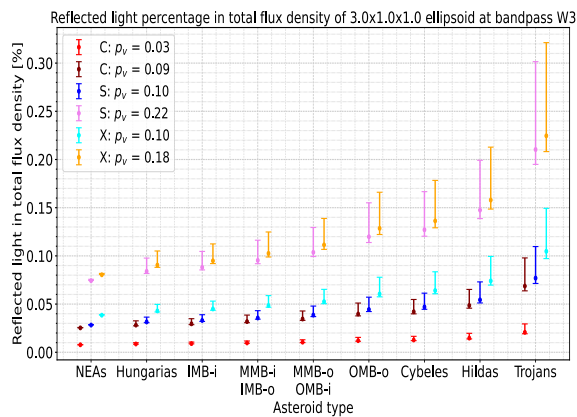
Figure 5.5.12: Idem as Figure 5.5.10 but at W3.
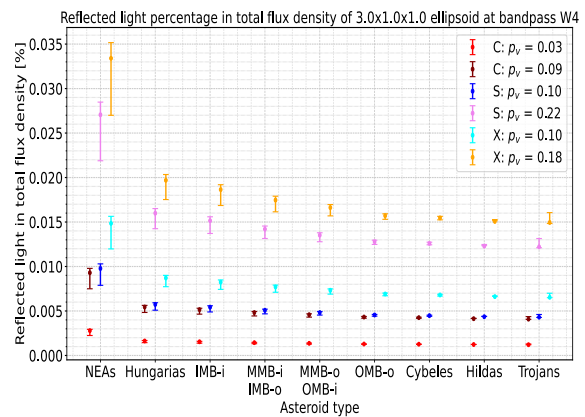
Figure 5.5.13: Idem as Figure 5.5.10 but at W4. Note due to the flip here, for NEAs to Cybeles, the upper bar is due to l.s., and the lower bar due to s.s. Contrary applies for Hildas and Trojans.

In general, from Figure 5.5.10 to Figure 5.5.13, it can be observed that naturally the smaller sides of the ellipsoid will produce the most increase in reflected light percentage, as seen from the length of the upward bars. Due to the flip occurring at bandpass W4, the smaller sides produce the greatest decrease in reflected percentage for NEAs to Cybeles, and the greatest increases for Hildas and Trojans. Furthermore, across different albedos and heliocentric distances, it can be seen that the larger sides of the ellipsoid are closer to producing the same reflected light percentage as a sphere, given that the lower bars (partially applicable at W4, where its the upper bars in this case for NEAs to Cybeles) are closer to the middle points. Moreover, at bandpass W1 and W2 as illustrated in Figure 5.5.10 and Figure 5.5.11 respectively, it can be seen that the smaller sides of some taxonomic types with lower albedo values are producing around the same reflected light percentage as the sphere but with a higher surface albedo. This can be especially seen in the case of X-types for NEAs to Cybeles, where the upper cyan bar of $p_v = 0.10$ is around the same value as the middle yellow point of $p_v = 0.18$. The S-types seem to be also producing the same relationship, but mostly at W1 and for a fewer number of asteroid types.

Since the maximum increase in the amount of reflected light in the total flux density is more compelling when wanting to find out if an ellipsoidal shape needs to account for reflected light, the focus will be given to that, and to which asteroid type it occurs per bandpass. From Figure 5.5.10, at bandpass W1, for C-types with a visible geometric albedo of 0.03, the largest increase in reflected light percentage due to an elongated shape is 20.9%, and occurs at the inner IMB region. For C-types with a visible geometric albedo of 0.09, it is 17.6%, and occurs at Hungarias. For S-types with $p_v = 0.10$ it also occurs at Hungarias, and is 15.9%. For S-types with $p_v = 0.22$, it is 12.1%, and occurs at NEAs. Finally, for X-types with $p_v = 0.10$, it is 15.0%, and occurs at Hungarias. For X-types with $p_v = 0.18$, it is 11.1%, and occurs at NEAs. Overall for bandpass W1, the maximum increase occurs for C-type asteroids with $p_v = 0.03$ in the inner IMB region with a change of about less than 21%. Furthermore, in general apart for the NEAs, it seems that the highest increase in reflected percentage occurs at shorter heliocentric distances and for the lower albedo values of each taxonomic type. Moreover, just for reference, the maximum decrease in reflected light is about 3-6% where it is greatest for C-types with $p_v = 0.03$, and found at the outer IMB region which actually has a closely similar percentage decrease as the inner IMB region.

At bandpass W2, as shown in Figure 5.5.11, for C-types with $p_v = 0.03$, the largest increase in reflected light percentage is by 18.7% occurring at the Trojan asteroid region. For C-types with $p_v = 0.09$, it is 19.9%, and is found at the Hildas. For S-types with $p_v = 0.10$, it is 20.1%, and occurs at the Cybeles. For S-types with $p_v = 0.22$, it is 18.8%, and occurs at the inner OMB region (outer MMB). Finally, for X-types with $p_v = 0.10$, it is 20.1%, and occurs at the Cybele's asteroid group. For X-types with $p_v = 0.18$, it is 18.6% and occurs at the outer OMB region. In general for bandpass W2, the maximum increase occurs this time for both S-type asteroids with $p_v = 0.10$, and X-type asteroids with $p_v = 0.10$, and both at the Cybeles region where the increase is about 20%. It should be noted that C-types with $p_v = 0.09$ have about the same percentage increase of 19.9%, and occurs at Hildas. The common parameter seems to be a relatively lower visible geometric albedo of around 0.1. Furthermore, it is interesting to see that bandpasses W2 and W1 have around the same percentage increase in their amount of reflected light at around 20% due to the ellipsoidal shape but for different albedo values and at different heliocentric distances/asteroid types. Moreover, in general, it seems that the highest increase in reflected percentage occurs this time at longer heliocentric distances and for the higher albedo values of each taxonomic type. However, as from the Hildas and Trojans, the highest increase is mostly due to the lower albedo values. Moreover, just as reference, the maximum decrease in reflected light is around 5-6%, where it is again greatest for C-type with for $p_v = 0.03$, and around the same asteroid region as its respective maximum increase occurring, that is the Trojan region.

From Figure 5.5.12, that is at bandpass W3, in general the maximum percentage increase occurs with the longest heliocentric distance, hence for the Trojan asteroids in this case as was also previously seen in Section 5.2, and for the relatively higher albedo values of their taxonomic range. This is confirmed by also looking at the diverging curves occurring with increasing heliocentric distance as seen in Figure 5.5.8. For C-types with $p_v = 0.03$, the largest increase in reflected light percentages is around 0.009%. For C-types with $p_v = 0.09$, it is 0.029%. For S-types with $p_v = 0.10$, it is 0.033%. For S-types with $p_v = 0.22$, it is 0.091%. Finally, for X-types with $p_v = 0.10$, it is 0.045%, for X-types with $p_v = 0.18$, it is 0.097%. Overall for bandpass W3, the maximum increase occurs this time for X-type asteroids with $p_v = 0.18$ at the Trojan asteroid region with an increase of less than 0.1%. It should be noted that S-type asteroids with $p_v = 0.22$ have nearly similar percentage increase too. This is again perhaps due to having around the same relatively higher geometric albedo of about 0.2. Moreover, just as reference, the maximum decrease in reflected light due to the other side of the ellipsoid is around 0.001-0.016% where the highest decrease is due to X-type with $p_v = 0.18$, and all occurred at the Trojan asteroid region too. Moreover, it should be noted that the smaller and larger sides of the ellipsoid at the NEA region are actually having their change in percentage of reflected light very close to each other, but in all taxonomic types, the smaller sides are marginally responsible for the greatest change in reflected light.

Now, at bandpass W4 as seen in Figure 5.5.13, the contrary holds where the maximum change occurs with the shortest heliocentric distance, hence for NEAs in this case, and for the relatively higher albedo values of their taxonomic range. This is in agreement with what was previously seen in Section 5.2, where the biggest difference in reflected percentages were for those parameters. Furthermore, the maximum increase at bandpass W4 as from 4 AUs, which concerns Hildas and Trojans, is still due to the smaller sides of the ellipsoid. Where actually for Hildas, the difference is minor between the two sides of the ellipsoids, and the smaller sides

have a marginally higher value. For the other asteroid types, all found below 4 AUs, the maximum increase is due to the larger sides of the ellipsoid. Since there is a flip in minimas and maximas occurring for all asteroid types except Hildas and Trojans, the decrease is more substantial than the increase in the reflected light percentage as the decrease is being governed by the smaller side. However, since the increase in percentage reflected light is the limiting factor to know if reflected has to be taken into account, the focus will be given to it. For C-types with $p_v = 0.03$, the largest increase in reflected light percentages is around 0.0001%. For C-types with $p_v = 0.09$, it is about 0.0005%. For S-types with $p_v = 0.10$, it is around 0.0005%. For S-types with $p_v = 0.22$, it is around 0.0014%. Finally, for X-types with $p_v = 0.10$, it is about 0.0008%. For X-types with $p_v = 0.18$, it is around 0.0017%.

Note that the increases occurring at the Trojan region due to the smaller sides are not too far off from the increases occurring at the NEA region due to the larger sides. For instance, for the higher albedo values of each taxonomic group, the percentage increase at the Trojan region for the C-, S-, and X-types respectively they are 0.0003%, 0.0009%, and 0.0011%. Moreover, just for reference, the maximum decrease in reflected light due to the smaller side of the ellipsoid occurring especially at the NEAs is around 0.0005-0.006% where the highest decrease is due to X-type with $p_v = 0.18$. Thus, in general for bandpass W4, the maximum increase occurs again for X-type asteroids with $p_v = 0.18$ for NEAs with around a value of 0.002%.

The findings found in this section actually explains why in the case of 15 Eunomia investigated in Section 5.4.1, due to its shape, the reflected percentage difference due to the homogeneous surface albedo light curve had the biggest variation at bandpass W2. When comparing Figure 5.5.10 versus Figure 5.5.11, it can be seen that at the IMB-i region ($r_{as} = 2.2$ AUs), at bandpass W1, the greatest variation in the S-type is for its relatively lower albedo, and the contrary applies at bandpass W2, where the greatest variation is for the relatively higher albedo. This is also why the initial analysis carried out here for the case of a C-type asteroid with geometric albedo of 0.09, seen in Figure 5.5.1 to Figure 5.5.4, had its greatest variation in its maximum and minimum reflected percentages at bandpass W2 too. Even though in this case it is found at OMB-i (MMB-o) region ($r_{as} = 2.8$ AUs), the C-type has its greatest variation for its relatively higher albedo at bandpass W2. Furthermore, this aforementioned explanation is further strengthened, since in the case of 216 Kleopatra as investigated in Section 5.4.2, the biggest variation in reflected percentage of its homogeneous light curve was found at bandpass W1 this time. However, since 216 Kleopatra has a relatively lower geometric albedo of 0.1164, When comparing Figure 5.5.10 versus Figure 5.5.11 at the IMB-i (MMB-o) region, at bandpass W1, the largest variation in the reflected percentage occurs for relatively lower albedos.

6
Conclusion

The main research question of this master thesis was to investigate *"the contribution of reflected light to the observable flux density of the four WISE bands, using an intermediate asteroid thermal model, that properly combines thermal and reflected light modelling?"*. This was successfully carried out through various steps, which will be first summarised. In Chapter 2, after an initial explanation of the scientific background concerning asteroids, the motivations for thermal modelling were also presented. Furthermore, after simple and advanced thermal models were explored, the proper modelling of reflected light through Kirchhoff's law was explained, and sub-question 1 was addressed. That is, what parameters affect the amount of reflected light in the observable flux density? They were found to be the albedo, the heliocentric distance, and the thermal property of the asteroid such as its emissivity. The created model to address the research question, named the Asteroid Thermal and Reflected light Model (ATRM), was presented in Chapter 3.

Moreover, an extensive verification and validation of the ATRM was carried out in Chapter 4. The thermal flux density validation was done against convex-shaped PHA 101955 Bennu where a relatively small percentage difference of 7.5% against the reference model was found between the obtained thermal flux densities. A potential correction to the surface temperatures on night-side of Bennu due to the limitation of ATRM at large phase angles was also explored, and a relatively good match with the reference thermal light curve was achieved after a certain factor was applied. The reflected flux density validation was carried out against the catalogued DAMIT observation data of near-convex shaped MBA 15 Eunomia, and more complex-shaped MBA 216 Kleopatra. Given the relative intensities being used by DAMIT due to the unknown magnitude zero point of the observations, the Lambertian scattering law used by the ATRM was implicitly validated when comparing it to the weighted Lommel-Seeliger-Lambertian scattering law used by DAMIT (to inversely derive its asteroid 3D shape models). This validation also confirmed that the ATRM is properly taking into account the frames of orbital reference, and the spin modelling of the asteroids.

After a successful verification and validation, sub-question 2 was addressed in Chapter 5, where initially in Section 5.2, a high-level investigation was pursued to quantify the amount of reflected light from a spherical asteroid for different heliocentric distances and homogeneous surface albedo values. The albedo values were categorised by the three most common taxonomic types, that is the C-, S-, and X-types where around more than 95% asteroids fall within them, and have an overall range of 0.03 to 0.22 concerning their visible geometric albedo. It was seen that the fraction of reflected light is most significant at bandpasses W1 and W2 of the WISE bands, which confirms the findings of Myhrvold, given that W1 and W2 are at the lower wavelengths of about 3-5 microns where reflected light has a greater contribution. At W1, it was found that the NEAs have around 2-19% reflected light in the observable flux density, MBAs can have around 43% to nearly 100%, and Trojans have purely reflected light with regards to the higher albedo values. At W2, depending on their reflectances, NEAs can have 0.2-1.7%, MBAs can have 2-57%, and Trojans have 61-95%. Interestingly, depending on the application and parameters of the asteroids, this suggests that the thermal modelling of NEAs can neglect the reflected light contribution at bandpass W2. Moreover, for any combination of heliocentric distances and surface albedos investigated, the reflected light percentages were found to be below 0.3% at bandpass W3, and below 0.04% at bandpass W4, which confirm why thermal models do not take into account reflected light

at longer wavelengths since they are considered negligible towards the observable flux density. In general, at bandpass W1 to W3, it was seen that the percentage of reflected light increased with increasing heliocentric distance, and at W4, it plateaued for increasing heliocentric distance.

Furthermore, it was also seen that if a bolometric emissivity of 0.8 or 1.0 was taken instead of the commonly assumed $\varepsilon = 0.9$ in the surface temperature calculation, the resulting reflected percentage can change by different amounts at different heliocentric distances for the four bandpasses. At W1, the maximum change of less $\pm 12\%$ occurs around the IMB region for C-type asteroids with visible geometric albedo $p_v = 0.03$. At W2, the maximum change occurs again for the same type of asteroid but this time at the Trojan asteroid region with a change of no more than $\pm 12.5\%$. Given that the reflected light was negligible at W3 and W4, the effect of using an emissivity of 0.8 or 1.0 did not have any significant impact on the reflected fraction, where they remained below the initially found percentages of 0.3% at W3, and 0.04% at W4. However, it is interesting to note that the greatest change at W3 and W4 occurred for asteroids with relatively higher albedos in this case, and at opposite ends of their heliocentric distances. That is, at W3, the maximum change was at the Trojan asteroid region, and at W4, it was at the NEA region.

In Section 5.4, an investigation of heterogeneous surface albedos on the amount of reflected light in the observable flux density was also undertaken. Instead of randomly varying the surface albedo distribution of any asteroid or idealised asteroid shape, an attempt was made under the Lambertian scattering law of the ATRM, to vary the surface albedo distribution of 15 Eunomia and 216 Kleopatra, so that their derived light curves would better match the observed data. A perfect match was not achieved, but some potential albedo maps with interesting behaviours were found and further investigated in the different WISE bands. It was shown that for a given orbital and rotational geometry, a certain heterogeneous albedo map could be mistaken for one having a homogeneous distribution which was most apparent in mosaic 6 of 15 Eunomia's case. Four albedo maps of 15 Eunomia and 216 Kleopatra deemed interesting were selected, and their influence to the reflected light was also investigated in the four WISE bands which addressed the third and last research sub-question.

Furthermore, it was seen that even though the size of an asteroid does not have an effect on the reflected fraction, the shape does, where in both cases the shape had a greater influence on the difference of reflected percentages than the previously derived distributed surface albedos themselves, especially at the shorter two bandpasses. 216 Kleopatra being more elongated had wider ranges in its reflected percentage than 15 Eunomia. Moreover, the distributed surface albedos kept behaving mostly in the same way especially at bandpasses W1 and W2 which had rather similar reflected patterns given that their bandpass wavelengths are close to each other. At W3 and W4, the reflected percentage curves seemed to be more affected by the relatively higher albedo values in view. Furthermore, a potential explanation for the extra minimas and maximas seen in the reflected light patterns was explored through Wien's displacement law. Finally, a flip in the local minimas and maximas was present at W4 in both 15 Eunomia and 216 Kleopatra's cases, but could not really be justified.

Through the previous investigation of those two asteroids, it was actually discovered that the shape of the asteroid can have a substantial effect on the reflected fraction across the four WISE bands. Since investigating every asteroidal shape is not practical, to have a general overview of this effect, a high-level investigation of different ellipsoidal dimensions sampled from various elongated asteroids was carried out in Section 5.5, where an ellipsoid of dimensions 3.0x1.0x1.0 was found to produce the most variation in its reflected fraction which was attributed to the fact that it was the most elongated + flat out of the sampled dimensions. This ellipsoid was further investigated across different heliocentric distances and surface albedo values where it was found that the maximum change in reflected fraction due to the shape of the ellipsoid at bandpass W1 was found to be for C-type asteroids with $p_v = 0.03$ in the IMB region which produced an increase of 20.9%. At bandpass W2, the maximum increase was due to S- and X- type asteroids at their lower albedo value of $p_v = 0.10$, and were found at the Cybeles region with an increase of 20.1%. Moreover, at bandpass W3 and W4, the maximum change was again relatively negligible since the reflected light itself is negligible at these wavelengths bands, and were found to around the earlier obtained percentages of 0.3% and 0.04%, albeit relatively higher than in the previous cases. The same relationship also occurred where, the changes in their reflected percentages were highest at the Trojan region for W3, and at the NEA region for W4. This investigation actually address sub-question one again, since another parameter affecting the contribution of reflected light to the total flux density was found, that is the shape of the asteroid.

7

Recommendations & Future works

Due to time and computational constraints, this master thesis project leaves some room for improvements and future works. Since the ATRM is only an intermediate thermal and reflected light model, most of the recommendations will be with respect to adapting the ATRM and making it a more advanced modelling tool. With a more advanced thermal and reflection modelling tool, the percentage of reflected light in the total flux density can be investigated for different parameters related to advanced models. Thus, the following recommendations are identified for any future works related to this project:

- Introduce heat conduction into the numerical code, whereby the assumptions of instantaneous thermal equilibrium and no thermal emission on the night-side are no longer needed. Initial attempts were made to do so, where the ATRM can compute the initial temperature condition, which is taken to be the mean equilibrium temperature of a facet over one rotation period. However, due to time and computing constraints, the Neumann boundary condition could not be implemented accurately beyond the thermal skin depth since a 'ghost point' was needed. Hence, a convergence in the final surface temperature could not be achieved. The methodology to do so has already been presented upon in Section 2.4. A potential alternative was explored in Section 4.5, where the mean equilibrium temperature was scaled and replaced to facets having zero temperatures or below a certain temperature threshold. Under the conditions that 101955 Bennu was, the derived scaled thermal light curves of the ATRM were closely matching the ones of Emery et al.'s. However, given that this was only applicable for those conditions, it was not explored beyond this point.

- Once thermal conduction is taken into account, the ATRM will no longer be limited to small phase angles. Then, the relationship between the fraction of reflected to the total observable flux density for different phase angles, and different thermal inertias, can be explored into more depth. However, it is predicted that the fraction of reflected to total flux density will decrease with increasing phase angle, as was already explained in Section 5.2.

- Extend the ATRM to complex non-convex shaped asteroids, with deep extrusions and long protrusions. This can be done by advanced shadowing algorithms such as a robust and time-efficient ray-tracing method to make sure that contributing facets are the ones which are being properly illuminated by the Sun and visible to the observer. Furthermore, by modelling more complex-shaped asteroids, multiple scattering and self-heating effects need to be modelled too as explained in Section 2.4, which are all computationally intensive.

- Implement surface roughness in the numerical code. Advanced thermal models do this placing a hemispherical crater at the center of each facet, which is found to be representative of the macro-surface roughness of an asteroid [77]. This will however double the computation time. Also, the actual depth and size of those craters need to be optimised for proper macro-surface roughness modelling. However, taking into account surface roughness in thermal flux density computation puts into question the validity of assuming a Lambertian surface. If a particular surface is too rough, the reflection/emission is longer perfectly diffused, but directional or directionally diffused.

- Introducing surface roughness in thermal modelling naturally allows the reflected flux density modelling to also take it into account. Lambertian scattering which is generally good for relatively brighter surfaces is no longer needed, where for example, an advanced scattering law such as that of Hapke's model [25] which takes into account surface roughness can be implemented and be more representative of the behaviour of an asteroid's surface under reflected light.

- A more tangent recommendation would be to model the Yarkovsky and YORP effects to be geared towards asteroid deflection for planetary protection or mining purposes. This means accurate orbital mechanics need to be taken into account, and other orbital perturbations also should be included to make sure the resulting Yarkovsky and YORP effects are a result of those two, and not the other effects. Then, the asteroid deflection technique of 'painting' parts of an asteroid which effectively changes the asteroid's surface albedo distribution could be implemented to alter the Yarkovsky and YORP effects and influence its orbital trajectory and spin state.

Appendices

A

Flux density conversions

For validation purposes, the thermal and reflected flux densities computed by the ATRM need to be converted to other units of concern, to match the observed/external data for proper comparison. These conversions are summarised here.

Converting SI spectral flux density from $W/m^2/m$ to Jansky (Jy) units is given by Equation (A.0.1), where λ is the wavelength at which the spectral flux density is being modelled/observed, and c is the speed of light in vacuum [64]. This conversion is especially useful for the validation of the thermal flux density.

$$F_{\lambda, \, Jy} = F_{\lambda, \, SI} \cdot 10^{26} \cdot \frac{\lambda^2}{c} \tag{A.0.1}$$

Converting SI spectral flux density from $W/m^2/m$ to the non-SI $erg \; s^{-1} \; cm^{-2} \; \mathring{A}^{-1}$ is given by Equation (A.0.2), where erg is a unit of energy equal to 10^{-7} joules, and $\mathring{A}$ is an angstrom unit which is a metric unit of length equal to $10^{-10} m$ [64].

$$F_{\lambda, \, non-SI} = F_{\lambda, \, SI} \cdot (c \cdot 10^{13}) \cdot \left(\frac{\lambda}{\lambda_{\mathring{A}}} \right)^2 \tag{A.0.2}$$

Once the spectral flux density has been converted to the non-SI $erg \; s^{-1} \; cm^{-2} \; \mathring{A}^{-1}$, using Equation (A.0.3) it can be further converted to magnitude units [17] [48]:

$$F_{\mathrm{mag}} = -2.5 \cdot \log_{10}(F_{\lambda, \, non-SI}) - \text{arbitrary shift} \tag{A.0.3}$$

For validation of the reflected flux density, which uses light curves from DAMIT [19], using Equation (A.0.4), the magnitude units are further converted to intensity units [17]:

$$F_{\mathrm{int}} = 10^{-0.4 \cdot F_{\mathrm{mag}}} \tag{A.0.4}$$

B

Relative spectral response function
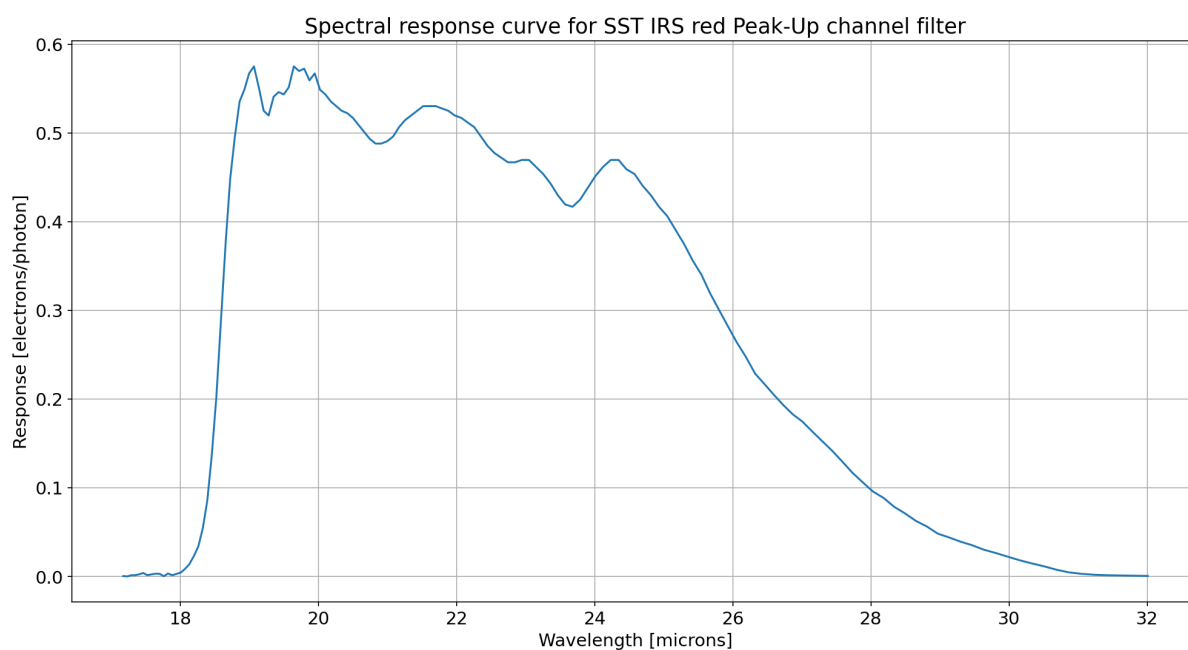
Figure B.0.1: SST IRS PUI red filter spectral response function [3].
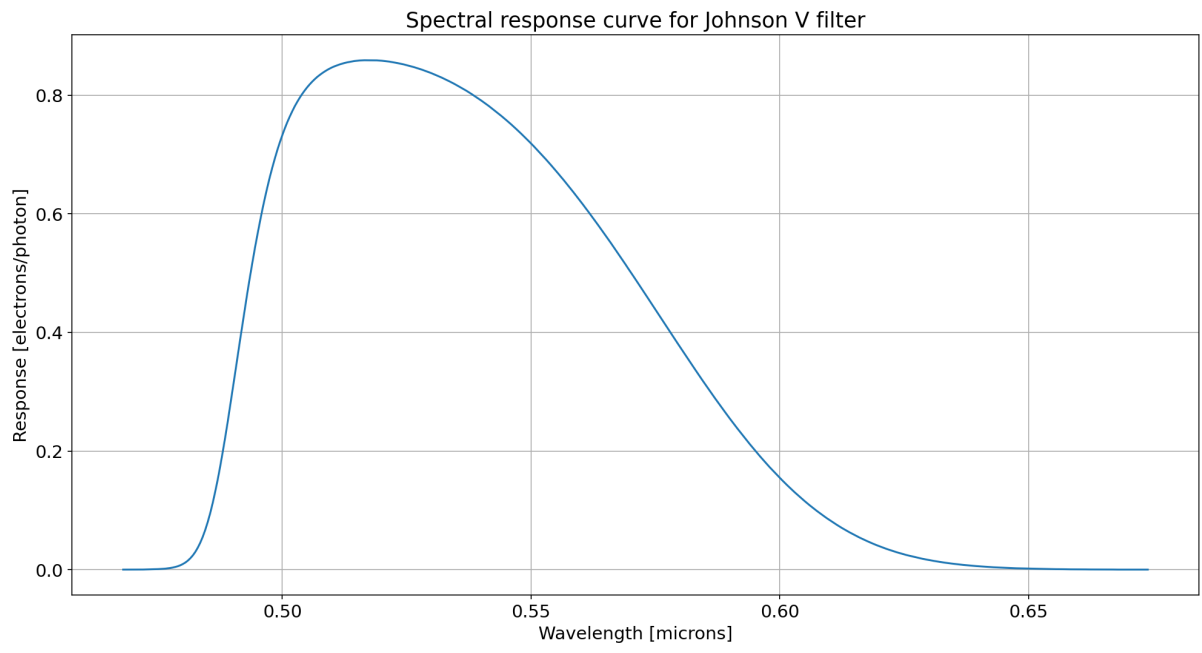
Figure B.0.2: Johnson-V filter spectral response [74].

C

Precise reflected light percentage contribution at W1-W4

Table 5.2.1 has been re-tabulated here to include the lower bounds of the reflected light percentages found at bandpasses W3 and W4. Please find table next page.

Table C.0.1: Summary of minimum and maximum percentages of reflected light in total flux density of various asteroids across heliocentric distance and Bus-DeMeo taxonomic type. NEAs: near-Earth asteroids, IMB-i: inner heliocentric distance of inner main-belt asteroids, MMB-i/MMB-o: inner and outer heliocentric distance of middle main-belt asteroid, OMB-o: outer heliocentric distance of outer main-belt asteroids. Note that MMB-i intersects with IMB-o, and MMB-o intersects with OMB-i, and hence have not been reproduced in the table.

Asteroid type	r_{as} [AU]	W1			W2			W3			W4		
		C	S	X	C	S	X	C	S	X	C	S	X
NEAs	~1	2.0-6.4	8.0-19.2	8.9-17.0	0.2-0.6	0.7-1.9	0.8-1.7	0.008-0.025	0.028-0.074	0.038-0.080	0.003-0.009	0.010-0.027	0.015-0.033
Hungarias	2	30.4-59.7	65.5-84.5	68.0-82.1	1.2-4.0	4.9-12.4	5.6-11.1	0.009-0.028	0.031-0.084	0.043-0.090	0.002-0.005	0.006-0.016	0.009-0.020
IMB-i	2.2	42.8-71.8	76.5-90.4	78.5-88.8	1.7-5.6	6.8-17.0	7.9-15.3	0.009-0.030	0.033-0.088	0.045-0.095	0.002-0.005	0.005-0.016	0.008-0.019
MMB-i	2.5	61.8-84.7	87.6-95.4	88.8-94.6	2.9-9.0	11.0-25.8	12.6-23.5	0.010-0.032	0.036-0.095	0.048-0.103	0.001-0.005	0.005-0.014	0.008-0.017
MMB-o	2.8	77.1-92.1	93.7-97.8	94.4-97.4	4.7-14.1	17.0-36.7	19.2-33.8	0.010-0.035	0.039-0.104	0.053-0.111	0.001-0.005	0.005-0.014	0.007-0.017
OMB-o	3.3	91.5-97.4	98.0-99.3	98.2-99.2	9.7-26.7	31.3-56.7	34.6-53.4	0.012-0.040	0.044-0.120	0.060-0.129	0.001-0.004	0.005-0.013	0.007-0.016
Cybeles	~3.5	94.4-98.3	98.7-99.6	98.8-99.5	12.7-33.2	38.3-64.1	41.8-60.9	0.013-0.042	0.047-0.127	0.064-0.136	0.001-0.004	0.005-0.013	0.007-0.015
Hildas	4	98.0-99.4	99.5-99.9	99.6-99.8	23.3-51.0	56.5-79.1	60.1-76.7	0.015-0.049	0.054-0.147	0.074-0.158	0.001-0.004	0.004-0.012	0.007-0.015
Trojans	5.2	99.8-99.9	100	100	60.9-84.3	87.1-95.3	88.6-94.6	0.021-0.069	0.077-0.210	0.105-0.225	0.001-0.004	0.004-0.012	0.007-0.015

Minimum and maximum percentages of reflected light in total flux density [%]

D

Influence of η and G on percentage of reflected light in WISE bands.

D.1. Effect of beaming parameter η
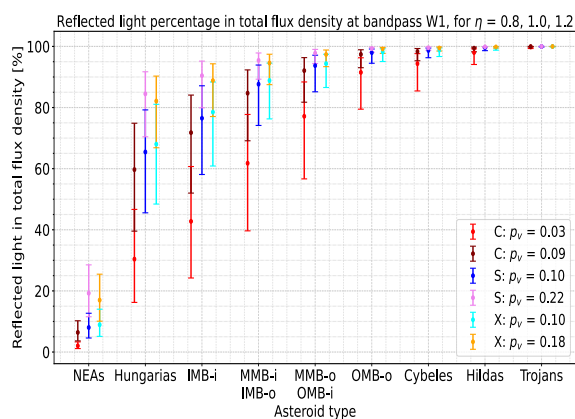
Figure D.1.1: Effect of η on percentage of reflected light in total flux density for different asteroid types with various albedos within bandpass W1. Lower bar is due $\eta = 0.8$, upper bar is due to $\varepsilon = 1.2$, and middle point is due $\eta = 1.0$. Note: $\alpha = 0°$, $\varepsilon = 0.9$, and $G = 0.15$.
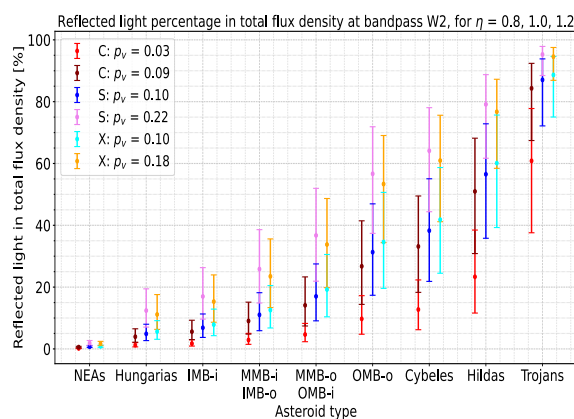
Figure D.1.2: Idem as Figure D.1.1 but at W2.
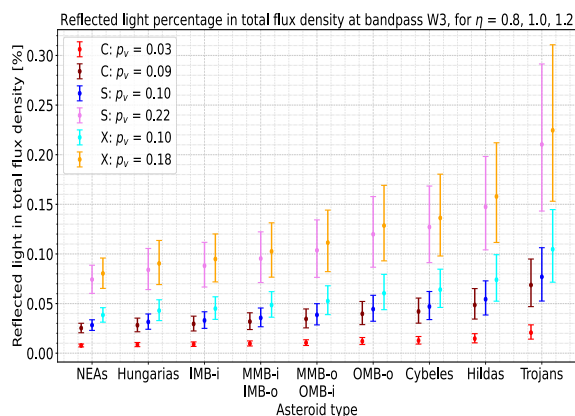
Figure D.1.3: Idem as Figure D.1.1 but at W3.
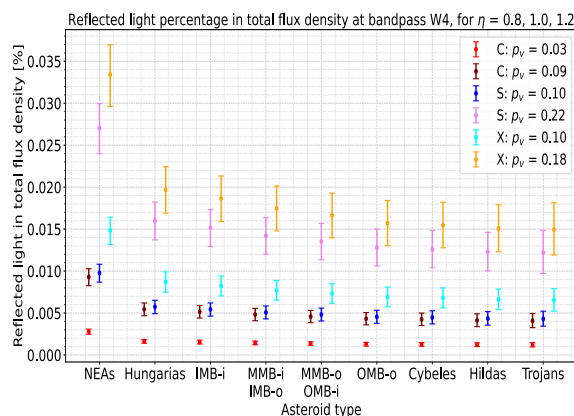
Figure D.1.4: Idem as Figure D.1.1 but at W4.

D.2. Effect of slope parameter G
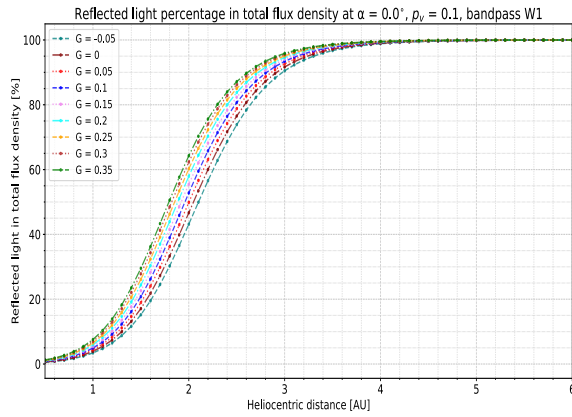
Figure D.2.1: Percentage of reflected light in total flux density across heliocentric distance for $p_v = 0.1$ and $R_{IR-Vis} = 1$ within bandpass W1. Note: $\alpha = 0°$ and $\varepsilon = 0.9$.
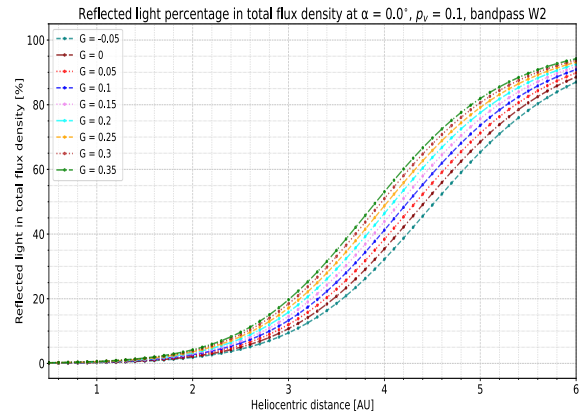
Figure D.2.2: Idem as Figure D.2.1 but at W2.
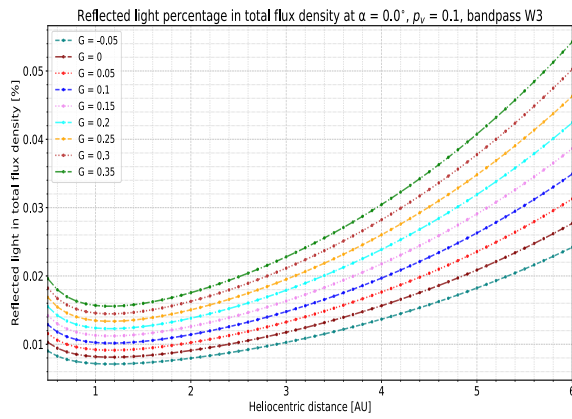
Figure D.2.3: Idem as Figure D.2.1 but at W3.
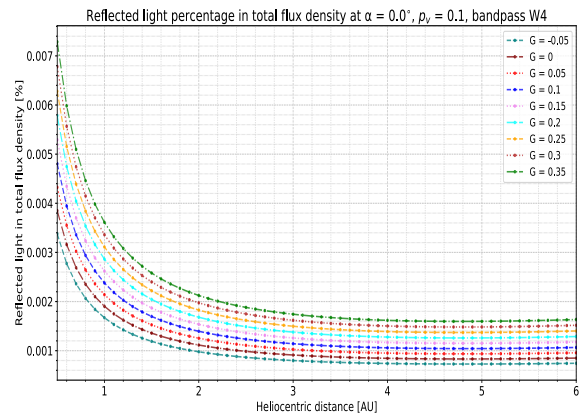
Figure D.2.4: Idem as Figure D.2.1 but at W4.

Effective facet area in view plots for mosaics of respective asteroids

E.1. 15 Eunomia with DAMIT light curve ID #8 for mosaics 1-12
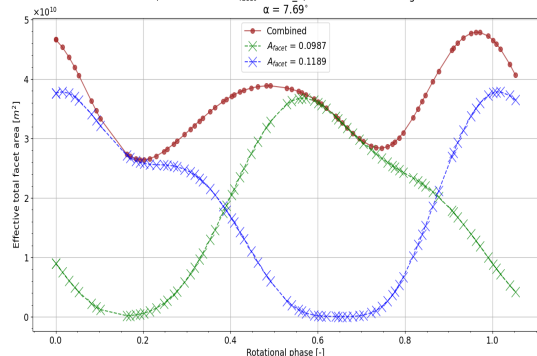
Figure E.1.1: Effective facet area in view versus rotational phase of 15 Eunomia under distributed surface albedo of mosaic 1 and light curve parameters of DAMIT ID #8.
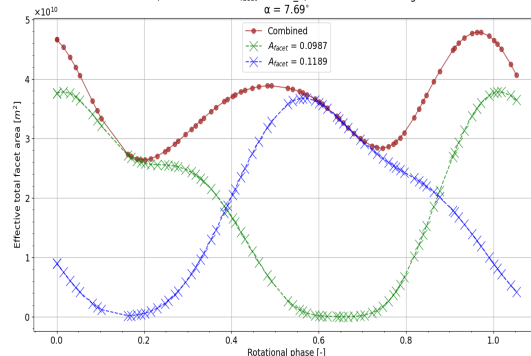
Figure E.1.2: Idem as Figure E.1.1 but for mosaic 2.
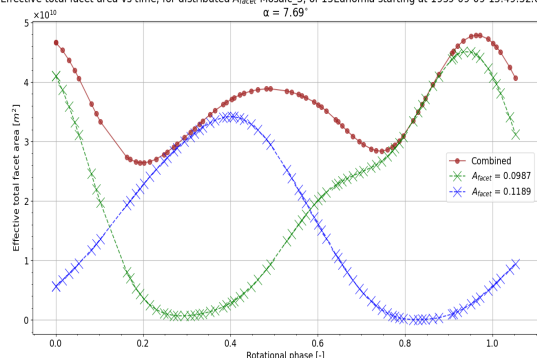
Figure E.1.3: Idem as Figure E.1.1 but for mosaic 3.
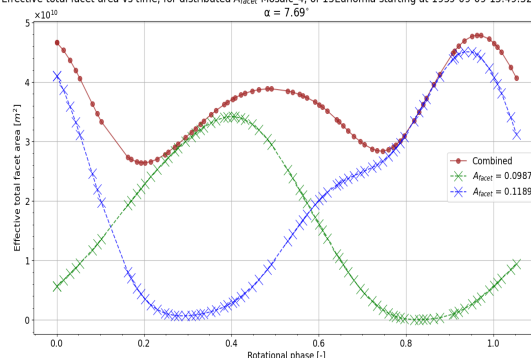
Figure E.1.4: Idem as Figure E.1.1 but for mosaic 4.
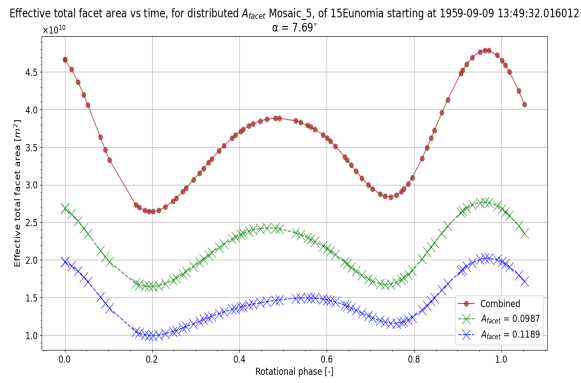
Figure E.1.5: Idem as Figure E.1.1 but for mosaic 5.
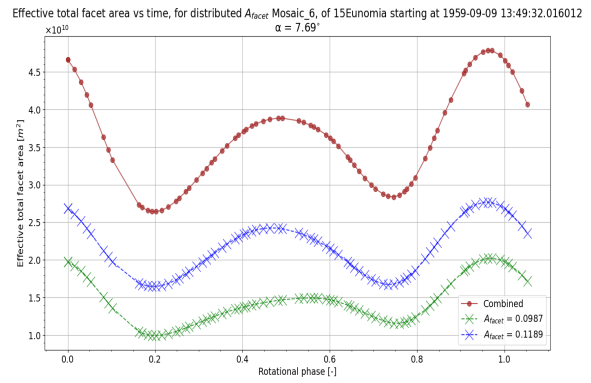
Figure E.1.6: Idem as Figure E.1.1 but for mosaic 6.
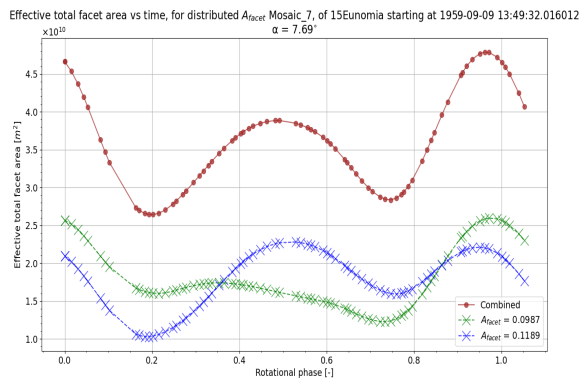
Figure E.1.7: Idem as Figure E.1.1 but for mosaic 7.
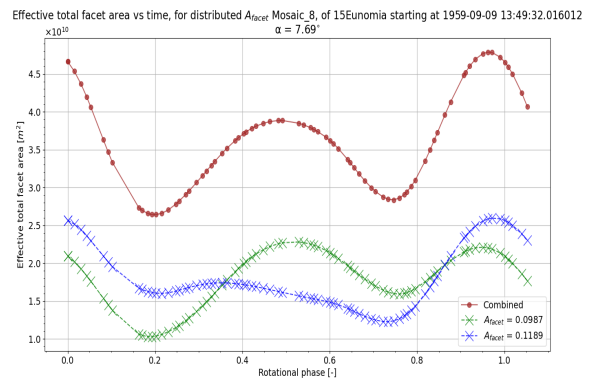
Figure E.1.8: Idem as Figure E.1.1 but for mosaic 8.
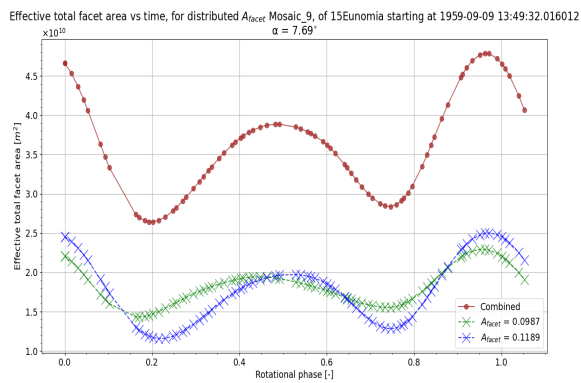
Figure E.1.9: Idem as Figure E.1.1 but for mosaic 9.
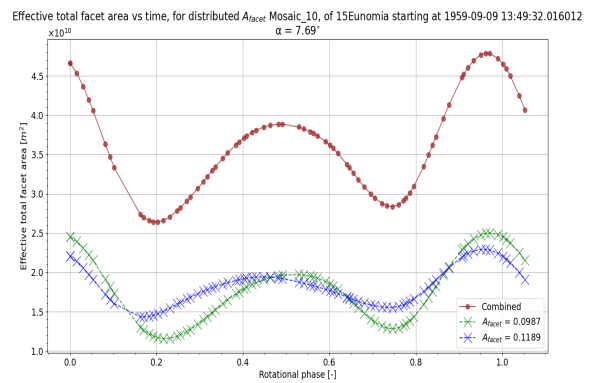
Figure E.1.10: Idem as Figure E.1.1 but for mosaic 10.
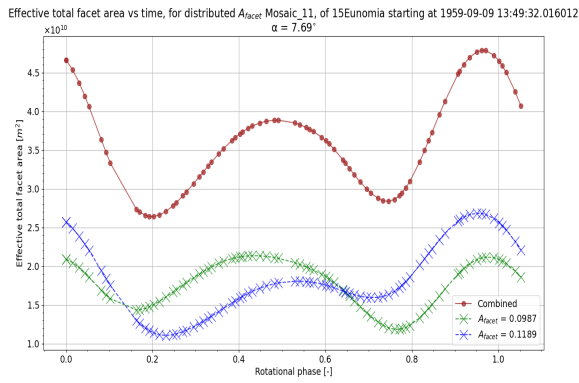
Figure E.1.11: Idem as Figure E.1.1 but for mosaic 11.
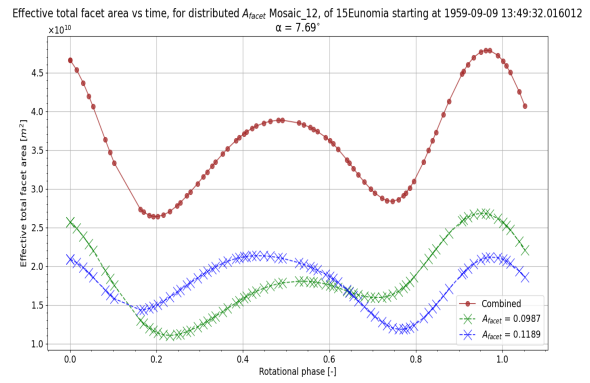
Figure E.1.12: Idem as Figure E.1.1 but for mosaic 12.

E.2. 216 Kleopatra with DAMIT light curve ID #8 for mosaics 1-12
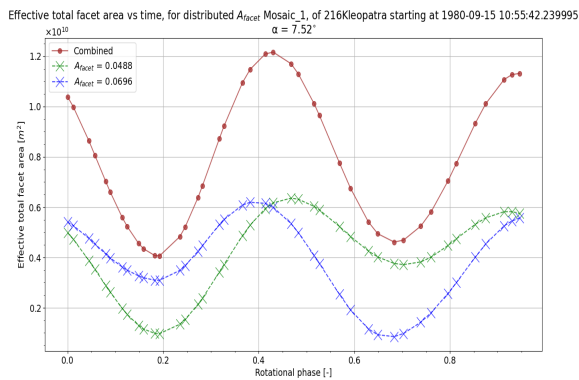
Figure E.2.1: Effective facet area in view versus rotational phase of 216 Kleopatra under distributed surface albedo of mosaic 1 and light curve parameters of DAMIT ID #8.
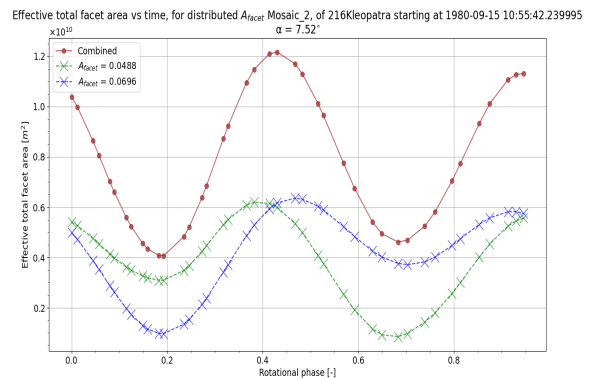
Figure E.2.2: Idem as Figure E.2.1 but for mosaic 2.
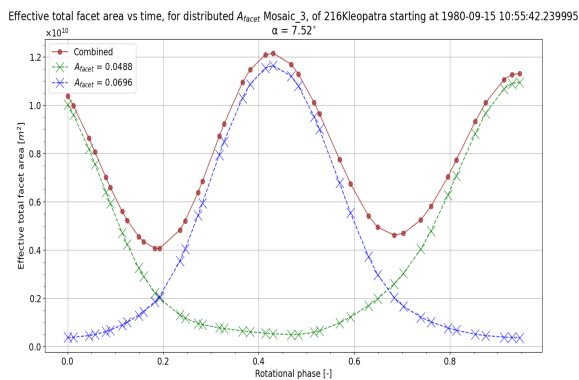
Figure E.2.3: Idem as Figure E.2.1 but for mosaic 3.
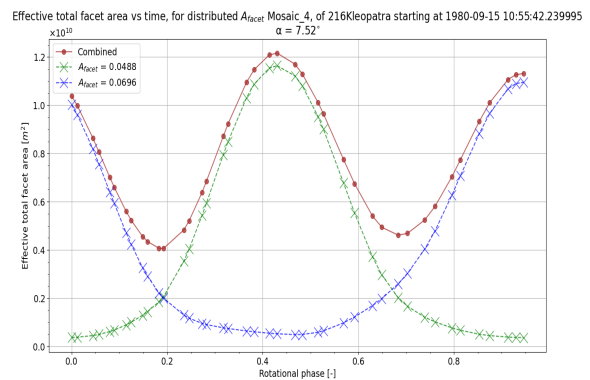
Figure E.2.4: Idem as Figure E.2.1 but for mosaic 4.
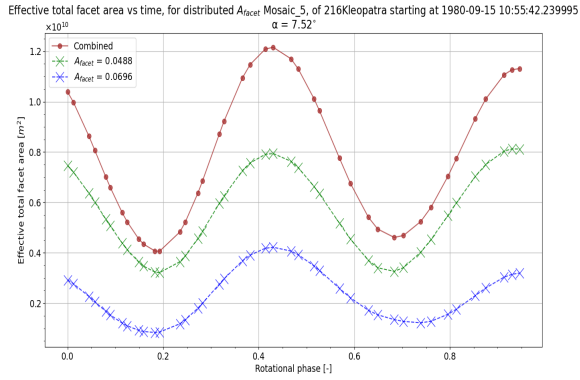
Figure E.2.5: Idem as Figure E.2.1 but for mosaic 5.
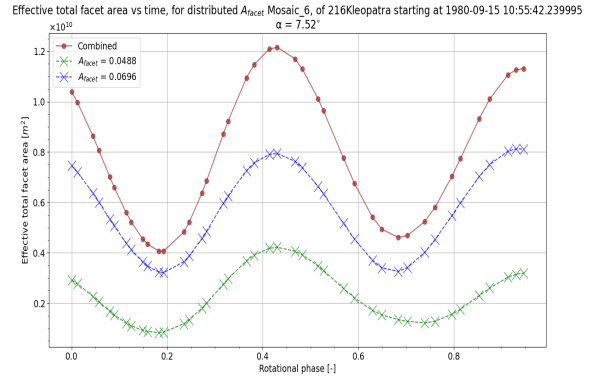
Figure E.2.6: Idem as Figure E.2.1 but for mosaic 6.
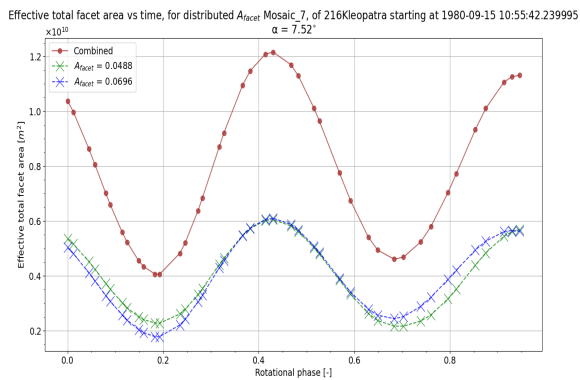
Figure E.2.7: Idem as Figure E.2.1 but for mosaic 7.
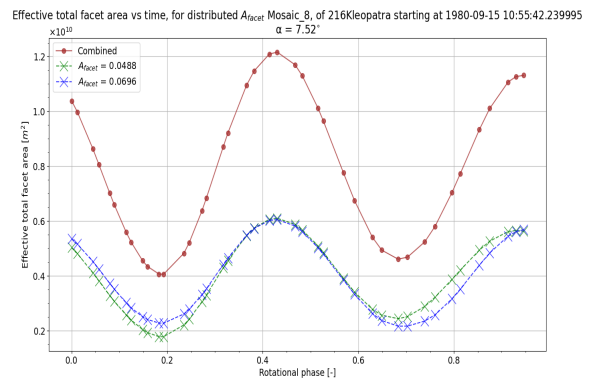
Figure E.2.8: Idem as Figure E.2.1 but for mosaic 8.
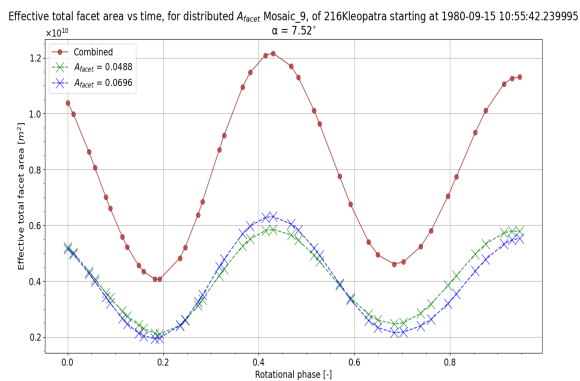
Figure E.2.9: Idem as Figure E.2.1 but for mosaic 9.
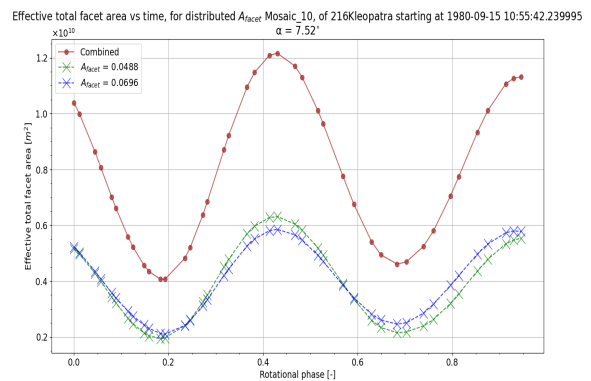
Figure E.2.10: Idem as Figure E.2.1 but for mosaic 10.
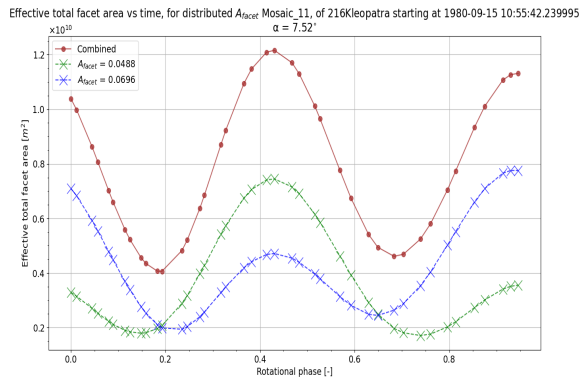
Figure E.2.11: Idem as Figure E.2.1 but for mosaic 11.
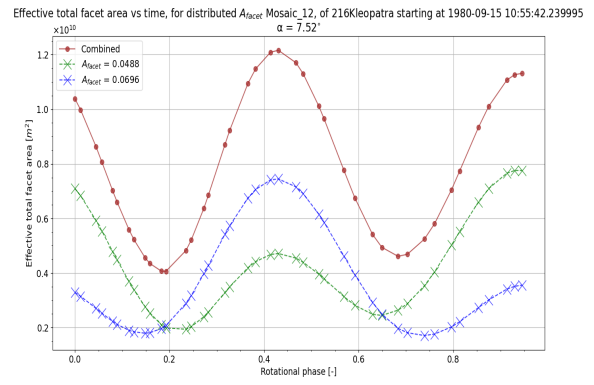
Figure E.2.12: Idem as Figure E.2.1 but for mosaic 12.

F

Percentage of reflected light in total flux density with constant relative reflectance across WISE bands

The reflected and thermal flux densities have been calculated without applying a corrective R_{IR-Vis} to the albedo across the four WISE bands. That is, it was assumed that the geometric albedo in the visible spectrum was the same in the four WISE bands.

F.1. 15 Eunomia
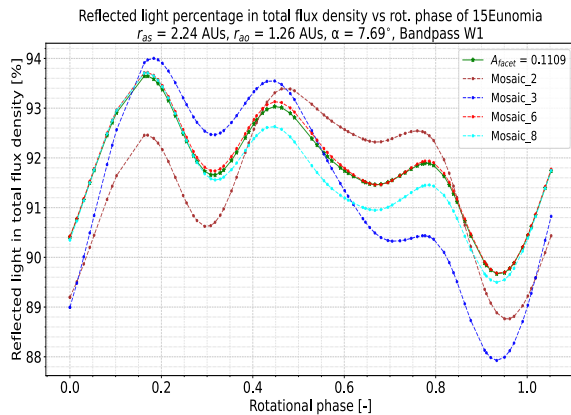
Figure F.1.1: Percentage of reflected to total flux density at bandpass W1 of 15 Eunomia against observation - DAMIT validation ID #8 taken from Chang et al. (1959). Percentage curves correspond to mosaics 2, 3, 6, & 8. The reflected light percentage produced by a homogeneous facet albedo of A_v plotted in solid green for reference. No R_{IR-Vis} factor applied.
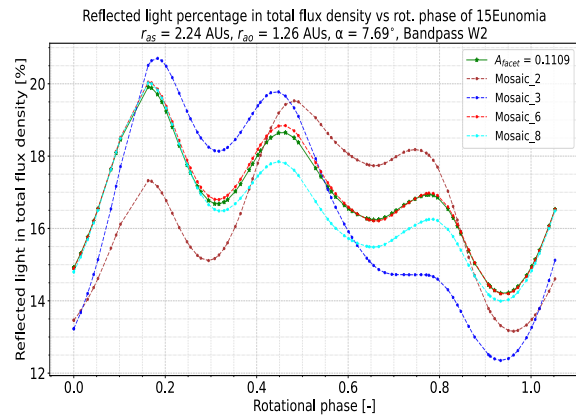
Figure F.1.2: Idem as Figure F.1.1 but at bandpass W2
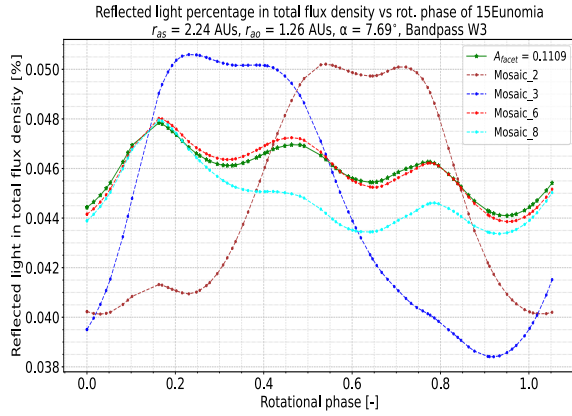
Figure F.1.3: Idem as Figure F.1.1 but at bandpass W3
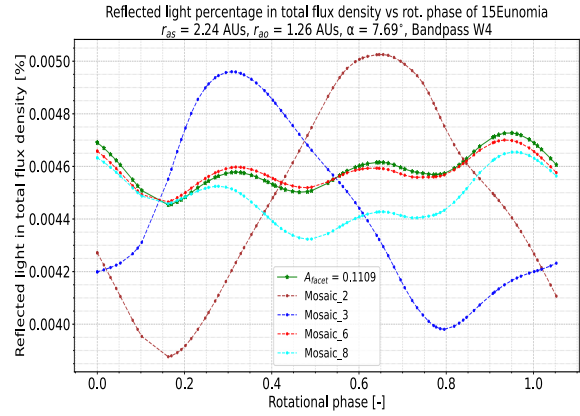
Figure F.1.4: Idem as Figure F.1.1 but at bandpass W4

F.2. 216 Kleopatra
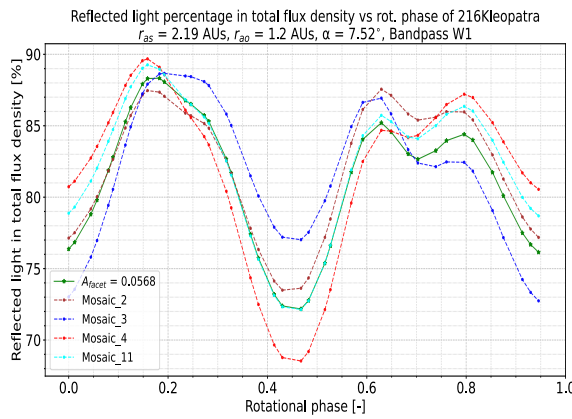
Figure F.2.1: Percentage of reflected to total flux density at bandpass W1 of 216 Kleopatra against observation - DAMIT validation ID #8 taken from Kennedy & Tholen (1982). Percentage curves correspond to mosaics 2, 3, 4, & 11. The reflected light percentage produced by a homogeneous facet albedo of A_v plotted in solid green for reference. No R_{IR-Vis} factor applied.
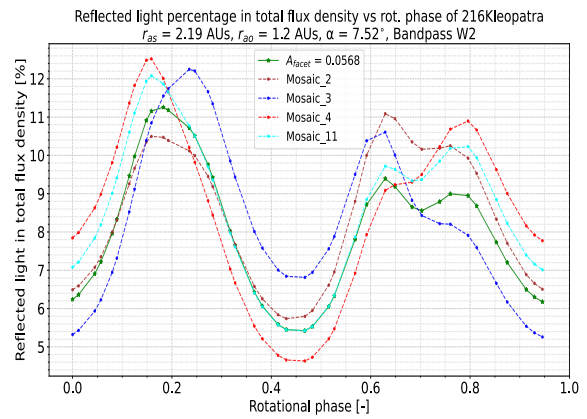
Figure F.2.2: Idem as Figure F.2.1 but at bandpass W2
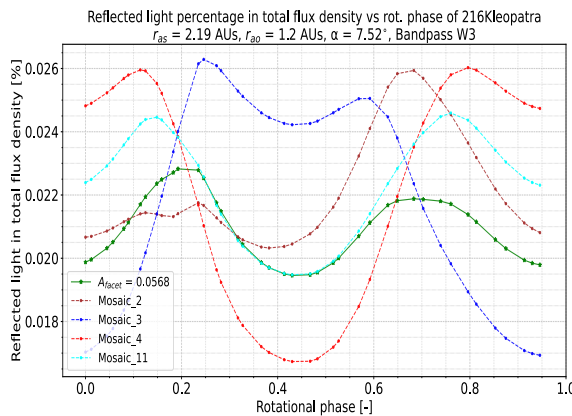
Figure F.2.3: Idem as Figure F.2.1 but at bandpass W3
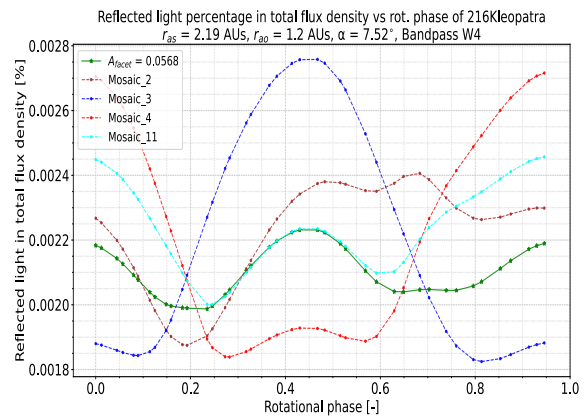
Figure F.2.4: Idem as Figure F.2.1 but at bandpass W4

G

Flux densities of different ellipsoidal dimensions
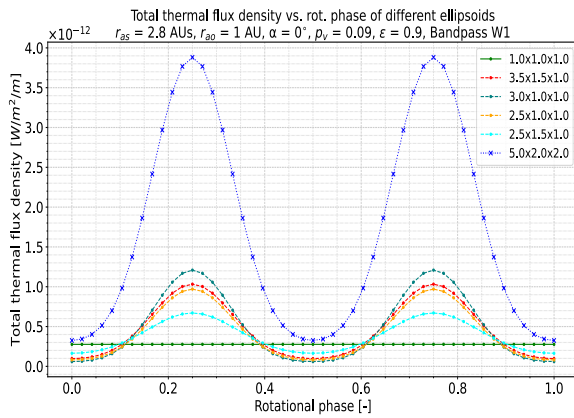
Figure G.0.1: Thermal flux density at bandpass W1 of different ellipsoids. All curves have a homogeneous surface albedo with $p_v = 0.09$. Green curve corresponds to that of a sphere. Heliocentric distance $r_{as} = 2.8$ AUs. $\alpha = 0°$, $\varepsilon = 0.9$, and $G = 0.15$.
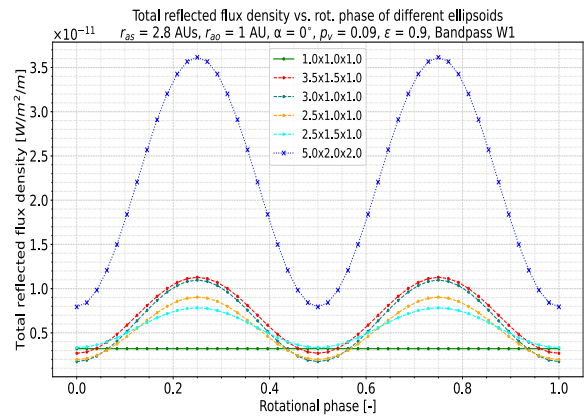
Figure G.0.2: Reflected flux density at bandpass W1 of different ellipsoids. All curves have a homogeneous surface albedo with $p_v = 0.09$. Green curve corresponds to that of a sphere. Heliocentric distance $r_{as} = 2.8$ AUs. $\alpha = 0°$, $\varepsilon = 0.9$, and $G = 0.15$.
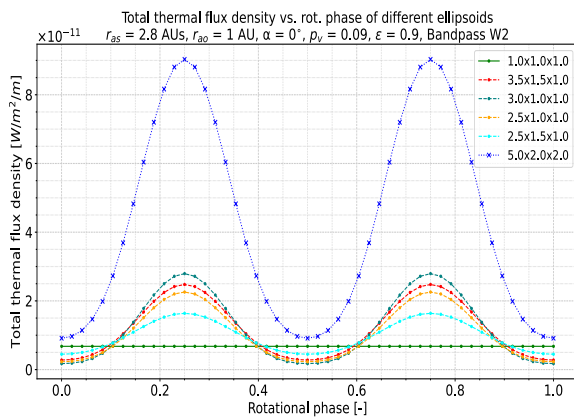
Figure G.0.3: Idem as Figure G.0.1 but at bandpass W2.
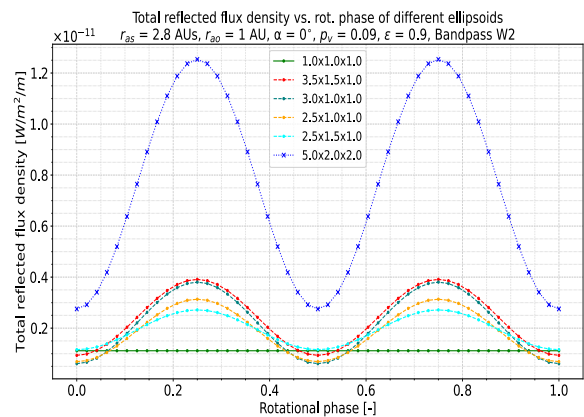
Figure G.0.4: Idem as Figure G.0.2 but at bandpass W2.
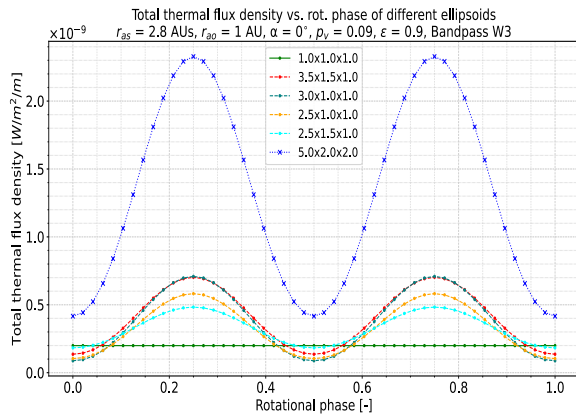
Figure G.0.5: Idem as Figure G.0.1 but at bandpass W3.
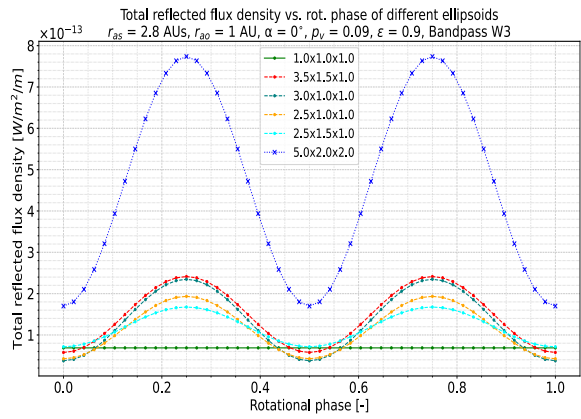
Figure G.0.6: Idem as Figure G.0.2 but at bandpass W3.
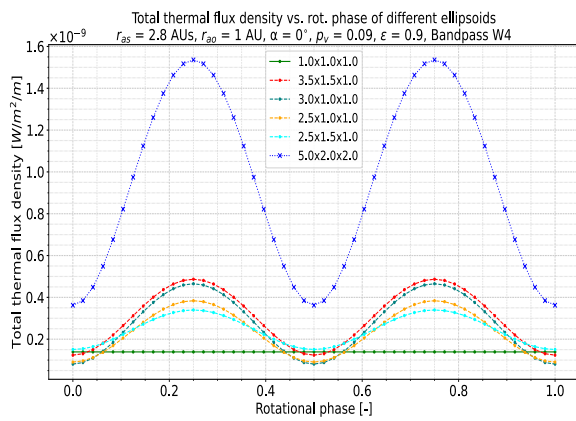
Figure G.0.7: Idem as Figure G.0.1 but at bandpass W4.
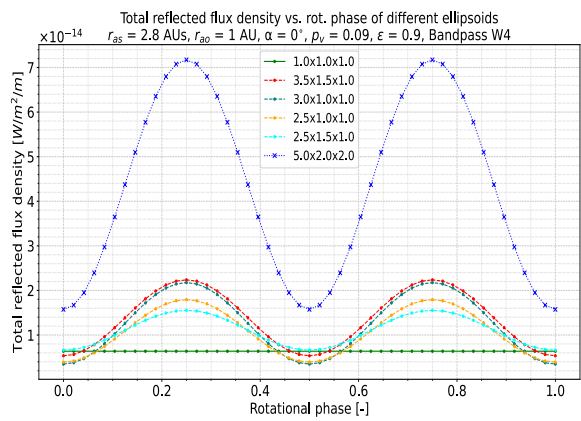
Figure G.0.8: Idem as Figure G.0.2 but at bandpass W4.

118

Bibliography

[1] P. A. Abell, B. W. Barbee, P. W. Chodas, J. Kawaguchi, R. R. Landis, D. D. Mazanek, and P. Michel. Human Exploration of Near-Earth Asteroids. In *Asteroids IV*, pages 855–880, 2015.

[2] Ag2gaeh. Ellipsoid: sphere, ellipsoid of revolution, triaxial ellipsoid, 2015. URL https://en.wikipedia.org/wiki/File:Ellipsoide.svg. Visited on: November 2020.

[3] NASA/IPAC Infrared Science Archive. IRS Instrument Handbook. 2.7 Peak-Up Imaging, 2020. URL https://irsa.ipac.caltech.edu/data/SPITZER/docs/irs/irsinstrumenthandbook/8/. Visited on: October 2020.

[4] R. P. Binzel. Human spaceflight: Find asteroids to get to Mars. *Nature*, 514(7524):559–561, 2014.

[5] W. F. Bottke, D. D. Durda, D. Nesvorný, R. Jedicke, A. Morbidelli, D. Vokrouhlický, and H. F. Levison. Linking the collisional history of the main asteroid belt to its dynamical excitation and depletion. *Icarus*, 179 (1):63–94, 2005.

[6] W. F. Bottke, D. Vokrouhlický, D. P. Rubincam, and D. Nesvorný. The Yarkovsky and Yorp Effects: Implications for Asteroid Dynamics. *Annual Review of Earth and Planetary Sciences*, 34:157–191, 2006.

[7] E. Bowell, B. Hapke, D. Domingue, K. Lumme, J. Peltoniemi, and A. W. Harris. Application of photometric models to asteroids. In *Asteroids II*, pages 524–556, 1989.

[8] R. H. Brown. Ellipsoidal geometry in asteroid thermal models: The standard radiometric model. *Icarus*, 64(1):53–63, 1985.

[9] H. Campins, K. Hargrove, N. Pinilla-Alonso, E. S. Howell, M. S. Kelley, J. Licandro, T. Mothé-Diniz, Y. Fernández, and J. Ziffer. Water ice and organics on the surface of the asteroid 24 Themis. *Nature*, 464(7293): 1320–1321, 2010.

[10] M. T. Capria, S. Marchi, M. C. de Sanctis, A. Coradini, and E. Ammannito. The activity of main belt comets. *Astronomy & Astrophysics*, 537:A71, 2012.

[11] P. R. Christensen, J. L. Bandfield, V. E. Hamilton, D. A. Howard, M. D. Lane, J. L. Piatek, S. W. Ruff, and W. L. Stefanov. A thermal emission spectral library of rock-forming minerals. *Journal of Geophysical Research*, 105(E4):9735–9740, 2000.

[12] M. Delbo and A. W. Harris. Physical properties of near-Earth asteroids from thermal infrared observations and thermal modeling. *Meteoritics & Planetary Science*, 37:1929–1936, 2002.

[13] M. Delbo, A. W. Harris, R. P. Binzel, P. Pravec, and J. K. Davies. Keck observations of near-Earth asteroids in the thermal infrared. *Icarus*, 166(1):116–130, 2003.

[14] M. Delbo, M. Mueller, J. P. Emery, B. Rozitis, and M. T. Capria. Asteroid thermophysical modeling. In *Asteroids IV*, pages 107–128, 2015.

[15] F. E. DeMeo, R. P. Binzel, S. M. Slivan, and S. J. Bus. An extension of the bus asteroid taxonomy into the near-infrared. *Icarus*, 202(1):160–180, 2009.

[16] DTR. Platonic solid, 2019. URL https://commons.wikimedia.org/wiki/Platonic_solid. Visited on: November 2020.

[17] J. Durech. Private communication, October 2020.

[18] J. Durech and V. Sidorin. DAMIT. https://astro.troja.mff.cuni.cz/projects/damit/, 2008. Visited on: April 2020.

[19] J. Durech, V. Sidorin, and M. Kaasalainen. DAMIT: a database of asteroid models. *Astronomy & Astrophysics*, vol. 513: pages A46, 2010.

[20] J. Durech, B. Carry, M. Delbo, M. Kaasalainen, and M. Viikinkoski. Asteroid Models from Multiple Data Sources. In *Asteroids IV*, pages 183–202, 2015.

[21] J. P. Emery, Y. R. Fernández, M. S. P. Kelley, K. T. Warden, C. Hergenrother, D. S. Lauretta, M. J. Drake, H. Campins, and J. Ziffer. Thermal infrared observations and thermophysical characterization of OSIRIS-REx target asteroid (101955) Bennu. *Icarus*, 234:17–35, 2014.

[22] A. Gibbings, J. M. Hopkins, D. Burns, M. Vasile, and I. Watson. On testing laser ablation processes for asteroid deflection. In *IAA Planetary Defense Conference*, 2011.

[23] C. A. Gueymard. The sun's total and spectral irradiance for solar energy applications and solar radiation models. *Solar Energy*, 76(4):423–453, 2004.

[24] H. H. Hsieh and D. Jewitt. A Population of Comets in the Main Asteroid Belt. *Science*, 312(5773):561–563, 2006.

[25] B. Hapke. *Theory of Reflectance and Emittance Spectroscopy*. Cambridge University Press, Cambridge, U.K., 2 edition, 2012.

[26] A. W. Harris. A Thermal Model for Near-Earth Asteroids. *Icarus*, 131:291–301, 1998.

[27] A. W. Harris and L. Drube. How to Find Metal-rich Asteroids. *Astrophysical Journal Letters*, 785(1):L4, 2014.

[28] A. W. Harris and J. S. V. Lagerros. Asteroids in the Thermal Infrared. In *Asteroids III*, pages 205–218, 2002.

[29] A. W. Harris, M. Boslough, C. R. Chapman, L. Drube, P. Michel, and A. W. Harris. Asteroid Impacts and Modern Civilization: Can We Prevent a Catastrophe? In *Asteroids IV*, pages 835–854, 2015.

[30] J. D. Hunter. Matplotlib: A 2D graphics environment. *Computing in Science & Engineering*, vol. 9: pages 90–95, 2007.

[31] IAU Minor Planet Center. Latest Published Data, 2020. URL https://minorplanetcenter.net//mpc/summary. Visited on: August 2020.

[32] H. Jiang, L. Yu, and J. Ji. Revisiting the Advanced Thermal Physical Model: New Perspectives on Thermophysical Characteristics of (341843) 2008 EV5 from Four-band WISE Data with the Sunlight-reflection Model. *Astrophysical Journal*, 158(5), 2019.

[33] H. L. Johnson. The Absolute Calibration of the Arizona Photometry. *Communications of the Lunar and Planetary Laboratory*, 3:73–77, 1965.

[34] M. Kaasalainen and J. Torppa. Optimization Methods for Asteroid Lightcurve Inversion. I. Shape Determination. *Icarus*, 153(1):24–36, 2001.

[35] K. Kosmo, M. Pryor, P. Lubin, G. Hughes, H. O'Neill, P. Meinhold, J. Suen, J. Riley, J. Griswold, B. V. Cook, I. Johansson, Q. Zhang, K. Walsh, C. Melis, M. Kangas, J. Bible, C. Motta, T. Brashears, S. Mathew, and J. Bollag. De-starlite - a directed energy planetary defense mission. *Proceedings of SPIE - The International Society for Optical Engineering*, 9226, 2014.

[36] M. Küppers, L. O'Rourke, D. Bockelée-Morvan, V. Zakharov, S. Lee, P. von Allmen, B. Carry, D. Teyssier, A. Marston, T. Müller, J. Crovisier, M. A. Barucci, and R. Moreno. Localized sources of water vapour on the dwarf planet (1) Ceres. *Nature*, 505(7484):525–527, 2014.

[37] C. I. Lagerkvist and P. Magnusson. Asteroid Photometric Catalog V1.1. EAR-A-3-DDR-APC-LIGHTCURVE-V1.1. *NASA Planetary Data System*, 2011.

[38] J. S. V. Lagerros. Thermal physics of asteroids. I. Effects of shape, heat conduction and beaming. *Astronomy & Astrophysics*, 310:1011–1020, 1996.

[39] J. S. V. Lagerros. Thermal physics of asteroids. IV. Thermal infrared beaming. *Astronomy & Astrophysics*, 332(4):1123–1132, 1998.

[40] G. A. Landis. Materials refining on the Moon. *Acta Astronautica*, 60:906 – 915, 2007.

[41] L. A. Lebofsky, M. V. Sykes, E. F. Tedesco, and et al. A refined "standard" thermal model for asteroids based on observations of 1 Ceres and 2 Pallas. *Icarus*, 68:239–251, 1986.

[42] J. Y. Li, P. Helfenstein, B. Buratti, D. Takir, and B. E. Clark. Asteroid Photometry. In *Asteroids IV*, pages 129–150, 2015.

[43] J. Licandro, H. Campins, M. Kelley, K. Hargrove, N. Pinilla-Alonso, D. Cruikshank, A. S. Rivkin, and J. Emery. (65) Cybele: detection of small silicate grains, water-ice, and organics. *Astronomy and Astrophysics*, 525:A34, 2011.

[44] C. Lienert. Vectors in Three Dimensions FLC. https://cnx.org/contents/udxJc5yYQ4/Vectors-in-Three-Dimensions-FLC, 2020. Visited on: October 2020.

[45] J. J. Lissauer and I. de Pater. *Fundamental Planetary Science*. Cambridge University Press, 32 Avenue of the Americas, New York, NY 10013-2473, USA, 2013.

[46] M. Murphy. History of Asteroid Classification. https://vissiniti.com/asteroid-classification/, 2019. Visited on: December 2020.

[47] A. Mainzer, F. Usui, and D. E. Trilling. Space-based thermal infrared studies of asteroids. In *Asteroids IV*, pages 89–106, 2015.

[48] S. R. Majewski. ASTR 5610 (Majewski) Lecture Notes: FLUXES, MAGNITUDES, COLORS, AND FILTER SYSTEMS, 2020. URL https://faculty.virginia.edu/ASTR5610/lectures/LECTURE2/lec2a.html. Visited on: November 2020.

[49] E. E. Mamajek, A. Prsa, G. Torres, P. Harmanec, M. Asplund, P. D. Bennett, N. Capitaine, J. Christensen-Dalsgaard, E. Depagne, W. M. Folkner, M. Haberreiter, S. Hekker, J. L. Hilton, V. Kostov, D. W. Kurtz, J. Laskar, B. D. Mason, E. F. Milone, M. M. Montgomery, M. T. Richards, J. Schou, and S. G. Stewart. IAU 2015 Resolution B3 on Recommended Nominal Conversion Constants for Selected Solar and Planetary Properties. *arXiv e-prints*, page arXiv:1510.07674, 2015.

[50] W. McKinney. Data structures for statistical computing in python. In *Proceedings of the 9th Python in Science Conference*, pages 51–56, 2010.

[51] P. Michel, F. E. DeMeo, and W. F. Bottke. *Asteroids IV*. University of Arizona Press, Tucson, USA, 2015.

[52] P. Michel, F. E. DeMeo, and W. F. Bottke. Asteroids: Recent Advances and New Perspectives. In *Asteroids IV*, pages 3–10, 2015.

[53] M. Mueller. Surface Properties of Asteroids from Mid-Infrared Observations and Thermophysical Modeling. *Freien Universität Berlin*, 2007.

[54] N. Myhrvold. Asteroid thermal modeling in the presence of reflected sunlight with an application to WISE/NEOWISE observational data. *ArXiv e-prints*, page arXiv:1605.06490, 2016.

[55] N. Myhrvold. Supplemental Information for "Asteroid thermal modeling in the presence of reflected sunlight". *Icarus*, 303:91–113, 2017.

[56] N. Myhrvold. Asteroid thermal modeling in the presence of reflected sunlight. *Icarus*, 303:91–113, 2018.

[57] N. Myhrvold. What's Wrong with NEOWISE, June 2018. URL https://medium.com/@nathanpmyhrvold/myhrvold-guide-to-neowise-4866a2f7b76d. Visited on: July 2020.

[58] N. Myhrvold. Response to Wright et al. 2018: Even more serious problems with NEOWISE. *ArXiv e-prints*, page arXiv:1812.06516, 2018.

[59] NASA. Asteroids. https://nssdc.gsfc.nasa.gov/planetary/text/asteroids.txt, 2015. Visited on: October 2020.

[60] NASA. NASA Response to Recent Paper on NEOWISE Asteroid Size Results, May 2016. URL https://www.nasa.gov/feature/nasa-response-to-recent-paper-on-neowise-asteroid-size-results. Visited on: July 2020.

[61] NASA. Asteroids, 2019. URL https://solarsystem.nasa.gov/asteroids-comets-and-meteors/asteroids/in-depth/. Visited on: August 2020.

[62] NASA-JPL. HORIZONS Web-Interface, 2020. URL https://ssd.jpl.nasa.gov/horizons.cgi. Visited on: November 2020.

[63] NASA-JPL. Solar System Dynamics: JPL Small-Body Database Browser, 2020. URL https://ssd.jpl.nasa.gov/sbdb.cgi#top. Visited on: November 2020.

[64] NASA/IPAC. Spitzer Telescope Handbook: Appendix A. Infrared Astronomy, 2020. URL https://irsa.ipac.caltech.edu/data/SPITZER/docs/spitzermission/missionoverview/spitzertelescopehandbook/19/. Visited on: November 2020.

[65] NASA/JPL-Caltech. NEO Basics, 2020. URL https://cneos.jpl.nasa.gov/about/neo_groups.html. Visited on: August 2020.

[66] NASA/JPL-Caltech/JAXA/ESA. Asteroids scale, 2011. URL https://en.wikipedia.org/wiki/File:Asteroidsscale.jpg. Visited on: July 2020.

[67] M. C. Nolan, C. Magri, E. S. Howell, L. A. M. Benner, J. D. Giorgini, C. W. Hergenrother, R. S. Hudson, D. S. Lauretta, J. L. Margot, S. J. Ostro, and D. J. Scheeres. Asteroid (101955) Bennu Shape Model V1.0. EAR-A-I0037-5-BENNUSHAPE-V1.0. *NASA Planetary Data System*, 2013.

[68] nschloe. meshzoo. https://github.com/nschloe/meshzoo, 2020. Visited on: September 2020.

[69] P. Scheirich. Asteroid (and Comet) Groups. http://sajri.astronomy.cz/asteroidgroups/groups.htm, 2018. Visited on: September 2020.

[70] R. Pierce. 3D Rotations and Euler angles in Python, 2020. URL https://www.meccanismocomplesso.org/en/3d-rotations-and-euler-angles-in-python/. Visited on: November 2020.

[71] L. Pohl. Heat diffusion equation and thermophysical modelling of asteroids. *Charles University in Prague*, 2014.

[72] D. Prialnik and E. D. Rosenberg. Can ice survive in main-belt comets? Long-term evolution models of comet 133P/Elst-Pizarro. *Monthly Notices of the Royal Astronomical Society*, 399(1):L79–L83, 2009.

[73] A. S. Rivkin and J. P. Emery. Detection of ice and organics on an asteroidal surface. *Nature*, 464(7293): 1322–1323, 2010.

[74] C. Rodrigo and E. Solano. The SVO Filter Profile Service, 2020. URL http://svo2.cab.inta-csic.es/theory/fps/index.php?mode=browse. Visited on: December 2020.

[75] G. Van Rossum and D. Jr Fred. *Python tutorial*. Centrum voor Wiskunde en Informatica, Amsterdam, The Netherlands, 1995.

[76] B. Rozitis. Private communication, January 2021.

[77] B. Rozitis and S. F. Green. Directional characteristics of thermal-infrared beaming from atmosphereless planetary surfaces - a new thermophysical model. *Monthly Notices of the Royal Astronomical Society*, 415: 2042–2062, 2011.

[78] B. Rozitis and S. F. Green. The influence of rough surface thermal-infrared beaming on the Yarkovsky and YORP effects. *Monthly Notices of the Royal Astronomical Society*, 423(1):367–388, 2012.

[79] J. W. Salisbury and N. Vergo. Infrared (2.1-25 μm) spectra of minerals. *Johns Hopkins University Press*, 346:267, 1992.

[80] J. W. Salisbury, D. M. D'Aria, and E. Jarosewich. Midinfrared (2.5-13.5 μm) reflectance spectra of powdered stony meteorites. *Icarus*, 92(2):280–297, 1991.

[81] N. Schorghofer. The Lifetime of Ice on Main Belt Asteroids. *Astrophysical Journal*, 682(1):697–705, 2008.

[82] Z. R. Sibbing. ARM: Asteroid Reflection Model. The implementation of an asteroid polarimetry model and its application to interpret asteroid (3200) Phaethon observations. *Delft University of Technology*, 2018.

[83] D. M. Stam. *AE4890-11 Planetary Sciences I: Light and Radiation.* TU Delft, November 2018.

[84] E. F. Tedesco. Asteroid. https://www.britannica.com/science/asteroid, 2020. Visited on: December 2020.

[85] The Guardian (by Zoe Corbyn). Nathan Myhrvold: 'NASA doesn't want to admit it's wrong about asteroids', June 2018. URL https://www.theguardian.com/science/2018/jun/24/nathan-myhrvold-inventor-microsoft-patent-nasa-asteroid-data-pizza-science. Visited on: July 2020.

[86] The New York Times (by Kenneth Chang). How Big Are Those Killer Asteroids? A Critic Says NASA Doesn't Know., May 2016. URL https://www.nytimes.com/2016/05/24/science/asteroids-nathan-myhrvold-nasa.html. Visited on: June 2020.

[87] Tschmits. UV Mapping, 2008. URL https://en.wikipedia.org/wiki/File:UVMapping.png. Visited on: November 2020.

[88] H. C. van de Hulst. *Multiple Light Scattering, Tables, Formulas, and Applications, Vols. 1 and 2.* Academic Press, New York, U.S.A., 1980.

[89] J. Ďurech, M. Delbo', B. Carry, J. Hanuš, and V. Alí-Lagoa. Asteroid shapes and thermal properties from combined optical and mid-infrared photometry inversion. *Astronomy & Astrophysics*, 604:A27, 2017.

[90] D. Vokrouhlický, W. F. Bottke, S. R. Chesley, D. J. Scheeres, and T. S. Statler. The Yarkovsky and YORP Effects. In *Asteroids IV*, pages 509–531, 2015.

[91] K. F. Wakker. *Fundamentals of Astrodynamics.* TU Delft, 2015.

[92] I. Webster. Asteroid Database and Mining Rankings - Asterank. http://www.asterank.com/, 2019. Visited on: July 2020.

[93] E. Wright, A. Mainzer, J. Masiero, T. Grav, R. Cutri, and J. Bauer. Response to "An empirical examination of WISE/NEOWISE asteroid analysis and results". *ArXiv e-prints*, page arXiv:1811.01454, 2018.

[94] E. L. Wright. Quadrature formulae for the WISE passbands. *American Astronomical Society Meeting Abstracts #221*, 221, 2013.

[95] R. M. Zubrin, A. C. Muscatello, and M. Berggren. Integrated Mars In Situ Propellant Production System. *Journal of Aerospace Engineering*, 26:43 – 56, 2013.